

MULTISCALE STOCHASTIC FRACTURE MECHANICS OF COMPOSITES INFORMED BY IN-SITU X-RAY CT TESTS

A thesis submitted to The University of Manchester for the degree of
Doctor of Philosophy
in the Faculty of Science and Engineering

2016

RĂZVAN M. SENCU

SCHOOL OF MECHANICAL, AEROSPACE AND CIVIL
ENGINEERING

TABLE OF CONTENTS

TABLE OF CONTENTS	2
NOMENCLATURE	10
LIST OF TABLES	14
LIST OF FIGURES	15
ABSTRACT	21
LAY ABSRACT	21
KEYWORDS	22
DECLARATION	23
COPYRIGHT	23
ACKNOWLEDGEMENTS	25
CHAPTER 1. INTRODUCTION	28

1.1. Motivation	28
1.2. Objectives.....	28
1.3. Outline of the thesis.....	29
CHAPTER 2. LITERATURE REVIEW	31
2.1. Introduction.....	31
2.2. Overview of existing multiscale modelling methods for scale transfer	32
2.3. Uncoupled models	32
2.4. Coupled models	34
2.4.1. Concurrent approach.....	37
2.4.2. Hierarchical approach	38
2.4.3. Mixed hierarchical-concurrent approach.....	43
2.5. Summary of existing multiscale modelling methods	46
2.6. Numerical Crack Models	48
2.7. X-ray Computed Tomography	49
2.7.1. Previous X-ray CT tests in fibre composites at fibre level.....	50
2.8. Summary	53
CHAPTER 3. A NEW METHOD FOR 2D MULTISCALE STOCHASTIC FRACTURE MODELLING	55
3.1. Introduction.....	55

3.2.	The new multiscale stochastic fracture mechanics framework	55
3.3.	Bayes inference model for overlapping MeEs with biased crack paths	59
3.4.	Construction of macro-scale elements (MaEs)	64
3.5.	Fracture energy mapping rules	68
3.7.1.	Merging and splitting approach	69
3.7.2.	Crack path decomposition approach	71
3.6.	Cohesive interface crack model	72
3.7.	Summary and conclusions	74
CHAPTER 4. IMPLEMENTATION AND VALIDATION OF THE NEW MULTI-SCALE STOCHASTIC METHOD OF MODELLING FRACTURE IN 2D		76
4.1.	Introduction	76
4.2.	Meso-scale finite element modelling and validation	76
4.3.	CASE STUDY 1: Investigation of volume fractions variability on fracture process	78
4.3.1.	Boundary conditions	80
4.3.2.	Material properties	80
4.3.3.	Mesh information	81
4.3.4.	Modelling of transverse crack growth	82
4.3.5.	Fibre breaking effects in longitudinal meso-scale model	85

4.4. CASE STUDY 2: Investigation of interface strength variability, boundary, size and stochastic effects.....	88
4.4.1. Geometrical surveying.....	88
4.4.2. Material properties	91
4.4.3. Effects of interface strength on fracture process.....	92
4.4.4. Boundary condition effects	94
4.4.5. Size effects	94
4.4.6. Stochastic simulations	99
4.4.7. Comparison of meso- and macro-crack propagation.....	102
4.5. Multiscale coupling using coarse meshes	104
4.6. Multiscale coupling using Bayesian inference model	106
4.7. Computer implementation.....	108
4.8. Summary	109
CHAPTER 5. IN-SITU X-RAY COMPUTED TOMOGRAPHY TESTS OF CARBON FIBRE REINFORCED POLYMERS	111
5.1. Introduction.....	111
5.2. Initial X-ray CT scan using laboratory cone emitter source	112
5.2.1. Experimental details at HMXIF facility	113
5.2.2. Attempts of direct segmentation	114
5.3. Non-X-ray CT loading tests.....	115

5.3.1.	Description of the Deben CT-500 rig	115
5.3.2.	In-situ loading test measurements.....	116
5.4.	Development of a new in-situ micro-loading rig.....	118
5.4.1.	The mechanical components	120
5.4.2.	Data acquisition system and sensors.....	121
5.4.3.	Force and displacement data readings	121
5.4.4.	Automation and loading control	122
5.4.5.	Digital controller system	123
5.4.6.	Loading modes	123
5.4.7.	Loading setups and preparation of samples	123
5.5.	Data acquisition at Diamond-Manchester Branchline I13-2	125
5.6.	Experimental strategy at I13-2 branchline	126
5.7.	Reconstruction of image projections	127
5.8.	In-situ X-ray CT tests.....	127
5.8.1.	In-situ X-ray CT uniaxial tensile test.....	128
5.8.2.	In-situ X-ray CT three-point bending test	131
5.9.	Summary and conclusions	134
CHAPTER 6. X-RAY CT IMAGE-BASED MODEL GENERATION OF CARBON FIBRE REINFORCED POLYMER COMPOSITES		136
6.1.	Introduction.....	136

6.2.	Imaging and high-fidelity modelling challenges	136
6.3.	Overview of existing segmentation models	137
6.4.	X-ray CT dataset for reconstruction and modelling	139
6.5.	Image-based model generation	140
6.5.1.	Images filtering and pre-processing.....	141
6.5.2.	Volume delineation of different plies	145
6.5.3.	Fibre identification algorithm.....	146
6.5.4.	Image binarisation.....	147
6.5.5.	Hybrid reconstruction using binary images.....	148
6.5.6.	New fibre tracking algorithm with stack conditioning	150
6.5.7.	Global overlapping stack filtering	151
6.5.8.	Estimation of image matching and fibre shifts	152
6.5.9.	Global Bayesian inference model for optimal kernel width.....	154
6.5.10.	Local Bayesian inference model for tracking individual fibres	157
6.5.11.	Calibration of local inference model.....	159
6.5.12.	Reconstructed data filtering before final mesh generation	160
6.5.13.	Geometry reconstruction and mesh generation	161
6.6.	Summary	164

CHAPTER 7. 3D X-RAY CT IMAGE-BASED MODELLING OF DAMAGE AND FRACTURE OF FIBRE REINFORCED COMPOSITES AND VALIDATION	166
7.1. Introduction	166
7.2. Methodology of multiscale modelling and validation	167
7.3. Modelling of damage and fracture in fibre reinforced composites	169
7.3.1. Three-fibre models	170
7.3.2. Modelling FRP with high volume fraction of fibres	171
7.4. Assumptions of multiscale modelling informed by in-situ X-ray CT tensile test ...	172
7.4.1. X-ray CT image-based models at fibre scale	172
7.4.2. Meso-scale element modelling	174
7.4.3. Meso-scale modelling responses	177
7.4.4. Strength anisotropy diagrams	182
7.4.5. Scale transfer	184
7.4.6. Macro-scale mesh generation and preparation for scale transfer	185
7.4.7. Macro-scale element sets	189
7.4.8. Multiscale model simulation and validation	190
7.4.9. FE simulation runtimes and use of high performance computing facility	193
7.5. Summary and conclusions	194

CHAPTER 8. CONCLUSIONS AND RECOMMENDATIONS FOR FUTURE RESEARCH	
.....	196
8.1. Conclusions.....	196
8.2. Recommendations for future research.....	197
APPENDIX-A: 2D MESO-SCALE STRESS-DISPLACEMENT AND STRESS STRAIN RESPONSES	199
REFERENCES	206

NOMENCLATURE**Acronyms**

MsSFrM	-multiscale stochastic fracture mechanics.
MeE	-meso-scale element.
MaE	-macro-scale element.
CIE	-cohesive interface element.
BCs	-boundary conditions.
MSA	-merging and splitting approach.
CDA	-crack path decomposition approach.
CFRP	-carbon fibre reinforced polymer.
X-ray CT	-X-ray Computed Tomography.
FoV	-field of view.
RoI	-region of interest.
<i>UEP</i>	-ultimate eroding point associated to a fibre centre.

2D boundary conditions at meso and global scales

B1-X, B2-X	-meso-scale boundary conditions on X direction.
B1-Y, B2-Y	-meso-scale boundary conditions on Y direction.
G1-X, G2-X	-global-scale boundary conditions used for validation on X direction.
G1-Y, G2-Y	-global-scale boundary conditions used for validation on Y direction.

3D boundary conditions at meso-scale

<i>type-A</i>	-uniaxial tensile with restrained sides.
<i>type-B</i>	-shearing using one-third edge size bandwidth.
<i>type-C</i>	-uniaxial tensile with single restrained side.

Algebra

C	-crack path to be filtered (kernel crack).
$P(C)$	-prior probability of crack path C evaluated as a path/ image integral.
$P(E C)$	-crack paths likelihood corresponding to surrounding cracks E to match the kernel crack path C .
$P(C E)$	-Bayesian updated probability of crack C given some overlapped neighbouring crack paths E .
C_m	-set of crack paths over a neighbouring cluster.
L_i	-reduced order integration line fitted on a random crack path.
σ_f	-ultimate strength equivalent to the onset of fracture.
$\sigma_{f,u} = \sigma(u)$	-softening evolution based on the ultimate strength pitch.
G_f	-fracture energy
$G_{f,short}$	-fracture energy evaluated for short overlapping criteria.
$G_{f,long}$	-fracture energy evaluated for long overlapping criteria.

u	-finite displacement.
u_f	-final displacement.
d	-scalar degradation variable.
d_{short}	-scalar degradation variable evaluated for short overlapping criteria.
d_{long}	-scalar degradation variable evaluated for long overlapping criteria.
V_f	-fibre volume fraction.
V_m	-matrix volume fraction.
f_{xy}	-pixel gray scale intensity at pixel position (x,y) .
k_{xy}	-processing kernel value corresponding to position (x,y) .
$conv(f, k)$	-convolution of image f using image processing kernel k .
\otimes	-convolution operator that performs a piecewise multiplication.
d	-overlapping stack containing a number of X-ray CT image slices.
$d/2$	-stack overlapping distance measure in number of X-ray CT image slices.
$cov(f, g)$	-covariance of two images f and g .
\bar{f}, \bar{g}	-average pixel intensity values of images f and g respectively.
$C_{NCC}, corr(f, g)$	-normalised correlation criterion of two images f and g .

$\Delta x, \Delta y$	-position coordinates at integer pixel precision of matching peak value from correlation of images f and g .
$\delta x, \delta y$	-interpolated position coordinates at sub-pixel precision from correlation of images f and g using the neighbouring subsets around a matching peak.
K_d	-overlapping stack of slices separated into kernel slices \mathbf{K} and neighbouring overlapping slices \mathbf{N} .
$P(\mathbf{N} \mathbf{K})$	-global probability of slices \mathbf{N} to match kernel slices \mathbf{K} . This probability is evaluated as a collection of overlapping fibre centres.
$P(K \mathbf{N})$	-global Bayesian updated probability of slices K to match neighbouring slices \mathbf{N} . This probability is evaluated using a Bayesian inference model.
K	-kernel slice as a collection of $UEPs$.
N	-neighbouring slice as a collection of $UEPs$.
$P(N K)$	-local probability of UEP coordinates in slice N to match kernel slice K . This probability is evaluated as individually on each fibre centre.
$P(K N)$	-local Bayesian updated probability of UEP coordinates in slice K to match neighbouring slice N . This probability is evaluated using a Bayesian inference model.

LIST OF TABLES

Table 2-1: Summary of existing multiscale models based on the finite element method.	47
Table 4-1: Input material parameters for validation modelling.	77
Table 4-2: Input material parameters for fracture modelling.	81
Table 4-3: Mesh information of stochastic MeE models.	81
Table 4-4: Material properties and modelling parameters.	92
Table 4-5: Image based MeE simulations with modelling parameters.	98
Table 6-1: Image filters for X-ray CT datasets.	142
Table 6-2: Bayesian overlapped stack width sensitivity study.	156
Table 6-3: An overlapped partition strategy to extract image-based fibre meshes for multiscale modelling.	163
Table 7-1: Material specifications and properties for meso-scale fracture modelling.	176
Table 7-2: X-ray CT image-based models extracted in overlapping pairs from a multidirectional CFRP sample as shown in Fig. 7-5.	181
Table 7-3: Meso-scale information and global multiscale modelling using ABAQUS.	188
Table 7-4: Coupling information of macro element sets contained in different fibre orientation plies.	189

LIST OF FIGURES

Fig. 2-1: A brief summary of existing multiscale models.	32
Fig. 2-2: Concurrent multiscale model based on sub-hierarchical Voronoi individual fibre cells, transition elements and detailed micro-scale windows (Ghosh, 2008).	37
Fig. 2-3: Microstructural sample extraction and packing assembly according to (Doškář and Novák, 2013).	41
Fig. 2-4: The generalised multiscale finite element method (GMsFEM): K is a target coarse block and ω is the oversampling domain (Efendiev et al., 2004; Efendiev et al., 2014).	42
Fig. 2-5: The embedded cell approach in (Trias et al., 2006b).	44
Fig. 2-6: A model assembly for computational multiscale homogenisation after (Li et al., 2013).	45
Fig. 2-7: Early X-ray CT scans to investigate the fracture process of an aluminum matrix/SiC SCS-8 fibre composite (Kinney and Nichols, 1992).	51
Fig. 2-8: 3D visualisation of a transverse fatigue crack progression that by-passes the 140 μm diameter fibres (Withers et al., 2012).	51
Fig. 2-9: Synchrotron in-situ X-ray CT tests of a single-tow SiC/SiC composite specimen at room 25°C and ultrahigh 1,750°C temperatures (Bale et al., 2012).	52
Fig. 3-1: A two-scale coupling scheme for stochastic fracture mechanics.	56
Fig. 3-2: Boundary conditions for meso-scale modelling and for global multiscale models.	57
Fig. 3-3: (a) A global domain discretised into 16 non-overlapped MeEs and (b) the modelled crack paths for each MeEs independently under B1-X boundary condition.	58
Fig. 3-4: Overlapping MeEs and crack paths under B1-X boundary.	59
Fig. 3-5: Illustration of crack sampling cases for the overlapping windows concept used with Bayesian criterion in Eq. 3-1. The dark-shaded elements represent four half size overlapping elements and soft-shaded elements represent four quarterly overlapping elements.	62
Fig. 3-6: Bayesian filtering procedure and threshold probability on a typical non-marginal MeE cluster.	63
Fig. 3-7: Filtered overlapping MeE crack path data after using the Bayesian inference model corresponding to Fig. 3-4-b and c.	63
Fig. 3-8: Illustration of (a) short to (b) long overlapping criteria. The colour intensities represent distinct MeE windows that are overlapped.	64
Fig. 3-9: Illustration of two possible macro-scale meshes. The crack paths are used as boundary constraints during the MaE mesh generation. The cracks are also represented by cohesive interface elements (CIE) in the global model.	66

Fig. 3-10: Illustration of the stress-displacement curve for the macro-scale bulk material properties. $\bar{\sigma}$ is the stress due to no damage, d is the scalar degradation variable and L is the characteristic length (Simulia/Abaqus).	68
Fig. 4-1: Comparison of stress contour plots on window size $125 \times 125 \mu\text{m}$ and fibre volume fraction 30% at three different load steps: (a) results in (Cid Alfaro et al., 2010a), (b) the present study.	78
Fig. 4-2: MeE windows size $70 \times 70 \mu\text{m}$ at four positions from micrographs of a CFRP specimen.	79
Fig. 4-3: Ideal hexagonal fibre arrangement in a computer generated MeE size $70 \times 70 \mu\text{m}$ and fibre volume fraction 50%.	79
Fig. 4-4: Illustration of the MeE-1 model: (a) boundary conditions, (b) CIEs in the matrix and (c) CIEs on the matrix-fibre interfaces.	80
Fig. 4-5: Stress contour plots at three different loading steps.	83
Fig. 4-6: Stress-displacement curves.	84
Fig. 4-7: Comparison of volume fractions, ultimate strengths and dissipated energies.	85
Fig. 4-8: Stress contour plots on X direction at different loading steps of a longitudinal MeE size $60 \times 60 \mu\text{m}$.	86
Fig. 4-9: Load-displacement curve of a longitudinal fibre model of size $60 \times 60 \mu\text{m}$. The annotations represent the displacement step plots in Fig. 4-8.	87
Fig. 4-10: $+45^\circ$ fibre ply in front of a notch tip with numbers indicating positions of the centres of imaging windows.	89
Fig. 4-11: Concentric surveying window sizes at Position-2 in Fig. 4-10.	89
Fig. 4-12: Variations of volume fractions of fibre (V_f) and matrix (V_m) with increasing MeE window size at different imaging positions for a carbon/epoxy ply $+45^\circ$.	90
Fig. 4-13: Stress contours at three load steps from MeE-3 of size $50 \times 50 \mu\text{m}$ using (a) poor, (b) weak, (c) strong and (d) perfect interface properties.	93
Fig. 4-14: Stress contours at three loading steps using G2-X boundaries and weak interfacial properties showing a two dominant cracks failure in MeE size $100 \times 100 \mu\text{m}$.	94
Fig. 4-15: Image-based MeEs of size $10 \times 10 \mu\text{m}$ and $20 \times 20 \mu\text{m}$ illustrating the concept of partitioned concentric windows by preserving mesh topology.	95
Fig. 4-16: G1-X crack paths in different image-based MeE sizes in μm for weak interface properties (the interface cohesive layer illustrated in red).	96
Fig. 4-17: G1-X crack paths in different image-based MeE sizes in μm for strong interface properties (the interface cohesive layer illustrated in red).	96
Fig. 4-18: Stress-displacement and stress-strain curves for G2-X boundary conditions on MeE step $10 \mu\text{m}$ to $100 \mu\text{m}$ by using weak interface properties.	97

Fig. 4-19: Size-strength results for MeE step 10 μm to 100 μm using (a) weak and (b) strong interface properties.	97
Fig. 4-20: Crack paths for the adaptive size-increasing non-overlapping MeE-16 \times 25 (a,d) to short overlapping MeE-16 \times 35 (b,e) and long overlapping MeE-16 \times 50 (e,f). The two sets are from using weak interface properties (a,b,c) and strong interface properties (d,e,f).	100
Fig. 4-21: Variation of MeE strengths with different overlapping areas: (a) weak and (b) strong interface properties.	101
Fig. 4-22: Comparison of separate crack paths between overlapping series MeE-16 \times 50 (shown in coloured lines) using B1 boundaries against full size MeE-100 (shown in black lines): (a) G1-X; (b) G1-Y; (c) G2-X and (d) G2-Y for weak interface properties.	102
Fig. 4-23: Comparison of separate crack paths between overlapping series MeE-16 \times 50 (shown in coloured lines) using B1 boundaries against full size MeE-100 (shown in black lines): (a) G1-X; (b) G1-Y; (c) G2-X and (d) G2-Y for strong interface properties.	103
Fig. 4-24: Nonlinear multiscale results for weak interface properties using the overlapping concept vs fully detailed simulations (solid curve: detailed MeE-100, dashed curve: using MeE-16 \times 50 assembly).	105
Fig. 4-25: Nonlinear multiscale results for strong interface properties using the overlapping concept vs fully detailed simulations (solid curve: detailed MeE-100, dashed curve: using MeE-16 \times 50 assembly).	105
Fig. 4-26: Filtered crack paths obtained after applying the Bayesian inference model.	106
Fig. 4-27: Comparison of simulation results using the multiscale stochastic coupling strategy for weak interface properties. The solid curves represent the detailed geometry models (i.e. MeE size 100 μm) and dashed curves are the Bayesian multiscale models.	107
Fig. 4-28: Comparison of simulation results using the multiscale stochastic coupling strategy for strong interface properties. The solid curves represent the detailed geometry models (i.e. MeE size 100 μm) and the dashed curves are the Bayesian multiscale models.	108
Fig. 5-1: X-ray CT volume renders from a CFRP sample scanned using the X-Radia micro-CT system at Henry Moseley X-ray Imaging Facility (HMXIF).	113
Fig. 5-2: Attempts of volume segmentation based on CFRP braided X-ray CT dataset using: (a) raw images and single threshold segmentation; (b) filtered images and single threshold segmentation. The processing and visualisation was conducted using AVIZO (FEI/Avizo).	114
Fig. 5-3: Illustration of the commercially available loading rig Deben CT-500 (DEBEN) and the short span three-point bending test of a notched CFRP sample.	116
Fig. 5-4: In-situ stepped loading tests under uniaxial compression on disc samples made of CFRP composites of different thicknesses: (a) 3 mm and (b) 1.2 mm.	117
Fig. 5-5: In-situ three point bending loading tests of cross-ply carbon fibre/ epoxy composite samples using the Deben CT-500 mechanical rig.	117

Fig. 5-6: A new micro-loading rig for in-situ X-ray CT experiments.....	119
Fig. 5-7: General assembly technical sheet illustrating main components of a fully-integrated new in-situ micro-loading rig.....	119
Fig. 5-8: Mechanical components of a new in-situ loading rig.	120
Fig. 5-9: Illustration of loading setups and sample support configurations.	124
Fig. 5-10: Branchline I13-2 setup configuration at Diamond Light Source in Oxfordshire. .	125
Fig. 5-11: In-situ X-ray CT tensile test setup and loading steps.....	128
Fig. 5-12: Sample dimensions and in-situ tensile loading setup.....	129
Fig. 5-13: Load-displacement relationship of the preliminary in-situ tensile loading test. ...	130
Fig. 5-14: In-situ X-ray CT volume renders of a cross-ply fibre composite under tensile loading. The images correlate to loading curves in Fig. 5-11.	131
Fig. 5-15: Illustration of general dimensions and in-situ three point bending setup of an unnotched CFRP sample.	132
Fig. 5-16: Loading data from three-point bending in-situ test.....	133
Fig. 5-17: In-situ X-ray CT volume renders of a braided carbon fibre composite under three-point bending test. The images correlate to the loading curves in Fig. 5-16.	133
Fig. 5-18: Rotated views of X-ray CT volume renders showing severe damage, fibre breaks and fracture from three-point bending in-situ loading test in braided carbon fibre composites.	134
Fig. 6-1: An in-situ X-ray CT volume render of the multidirectional CFRP sample under tension.....	139
Fig. 6-2: Illustration of image-based model extraction framework from X-ray CT images to FE meshes.	140
Fig. 6-3: De-noising of raw X-ray CT image stack using three different filter combinations explained in Table 6-1.	141
Fig. 6-4: Estimation of the convolution factors based on different smoothing functions; the insets typify the effect of the combined filter Filter-E and convolution using the step function estimates at the boundary between 0° to -45° plies.	144
Fig. 6-5: Illustration of the volume delineation tool used to delineate X-ray CT datasets based on fibre orientations (a,b,c). The schematic volume re-composition (f) is shown after combining the two orthonormal volumes (d,e).....	146
Fig. 6-6: Identification of the fibre centroids after applying Filter-E and image convolution. The RoI was taken at the 0°/ -45° ply boundary illustrating: (a) the fibre UEPs identification and (b) corresponding filtered volume render. Discontinuities are most significant in the inclined ply as shown with solid red lines.....	147

Fig. 6-7: Fibre tracking from binary images in a RoI at the $0^\circ/ -45^\circ$ ply boundary (the fibre discontinuities are highlighted using yellow arrows).	148
Fig. 6-8: Illustration of fibre centroid identification from binary slices. The RoI was taken at the $0^\circ/ -45^\circ$ ply boundary same position as in Fig. 6-6 boundary illustrating: (a) a binary reconstructed slice and (b) the corresponding binary dataset volume render. Discontinuities are most significant in the inclined ply as shown with solid red lines.	149
Fig. 6-9: Bayesian inference domains for fibre tracking applications with kernel stack domain d and stack overlap $d/2$	151
Fig. 6-10: Sensitivity of fibre tracking UEPs with different Bayesian overlapped stack widths, using the parameters in Table 2.	155
Fig. 6-11: Calibration of the local Bayesian tracking approach using Eq. 6-10 by inverse fitting for: (a) tolerant fibre shifts equivalent to less than 9 pixels and (b) restrictive fibre shifts to less than 4 pixels (the power law factors are: $p=0.2$, $q=0.3$).	159
Fig. 6-12: Reconstructed fibre centrelines of Fig. 6-1-b.	160
Fig. 6-13: Full size X-ray CT reconstructed fibre centrelines.	161
Fig. 6-14: X-ray CT image-based FE model with reconstructed fibre volume fraction $V_f = 37\%$	162
Fig. 7-1: Modelling framework and validation with in-situ X-ray CT experiments.	168
Fig. 7-2: Boundary conditions considered at meso-scale: (a) uniaxial tensile with restrained sides, (b) shearing using central bandwidth, and (c) uniaxial tensile with single restrained side.	169
Fig. 7-3: Crack simulation results in three fibres model using different boundary conditions: type-A: a-b-c, type-B: d-e, type-C: f.	170
Fig. 7-4: Illustration of numerical challenges induced by curvilinear fibres and local cutting edges.	171
Fig. 7-5: X-ray CT image-based models extraction from a multidirectional CFRP reconstructed region.	173
Fig. 7-6: An X-ray CT region render in 0° fibre oriented CFRP and the reconstructed image-based mesh associated with MeE-8 in Table 7-2.	174
Fig. 7-7: Image-based mesh reconstructed from in-situ X-ray CT dataset of a CFRP region.	175
Fig. 7-8: Sequence of damage and crack propagation in image-based model MeE-8 subjected to tensile loading along Z axis (parallel to fibre centrelines).	178
Fig. 7-9: Fracture surfaces of CFRPs obtained from MeEs containing 0° and 90° fibre orientation plies.	179
Fig. 7-10: Fracture surfaces of CFRPs obtained from MeEs containing -45° and $+45^\circ$ fibre orientation plies.	179

Fig. 7-11: Stress-displacement curves of CFRPs at fibre scale obtained from MeE simulations that contain (a) -45° and (b) $+45^\circ$ oriented fibres and different fracture modes.	180
Fig. 7-12: Stress-displacement curves of CFRPs at fibre scale scale obtained from MeE simulations that contain 90° oriented fibres and different fracture modes.	180
Fig. 7-13: Tensile strength anisotropy diagram of CFRPs at fibre scale using type-A boundary conditions.	183
Fig. 7-14: Shearing strength anisotropy diagram of CFRPs at fibre scale using type-B boundary conditions.	183
Fig. 7-15: Multiscale model at global scale showing geometrical idealisation and mesh-unit for scale transfer.	186
Fig. 7-16: Maximum stress contours in multiscale model at different damaging steps.	191
Fig. 7-17: Contour stresses along vertical loading direction Y in multiscale model at different damaging steps corresponding to Fig. 7-16.	191
Fig. 7-18: Comparison of damage and crack patterns in multidirectional CFRP sample from FE multiscale modelling and in-situ tensile test.	192
Fig. 7-19: Comparison of load-displacement curves in CFRP sample from FE multiscale modelling and in-situ tensile test.	192

ABSTRACT

This thesis presents the development of a new multiscale stochastic fracture mechanics modelling framework informed by in-situ X-ray Computed Tomography (X-ray CT) tests, which can be used to enhance the quality of new designs and prognosis practices for fibre reinforced composites. To reduce the empiricism and conservatism of existing methods, this PhD research systematically has tackled several challenging tasks including: (i) extension of the cohesive interface crack model to multi-phase composites in both 2D and 3D, (ii) development of a new in-house loading rig to support in-situ X-ray CT tests, (iii) reconstruction of low phase-contrast X-ray CT datasets of carbon fibre composites, (iv) integration of X-ray CT image-based models into detailed crack propagation FE modelling and (v) validation of a partially informed multiscale stochastic modelling method by direct comparison with in-situ X-ray CT tensile test results.

These tasks and the achievements of this research are summarised below:

(i) Multiscale modelling of crack propagation in 2D

In this method, a macro-scale domain is first discretised into a number of meso-scale elements (MeEs), in which potential discrete cracks are modelled by pre-inserted cohesive interface elements. A nonlinear microscale simulation is conducted for each MeE in parallel to obtain the crack patterns under different boundary conditions. Adaptively size-increasing MeEs are then simulated, until potential cracks seamlessly cross the boundaries of adjacent MeEs. The resultant cracks, are then integrated as Cohesive Interface Elements (CIEs) into a final anisotropic macro-scale model for modelling global mechanical responses.

(ii) Development of new in-situ loading rig for X-ray CT testing

A new in-situ X-ray CT loading rig was developed to overcome several shortcomings of the various commercially available equipment. The new rig included a number of innovative features such as: multipurpose loading modes and sample setups, fast sample mounting, fully integrated autonomous motion control, real-time data acquisition and flexibility in carrying out various in-situ loading programmes using under either tensile or compressive loading.

(iii) Reconstruction of low phase-contrast X-ray CT image-based models

The reconstruction approach is based on identifying the individual fibre centres using a local maxima method and a Bayesian inference model applied to the stack of images. Stacks with reduced width are overlapped to ensure 3D fibre continuity. The approach is illustrated for a [45/90/-45/0] carbon fibre reinforced laminae.

(iv) Integration of the X-ray CT image-based models in FE modelling

The numerical reconstruction method demonstrates that implementing realistic fibre mesh models in FE simulations of discrete cracks is currently feasible using a partitioning strategy in smaller size meso-scale models. Although the developed reconstruction method in this study is employed for tracking long and tortuous/ nonlinear fibres, the FE meso-scale modelling is implemented using cubic shape models of size 50 μ m.

(v) Validation of the multiscale stochastic fracture mechanics modelling framework

The model has been validated using a global model partially informed by X-ray CT in which the global simulation model incorporates details of meso-crack propagation mechanisms, carried out in parallel computation on the image-based meso-scale models. The two main validation tests are the load-displacement curves and the multidirectional damage patterns.

KEYWORDS

Multiscale Stochastic Fracture Mechanics; Multiscale Coupling; Cohesive Interface Crack Model; Size-Increasing Grid; Overlapping Grid; Scale Transfer; Fibre Reinforced Plastics (FRP); X-Ray Micro-Tomography; X-Ray Micro-CT; Synchrotron Radiation; Mesh Reconstruction; Fibre Segmentation; 3D Fibre Tracking; Image-Based Modelling; Reverse Engineering.

DECLARATION

No portion of the work referred to in the thesis has been submitted in support of an application for another degree or qualification of this or any other university or other institute of learning.

R. M. Sencu

2016

COPYRIGHT

The author of this thesis (including any appendices and/or schedules to this thesis) owns certain copyright or related rights in it (the “Copyright”) and s/he has given The University of Manchester certain rights to use such Copyright, including for administrative purposes.

Copies of this thesis, either in full or in extracts and whether in hard or electronic copy, may be made only in accordance with the Copyright, Designs and Patents Act 1988 (as amended) and regulations issued under it or, where appropriate, in accordance with licensing agreements which the University has from time to time. This page must form part of any such copies made.

The ownership of certain Copyright, patents, designs, trademarks and other intellectual property (the “Intellectual Property”) and any reproductions of copyright works in the thesis, for example graphs and tables (“Reproductions”), which may be described in this thesis, may not be owned by the author and may be owned by third parties. Such Intellectual Property and Reproductions cannot and must not be made available for use without the prior written permission of the owner(s) of the relevant Intellectual Property and/or Reproductions.

Further information on the conditions under which disclosure, publication and commercialisation of this thesis, the Copyright and any Intellectual Property University IP Policy (see <http://documents.manchester.ac.uk/display.aspx?DocID=24420>), in any relevant Thesis restriction declarations deposited in the University Library, The University Library’s regulations (see <http://www.library.manchester.ac.uk/about/regulations/>) and in The University’s policy on Presentation of Theses.

© ***COPYRIGHT***

R. M. Sencu

ACKNOWLEDGEMENTS

First, I would like to express my sincere appreciations to my supervisors Prof Zhenjun Yang and Prof Yong C. Wang for their long term and patient criticisms, suggestions and corrections that have constructively influenced this work, but also shaped me as a person and guided my staying in the United Kingdom. Indeed, they have given me opportunities to be around and work alongside internationally recognized professors, scientists and technicians at the University of Manchester and outside. It was a great pleasure for me to have been immersed in such a great oasis of scholarship.

I would like to acknowledge the main sponsors, the U.S. Air Force EOARD through grant FA8655-12-1-2100 and the EPSRC grant EP/J019763/1, for providing a three years' full-time studentship, and for their kind support towards attending conferences and the experimental cost.

I would like to thank Diamond-Manchester Imaging Branchline I13-2 at Diamond Light Source and the many staff and support officers who have had a direct or indirect contribution to the X-ray work of this thesis including Prof. Christoph Rau, Dr. Aaron Parson, Prof. Phil Withers, Dr. Tristan Lowe, Dr. Ying Wang, Prof. Peter Lee, Dr. Stephanie Mason and many others. They enabled the X-ray CT experimental session MT10456-2 to be successfully carried out. The help and assistance of Mr. Razvan Vasiliu and Mr. Alex Borsciov during the X-ray CT session at Diamond are also greatly appreciated.

Prof. Costas Soutis and Mr. Bill E. Godwin at the Northwest Composite Centre transferred to me some of their immense knowledge on composite materials and they also provided the CFRP composite specimens for testing.

Dr. William Bodel, Mr. Robert Numa and Prof. Paul Mummery of the Nuclear Research Group and C-Net helped with the acquisition of images from in-situ microscopy and provided helpful advice at the start of the research work.

The School of Materials and School of Computer Sciences, via the HMXIF support staff and in particular Dr. Lee Margetts, provided various training sessions, presentations at ICAM, Image Based Modelling, FE modelling, which all contributed to shaping the originality of this work.

I would like to acknowledge the use of the High-Performance Computing (HPC) facility at University of Manchester supported by Dr. George Leaver and Dr. Jonathan Boyle.

I would like to send special thanks to the School of Mechanical, Aerospace and Civil Engineering, where I was provided with friendly and effective technical support from Mr. Phil Oakes, Mr. David Jones, Mr. Dave Mortimer, Mr. Gus, Mr. Eddy White, Mr. Les Bray, Mr. Dave Golding, Mr. Paul Nedwell, Dr. Andy Weightman, Mrs. Christine Jinks, Dr. Jack Wu, Dr. Tom Swailes, Dr. Adel Salama and Dr. Sorin Stanescu.

Finally, I wish to thank my colleagues in the research group, including Dr. Wenyuan Ren, Dr. Ansam Qsymah, Dr. Xiaofeng Wang, Dr. Rajneesh Sharma, Mr. Yu Zhen, Mr. Junlong Yu, Dr. Burak Cirpici, Dr. Ashkan Shahbazian for their friendship, morale support, useful conversations, ideas and great moments we have shared in these beautiful Manchester years.

R. M. Sencu

2015

TO MY FAMILY AND FRIENDS

CHAPTER 1. INTRODUCTION

1.1. Motivation

Fibre reinforced composites are multi-phasic composite materials widely used in engineering structures of many industries (e.g. aerospace, automotive, marine, energy and construction) and support a wide range of societal needs. It is vital that modern fibre reinforced composite materials and structures are designed efficiently to meet the requirements of serviceability, safety, sustainability and long-term durability. An enhanced understanding of the damage and fracture behaviour is thus imperative to achieve this goal.

Fibre reinforced composites have intrinsically stochastic, heterogeneous and nonlinear physical and mechanical properties across multi-length scales, due to the random distribution of multiple phases of materials at nano, micro, meso to macro scales. Because the finer scale properties directly determine the performance and reliability of structures and systems at coarser scales, it is essential to understand the inter-scale relationships or scale transferability, which can only be achieved through multiscale computational modelling (de Borst, 2008; Kassner et al., 2005; Oden et al., 2003; Kanouté et al., 2009; Nguyen et al., 2012a). This is particularly true for fracture problems, as fracture always starts from micro-scale cracks at strain localisation sites, which then propagate, widen and coalesce into meso-scale cracks and finally discrete macro-scale cracks. This phenomenon spans a few length scales, demanding a multiscale modelling approach.

1.2. Objectives

This project aims to develop an innovative Multiscale Stochastic Fracture Mechanics (MsSFrM) framework for accurately modelling damage and fracture in fibre reinforced composites under external loadings. The research has two tasks: (1) multiscale experimental

studies to better understand the material's complex damage and fracture behaviour and also to develop realistic image-based finite element models for understanding such behaviour; and (2) development of a multiscale modelling methodology to obtain the stress-strain relationships of fibre reinforced composites and to critically evaluate the reliability and performance of the carbon fibre reinforced polymer (CFRP) microstructures for better quality, greater reliability and lower cost.

The main objectives are:

- (i) to carry out in-situ micro-scale X-Ray Computed Tomography (X-ray CT) tests of CFRP under progressive external loadings and to better understand the complicated damage and fracture behaviour by image processing;
- (ii) to develop efficient algorithms for segmenting and reconstructing the micro-scale X-ray CT images so as to build accurate and realistic image-based 3D finite element models;
- (iii) to develop an innovative multiscale stochastic fracture mechanics method in 2D and 3D to accurately predict damage and fracture of fibre reinforced composites; and to validate the multiscale fracture modelling method.

1.3. Outline of the thesis

The thesis is structured in eight chapters.

- 0 introduces the overall aim and objectives of this study.
- CHAPTER 2 reviews the existing literature that relates to the main objectives of the research and outlines the methodology for this research.
- CHAPTER 3 explains the methodology for modelling meso-to-macro crack propagation and scale transfer.

- CHAPTER 4 presents the implementation and validation of a new numerical algorithm for scale transfer and for modelling crack propagation in 2D.
- CHAPTER 5 presents details of the in-situ X-ray CT experimental work, including the development of the devices for the supporting experiments, using both the cone source X-rays emitter imaging technology at the Henry Moseley X-rays imaging facility (HMXIF) of the University of Manchester and at the national synchrotron radiation technology at Diamond Light Source.
- CHAPTER 6 develops the reconstruction and segmentation algorithms to generate the multiscale computational meshes based on the X-ray CT images.
- CHAPTER 7 extends the 2D modelling methodology discussed/ developed in CHAPTER 3 and CHAPTER 4 to 3D crack propagation modelling using the X-ray CT image-based models generated in CHAPTER 6.
- CHAPTER 8 summarises the research, presents the main findings and recommends future research directions.

CHAPTER 2. LITERATURE REVIEW

2.1. Introduction

As explained in 0, the two aims of this project are X-ray CT imaging of fibre reinforced polymer (FRP) composites and multiscale numerical modelling of fracture of FRP composites. This chapter will present a review on these two topics, with a view to justify the originality and methodology of the current research.

FRP composites are quasi-brittle materials and contain inherent defects at the fine length scales (nano, micro and meso) which affect the crack initiation and propagation processes. These can further have detrimental effects on the global behaviour of the FRP structures. Ideally, the mechanical behaviour of all the fine scales should be taken into account when simulating the fracture process of FRP composite structures. However, modelling crack propagation in FRP composites across various scales is challenging because of the existence of multiple material phases and their interactions. Furthermore, FRP composites contain stochastic heterogeneity at the fibre level as a result of manufacturing imperfections. This means that the traditional repetitive elements and statistical homogenisation approaches may not be able to reflect the true behaviour of FRP composites.

The main objective of this review is to identify the advantages and shortcomings of various existing multiscale simulation models for damage and fracture, and to establish the assumptions of a ‘rational’ multiscale model for crack propagation. This model should be realistically characterised with all the material’s features such as random distribution of initial defects and distinct material phases, obey the principle of energy conservation, and preserve the distribution of crack paths and orientations across scales. The morphological continuity should be preserved and mapping of material properties and anisotropy across scales should be accurate.

2.2. Overview of existing multiscale modelling methods for scale transfer

The multiscale methods integrate the fine scale features (lower scale) within the coarse scale models. These methods can be classified into the following two main categories of approaches, according to the sequence of operations and the type of information exchange:

- (i) uncoupled approaches (also called one-way models): the information is transferred in one direction, either bottom-up or top-down.
- (ii) coupled approaches: information is exchanged in both directions.

Fig. 2-1 presents a brief summary of these two approaches.

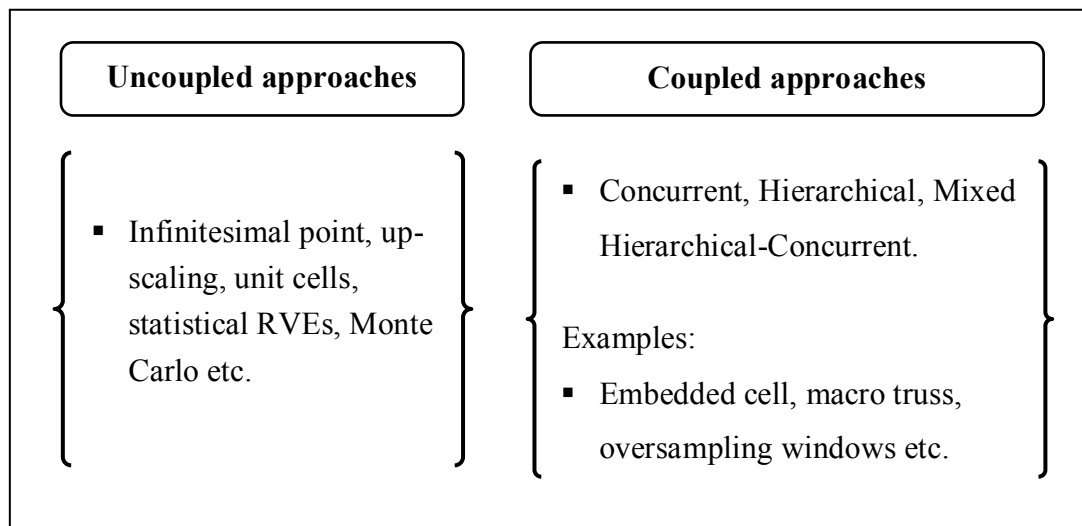


Fig. 2-1: A brief summary of existing multiscale models.

2.3. Uncoupled models

In the uncoupled models, the information from fine scales is used to drive processes on the coarse and larger scales (bottom-up) or vice versa (top-down). Reviews of these models can be found in (Panchal et al., 2012; Nguyen et al., 2011). Examples of such models include the up-scaling methods for atomic and molecular processes up to continuum matter, repetitive unit cells, infinitesimal point assumptions, reduced material phases assumption, statistical representative volume elements (SRVE) and statistical Monte Carlo approaches with indirect

packing of material properties (Su et al., 2009; Yang et al., 2009; Yang and Xu, 2008; de Frias et al., 2014; Xu et al., 2013; Singh and Talreja, 2013; Ruggles et al., 2013; Greco et al., 2013).

Most of the one-way approaches neglect microstructural continuity and often do not consider the random distribution of fibres across the continuum. Some improvements have been made by employing an unstructured macro-scale truss where each linear element represents a detailed microscopic window that leads to the so-called FE^2 coupled approach (Unger, 2013) of constant geometries. The fracture process is not modelled as discrete crack propagation, but as localised numerical degradation of linear lattice integration points. This makes this type of models similar to damage mechanics models by using admissible stresses or strengths. However, these models become computationally expensive mainly because of the iterative inverse fitting of deformation rates from coarser scales to finer scales (top-down). For example, given an initial displacement of the macroscopic truss, the deformation rates at micro scale are iterated to fit the macro scale behaviour. Therefore, these models can hardly be accepted in reliability analyses.

A similar scale-coupling enhancement was proposed in (Verhoosel et al., 2010), where periodic windows were decomposed on displacement basis and solved to find out localisation properties. This model excludes the continuity of the morphology which results in a number of side effects at the macro-scale such as unreliable predictions of global elastic constants and ultimate loads. This is because the global elastic constants are related to the exact strain rates of the microstructure that are not linked to macro-scale. In addition, the dissipated fracture energy is crack path dependent.

The typical shortcomings of the uncoupled models are summarised below:

- (i) deformation fields and rates often do not match at both scales;

- (ii) the fracture modelling at macro-scale is rarely acceptable because of the weak form formulations that disregard the geometrical nonlinearity;
- (iii) they are partially empirical and/or mathematical, for example, based on the Hill-Mandel macro-homogeneity relation (Li, 2011) that cannot model non-linear materials; and
- (iv) uncertainties exist on both scales.

Because of the above shortcomings, the uncoupled models will not be pursued in this research.

2.4. Coupled models

The coupled models use the information from both scales and combine them over the same temporal and/or spatial domains based on conservation principles. This means that some sort of dynamic constraints/or structural links may be pre-formulated and re-iterated to ensure deformation compatibility. Moreover, such models consider the expected macroscopic behaviour by boundary strategies, or by direct matching of high-fidelity deformation fields. In practice, such deformation fields may be obtained using Digital Image Correlation (DIC) techniques (Shen and Paulino, 2011; Amini and Kumar, 2014). However, it is generally not possible to obtain and transfer fully accurate deformation fields, from either measuring or modelling the fine scale substructures that would match the larger scale simulations, especially when large scale jumps are sought. This is because the direct characterisation/measuring techniques such as the DIC and X-ray CT, have limited fields of view (FoV). In addition, existing theoretical developments of inverse procedures for local load estimations in composite materials lag behind experimental techniques. Such an example using inverse wave propagation functions to understand the reflection of line loads on boundaries in composite laminates can be found in (Liu et al., 2002). The conclusions explain damage localisation and load estimation difficulties in heterogeneous materials. For example, although 2-D and 3-D DIC could be used to remotely measure deformation and strain fields, it is still currently rather complicated to relate them to material local stress fields. This is essential to fully understand the required

loading conditions that may realistically represent a set of numerical boundary conditions. If solved, this could potentially deliver the intrinsic information for the calibration of more accurate fully-nested multiscale models. However, the complicated time functions and disturbance from composite material interactions remain unsolved. Therefore, the estimation of inverse stress fields is one of the long-time persistent research topics in need of more efforts. As alternatives, the statistical and/or local deformation compatibility methods may be used but they should not be linked in multiscale platforms when information at the fine scale is missing without experimental validation.

The following section presents some coupling approaches that attempt to minimise or partially eliminate the deformation field biases at neighbouring locations. The currently available approaches in the literature can be classified into three main categories:

- (i) concurrent approach (CA);
- (ii) hierarchical approach (HA);
- (iii) mixed hierarchical-concurrent approach (MHCA).

Two-way coupling strategies are most commonly associated with CA models (Ghosh et al., 2007; González and Llorca, 2006), but can be mixed with HA models as well (Trias et al., 2006a). Typically, a single global analysis is carried out in the CA models using a hybrid mesh. The mesh contains various levels of discretisation which can go up to fully detailed microstructures of some limited region of interests (Ghosh, 2008; Ghosh et al., 2007). This idea is mainly used to capture damage localisation based on some predefined computational areas which incorporate sufficiently fine details for the investigated phenomena. It also means that coarser regions require a computational homogenisation scheme and the study of size dependence a priori. Once the complete modelling scheme is decided, the global simulation can be carried out deterministically. The approach is discussed in Section 0.

Generally, the HAs construct the global analysis based on information of detailed fine scale simulations. This means that computational homogenisation may not be necessary when boundary conditions are known a priori. However, continuity should be ensured at fine scales in order to accurately capture crack initiation and propagation across multiple computational domains. Statistical expansion methods may also be used to include some uncovered areas and to characterise the whole structural part (Clément et al., 2013; Guilleminot et al., 2009). It may also be obvious that when solving large degree of freedom (DoF) models, multiple meso-scale windows can be separated and computed in parallel. Using such strategies, effective computation of the entire domain can be enabled. The currently available HA strategies are discussed in detail in Section 2.4.2.

The MHCA approach aims at minimizing the boundary effects on fine scale analyses before scale transfer. An example of a MHCA model is the embedded cell approach (ECA). The ECA minimizes the boundary effects using an ideally homogeneous buffer around the statistical computed window (Trias et al., 2006a; Trias et al., 2006b; Li et al., 2013; Li and Zhou, 2013a). In this way, the boundary effects may be decided before the scale transfer. This approach is discussed in details in Section 2.4.3.

The typical challenges of the coupled models include high computational cost, large data memory, storage and transfer, complex mathematical formulations, and difficult programing. The following sections focus on the most important premises of different researchers to solve the scale transfer problem under the above the three distinct approaches.

2.4.1. Concurrent approach

The CA approach decomposes the computational domain into non-overlapping sub-domains which are discretized with different mesh densities (Ghosh and Paquet, 2013; Llorca et al., 2013; González and Llorca, 2006). This means that some parts assume reduced order definition, while other parts include more complicated definitions such as detailed microstructural evolution and damage. Periodic cells are usually employed in the sub-domains or where damage is rarely expected. The other sub-domains with damage potential are coupled with discretisations at fine-level and more complicated constitutive formulations.

A popular concurrent model based on Voronoi cell discretisation was reported in (Ghosh and Paquet, 2013; Ghosh, 2008; Ghosh et al., 2007). Although some sub-hierarchical links were made via Voronoi statistical fibre cells, the homogenisation for the upper scales in this model assumed the elastic constitutive behaviour, while the top-down scale transfer was ensured through localisation and damage relationships. The most critical failure regions are captured only when appropriate partitioning is performed, and transitional meshes are usually necessary, as illustrated in Fig. 2-2.

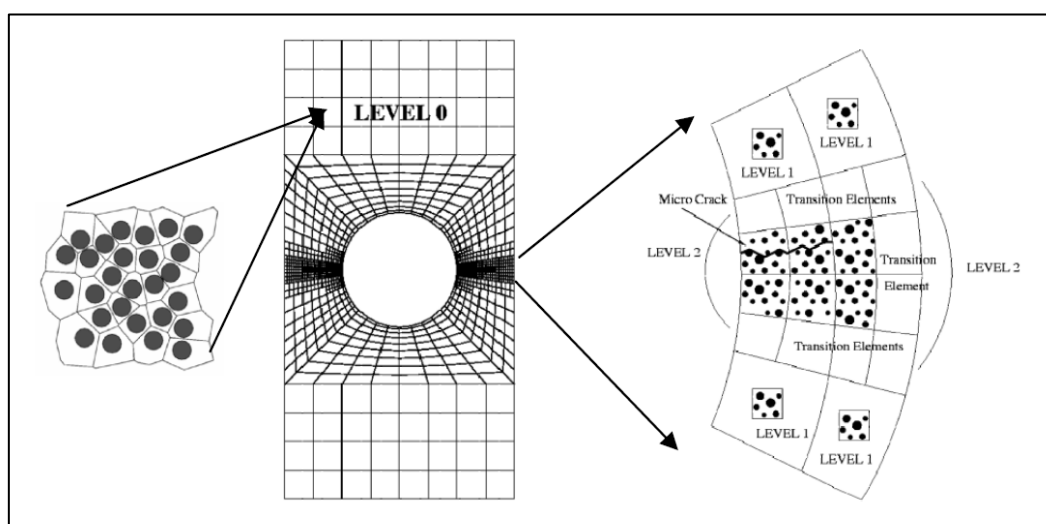


Fig. 2-2: Concurrent multiscale model based on sub-hierarchical Voronoi individual fibre cells, transition elements and detailed micro-scale windows (Ghosh, 2008).

Several restrictions were posed to the boundaries and discretisation cells in (Ghosh et al., 2007; Ghosh, 2008). It was also shown that the fully detailed simulations could only consider the fibre de-cohesion, avoiding more complicated realistic crack mechanisms. However, the main advantage of the concurrent method is that it can make use of the well-known fibre distribution statistics in (Matsuda et al., 2003; Pyrz, 1994), which can be linked directly to the localized damage mechanisms when stochastic meso-scale windows with minimum boundary condition effects are simulated. Such an extension of the Voronoi cells that were used in the homogenisation scheme of the current method remained unsolved.

In the modelling of fracture process, the CA methods naturally discretise the regions with strain localisation by fine meshes and the other regions by coarse meshes to save computational cost. This is particularly useful for problems with cracks or weak interfaces known a priori, where the crack-tip and the interfacial regions are modelled in detail for accurate understanding of the fracture mechanism at fine scales (e.g. (Ghosh and Paquet, 2013; Ghosh et al., 2007); (Canal et al., 2012; González and Llorca, 2007b); (Trias et al., 2006a; Trias et al., 2006c; Li et al., 2013)). However, for problems with many distributed cracks or unknown cracks, very dense meshes or adaptive meshing with local refinements may have to be used in the whole domain to simulate potential cracks, making the concurrent approaches computationally costly.

2.4.2. Hierarchical approach

In general, the hierarchical approaches can be separated in two categories: (i) sequential, and (ii) fully nested, according to the data exchange type during the scale transfer.

In the sequential approaches, a representative volume element (RVE) or unit cell, based on the classical homogenisation theory (Hill, 1963; Hashin, 1965), is assumed to exist at medium scales. Once the existence and size of the RVE is determined by detailed numerical analyses in fine scales, the domain at coarse scales is assumed homogeneous and modelled by a number of

RVEs. In doing so, a full analysis of the domain with fine-scale details is avoided giving favour to the concept of ‘separation of scales’ (Ostoja-Starzewski, 1998; Ostoja-Starzewski, 2005). However, recent studies (Phu Nguyen et al., 2010; Gitman et al., 2008; Gitman et al., 2007) find that the RVE exists only in linear-elastic and hardening regimes; once softening occurs as in fracture and damage, the RVE loses the ‘representative’ properties and cannot be found, because the material in softening shows localisation leading to the loss of statistical homogeneity. If the RVE does not exist, special measures must be taken for multiscale modelling to maintain the objectivity with respect to the size of the sample cells. Such measures may not be strictly accurate due to the large transfer ratios using separation of scales that range between 1:10 in case of RVE models to 1:100 in case of unit cells.

Some improvements to both sequential and fully nested hierarchical approaches have been made by linking different macro-scale sites with responses obtained from fine-scale models (Luscher et al., 2010; Unger, 2013; Zhuang et al., 2015; Reis and Andrade Pires, 2013). However, although the FE^2 modelling approach considered so far unrealistic constant and discontinuous microstructures, different scale coupling procedures were developed. For example, when fully nested, the linkage to macro-scale meshes could be achieved by telescoping of initial coarse displacements to local RVEs (Zhuang et al., 2015; Luscher et al., 2010). Similarly in (Unger, 2013), the nodal displacements of the fine scale domain are a function of the homogeneous strain, crack opening and a fluctuation part. In general, the boundary conditions can be informed in two different ways: (1) by applying prescribed fine-scale boundary conditions, sequentially dictating behaviour of macro-scale material models (Özdemir et al., 2008), and (2) using ‘uniquely linked’ RVEs with homogeneous mesh iterations and top-down displacement boundary translations (Gitman et al., 2008). It is then important to highlight, that when prescribed boundary conditions or initial homogeneous global

mesh models are used, nested approaches require comprehensive numerical verifications and experimental validation case studies.

Many other studies have assumed periodic boundary conditions as discussed in (Nguyen et al., 2012c; Nguyen et al., 2012a; Pham et al., 2013) in the context of computational homogenisation. However, these are now intrinsically solved by existing FE solvers and therefore their technicality is well established. In contrast, in (Karpov et al., 2006) a bi-layer material case study was separated using two concurrent domains, one reading the periodic boundary conditions and another hierarchically nesting multiscale informed boundary conditions in different sites, idea which was similarly studied in (Bosco et al., 2015). Of particular interest are the innovative hybrid-periodic boundary conditions that were developed in (Özdemir et al., 2008; Coenen et al., 2012b; Coenen et al., 2012c). In their definition, the ‘periodic’ term is enforced by a deformation ‘fluctuation field’.

Other innovative stiffness matrix constructors with novel boundary conditions have been presented in (Tjahjanto et al., 2010; Liu et al., 2010). Their approaches can also be directly informed by fine-scale iterations, although the ‘periodic’ boundary conditions are currently understood as being taken from infinitely fine-coarse grain interfaces at the material point level, while the analyses are often solved with initially prescribed boundary conditions. However, although these different numerical boundary approaches were abstracted in various research views, it is still not trivial to account for realistic multi-phase material definitions and to transpose the high-order responses of complicated fine-scale interactions within the required subsequent data updates.

Further optimisation and data exchange studies of particular interest were addressed to the simulation of large degree of freedom models with non-similar initial displacements (Larsson and Runesson, 2011), stochastic fine scales (Kouznetsova et al., 2004; Williams and Baxter, 2006) and damage localisation (Geers et al., 2010; Coenen et al., 2012c; Bosco et al., 2015). In

general, due to the complexity of data exchange often taken from homogenised material models, many of the scale separation ratios different than 1:1 may not support true heterogeneity of the microstructure for seamless macro- to micro- scale modelling. This is an essential step for simulating continuous crack growth, and may otherwise require enforced kinematic/ averaging or nested/multi grid meta models to bridge the missing layers. Examples of coarse macro-scale meshes taken at a structural scale that ultimately required averaging of smaller incompatible hierarchical meso-scale mesh elements and enforced kinematics couplings can be found in (Kouznetsova et al., 2004; Roubin et al., 2015).

In some ways, this inverse macro-to-meso numerical linkage is similar to the many existing top-down methods. Top-down multiscale methods employ statistical mapping procedures at macro-scale without following a strict requirement to ensure continuity of material microstructures. For example, in (Kaczmarczyk et al., 2008; Doškář and Novák, 2013) some randomly generated microstructure windows were sampled at arbitrary positions based on targeted volume fractions. Fig. 2-3 shows the assembling algorithm used in this case.

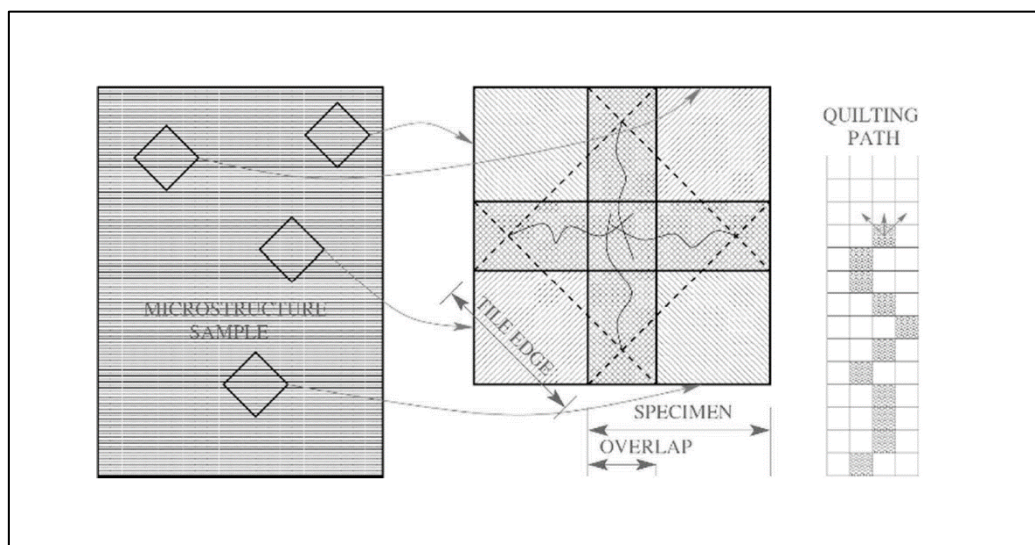


Fig. 2-3: Microstructural sample extraction and packing assembly according to (Doškář and Novák, 2013).

Although nonlinear modelling was not conducted in (Doškář and Novák, 2013), this may still be a mathematical vicious circle of solving some simple statistical generated micro-scale structures which should be avoided through direct control of the macroscopic properties by similar statistics. Also, in this method a small number of distinct windows were chosen to correlate the entire range of the investigated disordered microstructure (Novák et al., 2012; Doškář and Novák, 2013). This idea of pre-sampling is expected to lower the geometrical computational cost as for the continuous representation of the microstructure despite its unsuitability for elastic and plastic deformation compatibility between two neighbour samples.

A recent example of fully nested hierarchical approach is the oversampling strategy in the so-called generalised multiscale finite element method (GMsFEM) for solving flow problems in heterogeneous porous media (Hou and Wu, 1997; Chen et al., 2003; Aarnes et al., 2006; Efendiev et al., 2004; Efendiev et al., 2014; Calo et al., 2014). In the GMsFEM, the scale-coupling is realised using multiscale basis functions containing the deformation information of fine-scale elements (see Fig. 2-4). The oversampling strategy uses larger regions than the fine-scale elements to construct more accurate local basis functions, making the GMsFEM converge faster with fewer degrees of freedom.

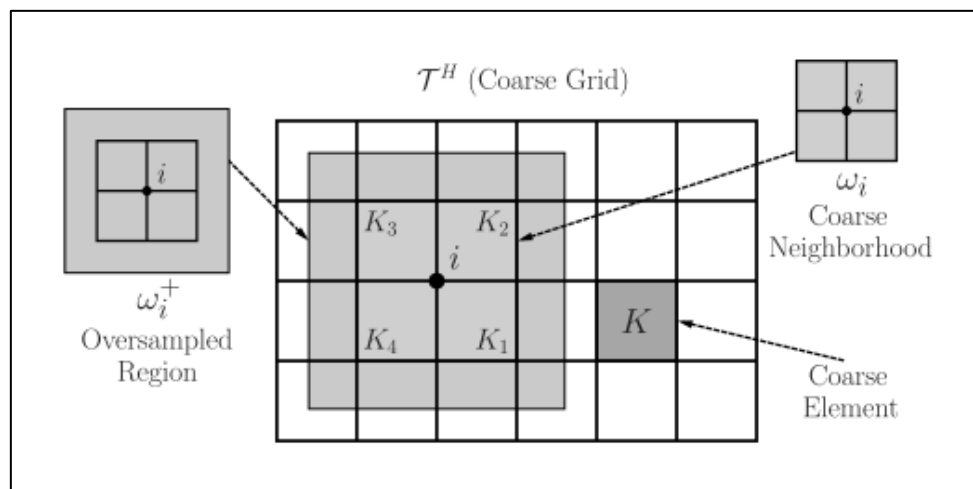


Fig. 2-4: The generalised multiscale finite element method (GMsFEM): K is a target coarse block and ω is the oversampling domain (Efendiev et al., 2004; Efendiev et al., 2014).

The GMsFEM with oversampling has recently been applied to linear elastic stress analyses (Chung et al., 2014) and seismic wave propagation (Gao et al., 2014). Its extension to complicated nonlinear fracture problems is not yet reported. Such an extension is very challenging due to the strain localisation and associated nonlinear material softening, which may presumably make it impossible to form the rigorous analytical derivation of the GMsFEM to ensure deformation compatibility between the fine-scale elements for general external boundary conditions. To address some of these issues, mixed hierarchical-concurrent strategies have also been attempted. The combination of the two is discussed below in Section 2.4.3, whereby deformation compatibility is partially tackled using homogeneous material buffers.

2.4.3. Mixed hierarchical-concurrent approach

The MHCA coupling scheme proposed in (Trias et al., 2006a) assumes random failure properties for macro-scale elements. At the fibre scale, the simulations also use the statistically representative volume concept to represent the microstructure windows in an embedded cell (EC) with homogeneous surrounding material as seen in Fig. 2-5. Because the distribution of stresses and strains at macro-scale boundaries has arbitrary values near the boundaries of the EC, statistical expressions are necessary to compensate for the constitutive behaviour. This step is done before the scale transfer and the link is done statistically.

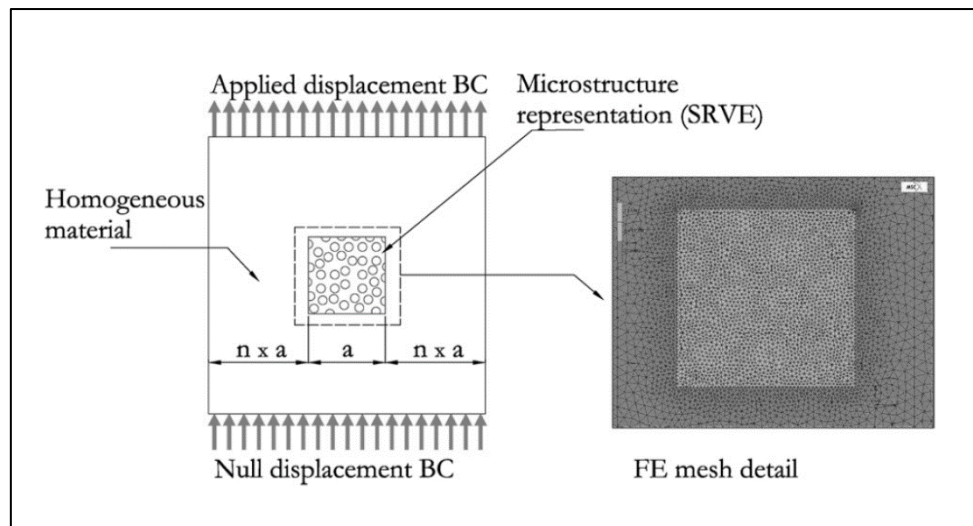


Fig. 2-5: The embedded cell approach in (Trias et al., 2006b).

Although the fracture process is boundary dependent, the compatibility compensations in EC method are based on statistical Weibull distributions of strain energy density. First, the transformations are applied to multiple meso-scale embedded windows. The macro-scale is then related to these computational windows via a one to one relationship of the stress tensors. The limitation in this case is that the preservation of the sampling continuity is extremely costly from a computational point of view. Since the probability space is used at macro-scale, the final global model would not necessarily represent the genuine crack localisation. In general, when using random and statistical fields to cover deformation fluctuations, the mapping continuity is lost. This means that both the elastic constants and fracture energies suffer of inexact integration domains and deformation rates from fine scales.

To some extent, the embedded cell idea was also used in (Li and Zhou, 2013a; Li and Zhou, 2013b; Li et al., 2013). In their works, a 3D multiscale homogenisation computational framework was developed to solve fracture problems with crystal plasticity. The embedded cell here was a meso-scale image-based mesh model as shown in Fig. 2-6. The method was based on the cohesive finite element model (CFEM) and used the Mori-Tanaka method to solve the scale transfer. The bulk and shear moduli were estimated based on stress intensity factors

computed using the J-integral concept (Li and Zhou, 2013b). The initial anisotropy due to the crystallographic orientations of the grains was not considered. Instead, in (Li and Zhou, 2013a) the material phases were assumed to follow the isotropic linear elastic constitutive relations. It is also unclear how the global anisotropy should be considered at macro-scale.

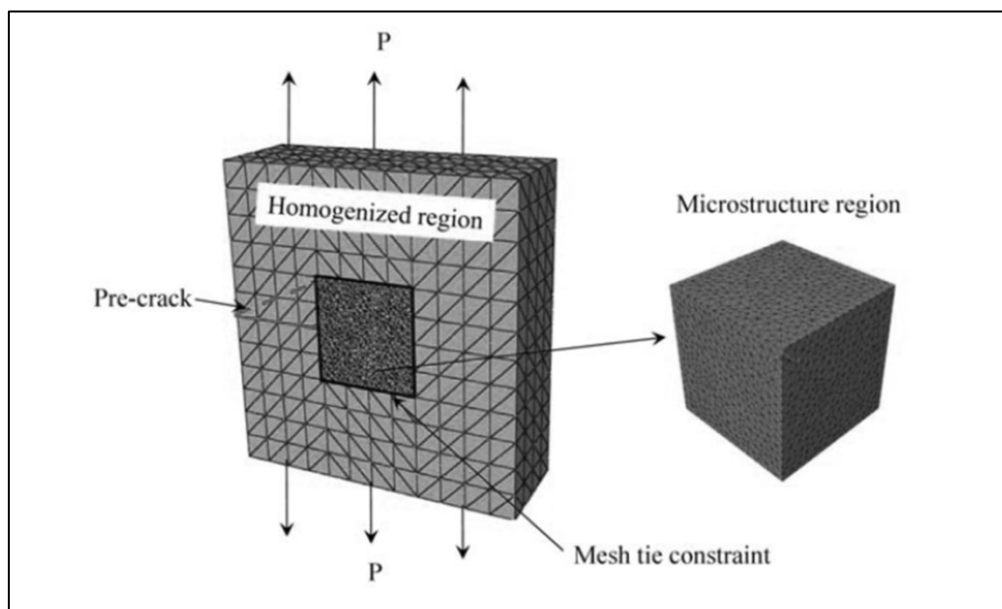


Fig. 2-6: A model assembly for computational multiscale homogenisation after (Li et al., 2013).

At the micro-scale, the hybrid mesh model used in (Li et al., 2013) shows how the mesh embeds a polycrystalline region of the sample (see Fig. 2-6). A kinematical tie constraint was used between the two regions so that mesh nodal conformity was not needed. An initial pre-crack was inserted in the homogeneous mesh. The fracture toughness was then evaluated using a hidden structured mesh which was also attached to the realistic microstructure.

No attempts were reported to solve the deformation continuity by means of compatible deformation rates between different stochastic neighbouring samples, although this is essential in the modelling of realistic multiscale behaviour.

2.5. Summary of existing multiscale modelling methods

Various multiscale models have been developed to solve the scale transfer dilemma, e.g., the coupled-volume multiscale model (Gitman et al., 2008), the multiscale aggregating discontinuities model (Belytschko et al., 2008; Loehnert and Belytschko, 2007), the multi-grid method (Miehe and Bayreuther, 2007; Kaczmarczyk et al., 2010), the homogenisation-localisation methods (Bosco et al., 2015; Coenen et al., 2012a), the enhanced continuous-discontinuous model (Nguyen et al., 2012b; Nguyen et al., 2011), the reduced integration order model (Fish, 2011; Fish and Shek, 1999), the two-scale homogenisation model (Greco et al., 2013; Cusatis and Cedolin, 2007; Desmorat and Lemaitre, 2001), the multi-fractal approach (Carpinteri et al., 2002; Carpinteri and Chiaia, 1997; Xu et al., 2013), and the variational and localized Lagrange multiplier method (Hautefeuille et al., 2012; Markovic and Ibrahimbegovic, 2004).

Table 2-1 summarises the currently available multiscale models based on the finite element method and highlights their main definition level, coupling scheme, specialty and numerical formulation. The general consensus is that multiscale modelling requires complicated numerical strategies to transfer both the continuous and discontinuous deformations. Three categories have been identified to address these issues, namely the concurrent, the hierarchical and the mixed hierarchical-concurrent approaches. However, so far the existing multiscale approaches are not embracing true composite behaviour and to ultimately represent the genuine material length scales, such as for example, to bridge the fibre level to component level mechanics.

Table 2-1: Summary of existing multiscale models based on the finite element method.

Method	Acronym	References	Definition level	Coupling strategy	Specialty/ Coupling Design
Representative Volume Element	RVE	(Coenen et al., 2012c)	Fine-scale	Enforced kinematical constraints	Constitutive relations/ top-down hierarchical.
Statistical Representative Volume Element	SRVE	(Trias et al., 2006a; Trias et al., 2006c)	Fine-scale	Statistical	Constitutive relations/ bottom-up hierarchical.
Indirect Heterogeneous & Stochastic Approaches	None	(Shen and Xu, 2010; Xu et al., 2009; Shen et al., 2009; Su et al., 2010b; Su et al., 2009)	Coarse-scale	Statistical, Multi-resolution approaches, random fields, fractals etc.	Deterministic with material characterization/ hierarchical.
Adaptive concurrent multi-level method	None	(Ghosh and Paquet, 2013; Ghosh, 2008; Ghosh et al., 2007)	Multiple length scales in single global model	Level ties	Detailed mechanics, mixing of homogenisation & global modelling/ concurrent and hierarchical coupling.
Computational homogenisation	CH	(Verhoosel et al., 2010; Cid Alfaro et al., 2010b; Kaczmarczyk et al., 2008)	Fine-scale	Macro statistics	Detailed mechanics & statistical mapping/ Energy-based hierarchical coupling.
Generalised multiscale finite element method	GMsFEM	(Hou and Wu, 1997; Chen et al., 2003; Aarnes et al., 2006; Efendiev et al., 2004; Efendiev et al., 2014; Calo et al., 2014)	Fine-to-coarse	Multi-grids & multiscale basis functions	Linear elasticity & fluid flow problems/ Energy-based hierarchical coupling.
Embedded cell approach	ECA	(Trias et al., 2006b) (Li et al., 2013)	Fine-scale	Statistical	Minimisation of boundary effects/ bottom-up mixed concurrent –hierarchical coupling.
Enhanced continuous-discontinuous multiscale method	ECDM	(Nguyen et al., 2012a; Nguyen et al., 2012b; Nguyen et al., 2012c; Nguyen et al., 2011)	Fine-to-coarse	Damage localisation	Detailed mechanics & damage localisation mapping/ bulk & crack homogenization with hierarchical coupling.

2.6. Numerical Crack Models

The previous section has focused on the transfer of data in multiscale modelling. This section reviews the most popular numerical methods currently employed to model crack growth. According to (Su et al., 2010a) these methods can be categorized as: (i) discrete crack models explicitly separating the crack surfaces, (ii) smeared crack models based on continuum mechanics, and (ii) indirect models such as the lattice, truss and fractals, as examples. The discrete crack models were mainly developed for 2D problems and only recently, complicated 3D fracture behaviour has been simulated mainly in concrete and asphalt materials (Gasser and Holzapfel, 2005; Su et al., 2010b; Rahman and Chakraborty, 2011; Yin et al., 2013; Ren et al., 2015; Huang et al., 2015). Some simplified 3D damage simulations for unidirectional fibre composites can be also found in (Mishnaevsky, 2012; Mishnaevsky Jr and Brøndsted, 2009; Wang et al., 2014). However, in these simulations the damage modelling is understood by a simple stress intensity threshold.

The broad assumptions of the different crack models are:

- (i) Discrete crack models based on re-meshing techniques (Yang and Chen, 2004; Réthoré et al., 2004; Ooi and Yang, 2009): a representative semi-analytical method based on a re-meshing routine is the Scaled Boundary Finite Element Method (SBFEM) (Ooi and Yang, 2009). The method is designed for modelling problems with discontinuities and singularities (Ooi and Yang, 2011).
- (ii) Smeared crack models (Pham et al., 2006): an infinite number of parallel cracks of infinitesimal thickness are assumed to distribute over the finite elements (Kwak and Filippou, 1990). The crack propagation is then introduced by reduction of the stiffness and strength of the material. A comprehensive literature review including the limitations of these models is given in (Gálvez et al., 2002).

- (iii) Nodal enrichment models such as the Extended Finite Element Method (X-FEM) (Meschke and Dumstorff, 2007; Markus, 2007) endorse the concept of local nodal enrichment of the finite elements. This is achieved by partitioning and allows the discontinuous displacement field to take place.
- (iv) Cohesive crack models are most commonly based on pre-embedding cohesive interface elements without re-meshing (Su et al., 2009; Yang et al., 2009; Su et al., 2010b; Xie and Waas, 2006; Yang and Xu, 2008). They assume the existence of a fracture process zone (FPZ), originally introduced by (Barenblatt, 1959; Dugdale, 1960) for elastoplastic fracture of ductile materials and later elaborated by (Hillerborg et al., 1976) to include the quasi-brittle material effects in the so-called ‘fictitious crack model’. This model has been later adopted and developed by many other authors (Tvergaard and Hutchinson, 1992; de Borst, 2003; Bažant and Oh, 1983; Seagraves and Radovitzky, 2010; Yang and Xu, 2008; Carpinteri, 1989).

To summarise, it can be noted that most of the existing crack propagation models have tackled fracture problems with single, a few cracks or pre-defined bi-material interfaces. The fine-scale multiphase structures are mostly assumed and the numerical results are difficult to be accurately validated.

2.7. X-ray Computed Tomography

Traditionally, the model validation of the FRP parts for fracture resistance was done either by testing the full-size component or by using a series of small probes (Kabele, 2007; Molent et al., 1989). An inverse modelling approach was then undertaken to extract relevant material properties. This is a costly approach. More importantly, many essential mechanical data cannot be obtained due to the lack of intrusive measurements. A relatively new testing and validation technique is the X-ray Computer Tomography (X-ray CT). From such tests, image based models can be built. The research focuses now mainly on the use of image-based models to

improve and validate numerical models. The advantage is that the numerically simulated deformation steps or damage progression can be directly compared to the actual mechanical test results.

So far, the image-based modelling has not been used in multiscale modelling and validation. In addition, multiscale models considering the effects and inter-scale transfer of stochastic information are still largely limited to the prediction of homogenised elastic properties (Xu and Graham-Brady, 2005; Xu and Chen, 2009) rather than complicated fracture evolution. In fact, realistic 3D multiscale modelling of fracture in composite materials has rarely been reported, probably due to the very large number of degrees of freedom in the fine-scale models that are beyond the power of conventional computers. Therefore, much research is still needed to develop more robust multiscale methods for complicated fracture modelling, as also pointed out by a report of U.S.A. National Committee on Theoretical and Applied Mechanics (Belytschko, 2007). This thesis will address the earlier issues considering a hierarchical multiscale modelling approach. The meso-scale domain will be separated into non-overlapping and adaptive size-increasing overlapping elements in both 2D using digital micrographs, and 3D using reconstructed X-ray CT models.

2.7.1. Previous X-ray CT tests in fibre composites at fibre level

One of the first X-ray CT tests using the synchrotron radiation technology to investigate the fracture process in fibre composites is the work in (Kinney and Nichols, 1992). The material scanned was an aluminum matrix/SiC SCS-8 fibre composite. The fibre outer diameter was approximately 100 μm with a 30 μm carbon core. The X-ray CT resolution was approximately 2-3 $\mu\text{m}/\text{voxel}$. Fig. 2-7 shows the 2D projections of the fracture surface and the 3D volume render of a small portion containing a fibre pull-out failure mechanism.

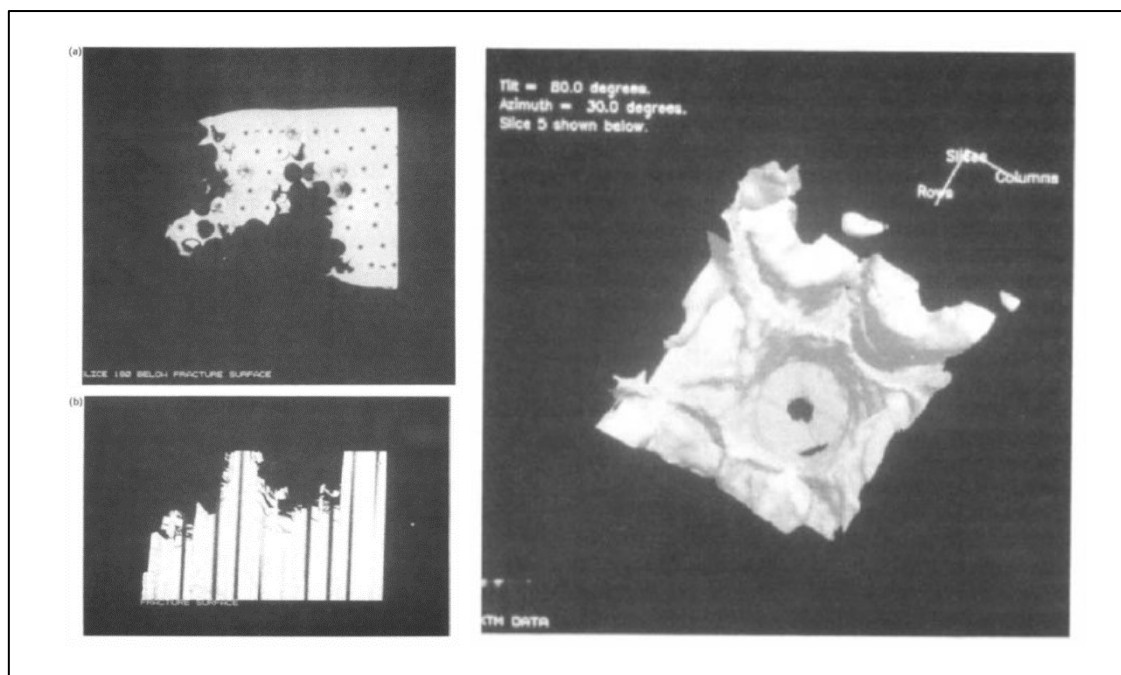


Fig. 2-7: Early X-ray CT scans to investigate the fracture process of an aluminum matrix/SiC SCS-8 fibre composite (Kinney and Nichols, 1992).

A similar Ti-6Al-4V/ SCS-6 SiC monofilament metal matrix composite was scanned in (Withers et al., 2012). The fibre diameter was $140\text{ }\mu\text{m}$ with carbon core. The resolution was $1.59\text{ }\mu\text{m/pixel}$. A combined approach with high spatial resolution diffraction and synchrotron X-rays imaging was used to monitor fatigue crack growth. Fig. 2-8 shows the gradual progression of the crack that by-passes the thick SiC fibres.

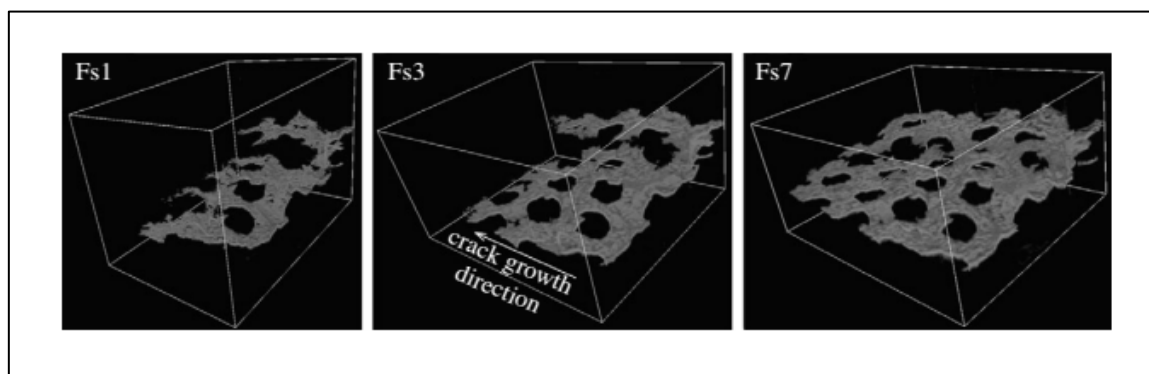


Fig. 2-8: 3D visualisation of a transverse fatigue crack progression that by-passes the $140\text{ }\mu\text{m}$ diameter fibres (Withers et al., 2012).

Other excellent in-situ X-ray CT scans of SiC/ SiC composite rods (Fig. 2-9) were successfully captured at room and ultrahigh temperatures under the synchrotron radiation in (Bale et al., 2012). The SiC fibre diameter was approximately 12 μm . The resolution was 0.65 $\mu\text{m}/\text{voxel}$ and the scan area was approximately 5 mm by volume stitching.

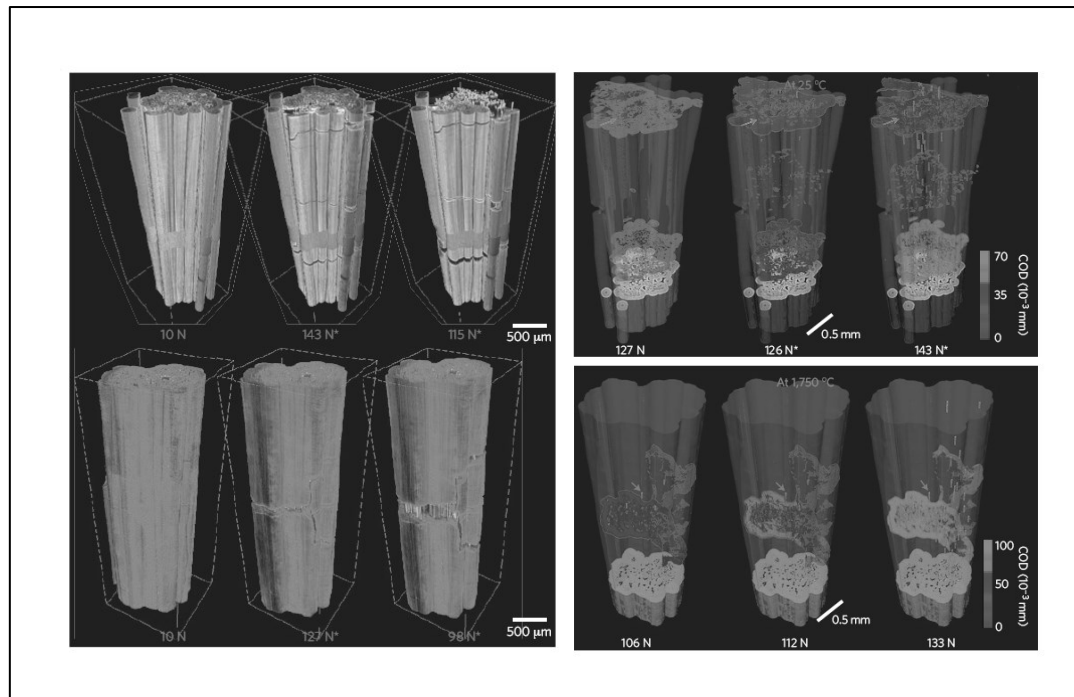


Fig. 2-9: Synchrotron in-situ X-ray CT tests of a single-tow SiC/SiC composite specimen at room 25°C and ultrahigh 1,750°C temperatures (Bale et al., 2012).

Many other in-situ X-ray CT experiments in fibre composites studied the material microstructures (either intact or post-mortem) at fabric level only rather than capturing the fracture mechanism, mainly due to the lack of in-situ loading rigs (McCombe et al., 2012; Enfedaque et al., 2010; Yu et al., 2015b; Müller et al., 2015).

2.8. Summary

A state-of-the-art review has been presented in this chapter. It is found that there exist two main multiscale modelling methods, namely, the uncoupled and coupled methods. The uncoupled models (one-way models) either start with a macroscopic model (top-down) with known boundary conditions or a microscopic model that is statistically linked to the global scale (bottom-up). Although in the top-down uncoupled approach, the external boundaries and macroscopic structure details are often known a priori (e.g. the load-displacement curve, time to failure from test records), the desired microstructural response is often based on enforced kinematical windows with loose stiffness assemblies that are contradictory to standard FE method. On the other hand, due to the difficulty in finding the right balance in coupled methods between the external and internal forces, the coupled models need artificial boundary conditions to ensure deformation compatibility between the two scales. However, the boundaries at the fine scale may be completely non-existent for certain phenomena. Modifications should be made to avoid such inherent difficulties that come with the coupling of scales for scale transfer. This is a major achievement of this project and the new method will be presented in CHAPTER 3 and CHAPTER 4 of this thesis. Providing X-ray CT data of detailed fracture process of FRP composites and reconstruction of the raw X-ray CT data to generate meshes for multiscale finite element modelling of FRP composite fracture is another pillar of this research project.

In this research, a hierarchical multiscale modelling approach is used to combine reconstructed image-based meso-scale elements with a global model. Two main assumptions are made herein without losing the ergodic multiscale objective in quasi-brittle materials: (i) image-based models are computed in parallel using a complete set of boundary conditions with high expectation to occur at fibre level and (ii) stochastic variation of material properties can be used to populate global multiscale models wherever material fine scale information is inexistent.

The first is acceptable due to the relatively low sensitivity of the crack propagation process to strain fields developed in each of the constituent phases of the quasi-brittle carbon fibre material used in this study. The second assumption is necessary due to the large scales jumps that cannot be currently fully characterised with the X-ray CT and emerged with the available post-processing tools.

CHAPTER 3. A NEW METHOD FOR 2D MULTISCALE STOCHASTIC FRACTURE MODELLING

3.1. Introduction

A new coupled method for multiscale stochastic fracture modelling (MsSFrM) is developed. The coupling is based on fracture energy conservation and exact crack mapping. A key difference between this new method and other methods is that the mapping is performed before discretisation of the macro-scale model, and based on the detailed crack paths obtained from meso-scale simulations. The technique of pre-embedding cohesive interfacial elements is used in the meso-scale simulations so that complicated multi-crack initiation and propagation can be modelled. The new method has been developed to enable computation of structures of heterogeneous quasi-brittle composites with a large number of degrees of freedom (DoF), in particular, when high-resolution micrographs or X-ray CT images exhibiting multiscale details are available.

The chapter presents the 2D development of the new multiscale method. The implementation and validation of the proposed 2D multiscale method will be presented in CHAPTER 4. The extension to 3D fracture problems will be presented in CHAPTER 7.

3.2. The new multiscale stochastic fracture mechanics framework

Fig. 3-1 shows the framework of the new method with the key computational modules highlighted. It starts with acquiring a high-resolution image of the global domain by micro-tests using advanced techniques such as high-resolution cameras, microscopes and X-ray CT images. The image is then processed and segmented into different material constituent phases. For validation purpose, if the crack paths and load-carrying capacities are not available from the micro-tests, a full micro-scale FE modelling of the global domain is carried out. In this case, the global-domain image is first transformed into FE meshes of solid elements. Cohesive

interface elements with softening traction-displacement constitutive laws in normal and shear directions are then inserted into the matrix mesh and between the matrix-inclusion interfaces, to model potential cracks.

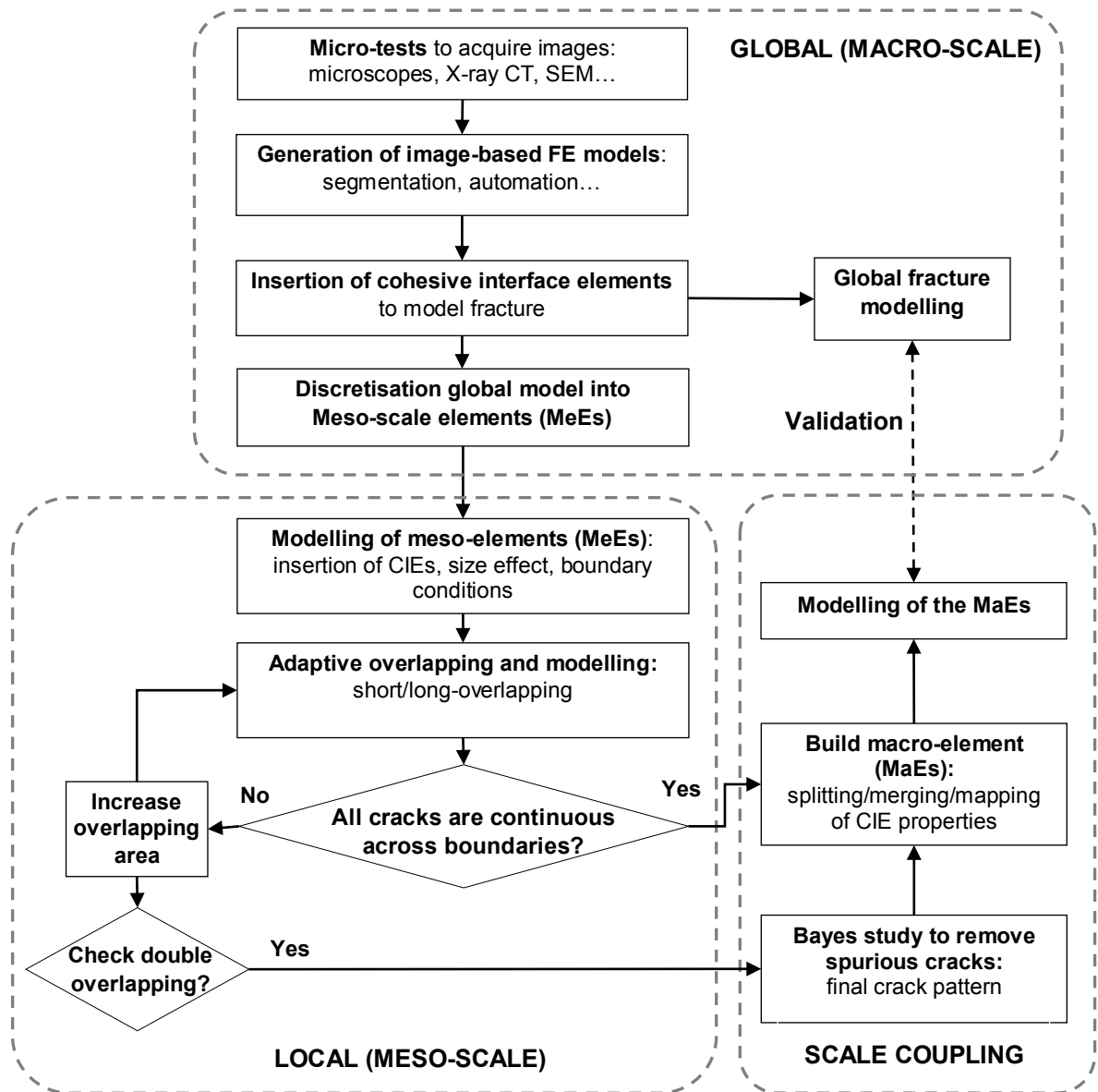


Fig. 3-1: A two-scale coupling scheme for stochastic fracture mechanics.

The global domain is then divided into a grid with a number of non-overlapped rectangular meso- elements (MeEs), illustrated in Fig. 3-3-a as an example. For each MeE, its micro-structure is meshed with CIEs inserted and a nonlinear FE analysis is conducted. Size effect studies on the strength are carried out to determine a proper number and size of the MeEs. Two

boundary conditions as illustrated on the first row in Fig. 3-2, noted as $B1$ and $B2$ are necessary for the MeEs and scale transfer. $B1$ is the uniaxial tensile condition and $B2$ is the shear condition necessary for the nonlinear integration of tractions for the global CIEs. At the global scale, two types of external uniaxial boundary conditions $G1$ and $G2$ are modelled, as illustrated in Fig. 3-2-c and d, respectively. The $G1$ condition tends to result in the pure mode-I fracture mode, while $G2$ allows core rotations and may lead to two main cracks. The $G2$ condition has also been increasingly used (Park and Paulino, 2012; Wang et al., 2015b; Ren et al., 2015). In this study, this is not implemented as a boundary condition for the scale transfer because it allows core rotations that bifurcates the global crack path.

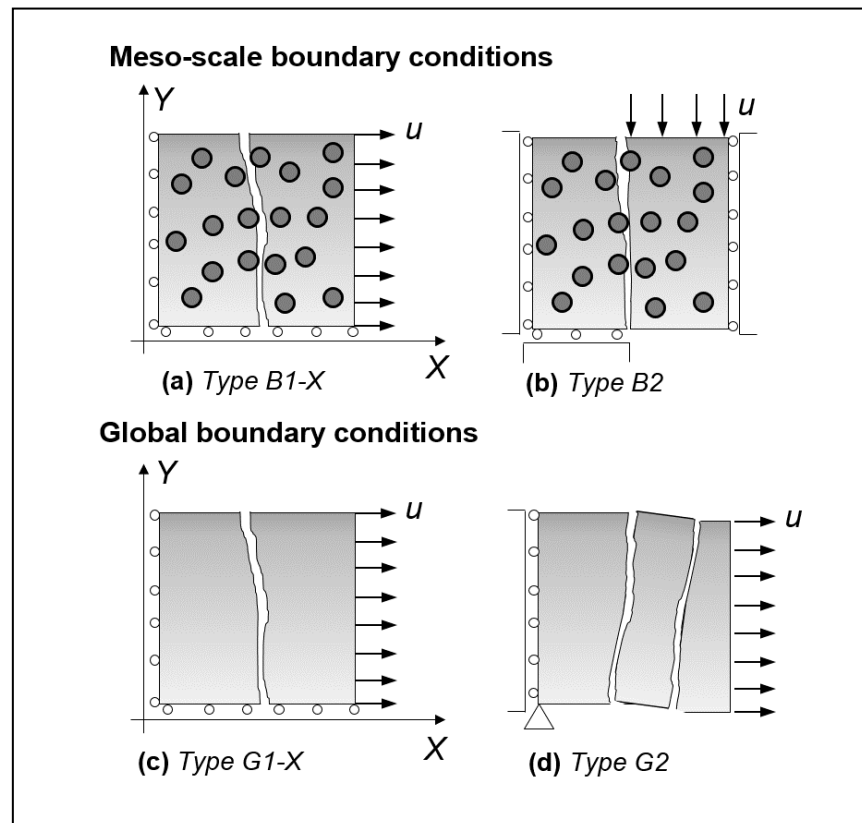


Fig. 3-2: Boundary conditions for meso-scale modelling and for global multiscale models.

Fig. 3-3-b shows the crack paths from 16 independent nonlinear simulations of MeEs under the $B1$ - X condition (X means horizontal and Y vertical direction).

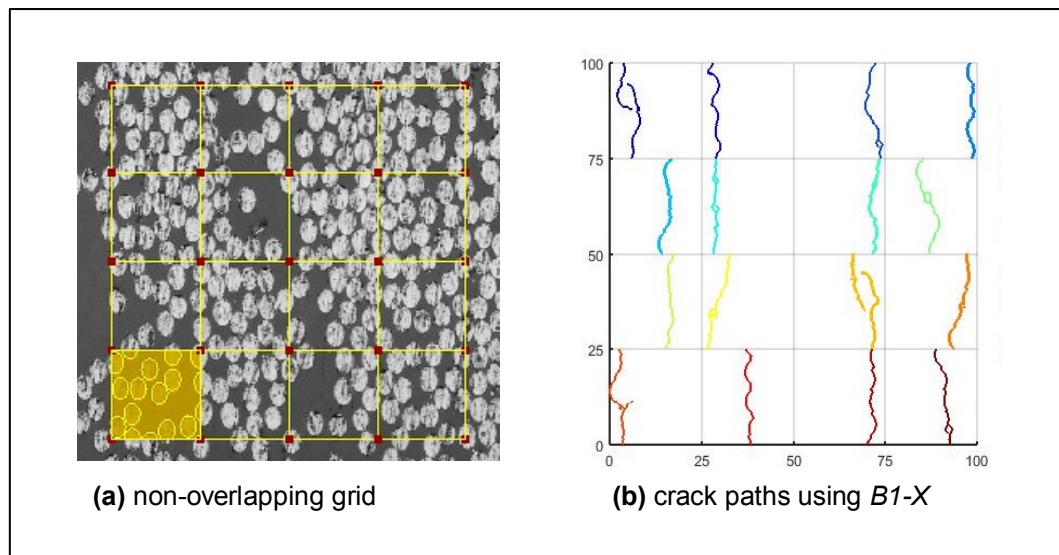


Fig. 3-3: (a) A global domain discretised into 16 non-overlapped MeEs and (b) the modelled crack paths for each MeEs independently under $B1-X$ boundary condition.

From Fig. 3-3-b it can be seen that not all the cracks across the MeEs' boundaries are continuous, indicating that deformation compatibility and crack matching does not hold. This usually occurs when a non-overlapping grid is used. To improve the situation, an overlapping grid in Fig. 3-4-a is then designed with the same number and position but larger size MeEs. All the MeEs are again modelled independently. The resulting crack paths are shown in Fig. 3-4-b. It can be seen that most of the crack paths now cross the MeEs' boundaries continuously, indicating improvement of the overlapping grid over the non-overlapping grid (see Fig. 3-3-b). Subsequent overlapping grids with larger MeEs can be further designed and modelled if necessary. Fig. 3-4-c shows the final crack paths which nearly seamlessly cross all the MeEs' boundaries. This algorithm of using adaptively size-increasing overlapping grids works because the larger the overlapping regions become, the better deformation compatible support is provided.

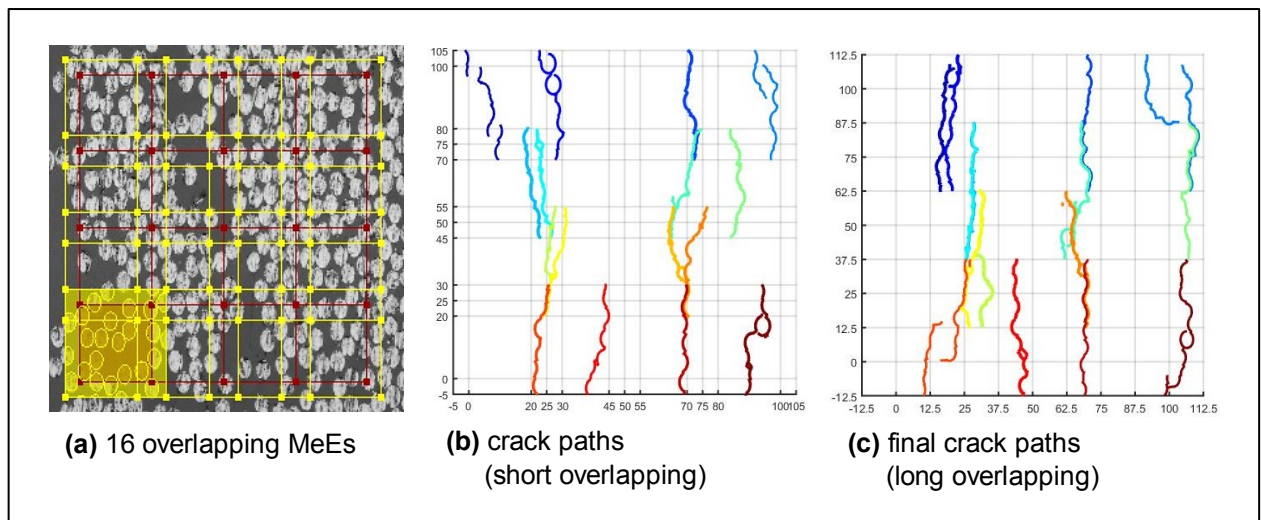


Fig. 3-4: Overlapping MeEs and crack paths under $BI-X$ boundary.

However, because the MeEs are separately modelled and the deformation compatibility cannot be rigorously ensured, some non-critical or possibly non-physical overlapped or biased crack paths may still be predicted. To improve this situation further, the Bayes inference model is applied to filter the crack paths to preserve the most critical cracks only for subsequent scale transfer. This is achieved through filtering between the neighbouring windows as discussed in detail below.

3.3. Bayes inference model for overlapping MeEs with biased crack paths

The local crack probability between overlapping MeE neighbours with non-matching or biased crack paths can be established using the Bayesian inference model in Eq. 3-1. To build a local crack probability space, the discrete crack surfaces are first identified within all MeEs. Using this filtering approach, the overlapping regions learn their integration domains using neighbouring searches as suggested in Fig. 3-5 and the Bayesian probability rule in Eq. 3-1. In other words, the Bayesian filter checks when cracks are matching at the boundaries and removes biased cracks according to following equation:

$$P(C|E) = \frac{P(E|C)}{\sum_m P(E|C_m)P(C_m)} \cdot P(C) \quad \text{Eq. 3-1}$$

where C represents the crack path to be filtered, E represents the surrounding cracks from neighbouring simulations. For simplicity, the likelihood $P(E|C)$ and prior probability of crack matching $P(C)$ are evaluated using their corresponding image space further explained with Eq. 3-2.

Suppose that the fracture process is generating several independent crack events E_n which come from similar boundary conditions, but their distributions are stochastic in relation to C . The model in Eq. 3-1 evaluates the degree of matching of a single crack path with all the neighbouring cracks. For the initialisation, all adjacent crack models obtained from parallel simulations are collected in C_m . In practice, each non-marginal MeE cluster belonging to C_m receives eight surrounding elements that yield eight separate crack paths and is used to construct a local filter. This is because the MeE shape is rectangular. For example, Fig. 3-5-b explains the non-marginal MeE cluster approach, although similar steps can be conducted on other cases. Suppose that the denominator of Eq. 3-1 is represented by some equally distributed probabilities $P(C_m)$ for all the adjacent half-overlapping MeEs and quarterly overlapping MeEs. These probabilities can be fixed to any equal numerical quotients so that $\sum_{m=8} P(C_m) = 1$, but otherwise these values are arbitrary. Such arbitrary values are typically accepted in Bayesian and other filtering models due to the necessary normalisation of data. Therefore, the separate probability values $P(E|C_m)$ also correspond to the surrounding cracks individually, where $m=1, 2, 3.. 8$ remain fixed over a typical cluster.

Furthermore, the posterior probability $P(C|E)$ of an element crack to match any of the neighbouring cracks is checked against collectively with all of crack surfaces at once (see Fig. 3-6-a). Eq. 3-2 explains how the multiplication of the two probabilities can be interpreted in a

general image space integral. This is taken here by evaluating their pixel intensity distributions after multiplication, thus:

$$P(E | C)P(C) = \iint f(x, y)g(x, y) \, dx dy \quad \text{Eq. 3-2}$$

where functions $f(x, y)$ and $g(x, y)$ are the pixel intensity distribution functions and define the two images containing surrounding crack paths and crack path C respectively.

By further analysis of the Bayesian model at Eq. 3-1 and Eq. 3-2, it can be seen that the so-called likelihood $P(E|C)$ (here represented by an image $f(x, y)$ containing all surrounding cracks) is used to update the posterior probability $P(C|E)$ given a test/ prior probability $P(C)$ as illustrated in Fig. 3-6-a. This is possible due to the overlapping support of the method as also illustrated in Fig. 3-5. Finally, the evaluated probability $P(C|E)$ can be therefore used to threshold and filter continuous/discontinuous crack paths by evaluating the number of overlapped pixels.

It should be mentioned that only one set of boundary conditions is used at a time; nevertheless, the algorithm can be easily replicated or used collectively to multiple boundary conditions and Markov chain analogies as for multiple overlapping grids. An example of a binary hidden Markov model with Bayesian algorithm can be found in (Volant et al., 2012). Alternatively, as in this thesis, the Bayesian values $P(E|C)$ and $P(C)$ were initially evaluated using a reduced number of discrete key-points taken at known locations.

As a discussion, there may also exist two general crack path cases shown in Fig. 3-5-a as follows: (1) grid intersecting cracks and (2) grid-free cracks exemplified in Fig. 3-5-a. The grid-free cracks can be further split in: overlapping domain cracks and non-overlapping domain cracks when the short overlapping criterion is used (Fig. 3-5-a). Furthermore, if overlapping length is equal to or larger than half size of the MeE grid distance, the grid free non-overlapping cracks merge into grid-free overlapping cracks. This becomes valid for all the non-marginal

elements due to full overlapping length as illustrated in Fig. 3-5-b. If overlapping length exceeds half-length of the MeE grid distance, double overlapping regions appear. Those correspond to twice the exceeding length for non-marginal elements. However, due to complexity in multiscale transfer, this section deals with single overlapping grids of full-length only, which bounds the long overlapping criteria to half the length of MeE size.

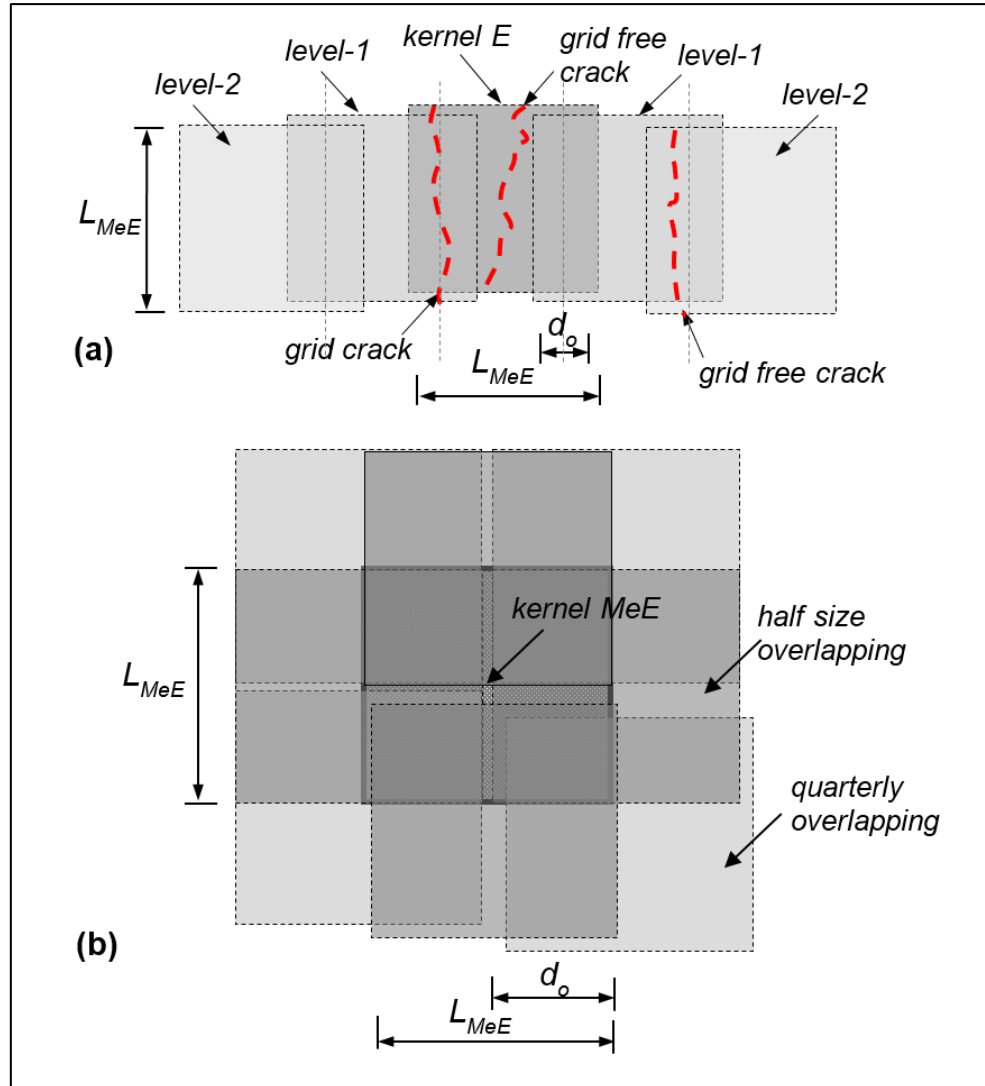


Fig. 3-5: Illustration of crack sampling cases for the overlapping windows concept used with Bayesian criterion in Eq. 3-1. The dark-shaded elements represent four half size overlapping elements and soft-shaded elements represent four quarterly overlapping elements.

To quantify the matching degree with less computational effort, only two key-points were initially used in this study. For example, the intersecting points of crack paths cross-cutting the

non-overlapping grid. These points are valid when using any overlapping MeE sizes but may struggle when using multiple boundary conditions at the same time. Therefore, the general case is implemented using matrices based on pixel metrics. Fig. 3-6 shows the implemented procedure and results on an element when using the half size overlapping criteria.

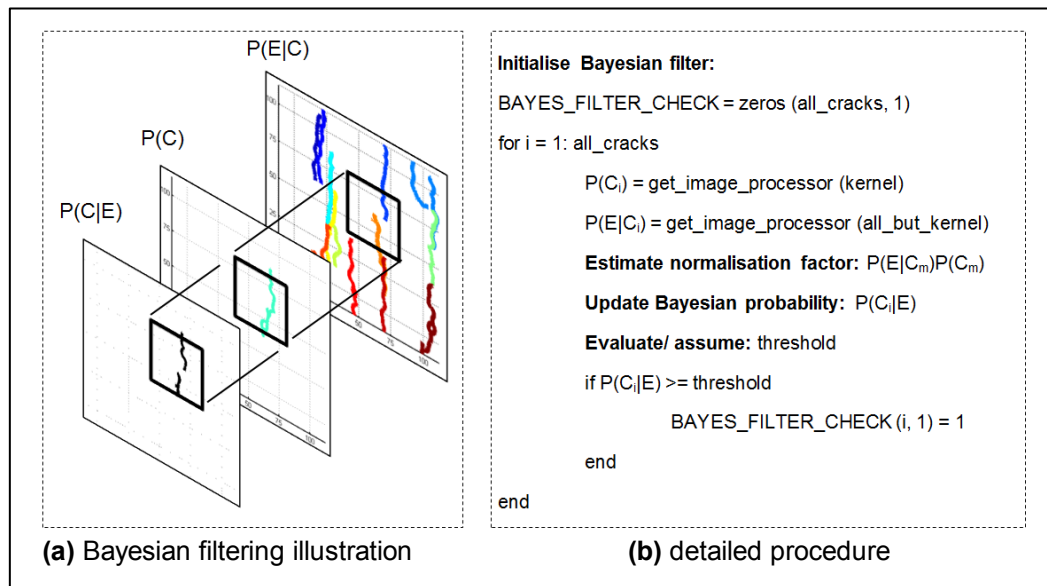


Fig. 3-6: Bayesian filtering procedure and threshold probability on a typical non-marginal MeE cluster.

Fig. 3-7 shows the final crack paths after using Bayesian filtering method proposed in this paper for two cases using the short and long overlapping grids (half the size of an MeE).

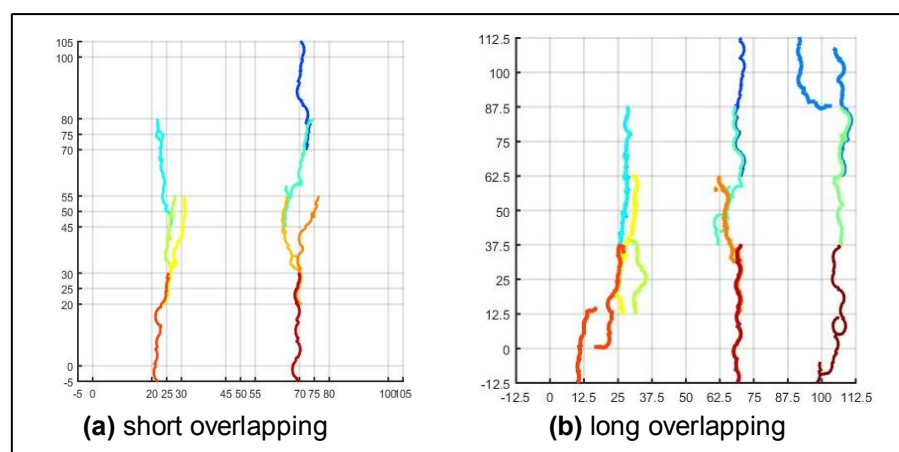


Fig. 3-7: Filtered overlapping MeE crack path data after using the Bayesian inference model corresponding to Fig. 3-4-b and c.

Since the model in this study is overlapping up to half the size of element surfaces (see Fig. 3-5-a and b) probabilities of spaced kernels can only be linked by level-1 searches. Level-2 links are not possible herein because of the maximum overlapping criteria. Consequently, the method may not currently capture potentially matching cracks that belong to distant computational domains (such as between spaced elements). Although this was less important in this case study, the limited overlapping assumption may obscure important cracks from scale transfer in other applications and it requires further investigation.

3.4. Construction of macro-scale elements (MaEs)

In general, short and long overlapping can be used as illustrated in Fig. 3-8. This depends on the size establishment as for the MeE overlapping grid and are limited to single overlapping regions. This means that the size of an overlapping MeE cannot be larger than twice the MeE non-overlapping grid size (see Fig. 3-3-a and Fig. 3-4-a). In this research, it is found that for defective materials, the short to long overlapping method may be used. For less defective materials, non-overlapping as for elastic studies or short overlapping discretisation in fracture mechanics may be used.

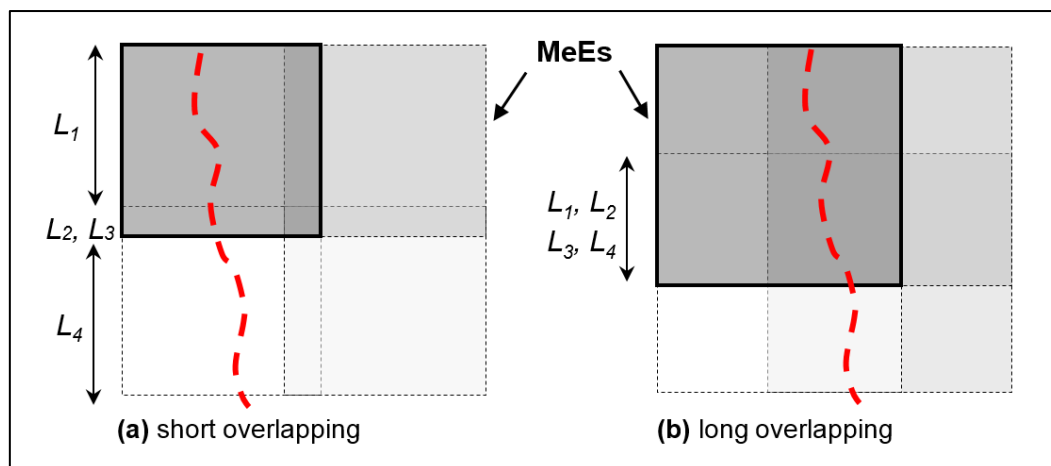


Fig. 3-8: Illustration of (a) short to (b) long overlapping criteria. The colour intensities represent distinct MeE windows that are overlapped.

The average fracture properties from corresponding crack path lengths are denoted with L_i in Fig. 3-8, where i is the corresponding overlapped crack path. Therefore, the obtained crack paths are integrated using simplified lines and transferred to the macro-scale by inserting cohesive elements. The macro-scale elements are constructed after the optimised crack paths are found. The final meso-scale crack paths and non-overlapping grids are naturally used as guidelines to discretise the domain into a macro-mesh with a number of MaEs. The softening constitutive laws are piece-wisely mapped from the meso- CIEs so that energy conservation is ensured in the scale transfer (see Fig. 3-9).

The macro-scale mesh discretisation includes the intersection nodes, the assembly of the MaE model and the insertion of macro-scale cohesive interface elements. Fig. 3-9 sketches two possible macro-scale models. The crack paths are identified based on the scalar degradation parameter d and the energy dissipation rate per unit volume of damage. In the case of short overlapping MeEs, the MaE nodes are at the intersections of the crack paths that cross cut the non-overlapping grids. The example illustrated in Fig. 3-9 uses the $BI-X$ boundary conditions. Two operations are used in the construction of the macro-meshes: merging and splitting (see Fig. 3-9-a and b). These operations are generally used to reduce the integration order of the macro-model. However, they also become necessary when the crack path is very close or intersecting the non-overlapping grid. Their implications on the energy mapping rules are discussed in next section.

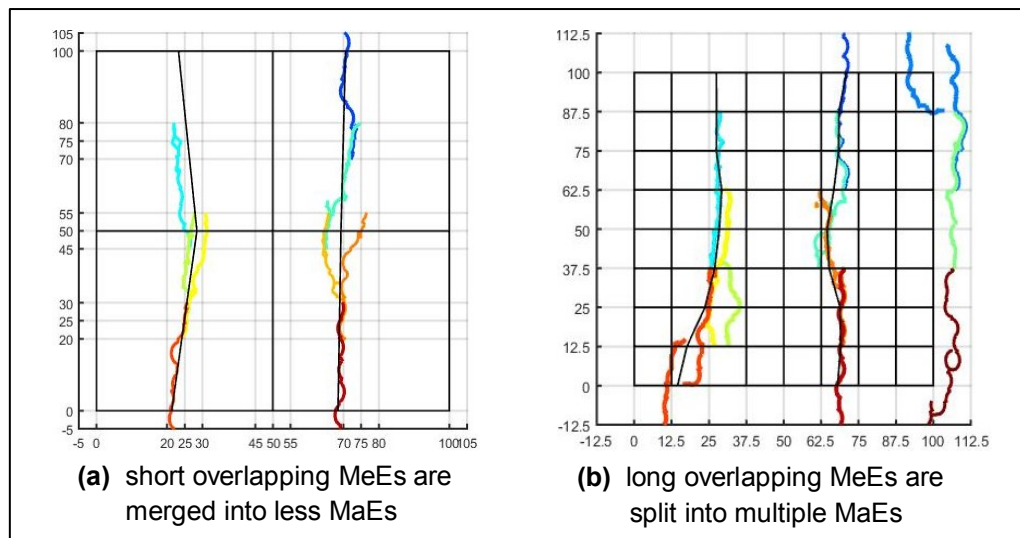


Fig. 3-9: Illustration of two possible macro-scale meshes. The crack paths are used as boundary constraints during the MaE mesh generation. The cracks are also represented by cohesive interface elements (CIE) in the global model.

In fact, many other mesh models can be created at global length scale once the most critical crack paths avail the detailed simulations. For example, it is possible to build reduced integration meshes, either by using triangular or non-structured quads or by keeping details of the heterogeneous meso-scale mesh with coarser macro-scale elements and only inserting cohesive elements or enrichment nodes where necessary. However, there are some sources of uncertainty associated with the above strategy, especially for the softening part and their solutions, for example:

- (i) the centreline of the deformed cohesive crack MaEs may not be the same as the initial zero-thickness crack path which is used to build the MaE elements; this is due to the reversing of damage process for crack identification paths which were obtained using prescribed boundary conditions based on the stochastic element cluster assumption.
- (ii) the superposed straight edges of MaE elements in reduced order strategies may not be in line with the true integration crack paths which have a certain tortuosity; however, it

is a reasonable assumption when using invariant crack paths to MeE boundary effects.

This strategy can be used to reduce the global model size considerably.

- (iii) using more complicated mixed-mode boundary conditions (BCs) and highly non-homogeneous distributions of defects, two dominant crack failure modes can appear which may be tackled with a rotational centre. This imposes geometrical non-linearity in the macro- cohesive model which was not tested in this study.

3.5. Fracture energy mapping rules

After the macro-mesh is constructed, the traction-displacement softening curves of macro-CIEs need to be mapped from the meso-CIEs at the same position to ensure energy conservation. The conversion of stress displacement curves in fracture energy is done according to the assumption in (Hillerborg et al., 1976) which defines the fracture energy required to open a unit area of crack by:

$$G_f = \int_{u_0}^{u_f} \sigma_{f,u} du \quad \text{Eq. 3-3}$$

$$\sigma_{f,u} = \sigma(u)$$

where σ_f and u_0 are the ultimate strength and displacement at the onset of fracture.

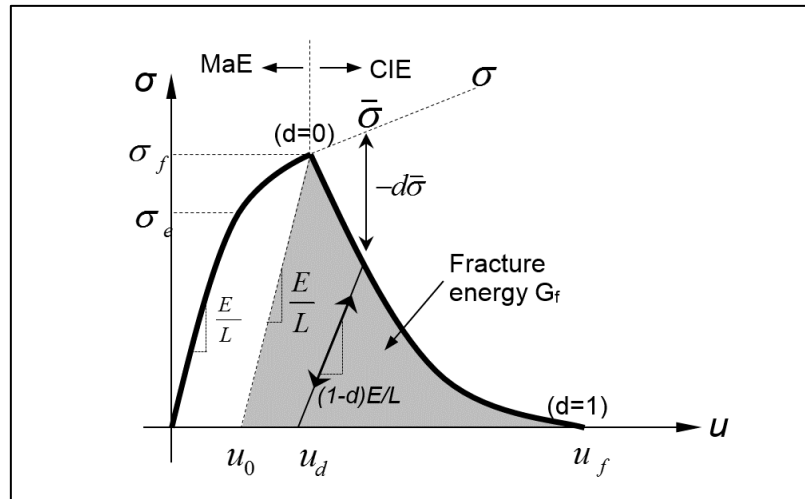


Fig. 3-10: Illustration of the stress-displacement curve for the macro-scale bulk material properties. $\bar{\sigma}$ is the stress due to no damage, d is the scalar degradation variable and L is the characteristic length (Simulia/Abaqus).

For accurate integration across the scale transfer, L in Fig. 3-8 can be represented by the actual crack length. This is feasible when appropriate scale discretisation and mesh order reduction strategy is considered. To prove the suitability of the new multiscale concept, ABAQUS/Explicit is used. In general, the estimated fracture energy from the collection of

detailed MeE integration domains is consumed at macro-scale by the opening of macro cohesive elements. The method can be implemented by using both non-overlapping and overlapping adaptive strategy as discussed above. However, because the strategy uses fixed or enlarged computational areas but multiple parallel windows, this particular concept can be used to capture localised fracture behaviour with lower single simulation computational effort compared with large full-size detailed models. Two other advantages of the overlapping approach in this paper are: the capability of coupling weak to relatively strong interface models and its fully anisotropic formulation for analyses of complicated materials. This means that larger MeE windows can be adaptively employed for modelling materials with various degrees of flaws and fully anisotropic properties at any length scale.

Different energy mapping rules are derived for merging and splitting operation respectively, considering both short and long overlapping.

3.7.1. Merging and splitting approach

The merging and splitting approach (MSA) is an edge oriented multiscale cohesive crack model. The neighbour cluster of stochastic MeEs is either merged into larger size MaEs or split into several smaller size MaEs. The fracture energy dissipated is derived accordingly for the general cases based on average weighting factors of the overlapping regions as given in Eq. 3-4 and Eq. 3-5 for short and long overlapping respectively. Therefore, it should be noted that before using these two mapping rules, the existence of L_i factors contributing towards the macro-CIE should be first checked (see Fig. 3-8).

$$G_{f,short} = \int_{u_0}^{u_f} \sigma_{f,L1} du + \frac{1}{2} \left(\int_{u_0}^{u_f} \sigma_{f,L2} du + \int_{u_0}^{u_f} \sigma_{f,L3} du \right) + \int_{u_0}^{u_f} \sigma_{f,L4} du \quad \text{Eq. 3-4}$$

$$G_{f,long} = \frac{1}{4} \left(\int_{u_0}^{u_f} \sigma_{f,L1} du + \int_{u_0}^{u_f} \sigma_{f,L2} du + \int_{u_0}^{u_f} \sigma_{f,L3} du + \int_{u_0}^{u_f} \sigma_{f,L4} du \right) \quad \text{Eq. 3-5}$$

It is important to highlight, that the sum of the weighting factors presented in the above equations Eq. 3-4 and Eq. 3-5 stand for the short and long overlapping criteria, and their summation do not need to equal 1. This is because the method is a non-unity approach. This is in contrast to classical continuum mechanics where stress is usually homogeneous and the integration is self-contained within each element under the inner Gauss points. Here, due to the nested/overlapping global discretisation and the stochastic arrangement of fibres, all stress fields are heterogeneous that ultimately result in stochastic crack paths also overlapping on different portions.

The crack evolution at macro-scale can be also defined by means of a scalar degradation variable d which ranges between 0 and 1 (see explanation in Fig. 3-10). The linear formulation of d can be expressed as:

$$d = \frac{u}{u_f} = \frac{2G_{f,L_i}}{u_f \sigma_{f,L_i}} \quad \text{Eq. 3-6}$$

Combining the Eq. 3-4 and Eq. 3-5 with Eq. 3-6, the linear degradation variables become:

$$d_{short} = \frac{1}{3} \left(\frac{2G_{f,L_1}}{u_{f,L_1} \sigma_{f,L_1}} + \frac{G_{f,L_2}}{u_{f,L_2} \sigma_{f,L_2}} + \frac{G_{f,L_3}}{u_{f,L_3} \sigma_{f,L_3}} + \frac{2G_{f,L_4}}{u_{f,L_4} \sigma_{f,L_4}} \right) \quad \text{Eq. 3-7}$$

$$d_{long} = \frac{1}{4} \left(\frac{2G_{f,L_1}}{u_{f,L_1} \sigma_{f,L_1}} + \frac{2G_{f,L_2}}{u_{f,L_2} \sigma_{f,L_2}} + \frac{2G_{f,L_3}}{u_{f,L_3} \sigma_{f,L_3}} + \frac{2G_{f,L_4}}{u_{f,L_4} \sigma_{f,L_4}} \right) \quad \text{Eq. 3-8}$$

The degradation rates d can be also expressed exponentially. To ensure that the total energy dissipation on softening equals the total fracture energy G_f , the following expressions are derived:

$$d_{short} = 1/3d_1 + 1/6(d_2 + d_3) + 1/3d_4 \quad \text{Eq. 3-9}$$

$$d_{long} = 1 / 4(d_1 + d_2 + d_3 + d_4) \quad \text{Eq. 3-10}$$

where d_i are the individual contributions of MeEs to the degradation of the macro-cohesive element as illustrated in Fig. 3-8 and given by:

$$d_i = 1 - \exp\left(-\int_{u_0}^{u_f} \sigma_{f,u,Li} du / G_{f,Li}\right) \quad \text{Eq. 3-11}$$

This ensures that the fracture energy is gradually consumed during each displacement increment u_{Li} .

3.7.2. Crack path decomposition approach

The crack path decomposition approach (CDA) is an explicit model, in the sense that cohesive elements are inserted only where necessary, while the homogenized continuum elements MaEs are integrated correspondingly so as to preserve the individual phases or composite elasticity. The material properties of cohesive elements for the overlapped mesh can be avoided if similar crack paths are repeating. Therefore, the general energy mapping rule involving non-overlapping single cracks or single-split cracks that overlap such as in Fig. 3-9-b reduces to:

$$G_{f,Li} = \int_{u_0}^{u_f} \sigma_{f,u,Li} du \quad \text{Eq. 3-12}$$

where the linear degradation variables are:

$$d_i = \frac{2G_{f,Li}}{u_{f,Li} \sigma_{f,u,Li}} \quad \text{Eq. 3-13}$$

and the exponential degradation variables are:

$$d_i = 1 - \exp\left(-\int_{u_0}^{u_f} \sigma_{f,u,Li} du / G_{f,Li}\right) \quad \text{Eq. 3-14}$$

where i corresponds to the crack site that is replaced by a 4-noded cohesive element. L refers to the actual crack length that is mapped to a macro-scale element edge. Alternatively, an exact stress strain evolution can be used giving tabular inputs (Simulia/Abaqus).

3.6. Cohesive interface crack model

The cohesive interface crack model in this chapter is based on the method of pre-inserting cohesive interface elements developed in (Yang et al., 2009). The constitutive relation of cohesive elements is described by a traction-separation law. The initially linear traction-separation curve with linear softening is used here for simplicity although other alternatives can also be used in ABAQUS(Simulia/Abaqus). The response of the cohesive element before damage initiation is:

$$\{t\} = K\{\varepsilon\} \quad \text{Eq. 3-15}$$

where the nominal traction stress $\{t\}$ is decomposed into two directional components t_n and t_s which represent the normal and shear tractions respectively. The nominal strains are:

$$\varepsilon_n = \frac{\delta_n}{L_0}, \quad \varepsilon_s = \frac{\delta_s}{L_0} \quad \text{Eq. 3-16}$$

where L_0 is the initial constitutive (not geometric) thickness of the cohesive elements which is equal to 1.0 by default in ABAQUS (Simulia/Abaqus). The salient feature of these elements is that they are based on the damage irreversibility concept in which the stiffness tensor $K(k_n, k_s)$ is degraded upon loading and unloading with the increase of the applied displacements δ_n and δ_s . The nominal quadratic stress damage initiation criterion based on the quadratic mixed mode tractions is used in this study:

$$\left\{ \frac{\langle t_n \rangle}{t_{n0}} \right\}^2 + \left\{ \frac{t_s}{t_{s0}} \right\}^2 = 1 \quad \text{Eq. 3-17}$$

where t_{n0} and t_{s0} are the tensile and shear strengths. Once the damage initiation is reached, the damage evolution upon unloading and reloading can be based on a similar scalar damage index D , which is a function of the effective relative displacement

$$\delta_m = \sqrt{\langle \delta_n \rangle^2 + \delta_s^2}, \quad \text{Eq. 3-18}$$

where $\langle \delta_n \rangle = \begin{cases} \delta_n, & \delta_n \geq 0 \text{ (tension)} \\ 0, & \delta_n < 0 \text{ (compression)} \end{cases}$, and the damage index is

$$D = \frac{\delta_{mf}(\delta_{m,\max} - \delta_{m0})}{\delta_{m,\max}(\delta_{mf} - \delta_{m0})}, \quad \text{Eq. 3-19}$$

where $\delta_{m,\max}$ is the maximum effective relative displacement during the loading history. δ_{m0} and δ_{mf} are the effective relative displacements corresponding to damage onset and complete failure. D monotonically increases between 0 and 1. Using the damage index D , the new stiffnesses k_n and k_s are computed based on the following relations:

$$\begin{aligned} k_n &= (1 - D)k_{n0} \\ k_s &= (1 - D)k_{s0} \end{aligned} \quad \text{Eq. 3-20}$$

and the new corresponding traction limits are accordingly:

$$\begin{aligned} t_n &= \begin{cases} (1 - D)\bar{t}_n, & \bar{t}_n \geq 0 \\ \bar{t}_n, & \bar{t}_n < 0 \text{ (no compressive damage)} \end{cases} \\ t_s &= (1 - D)\bar{t}_s \end{aligned} \quad \text{Eq. 3-21}$$

where \bar{t}_n and \bar{t}_s are the initial tractions which are equal to the initial stiffness times the current relative displacements.

Alternatively, using the mixed mode fracture energy formulation, the damage evolution upon softening is defined by the following criterion:

$$\left\{ \frac{G_n}{G_{nC}} \right\}^\alpha + \left\{ \frac{G_s}{G_{sC}} \right\}^\alpha = 1, \quad \alpha = 2 \quad \text{Eq. 3-22}$$

where G_{nC} and G_{sC} are the critical fracture toughness of the material corresponding to fracture modes 1 and 2. The second order power law is used in this study.

The extension of the cohesive interface crack model to multiphase materials in 2D was developed in a conference paper (Sencu et al., 2014), a book chapter (Sencu et al., 2015) and a journal publication (Sencu et al., 2016).

3.7. Summary and conclusions

This chapter has presented the development of a new multiscale method for modelling crack growth in quasi-brittle materials in 2D with heterogeneous distribution of different phases of the material at meso-scale. The main innovative features of the method are:

- (i) the continuity of the microstructure is ensured
- (ii) a new overlapping discretisation procedure is used for more accurate scale transfer of meso-to-macro scale mechanics
- (iii) a new filtering method of non-critical crack paths arising from biased neighbouring paths
- (iv) a new mapping algorithm of potential crack paths and material properties from meso-to-macro scales

- (v) generation of aligned mesh models at macro-scale that ensure the scale transfer of random crack paths from multiple loading schemes
- (vi) crack growth is modelled on both scales using cohesive interface elements; and
- (vii) parallelisation of fine-scale models is enabled for use in quasi-brittle materials

CHAPTER 4 will present details of the implementation in 2D of this method and validation examples.

The new method can be extended to 3D modelling and can be used in conjunction with image-based modelling. This will be demonstrated in CHAPTER 7.

CHAPTER 4. IMPLEMENTATION AND VALIDATION OF THE NEW MULTI-SCALE STOCHASTIC METHOD OF MODELLING FRACTURE IN 2D

4.1. Introduction

This chapter presents the implementation and validation of the new method presented in CHAPTER 3 for 2D multiscale stochastic modelling of fracture in quasi-brittle materials. Validation of the method is demonstrated by two case studies of carbon fibre reinforced polymer (CFRP) composites. The main outputs of the new method include elasticity moduli, ultimate strengths, crack paths and fracture energies of the material under different loading and boundary conditions.

The first case study (presented in Section 4.3) investigated the effects of variable geometric fibre volume fraction and fibre breakage on fracture process. In the second case study (presented in Section 4.4), 2D micrographs of CFRP acquired using a laser confocal microscope and the micrographs were reconstructed to form image-based meso-scale models to validate the multiscale fracture modelling method in CHAPTER 3. Due to a lack of detailed experimental results, the validation is demonstrated through direct comparisons of the results from using the multiscale models with full size models. The full size models cover the entire analysis domain used to build the meso-scale models, but incorporate detailed meshing at the fibre-level. The validation of the meso-scale cohesive fracture modelling is carried out in Section 4.2 via a direct comparison of stress fields and crack.

4.2. Meso-scale finite element modelling and validation

The meso-scale heterogeneous discretisation was performed using an in-house MATLAB code based on the pre-inserting cohesive interface elements (CIE) (Yang et al., 2009).

The mesh consists of a mixture of two types of linear integration finite elements: triangular solid elements CPS3 and initially zero-thickness cohesive elements COH2D4. The approximate element size was 1 μm and the simulation was conducted using the ABAQUS/ Explicit solver with a total time step of 0.04 s. This value was considered adequate loading time for quasi-static loading condition. The linear traction-separation law with maximum stress initiation criterion (MAXS) were used for cohesive damage modelling. A complete list of input material parameters used in the validation simulation is given in Table 4-1.

Table 4-1: Input material parameters for validation modelling.

Parameters	Units	S-glass fibre	Epoxy resin	Interface
Elastic modulus E	(GPa)	86.9	3.9	3.9
Traction strength $t_n=t_s$	(MPa)	600	50	25
Poisson's ratio ν	-	0.23	0.37	0.37
Fracture energy $G_{11}=G_{22}$	(N/mm)	2000e-03	60e-03	35e-03
Volume fraction	(%)	30	70	n/a
Fibre diameter	(μm)	10	n/a	n/a
Density	(kg/m^3)	1500		

Validation of meso-scale modelling was conducted by comparison with results in (Cid Alfaro et al., 2010a). An artificially created meso-scale window of S-glass fibre (30%) and epoxy resin was modelled. Three different cohesive interface element sets are used to represent the fibre, matrix and fibre-matrix interfaces. A good agreement was found in terms of stress contour plots and crack propagation patterns. Fig. 4-1 shows the comparable fracture behaviour. The cracks are represented by the cohesive interface elements with damage index $\text{SDEG} \geq 0.9$.

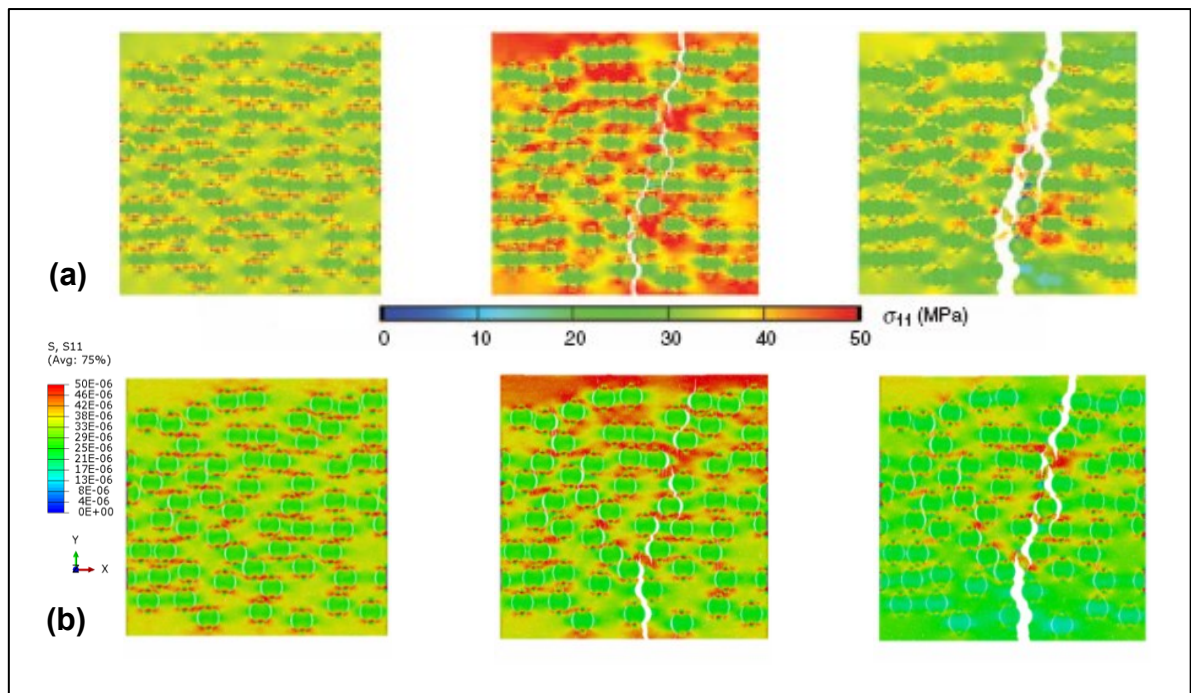


Fig. 4-1: Comparison of stress contour plots on window size $125 \times 125 \mu\text{m}$ and fibre volume fraction 30% at three different load steps: (a) results in (Cid Alfaro et al., 2010a), (b) the present study.

4.3. CASE STUDY 1: Investigation of volume fractions variability on fracture process

This section uses the cohesive crack model validated in Section 4.2 to simulate crack propagation in a CFRP transverse ply at different locations. Four targeted image-based meso-scale elements (MeEs) were extracted from optical micrographs taken from a CFRP ply. As also discussed later in detail Section 4.4.5, the MeE window size has to be at least $5 \times$ larger than the feature size. In this case study, the carbon fibre diameter is approximately $5 \mu\text{m}$ and the considered MeE size is $70 \times 70 \mu\text{m}$ as shown in Fig. 4-2.

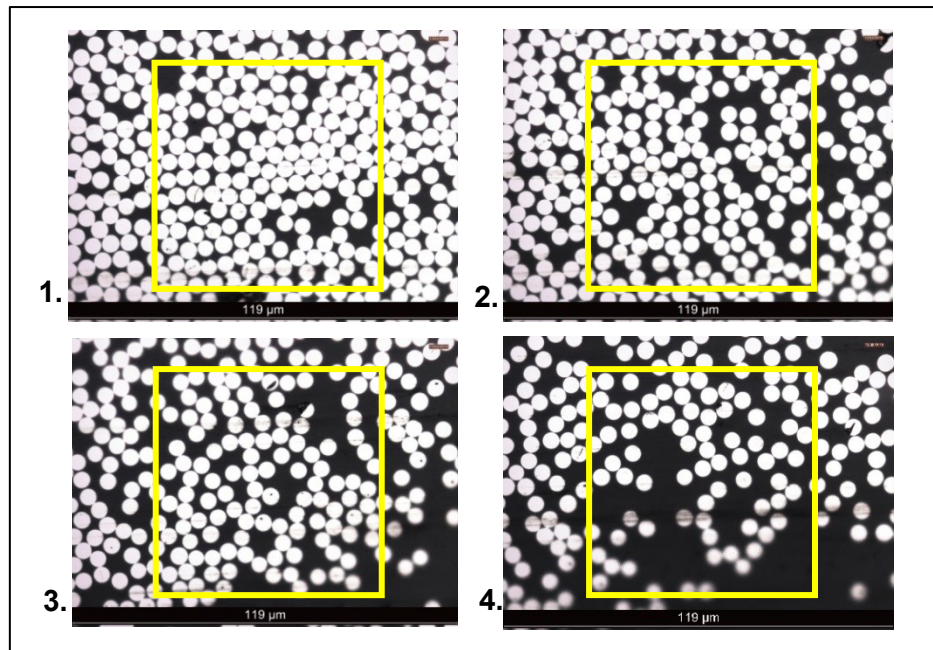


Fig. 4-2: MeE windows size $70 \times 70 \mu\text{m}$ at four positions from micrographs of a CFRP specimen.

As shown in Fig. 4-2, the MeE windows contain different volume fractions and stochastic fibre distributions. The models are simulated separately and compared to a hexagonal fibre arrangement model of 50% fibre volume fraction shown in Fig. 4-3.

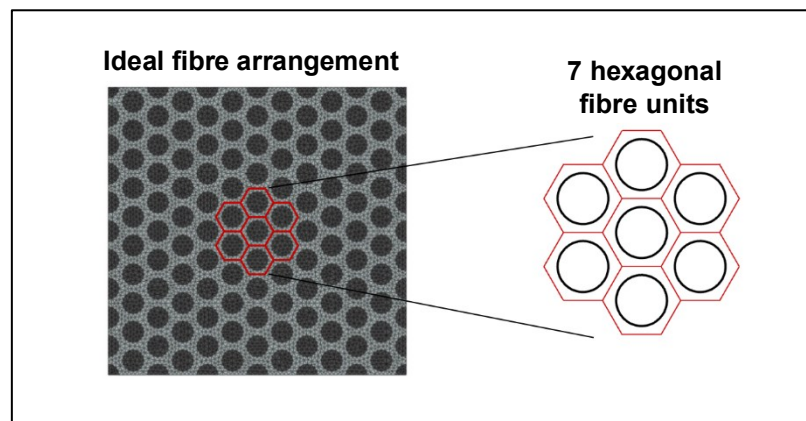


Fig. 4-3: Ideal hexagonal fibre arrangement in a computer generated MeE size $70 \times 70 \mu\text{m}$ and fibre volume fraction 50%.

4.3.1. Boundary conditions

The type of boundary conditions considered in this case study is the tensile loading configuration as shown in Fig. 4-4 and previously discussed in CHAPTER 3. This loading configuration allows core rotations as seen in Fig. 4-5 at MeE-2 and minimises the boundary effects of single scale simulations. This is because these boundary conditions allow vertical sliding at the right edge. Fig. 4-4-b and c show the CIE sets in the matrix and on the matrix-fibre interfaces, respectively. It should be noted that the cracks were not allowed to propagate within fibres in this case study. This is allowed in later simulations due to the incorporation of CIEs within the fibre domains, which is particularly important for 3D simulations of fibre breakage.

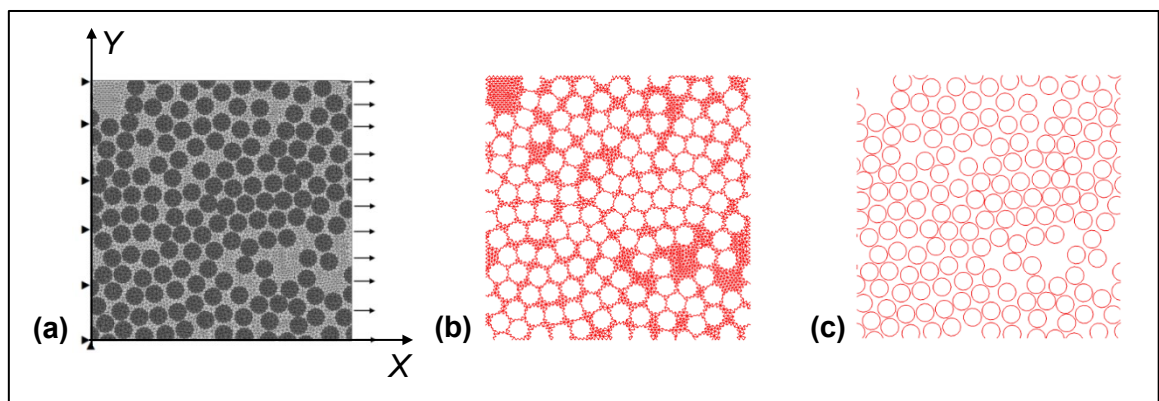


Fig. 4-4: Illustration of the MeE-1 model: (a) boundary conditions, (b) CIEs in the matrix and (c) CIEs on the matrix-fibre interfaces.

4.3.2. Material properties

The fracture energy is estimated by the stress-displacement area. The maximum admissible strength of epoxy in this case was 82 MPa and the interface was expected to fail at around 2 μm (the upper limit which leads to perfect debonding and fracture energy). Approximating the softening with a simple triangular area, the fracture energy of the epoxy resin would become $G_f = 82 \times 0.002 / 2 = 82 \times 10^{-3} \text{ N/mm}$. Due to experimental observations on such thermoset resins, this value can be used as an upper limit of their fracture energies. However, to account for a

more realistic exponential decaying, the fracture energy estimates in this case study are decreased with approximately 20%. The other values taken in the present case study are given in Table 4-2. Similar estimates will be made in Section 4.4.

Table 4-2: Input material parameters for fracture modelling.

Parameters	Units	Carbon fibre	Epoxy resin	Interface
Elastic modulus E	(GPa)	85	3.35	3.35
Traction strength $t_n=t_s$	(MPa)	600	82	45
Poisson's ratio ν		0.22	0.37	0.37
Fracture energy $G_{11}=G_{22}$	(N/mm)	200e-03	60e-03	35e-03
Density	(kg/m ³)	1500		

4.3.3. Mesh information

The approximate mesh size was 1.0 μm . The total number of finite elements for the largest model in this case was 67323, as seen in Table 4-3.

Table 4-3: Mesh information of stochastic MeE models.

Model	Fibre CPS3	Fibre COH2D4	Matrix CPS3	Matrix COH2D4	Interface COH2D4	Elements Total	Insertion CPU time (s)
MeE-1	6199	8020	5394	7034	2404	29051	225.23
MeE-2	5320	6875	6490	8640	2065	29390	240.05
MeE-3	4635	6010	7273	9956	1790	29664	245.85
MeE-4	3075	3976	19119	39951	1202	67323	306.48

4.3.4. Modelling of transverse crack growth

Crack initiation in this case study was determined by the maximum stress (MAXS) damage criterion available in ABAQUS (Simulia/Abaqus). The stress field mainly depends on the fibre distribution and loading configuration. Before the onset of any crack, the stress field is influenced by the distribution of fibres and material properties. After first crack opening, further cracks tend to follow the shortest paths in the matrix and along the fibre/matrix interfaces. Interface cracking or debonding occur in Fig. 4-5 because a relatively weak fibre-matrix interface is assumed (see Table 4-2).

Due to the random distribution of fibres, the crack paths on the four MeEs are different from each other. This means that due to the stochastic nature of composite microstructures, both the crack initiation and propagation are influenced by the location of the simulation window. Fig. 4-5 shows how the stress contours develop in the four MeE models at three loading steps with the associated crack growth.

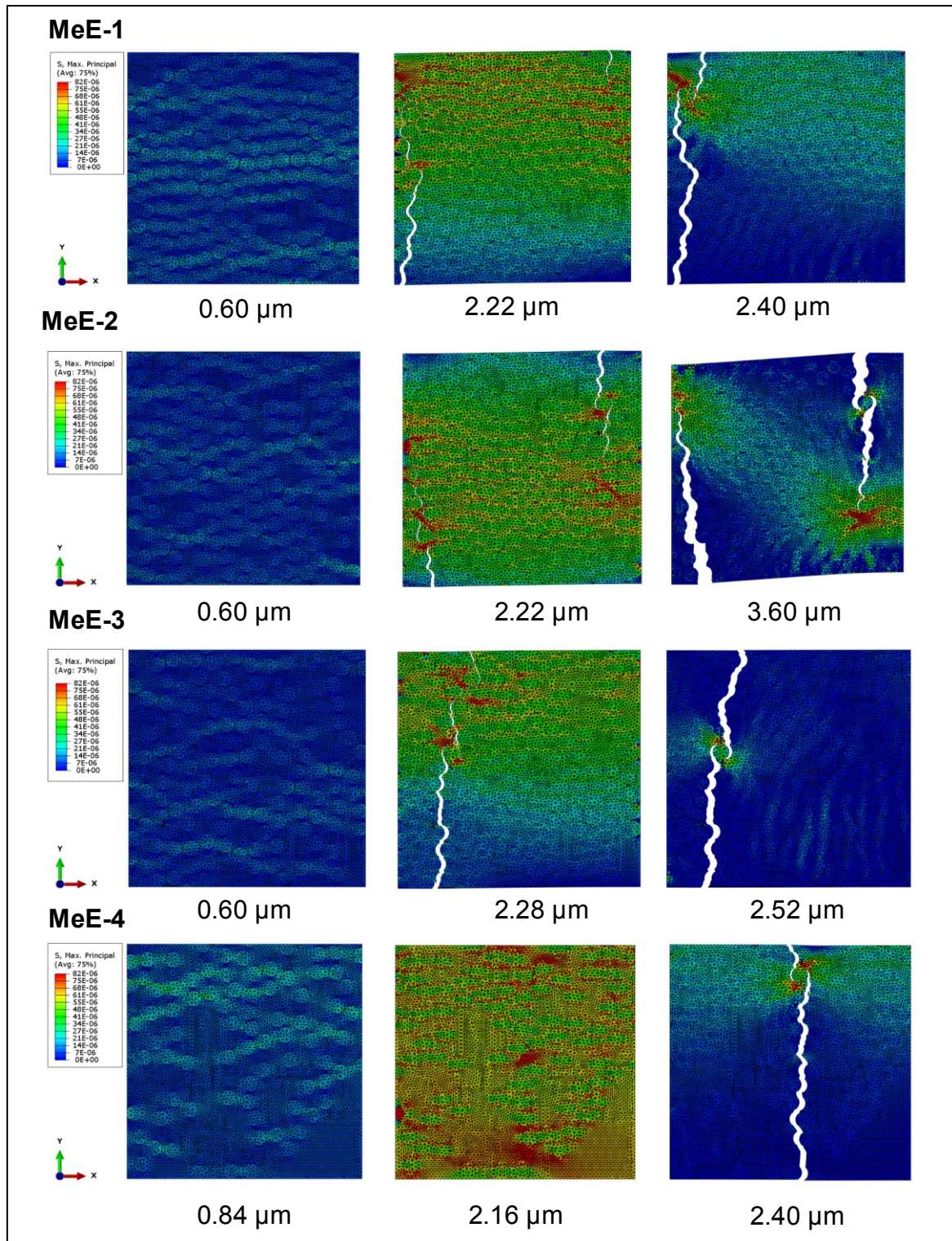


Fig. 4-5: Stress contour plots at three different loading steps.

Fig. 4-6 compares the stress-displacement and stress-strain relationships of the five models including four image-based models and an ideal hexagonal fibre arrangement model that was parametrically generated. The crack paths in Fig. 4-5 are directly related to the softening curves

in Fig. 4-6. In general, such a weak interface as considered in Table 4-2 gives a more tortuous crack path which ultimately results in a higher dissipated energy and permits fibre debonding (see for example the crack path of MeE-2 in Fig. 4-5). For the artificially generated hexagonal fibre arrangements and MeE windows with relatively large matrix volume fractions, the fracture happens more suddenly, although higher transverse strengths are obtained (see results of MeE-4 and HEX-50 in Fig. 4-7). This behaviour is also associated with lower dissipated fracture energy as seen in Fig. 4-7.

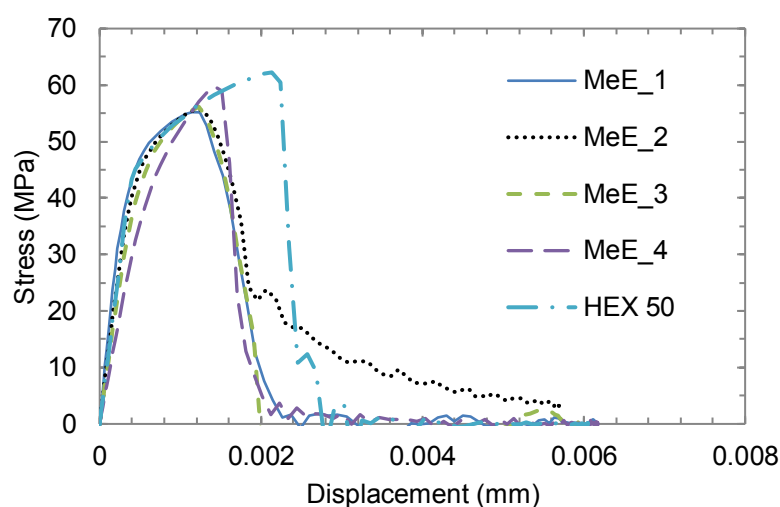


Fig. 4-6: Stress-displacement curves.

Finally, Fig. 4-7 compares the volume fractions, ultimate strengths and dissipated energies of this case study for the four image-based MeE models with the ideal hexagonal fibre arrangement model.

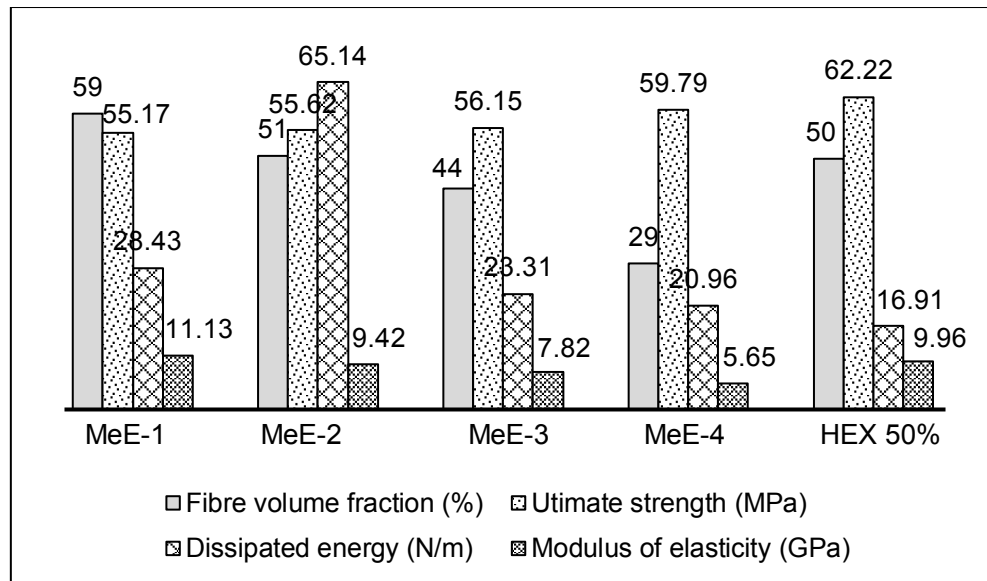


Fig. 4-7: Comparison of volume fractions, ultimate strengths and dissipated energies.

4.3.5. Fibre breaking effects in longitudinal meso-scale model

In this section, a longitudinal MeE of size $60 \times 60 \mu\text{m}$ was generated from a transverse fibre profile containing five fibres of different diameters between $5\text{--}7 \mu\text{m}$. The solid FE mesh was then inserted with corresponding CIEs to model cracks in the three different phases as usual, i.e. fibre, matrix and interface between fibre and matrix. The model was then simulated in tension using the type *BI-X* boundary conditions previously explained in CHAPTER 3. The stress contour plots in the horizontal direction *X* at four different steps are shown in Fig. 4-8.

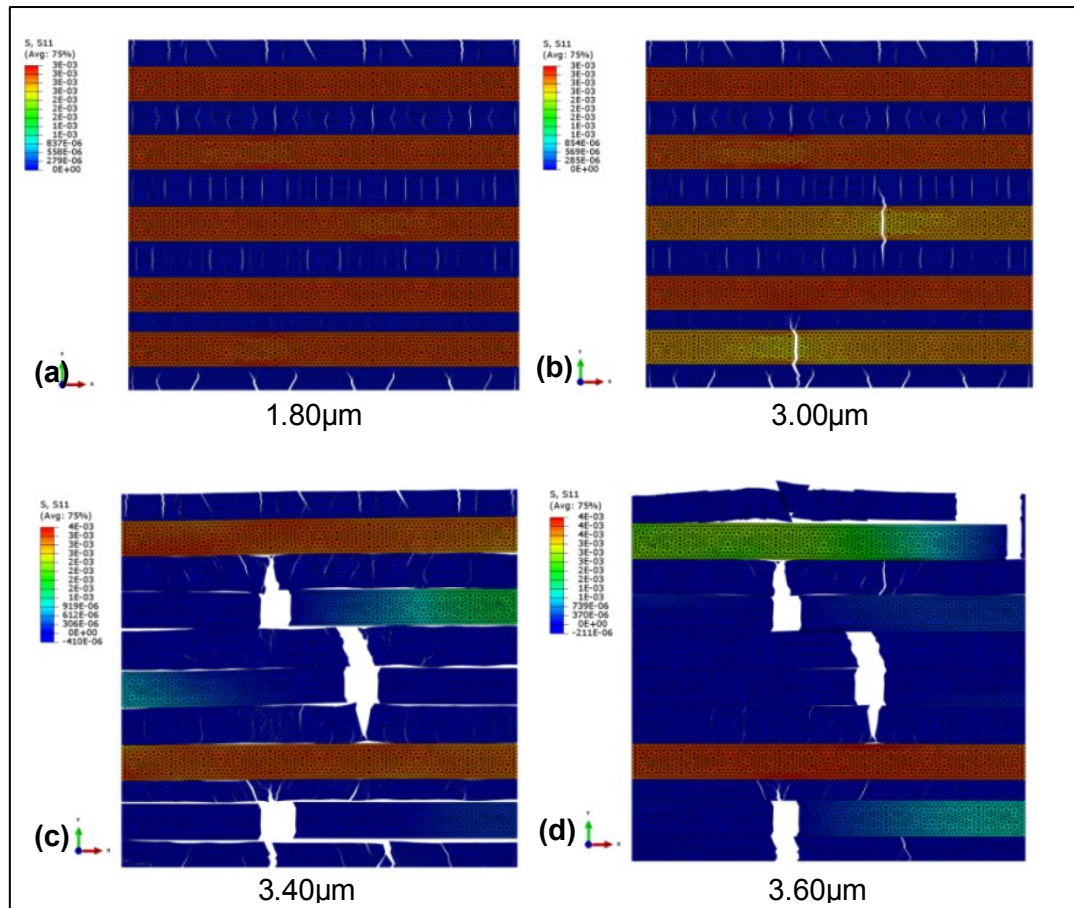


Fig. 4-8: Stress contour plots on X direction at different loading steps of a longitudinal MeE size $60 \times 60 \mu\text{m}$.

Fig. 4-8 shows the load-displacement curve. It can be seen that several load-displacement spike-effects could be simulated with the cohesive interface crack model. These effects correspond to the fibre breaks illustrated in Fig. 4-8 after the crack tunnelling through the surrounding matrix (see the multiple matrix cracks on blue layer in Fig. 4-8-a and b).

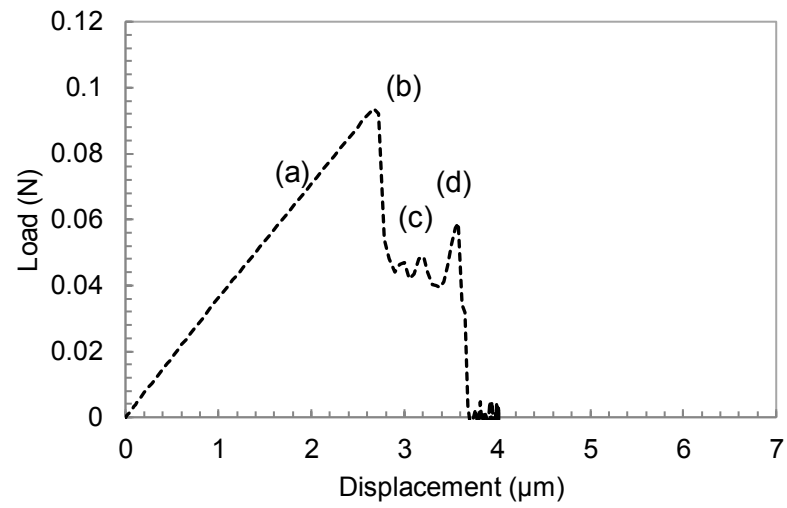


Fig. 4-9: Load-displacement curve of a longitudinal fibre model of size $60 \times 60 \mu\text{m}$. The annotations represent the displacement step plots in Fig. 4-8.

4.4. CASE STUDY 2: Investigation of interface strength variability, boundary, size and stochastic effects

In this section, several investigations are conducted for a better understanding of the meso-scale fracture mechanisms of CFRP in 2D. The case study starts with the detailed geometrical surveying of a transverse inclined ply by using concentric size increasing windows. The adhesion effects are investigated by considering four different interface strength properties in Section 4.4.3. The considered boundary effects are discussed in Section 4.4.4. Section 4.4.5 further simulates the surveying concentric windows at position-2 in Fig. 4-10 under all boundary conditions to investigate boundary and size effects.

In Sections 4.4.6 and 4.4.7 the collection of a four by four MeE grid is conducted. The resulted stochastic MeEs are simulated under the micro-scale set of boundary conditions used with the multiscale coupling strategy previously explained in CHAPTER 3. Thus, all separate MeE crack path results are first compared with the corresponding detailed MeE covering the whole surface of the 4×4 decomposition grid. The multiscale methodology is then implemented in Sections 4.5 and 4.6. These two sections present the results of two multiscale models versus the simulation results of the detailed full size MeE. This strategy is used as a mean of numerical validation. Two multiscale models are tried. The first multiscale model uses a coarse mesh with reduced order integration elements, and second model represents a fully detailed mesh minus the unnecessary cohesive interface elements. The second model is built using the Bayesian methodology that preserves the most critical and continuous crack paths discussed in CHAPTER 3.

4.4.1. Geometrical surveying

A geometrical survey was carried out first within the thickness of a ply to investigate the volume fraction variations (see Fig. 4-10). The searching approach is similar to the one originally used for aluminum alloys (Graham and Yang, 2002) .

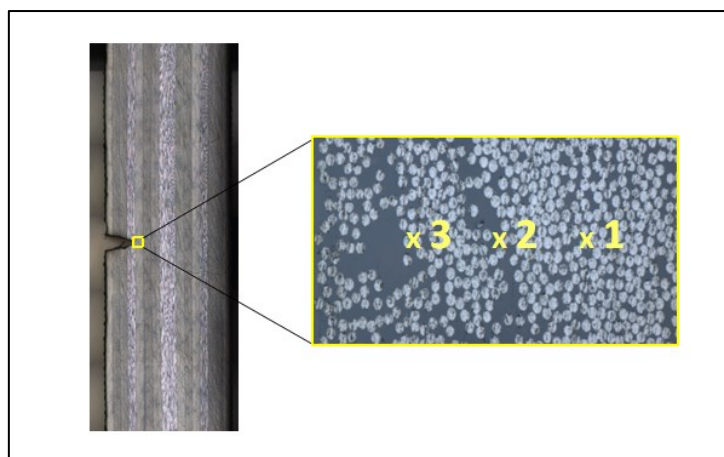


Fig. 4-10: $+45^\circ$ fibre ply in front of a notch tip with numbers indicating positions of the centres of imaging windows.

Fig. 4-10 shows a micrograph extracted from a multi-layered CFRP beam with a V-shape notch. The images were acquired by image stitching from a laser confocal microscope. The micrograph covered the thickness of a single layer of about $220\ \mu\text{m}$. For this particular example, the elliptical fibres have approximately $5\ \mu\text{m}$ shorter diameter because the ply ran at an inclined angle of $+45^\circ$. Three concentric square windows of different sizes were used to acquire the geometrical data. Fig. 4-11 shows the typical acquisition windows at the mid position in Fig. 4-10. Fig. 4-12 summarises the surveying results.

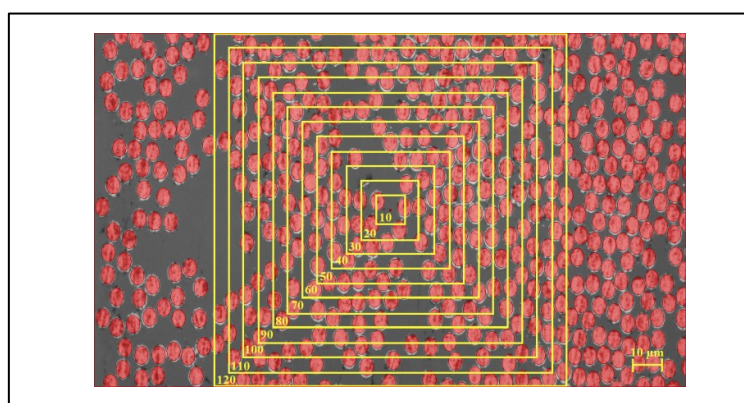


Fig. 4-11: Concentric surveying window sizes at *Position-2* in Fig. 4-10.

Fig. 4-12 also shows that within the ply thickness, the selection of the MeE window is morphologically important. The volume fraction statistics were found to be both position and

size dependent. Apparently, the volume fractions converged when the window size was approximately 50 μm , and the variation was more evident for small window sizes (10, 20 and 30 μm) than larger sizes.

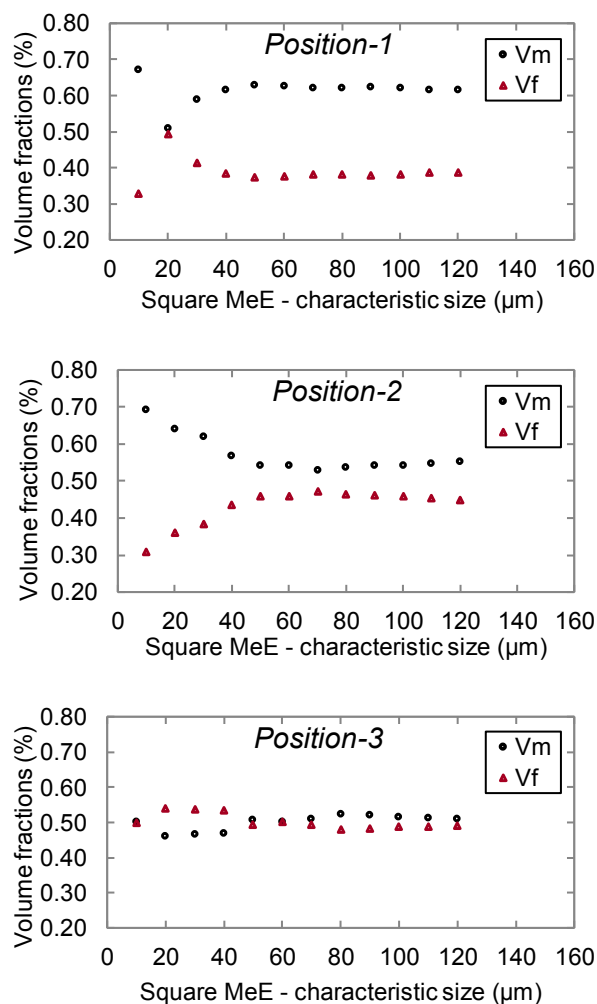


Fig. 4-12: Variations of volume fractions of fibre (V_f) and matrix (V_m) with increasing MeE window size at different imaging positions for a carbon/epoxy ply +45°.

4.4.2. Material properties

To further simplify the modelling, it was assumed that the shear strength and fracture energy of each individual phase were equal to their normal ones respectively (Cid Alfaro et al., 2010a; Vaughan and McCarthy, 2011; González and Llorca, 2007a; Yang et al., 2009).

This assumption is acceptable because currently it seems that there is no phenomenological observation in the literature to clearly demonstrate that the fibre-matrix interface has different properties in different fracture modes, although the mode-mixity can be easily accounted for in ABAQUS. The implications of using mode-mixity properties require no changes in the proposed modelling framework. This is due to the crack path stochasticity assumption before undertaking the scale transfer.

Table 4-4 gives the main material parameters and the volume fractions used in the simulations of this case study. Four types of fibre-matrix interfaces with different strengths and fracture energies, namely: poor, weak, strong and perfect, were modelled. The fracture energy is estimated by the stress-displacement area and its estimates are larger than expected in real at micro-scale. The maximum admissible strength of epoxy in this case was 50 MPa and the interface was expected to fail at around 2 μm (the upper limit which leads to perfect debonding and fracture energy). Approximating the softening with a simple triangular area, the fracture energy becomes $G_f = 50 \times 0.002 / 2 = 50\text{e-}03 \text{ N/mm}$. The other values were parametrically taken in this study. Similar estimates will be made in CHAPTER 7.

Table 4-4: Material properties and modelling parameters.

	Carbon fibre	Epoxy resin	Interface
Elastic modulus E (GPa)	85	3.35	3.35
Poisson's ratio ν	0.22	0.35	0.35
Traction strength $t_n=t_s$ (MPa)	200	50	15 (poor), 25 (weak), 40 (strong), 50 (perfect)
Fracture energy $G_{fn}=G_{fs}$ (N/mm)	200e-03	50e-03	15e-03 (poor), 25e-03 (weak), 40e-03 (strong), 50e-03 (perfect)
Volume fraction (%)	30-60	70-40	-
Density (kg/m^3)	1500		

4.4.3. Effects of interface strength on fracture process

To demonstrate the importance of the fibre-matrix interface strength, a MeE of size $50 \times 50 \mu\text{m}$ was simulated using the four interfacial types in Table 1. Fig. 4-13 shows that the interface properties can greatly influence the meso-scale cracking mechanism which has important effects on the macro-scale fracture. This is because local stress concentrations may potentially divert crack propagation for certain global boundary conditions. Experiments are thus necessary to examine the interface properties between fibres and the matrix and their mechanical effects.

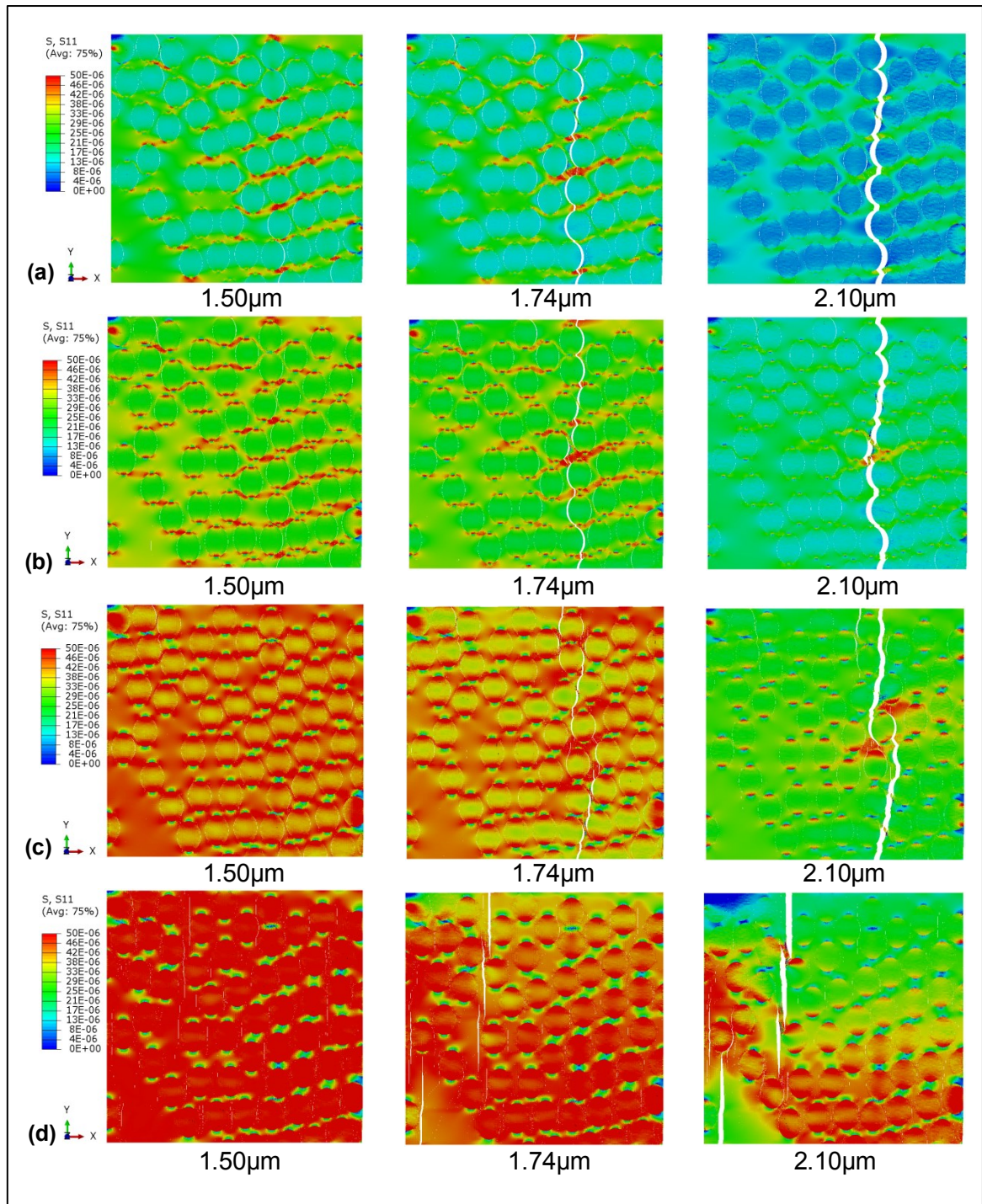


Fig. 4-13: Stress contours at three load steps from MeE-3 of size $50 \times 50 \mu\text{m}$ using (a) poor, (b) weak, (c) strong and (d) perfect interface properties.

4.4.4. Boundary condition effects

Boundaries also influence crack initiation and propagation and therefore the overall dissipated energy. Fig. 4-14 shows a two-crack dominant failure in the MeE size $100 \times 100 \mu\text{m}$ image-based model using the *G2-X* type boundary conditions from CHAPTER 3. In general, such effects were not observed on the other boundary types; thus only *B1* type that is identical to *G1* boundaries was further used in the scale coupling.

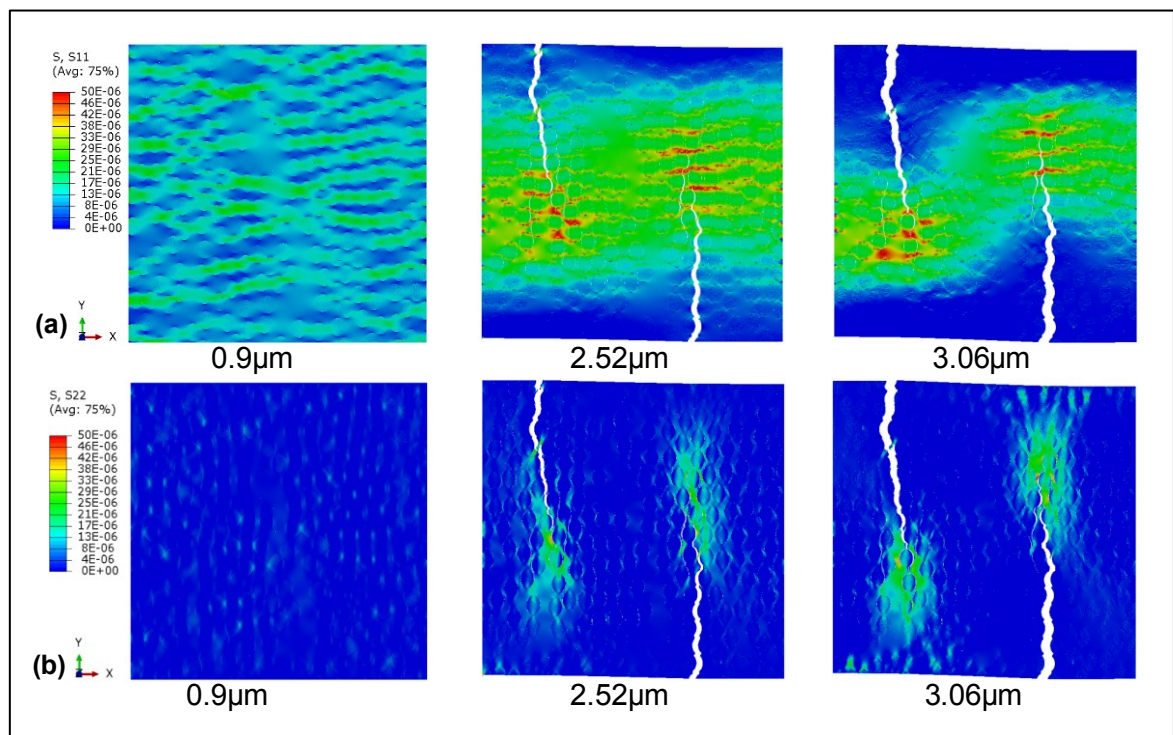


Fig. 4-14: Stress contours at three loading steps using *G2-X* boundaries and weak interfacial properties showing a two dominant cracks failure in MeE size $100 \times 100 \mu\text{m}$.

4.4.5. Size effects

Simulations for different MeE sizes, in increments of $10 \mu\text{m}$ up to $100 \mu\text{m}$, with centre at *Position-2* in Fig. 4-10, were carried out to investigate size effects on crack paths and load-displacement curves. To avoid problems of localisation and mesh interface disclosure for zoom-out resolution, surface partitions were conducted so that the same mesh in smaller MeE is contained in larger ones (see Fig. 4-15).

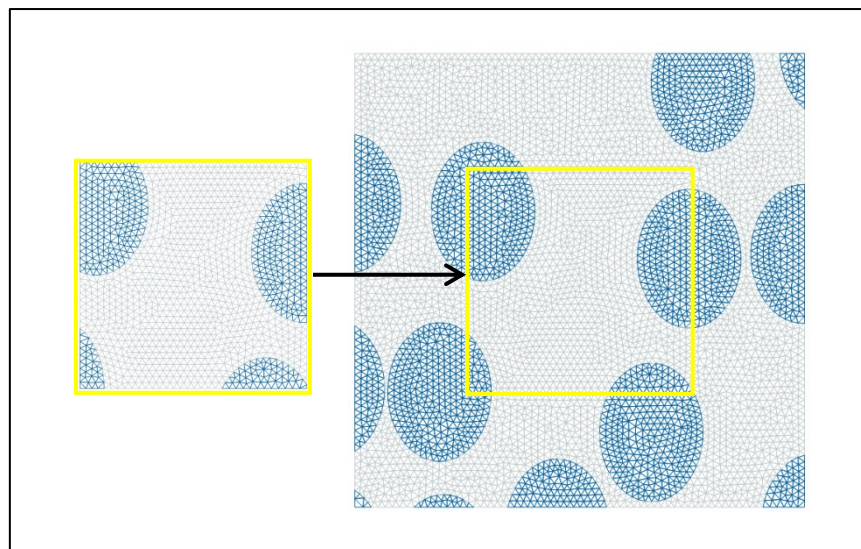


Fig. 4-15: Image-based MeEs of size $10 \times 10 \mu\text{m}$ and $20 \times 20 \mu\text{m}$ illustrating the concept of partitioned concentric windows by preserving mesh topology.

It is interesting to see that from one size to another, dissimilar crack paths appear when using *GI-X* loading conditions (see Fig. 4-16 and Fig. 4-17). This is expected since image-based models have random inclusions and defects. Also the window sizes are often not sufficiently large to achieve a more uniform failure mode. A typical set of stress-displacement curves and the equivalent stress-strain curves are shown in Fig. 4-18-a and b respectively.

Fig. 4-18-b shows that a more sudden failure occurs as the MeE size increases. A strong size effect of the peak stress was found especially when weak interface properties were simulated. For all types of interfaces, the size effect of the strength decreases when the window size is larger than $20 - 30 \mu\text{m}$ which was set as a minimum size of the MeE required for the scale transfer (see Fig. 4-19). This is consistent with the statistical analysis of volume fractions in Fig. 4-12.

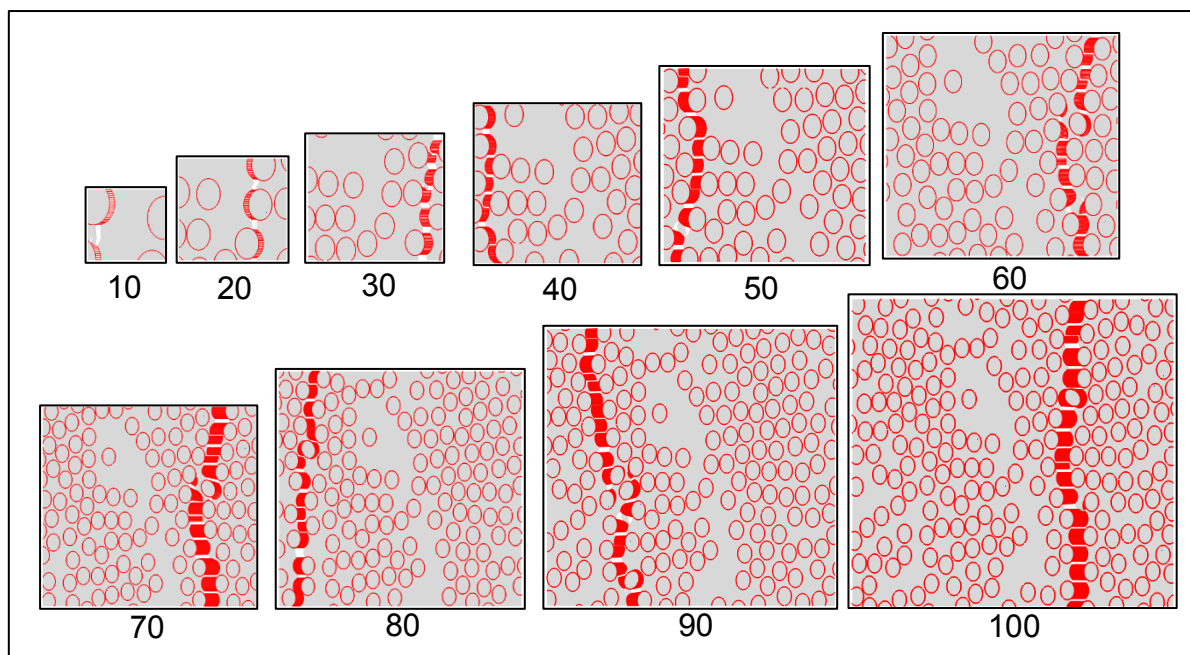


Fig. 4-16: G1-X crack paths in different image-based MeE sizes in μm for weak interface properties (the interface cohesive layer illustrated in red).

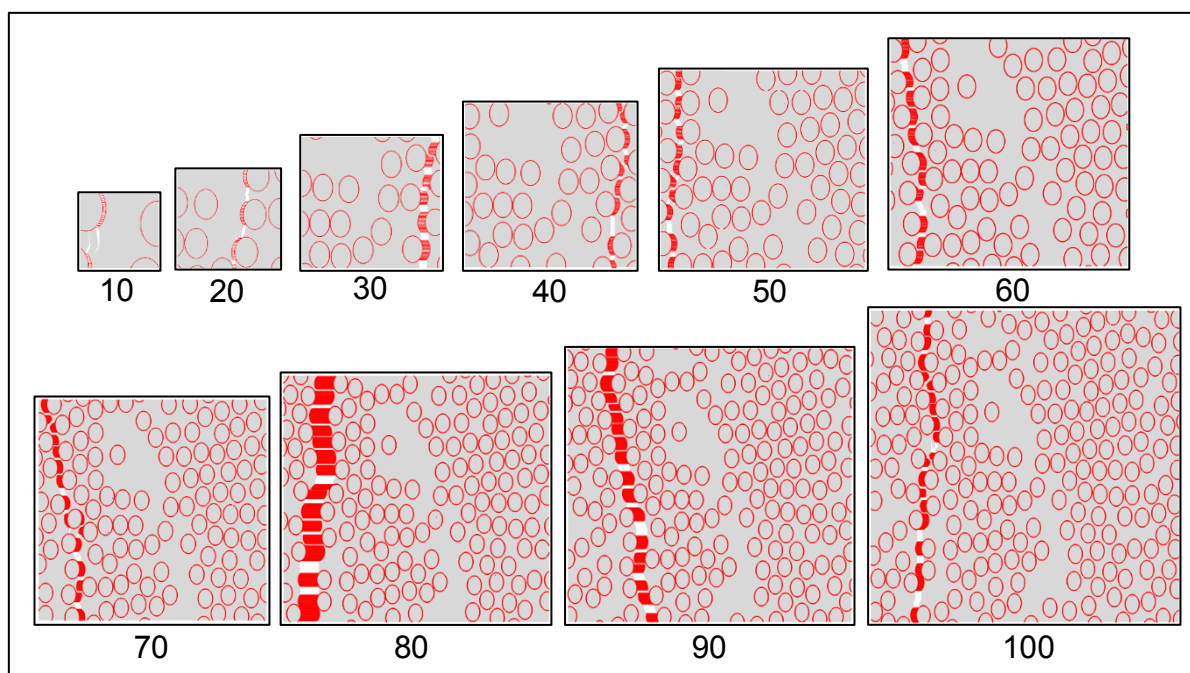


Fig. 4-17: G1-X crack paths in different image-based MeE sizes in μm for strong interface properties (the interface cohesive layer illustrated in red).

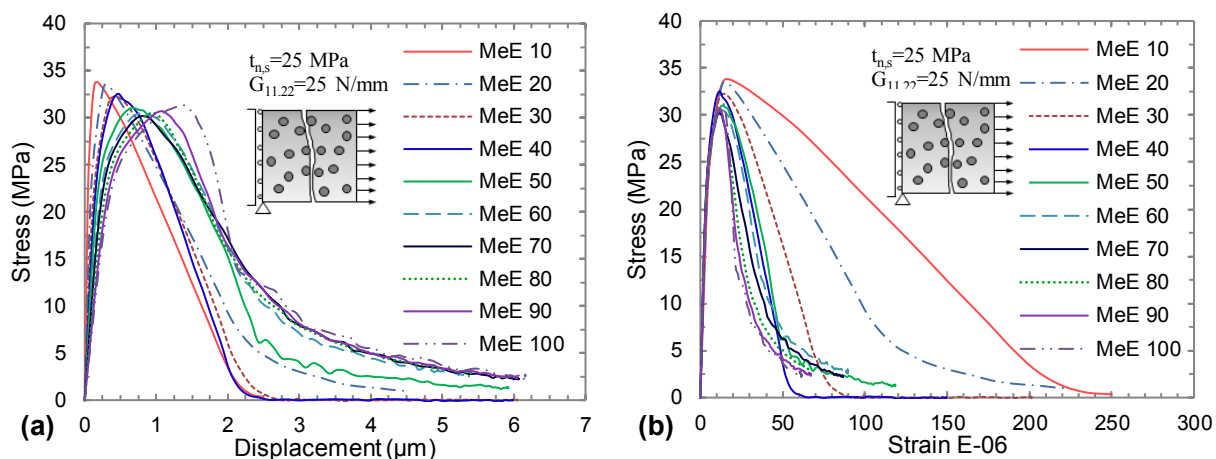


Fig. 4-18: Stress-displacement and stress-strain curves for $G2-X$ boundary conditions on MeE step 10 μm to 100 μm by using weak interface properties.

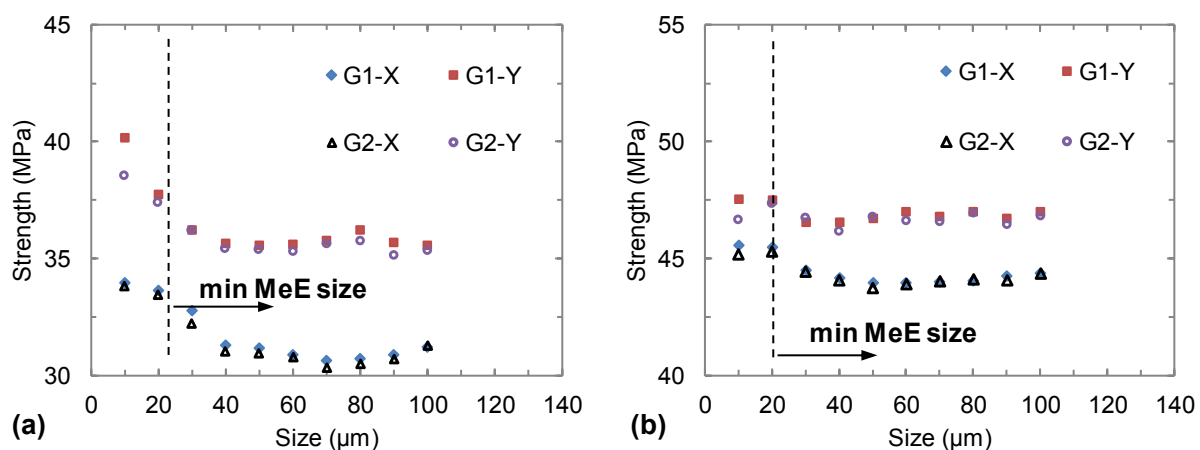


Fig. 4-19: Size-strength results for MeE step 10 μm to 100 μm using (a) weak and (b) strong interface properties.

Table 4-5 summarizes all the image-based simulations that were carried out in this particular case study. The boundary conditions and interface properties are included in this table, while the other material properties were shown in Table 4-4.

Table 4-5: Image based MeE simulations with modelling parameters.

Reference	Changing Parameters			Number of simulations per series
	Interface		Boundary conditions	
	t _n =t _s (MPa)	G _{fn} =G _{fs} (N/mm)		
MeE-10/100/W	25	25e-03	G1-X, G1-Y, G2-X, G2-Y	40
MeE-10/100/S	40	40e-03	G1-X, G1-Y, G2-X, G2-Y	40
MeE-16×25/P	15	15e-03	B1-X, B1-Y, B2-X, B2-Y	64
MeE-16×25/W	25	25e-03	B1-X, B1-Y, B2-X, B2-Y	64
MeE-16×25/S	40	40e-03	B1-X, B1-Y, B2-X, B2-Y	64
MeE-16×25/I	50	50e-03	B1-X, B1-Y, B2-X, B2-Y	64
MeE-16×35/W	25	25e-03	B1-X, B1-Y, B2-X, B2-Y	64
MeE-16×35/S	40	40e-03	B1-X, B1-Y, B2-X, B2-Y	64
MeE-16×50/W	25	25e-03	B1-X, B1-Y, B2-X, B2-Y	64
MeE-16×50/S	40	40e-03	B1-X, B1-Y, B2-X, B2-Y	64

Note: The first number of all series is the number of MeE windows. The second number in the MeE-10/100 series is the largest computed window in increments of size 10 μm . The second number in the MeE-16× series is the overlapping grid size based on a non-overlapping grid base of size of 25 μm .

4.4.6. Stochastic simulations

To investigate the effects of crack path bias and local orientation diversions in scale transfer, non-overlapping meso-scale windows such as shown in Fig. 4-20-a were used in simulations first. The square MeE windows were simulated using the full sets of boundary conditions such as in Table 4-5. The adaptive short to long-overlapping MeE grid discretisation was then used to tackle the problem of neighbouring crack paths bias. The idea is to share an overlapped support as to solve deformation compatibility. The concept may be also understood as an inverted overlapping limit. The upper bound corresponds to $2\times$ computation of the same core MeE windows. This means that for long overlapping the integration must be limited by the distance between two neighbouring mass centres to avoid complicated double overlapping areas. This is useful particularly when strength and fracture energy variances are relatively small which holds in most composites with random distribution of features. Obviously, the short or narrow overlapping criteria will bring further computation savings as the computational areas are closer to the non-overlapping model. However, for both cases the main advantage is that the simulation of global large models can be parallelized to achieve a high computational efficiency.

In Fig. 4-20, the results for two main scenarios are presented as follows: (a,b,c) show weak interface crack paths and (d,e,f) show strong interface crack paths which were obtained using *BI* boundaries on the orthotropic directions *X* and *Y*. Thus, given the random distribution of fibres, the interface layer between the fibres and matrix can be considered an intrinsic defect entity in this study. It can be seen that, when the non-overlapping method was used (a,d), the fracture paths rarely matched between the neighbouring MeE elements.

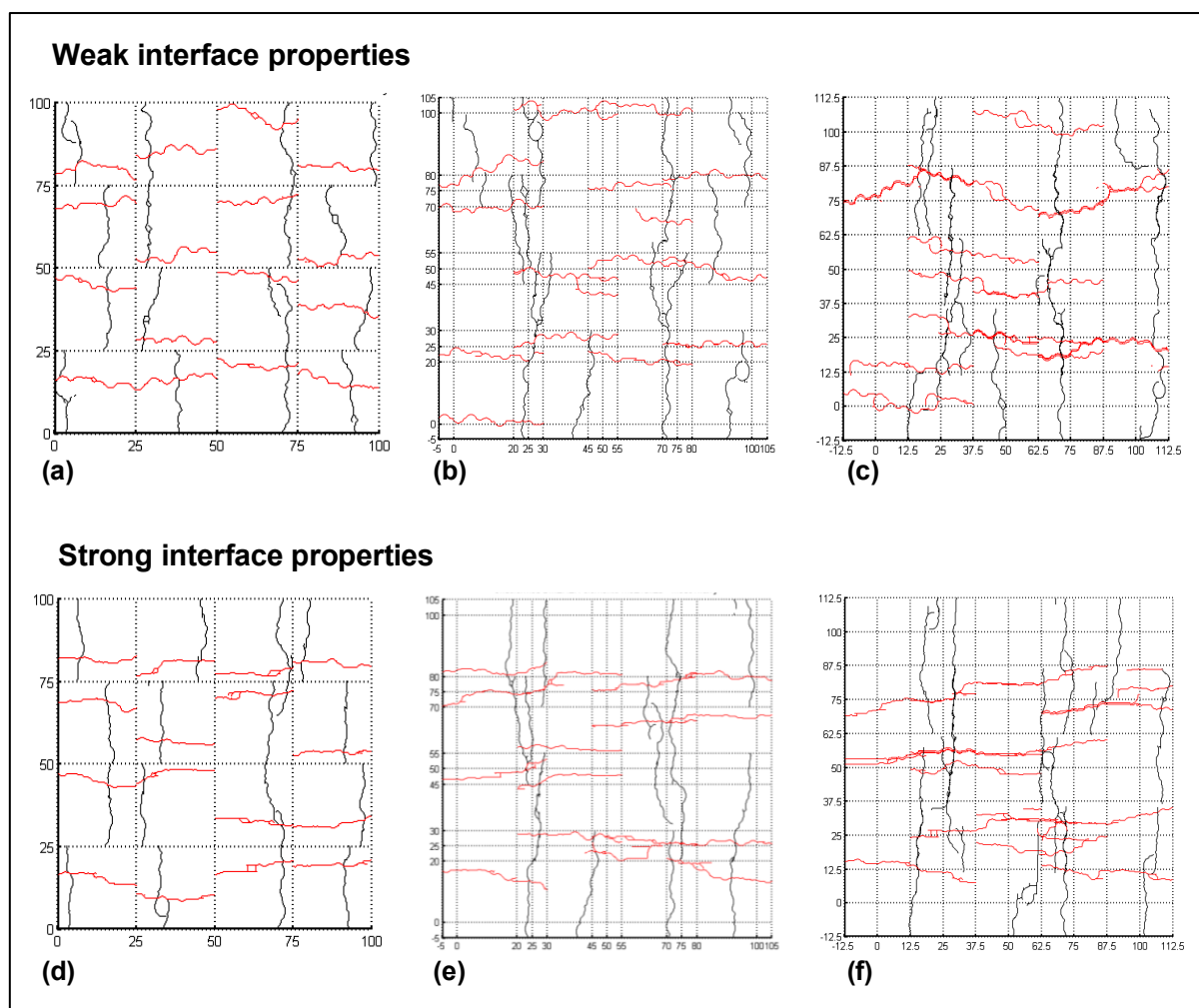


Fig. 4-20: Crack paths for the adaptive size-increasing non-overlapping MeE-16 \times 25 (a,d) to short overlapping MeE-16 \times 35 (b,e) and long overlapping MeE-16 \times 50 (e,f). The two sets are from using weak interface properties (a,b,c) and strong interface properties (d,e,f).

When overlapping MeE windows were used, the matching rates were better in the case of weak interface properties (see Fig. 4-20). In addition, there was a clear enhancement in crack site prediction compared with the non-overlapping results for cracks near edges (see and compare Fig. 4-20 a,b,c and d,e,f). Fig. 4-21 shows the variation of the predicted ultimate strengths with varying overlapping areas for different MeEs. Smaller strength variance with larger prediction errors were obtained for the strong interface models (see Fig. 4-21-b MeE-12 and MeE-14).

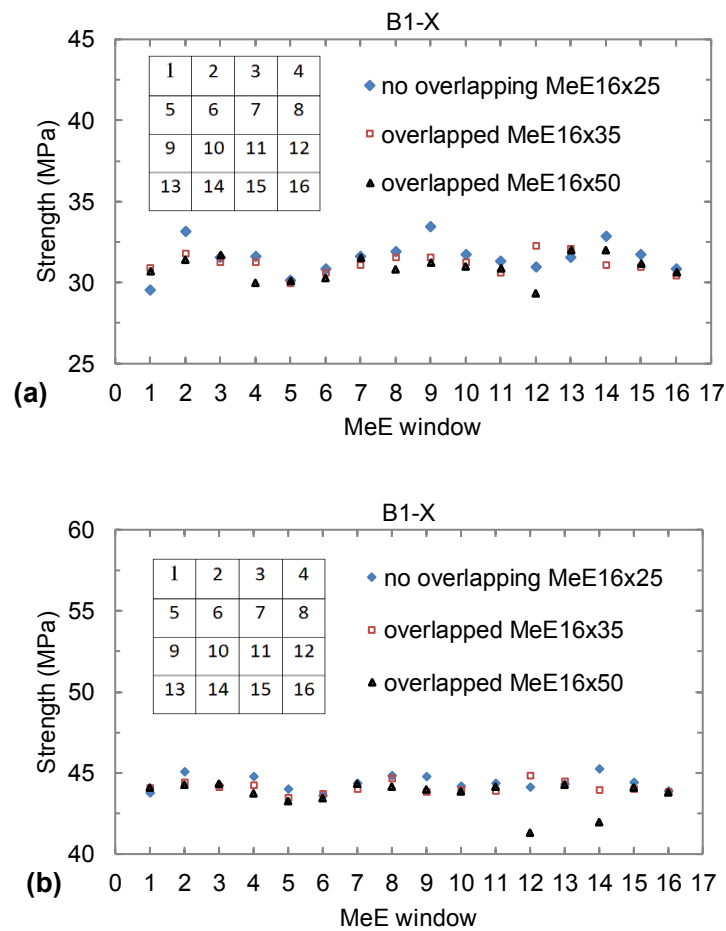


Fig. 4-21: Variation of MeE strengths with different overlapping areas:
(a) weak and (b) strong interface properties.

It should also be mentioned that for the scale transfer the $B2-X$ and $B2-Y$ boundary conditions explained in CHAPTER 3 are primarily necessary. The confidence domain for the softening part in such a case was limited to small sliding. This domain is equal to about $0.2 \mu\text{m}$ which is approximately the size of one finite element used in the simulations. A mesh example is shown in Fig. 4-15. The set of all curves from stochastic MeE simulations under all boundary conditions were added in the Appendix A.

In the following sections, the validation of the proposed multiscale modelling method is established by comparing the detailed crack propagation results and energy dissipation mechanisms on both scales.

4.4.7. Comparison of meso- and macro-crack propagation

This section elucidates the most convenient approach to solving the scale transfer problem when using different interface properties. Fig. 4-22 and Fig. 4-23 compare all the crack paths of uncoupled overlapping MeEs using *BI* boundaries (shown in coloured lines) against the corresponding fully detailed MeE-100 simulations (shown in black lines) using *G1* and *G2* cases on *X* and *Y* respectively.

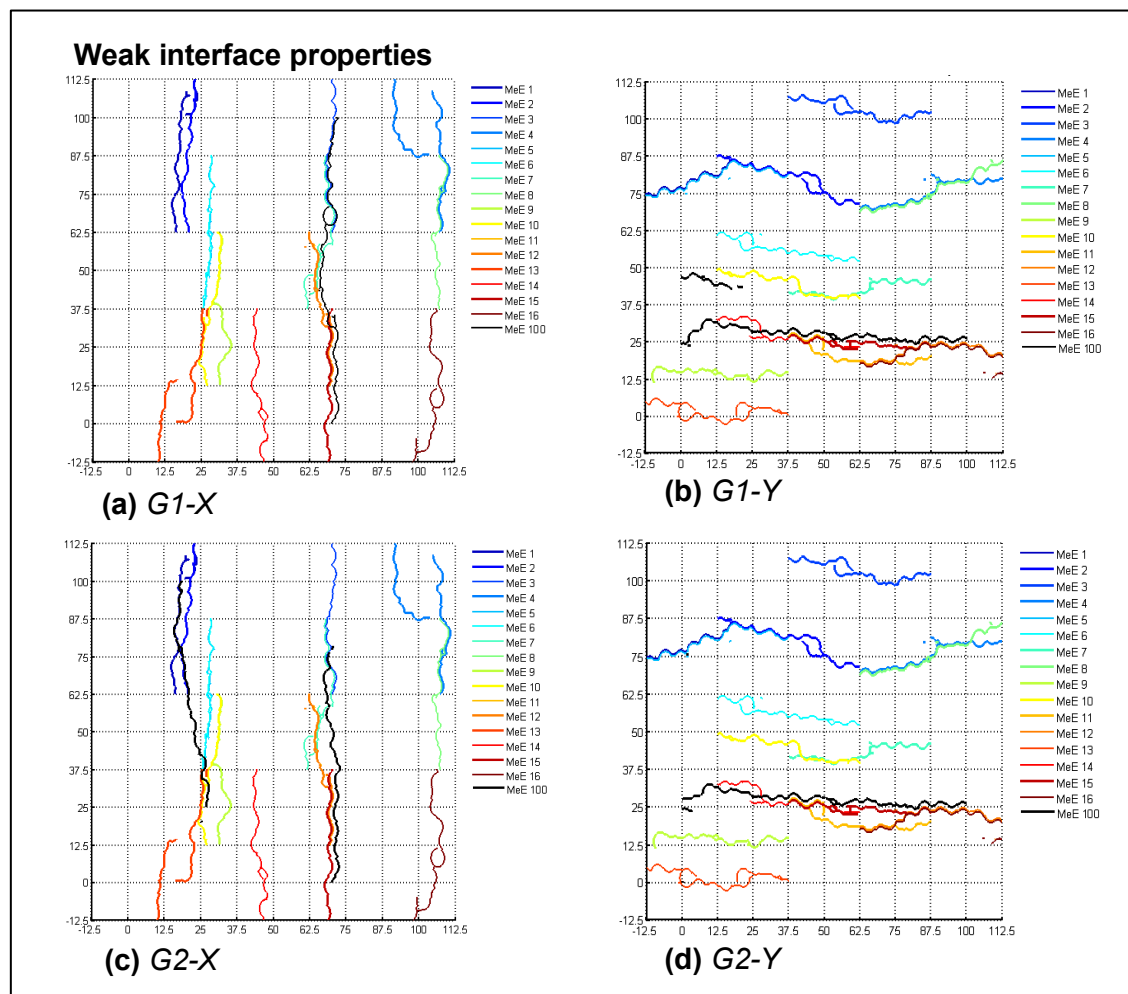


Fig. 4-22: Comparison of separate crack paths between overlapping series MeE-16 \times 50 (shown in coloured lines) using *BI* boundaries against full size MeE-100 (shown in black lines): (a) *G1-X*; (b) *G1-Y*; (c) *G2-X* and (d) *G2-Y* for weak interface properties.

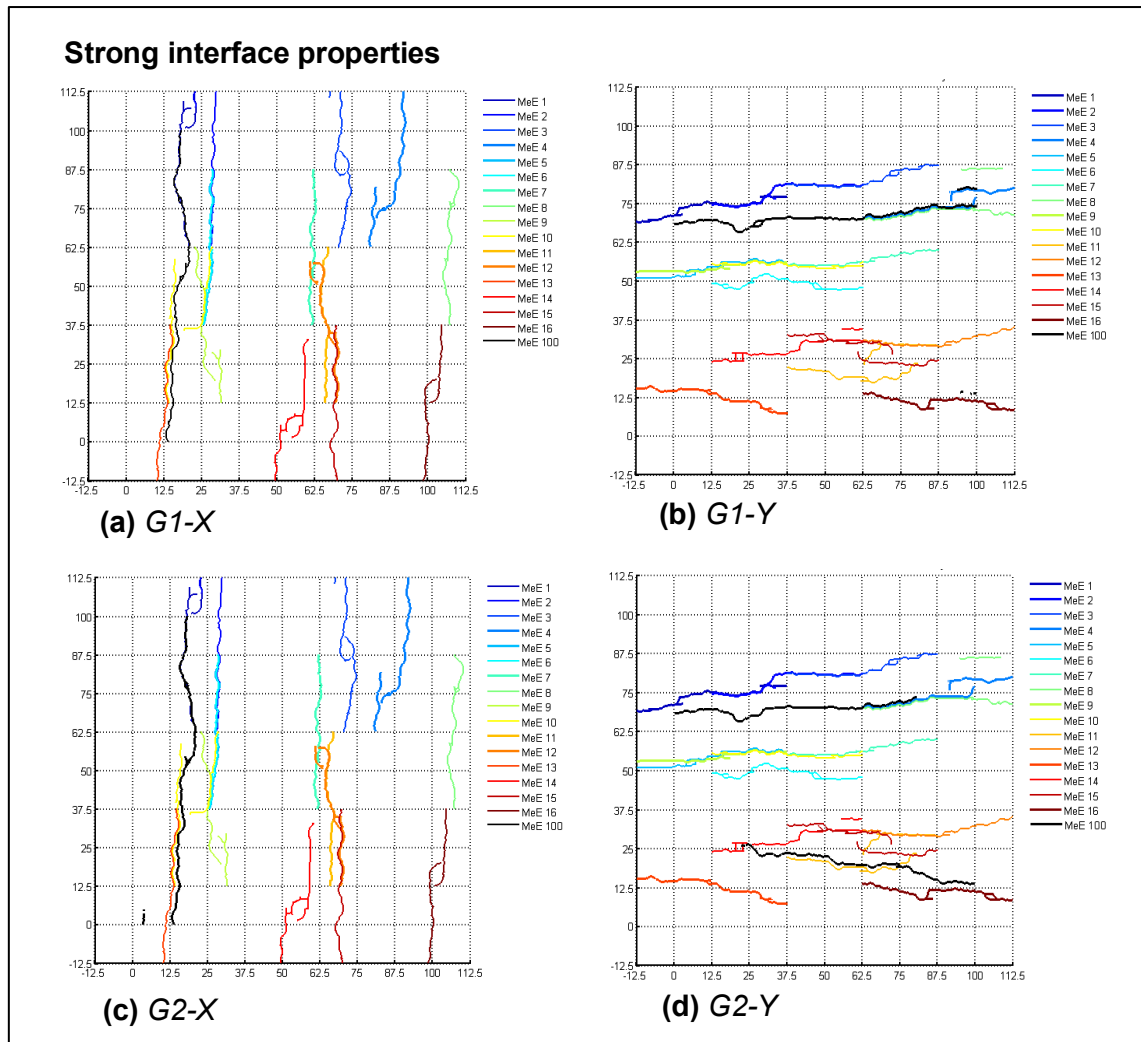


Fig. 4-23: Comparison of separate crack paths between overlapping series MeE-16 \times 50 (shown in coloured lines) using B1 boundaries against full size MeE-100 (shown in black lines): (a) *G1-X*; (b) *G1-Y*; (c) *G2-X* and (d) *G2-Y* for strong interface properties.

After analysing continuity of the crack paths obtained with different interface properties, such as in Fig. 4-22 and Fig. 4-23, it can be concluded that the predicted cracks agree confidently their verification crack paths. However, the results have not been perfectly verified in the case of strong material interface model shown in Fig. 4-23-d. In this case, the model is loaded along the longitudinal axis of the elliptical shape fibre cross-section. The shifted results can be attributed to the sensitivity effect of the chosen boundary conditions at meso-scale and the stochastic stress concentrations with respect to the separation of scales. This may also be

attributed to the context of a minimum window size that has been imposed by the investigated size effect study conducted in Section 4.4.5.

4.5. Multiscale coupling using coarse meshes

Fig. 4-24 and Fig. 4-25 compare the stress-displacement relationships of multiscale models from using overlapping series MeE-16 \times 50 and detailed MeE-100 for weak and strong interface properties respectively. These models use coarse meshes and integrate material properties according to the methodology in CHAPTER 3. The effective stiffness and fracture energy for each individual MeE was evaluated based on the MeE results. However, ABAQUS offers an orthotropic elasticity model defined by an orthotropic stiffness matrix. Therefore, this matrix incorporates the effects of individual fracture modes on X and Y directions and the combined effects (Simulia/Abaqus). A local coordinates system is defined for the orthonormal directions X and Y to map solid elements and cohesive elements, that are also linked to the corresponding meso-scale fracture energies.

The corresponding crack paths of both meso and macro-scale simulations are also inserted in the upper right regions of the plots. It can be seen that the agreement was good when a single crack dominant path was modelled. If there are two distant crack paths, the matching locations could be established only in the case of weak interface properties (see the $G2-X$ results in Fig. 4-24 and Fig. 4-25). The reason is that the global macro-mesh is not fine enough to minimise the global boundary effects in the case of strong interface properties.

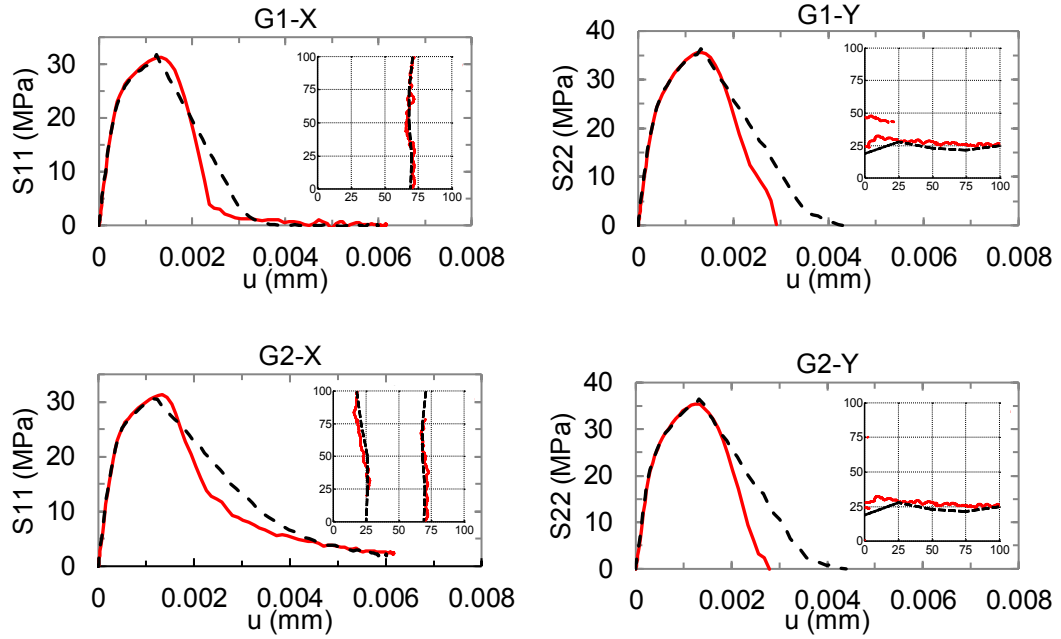


Fig. 4-24: Nonlinear multiscale results for weak interface properties using the overlapping concept vs fully detailed simulations (solid curve: detailed MeE-100, dashed curve: using MeE-16 \times 50 assembly).

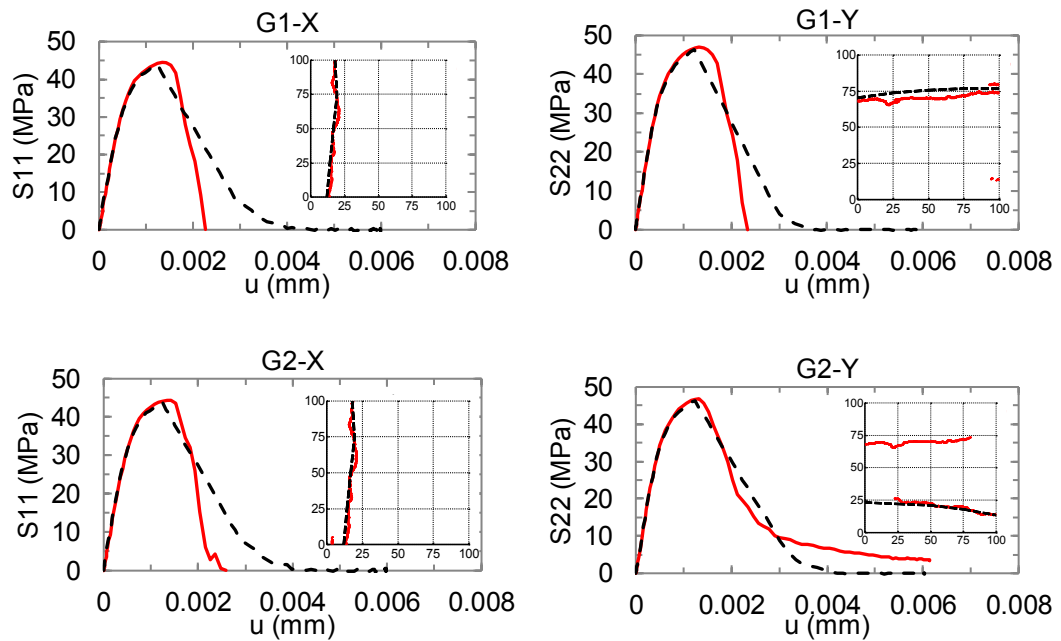


Fig. 4-25: Nonlinear multiscale results for strong interface properties using the overlapping concept vs fully detailed simulations (solid curve: detailed MeE-100, dashed curve: using MeE-16 \times 50 assembly).

4.6. Multiscale coupling using Bayesian inference model

It has been shown in Section 4.4.7 that the crack propagation continuity and scale coupling at global scale is ensured by the adaptively size-increasing overlapping strategy. The Bayesian inference model is then used to filter the unnecessary crack paths. Usually, crack bias situations arise in less heterogeneous materials or regions where crack sensibility is high. Although it is possible to map all the crack paths, the proposed Bayesian inference model reduces possible crack propagation errors, leading to a more accurate global model. This is due to updating the crack probability between adjacent element clusters. This filter ultimately checks if crack continuity is ensured. Fig. 4-26 shows the resultant crack paths after the Bayesian filter is applied, compared with Fig. 4-22-a-b and Fig. 4-23-a-b, before filtering.

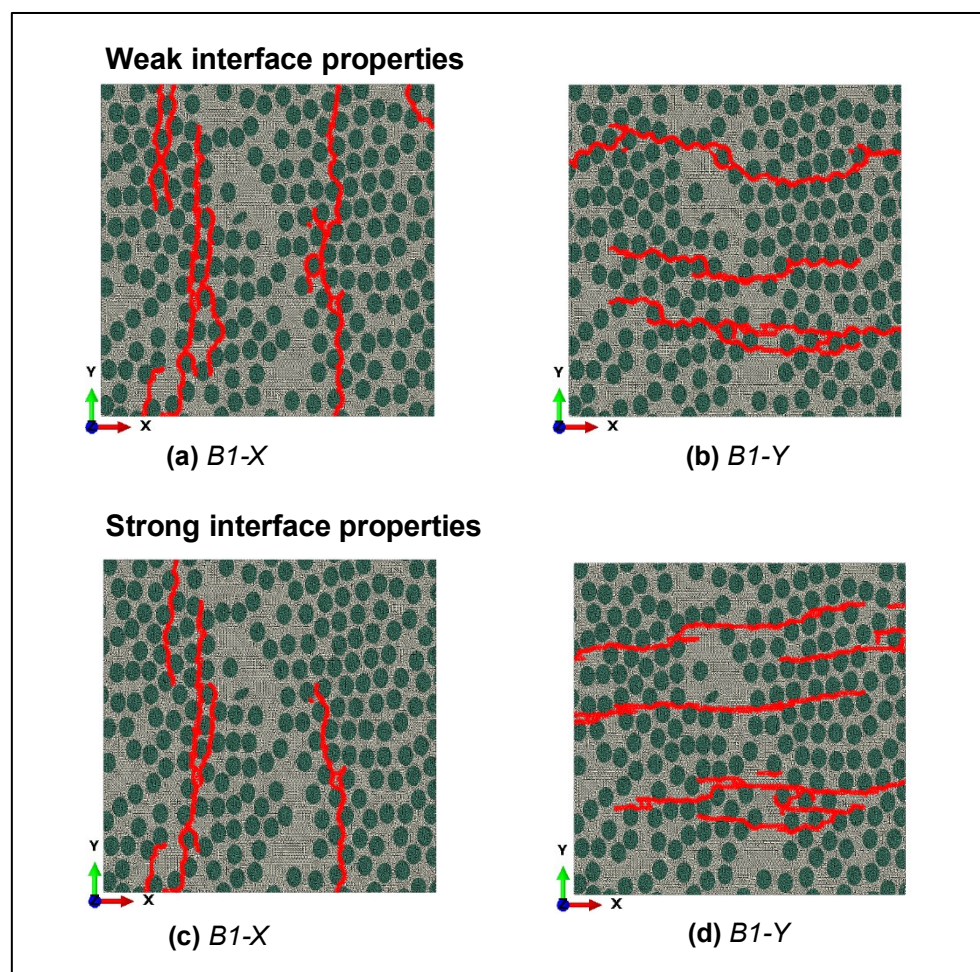


Fig. 4-26: Filtered crack paths obtained after applying the Bayesian inference model.

For validation purposes, the multiscale simulations in this section were carried out using fine meshes that were mapped accordingly. Although a variety of choices were tried, the mapping was conducted using a simple Euclidean distance to filter element indices of the new macro-scale meshes. Fig. 4-27 and Fig. 4-28 show that highly nonlinear situations at global scale could be captured effectively by mapping the macro-CIEs where meso-scale crack paths were identified. This approach was used to transfer the crack paths from separate MeEs to the global scale. The results show a good agreement especially for the two dominant crack paths in Fig. 4-9 and Fig. 4-10 using $G2-X$ and $G2-Y$ boundaries respectively.

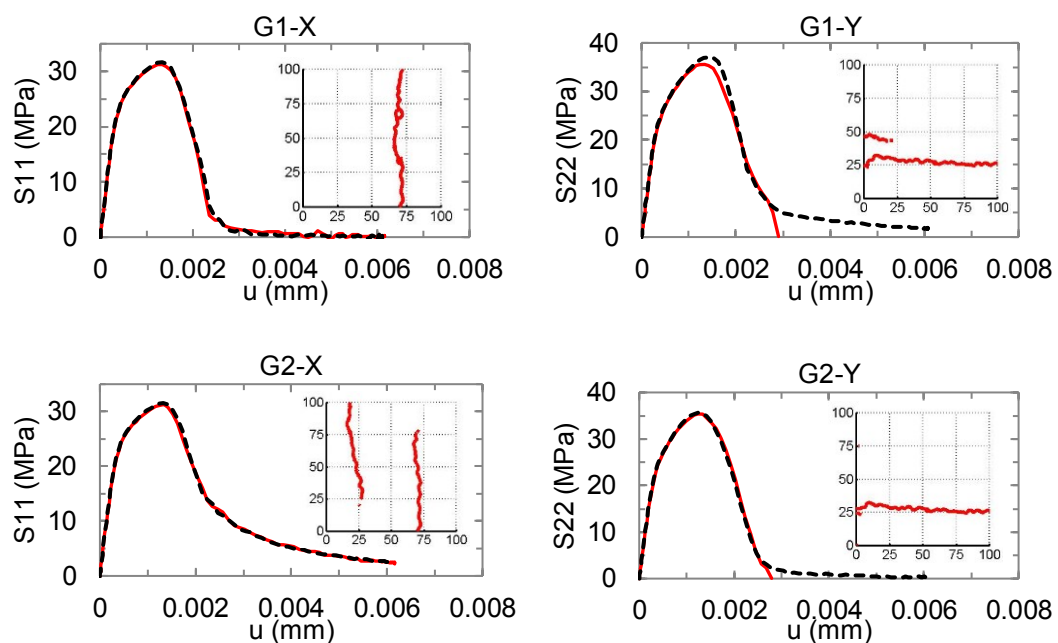


Fig. 4-27: Comparison of simulation results using the multiscale stochastic coupling strategy for weak interface properties. The solid curves represent the detailed geometry models (i.e. MeE size 100 μm) and dashed curves are the Bayesian multiscale models.

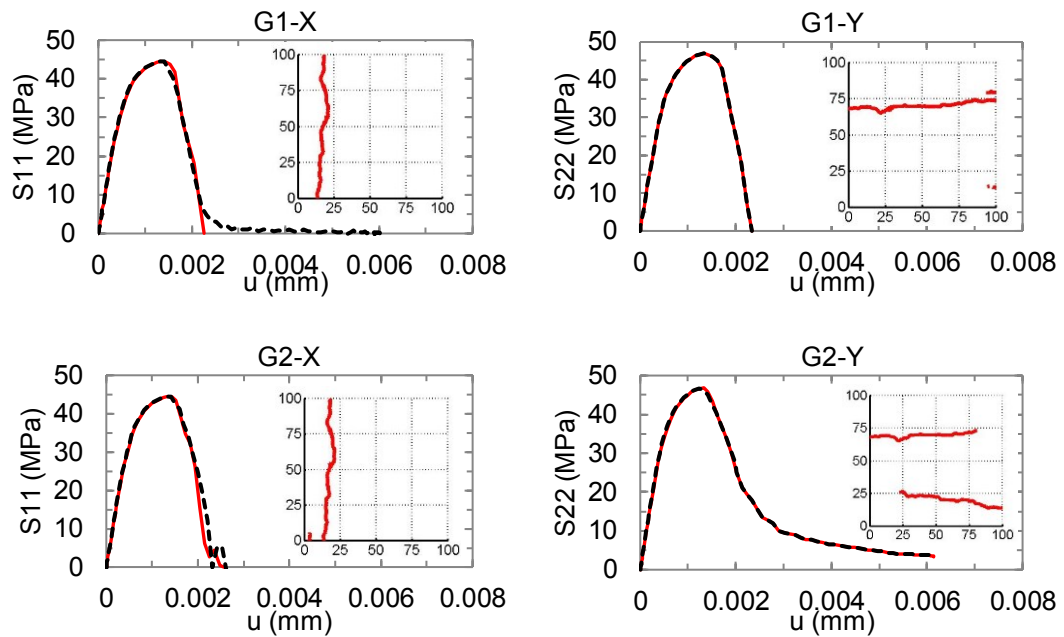


Fig. 4-28: Comparison of simulation results using the multiscale stochastic coupling strategy for strong interface properties. The solid curves represent the detailed geometry models (i.e. MeE size 100 μm) and the dashed curves are the Bayesian multiscale models.

4.7. Computer implementation

As shown above, the methodology in CHAPTER 3 was implemented in a number of computer programs. The meshing and extraction of traction-displacement curves of CIEs are conducted using Matlab and Python scripts. The pre-insertion of CIEs is based on (Su et al., 2009; Yang et al., 2009). The construction of MaEs and energy mapping for global modelling are implemented with Matlab codes.

The MeE overlapping series were computed on parallel CPUs. The CPU time on a desktop computer using Intel(R) processor i7-2600 @ 3.40 GHz with 8 threads was about 5 to 6 hours per simulation, while when the high performance parallel computing facility at University of Manchester was used with 48 cores, the average time was 45 min. Simulating the full-sized 100 μm model for validation of multiscale modelling took about 14 hours using 48 cores in parallel.

4.8. Summary

This chapter has used two detailed case studies to validate the new multiscale stochastic modelling method developed in CHAPTER 3 for complicated fracture modelling of quasi-brittle materials such as fibre reinforced composites. The main conclusions of this chapter are:

- (i) The selection of meso-scale window sizes is not related only to the distribution of volume fractions. The strength variation of MeE clusters need to be distinctive. For accurate multiscale coupling, it is necessary to ensure morphological continuity by accurate mapping of the individual MeEs.
- (ii) Increasing the MeE window size does not necessarily stabilise the fracture behaviour, thus invalidating the classical RVE (representative volume element) approach. Nevertheless, by choosing the appropriate MeE window size and resolving the boundary deformation compatibility via the overlapped windows concept, the crack bias effects can be minimized and therefore the scale transfer could be captured effectively.
- (iii) The energy mapping rules proposed in CHAPTER 3 were tested for different interface properties and crack matching criteria. For defective materials, the short to long overlapping method may be used. For less defective materials, non-overlapping as for elastic studies or short overlapping discretisation in fracture mechanics can be used.
- (iv) The Bayesian inference model can be used to reduce the uncertainty of bias crack paths in the multiscale transfer, owing to its ability to update the matching state of belief using element cluster searches.
- (v) The new multiscale stochastic modelling method offers a more accurate modelling framework for multiphase heterogeneous materials with various levels of defects. Heterogeneity features such as material defects, inclusions and voids can be incorporated at both scales.

- (vi) In this study, the material information is collected in a stochastic manner according to their real feature distribution and physical space. However, as a proof of concept, only the most critical boundary results were included in the scale transfer. Monte Carlo simulations can be further added to solve more complicated loading cases.
- (vii) Although all MeE crack paths in this study were bounded by their reduced window sizes (up to 50 μm), they became longer due to matching in the overlapping domains. Exploring this advantage, the proposed multiscale modelling scheme can be extended to virtually unlimited computational domains.
- (viii) Finally, the proposed multiscale models predicted cracks paths in good agreement with those from the full-sized model.

CHAPTER 5. IN-SITU X-RAY COMPUTED TOMOGRAPHY TESTS OF CARBON FIBRE REINFORCED POLYMERS

5.1. Introduction

To develop a thorough understanding of multiscale mechanical relationships in CFRP composites and to justify material selection in different engineering applications, it is important to have reliable experimental data revealing crack propagation across scales. Such data will not only reveal detailed material behaviour, but also provide data for the calibration of advanced crack propagation modelling methodologies, which could apply the limited testing data from small size components to more realistic real-life structures. As discussed in the literature review in CHAPTER 2, the most advanced technique nowadays for acquiring the necessary experimental data is the in-situ X-ray CT scanning. However, conducting in-situ X-ray CT fracture test of fibre composites with thin fibre diameter is a well-known challenge. Previous X-ray CT scans at room and elevated temperatures (Bale et al., 2012) were only possible under synchrotron radiation due to the required radiation energy flux and image acquisition speed to capture the in-situ deformation steps. There were also imaging problems in revealing details at the fibre scale even though the fibre diameters were about twice the size of carbon fibres used in aerospace industry.

Other static in-situ X-ray CT tests were reported in (Moffat et al., 2010; Scott et al., 2011; Sket et al., 2012) using synchrotron imaging. Although damage progression was captured in some of these studies, the datasets were not reported in further image-based modelling at fibre scale. In contrast, using laboratory cone emitter X-ray sources gave poor quality image results at fibre level. Although it would be possible to enhance the spatial resolution by reducing the distance between the sample and the cone emitter (McCombe et al., 2012) and enhancing the X-rays flux energy and phase-contrast (Enfedaque et al., 2010; Rouse, 2012), the fibre resolution still

remains unresolved so far. Another recent work (Yu et al., 2015a) used time-lapsed X-ray CT captures of E-glass fibre composites under tension and performed a meta-segmentation of the resin, weft and binder yarns to quantify damage progression but still not up to the fibre scale.

Currently the United Kingdom is well equipped with X-ray CT imaging facilities. However, the loading rigs are not considered suitable for in-situ loading tests at the fibre scale, which is the focus of this study. Therefore, this chapter will present the development of a new loading device to be incorporated with X-ray CT machines at the national synchrotron Diamond Light Source in Oxfordshire.

Using the I13-2 Branchline at the Diamond facility incorporating the loading device, two sets of experiments were carried out: (i) uniaxial tensile tests using double-edge notched samples and (ii) three-point bending tests of small beams. This chapter will also describe the test setup and some scanning results to demonstrate suitability of the adopted experimental method.

5.2. Initial X-ray CT scan using laboratory cone emitter source

An attempt was made first to get images of CFRP samples using an X-Radia micro-CT system at Henry Moseley X-ray Imaging Facility (HMXIF) with cone emitter source. The scan took approximately 30 hours to complete due to the use of long exposure time (40 seconds per slice). This long exposure time was necessary because the X-ray energy flux was not sufficiently powerful. In contrast, acquisition of raw image projections of a complete tomography is 2 to 8 minutes when the synchrotron technology was used, as seen later in Section 5.5.

Fig. 5-1 shows the captured field-of-view (FoV) and two other increased volume renders that were extracted at different regions of interest (RoI) for quality inspection. The sample is a disc cut from a braided CFRP laminate using a novel laser cutting procedure developed at University of Manchester. The X-ray CT machine used has a resolution range of 5 to 120 $\mu\text{m}/\text{pixels}$. The

highest optical magnification available is 20 times. This leads to an effective tomography diameter of approximately 1.25 mm.

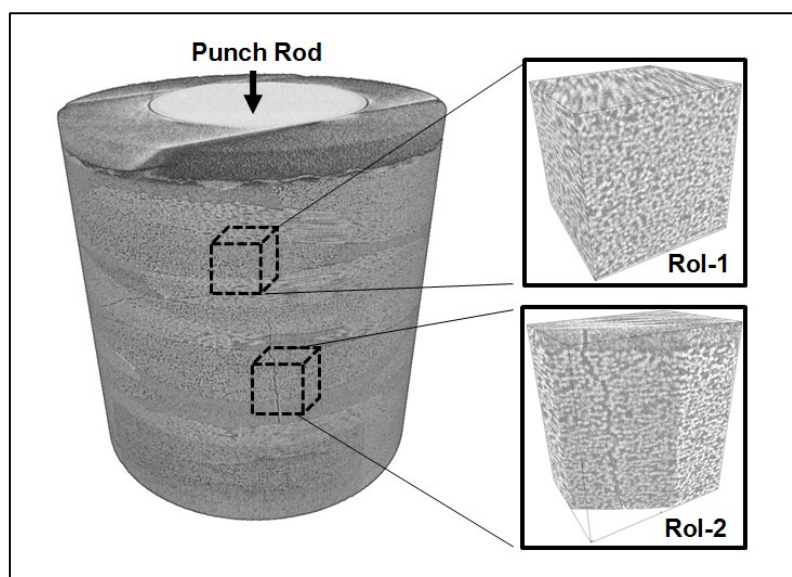


Fig. 5-1: X-ray CT volume renders from a CFRP sample scanned using the X-Radia micro-CT system at Henry Moseley X-ray Imaging Facility (HMXIF).

5.2.1. Experimental details at HMXIF facility

The X-ray CT imaging was taken through a clear Perspex tube (Fig. 5-6). The tube was part of the loading rig used during the X-ray CT tests. The selection of the Perspex material was made to minimise material absorption of the X-rays.

An initial compression loading of 320 N was applied manually using a micrometre head. The loading was transferred via a cone shape punch rod. The punch rod was made of steel metal and was attached to the loading bar of the rig. The tip of the punch rod is visible in the FoV area of Fig. 5-1 at the top of the sample. In this case, the reduced FoV could capture the full thickness of the sample but not the entire disc sample.

Fig. 5-1 reveals some fabric architectures that can be obtained using the cone emitter X-ray CT scanner. However, the optical resolution and imaging quality are not sufficient to distinguish the exact fibre scale geometry by means of a volume segmentation approach, as will be shown

below in Section 5.2.2. Nevertheless, this technology provides a good phase-contrast to distinguish the material phases and the crack surfaces, as in Fig. 5-1 for RoI-1 and RoI-2 respectively.

5.2.2. Attempts of direct segmentation

In addition to the long exposure time, another major problem with using the X-Radia facility is the low quality of images for the CFRP material. Several attempts of volume segmentation were carried out using the AVIZO image processing and visualisation package (FEI/Avizo). The segmentation process assigns separate material labels to different material phases after the delineation of images. This means that the phase separation depends on the contrast between pixel intensities that are naturally mapped on these regions. In the CFRP materials, the individual fibre and matrix phases could not be separated although multiple RoI areas have been closely inspected. For example, in Fig. 5-2 two attempts of direct volume segmentation were conducted as follows: (i) splitting the raw images into two main phases (matrix and fibres) by using a constant pixel intensity threshold strategy (Fig. 5-2-a) (ii) applying a series of noise smoothing and image pre-processing filters followed by direct segmentation (Fig. 5-2-b).

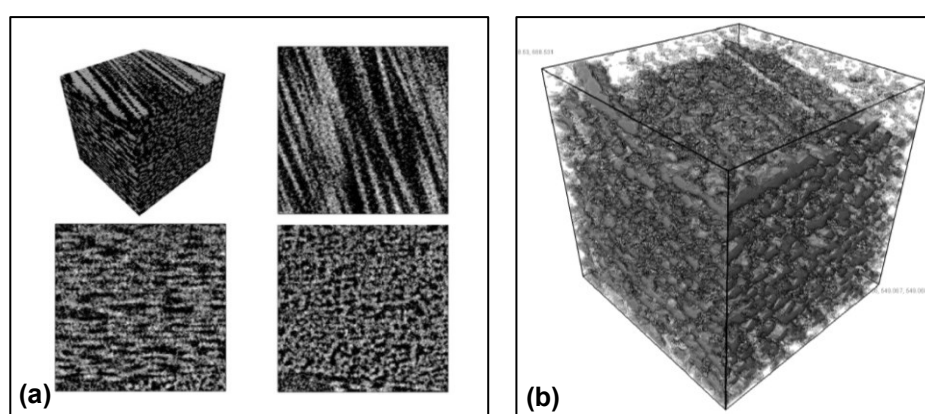


Fig. 5-2: Attempts of volume segmentation based on CFRP braided X-ray CT dataset using: (a) raw images and single threshold segmentation; (b) filtered images and single threshold segmentation. The processing and visualisation was conducted using AVIZO (FEI/Avizo).

Fig. 5-2 shows that due to a combination of low quality images and the high fibre volume fraction (manufacturer specification 50%), the X-ray CT dataset could not be further used in any detailed fibre-level modelling.

5.3. Non-X-ray CT loading tests

Before in-situ X-ray CT tests were carried out, the commercially available Deben CT-500 rig (DEBEN) was tried to identify a proper loading scheme and investigate the suitability of existing rigs for fibre composite materials.

5.3.1. Description of the Deben CT-500 rig

The Deben CT-500 rig has two loading modes: tensile and compression. The relative travelling distances between the jaws (one fixed and one mobile) in both tensile and compression modes is approximately 10 mm. The rig consists of a main body applying the loading, which is placed at the bottom as shown in Fig. 5-3. According to the design specifications, the Deben CT-500 micro-loading rig is most suitable for high flux energy radiation sources. This is because of the use of an X-rays retention outer tube, which is part of the loading frame necessary to transfer the in-situ load. The tube is made of an opaque carbon treated glass with an outer diameter of 50 mm. The advantage of this testing rig is that the maximum force can reach 5 kN. However, the maximum loading speed is only 0.3 $\mu\text{m/s}$. Although the rig has a displacement control, the sample targeting and re-positioning takes the users a long time (about an hour), typically by using a series of normalised radiography trials. Fig. 5-3 shows the mechanical rig and a three-point bending setup used in the non-X-ray CT tests.

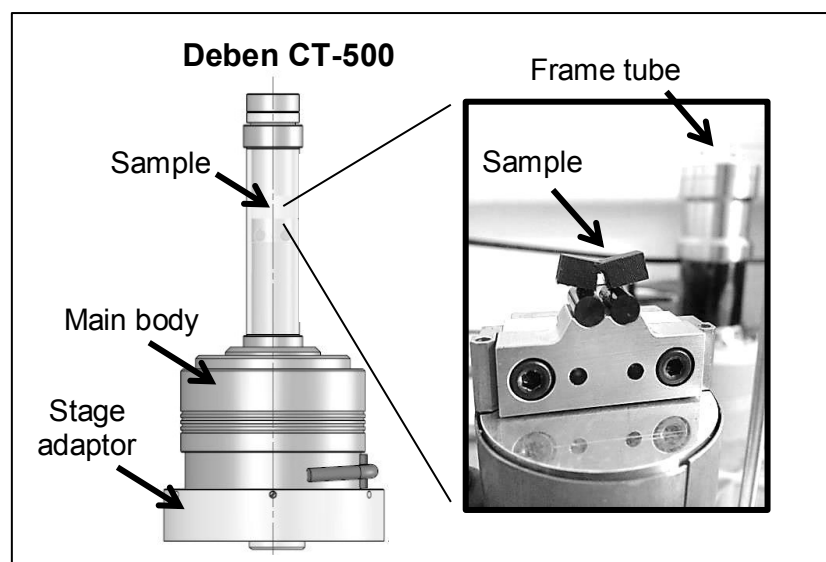


Fig. 5-3: Illustration of the commercially available loading rig Deben CT-500 (DEBEN) and the short span three-point bending test of a notched CFRP sample.

In total, six in-situ loading tests were carried out to assess the suitability of the Deben system for the CFRP. The tests were conducted on notched samples as shown in Fig. 5-3. The results were primarily used to aid the design of a new in-house loading rig.

5.3.2. In-situ loading test measurements

Both uniaxial compression and three-point bending tests (Fig. 5-3) were carried out. The uniaxial compression loading tests were conducted on disc samples with nominal thickness of 2 mm diameter and diameter of approximately 1.2 mm, 2 mm and 3.8 mm. Such samples were cut using a novel laser cutting technology. The electroplated diamond core drills were also tried but they visibly damaged the inner disc samples and thus were not used further.

The uniaxial compression tests were mainly conducted to explore the load-relaxation effects during the waiting time which was needed to apply the in-situ loading. Fig. 5-4 shows the recorded forces versus time curves from the disc tests. Significant load-relaxation effects can be observed, which can be attributed to progressive damage of the internal microstructure of the sample. This load-relaxation effect started from very low loading levels.

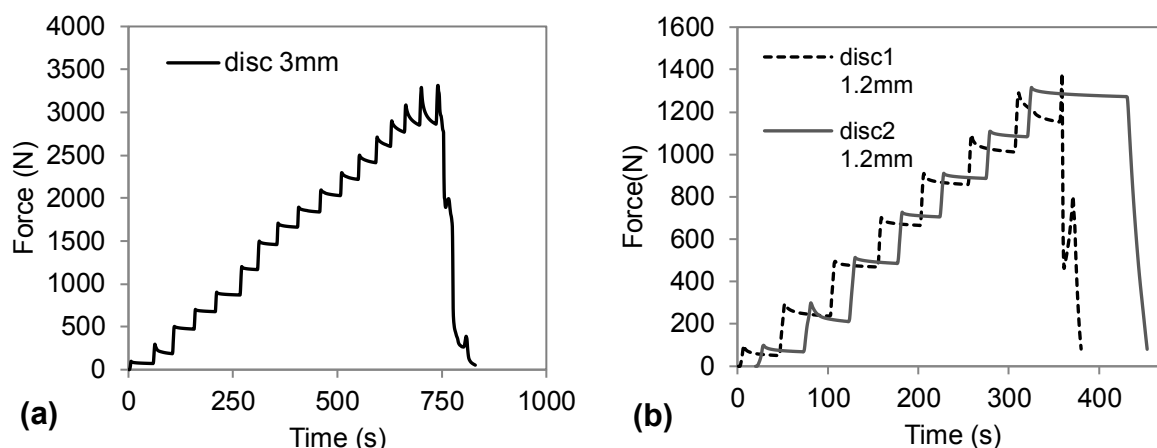


Fig. 5-4: In-situ stepped loading tests under uniaxial compression on disc samples made of CFRP composites of different thicknesses: (a) 3 mm and (b) 1.2 mm.

Fig. 5-5 illustrates the force measurements of three-point bending tests using continuous, stepped and cyclic-stepped loading programs. However, the sample setup is not standard three-point bending setup due to the small size of the sample. To be able to test small size samples, the upper short-span part of the provided four-point bending setup within rig package was used. Therefore, the short-span bending supports were mounted upside-down as shown in Fig. 5-3.

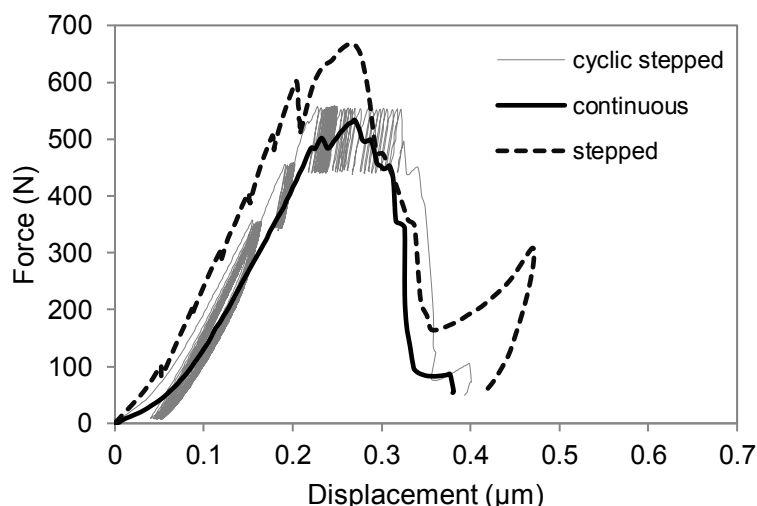


Fig. 5-5: In-situ three point bending loading tests of cross-ply carbon fibre/ epoxy composite samples using the Deben CT-500 mechanical rig.

The three-point bending samples were cut from a cross-ply carbon fibre/ epoxy composite with a total of 16 multidirectional plies. The samples size was $15 \times 3.8 \times 4$ mm. They were notched at mid-span on a single side as shown in Fig. 5-3. The notch was machined using a 0.3 mm thick carbide blade. Results in Fig. 5-5 show that during the in-situ stepped loading programme, the elastic stiffness hardening was less evident than the continuous and cyclic loading programmes. This was due to potential fibre locking effects at micro-scale of the tensioned part. In addition, a considerably higher ultimate force was measured using the stepped loading program. Unfortunately, the non-X-ray CT loading experiments conducted here could not be visualised during the loading progression. This was due to the opaque carbon treated tube of the loading rig (see Fig. 5-3). This tube makes it extremely difficult for the users to position small sample setups for X-ray CT experiments. Therefore, a new testing rig is designed in this study, as detailed below.

5.4. Development of a new in-situ micro-loading rig

In an in-situ X-ray CT test, the imaged object should remain as stable as possible. This is particularly important when the scanned FoV is smaller than the sample geometry size. Fixed metallic markers of known coordinates can be used to record the deformation of regions outside the FoV. The new loading rig was designed with a fixed bottom jaw that can be used as a reference in different loading modes. Fig. 5-6 shows a picture of the loading rig.

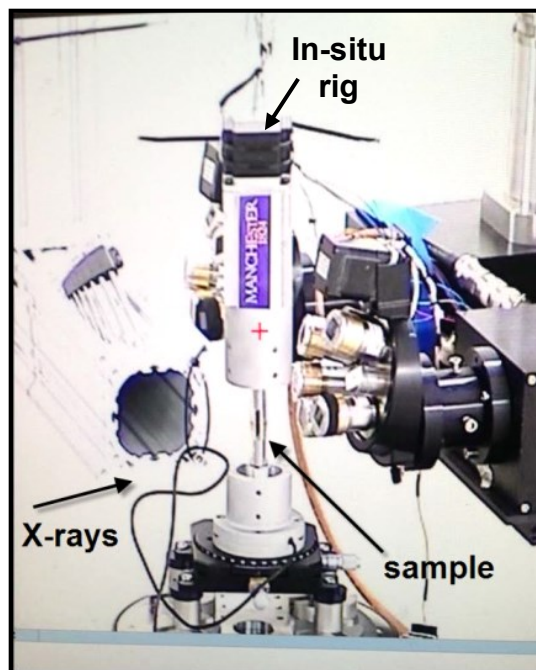


Fig. 5-6: A new micro-loading rig for in-situ X-ray CT experiments.

Fig. 5-7 shows the fully integrated electrical, mechanical and digital assembly of the new in-situ micro-loading rig. It consists of four main parts: (1) the mechanical components, (2) an integrated controller box, (3) a data acquisition system (DAQ) and (4) a digital box.

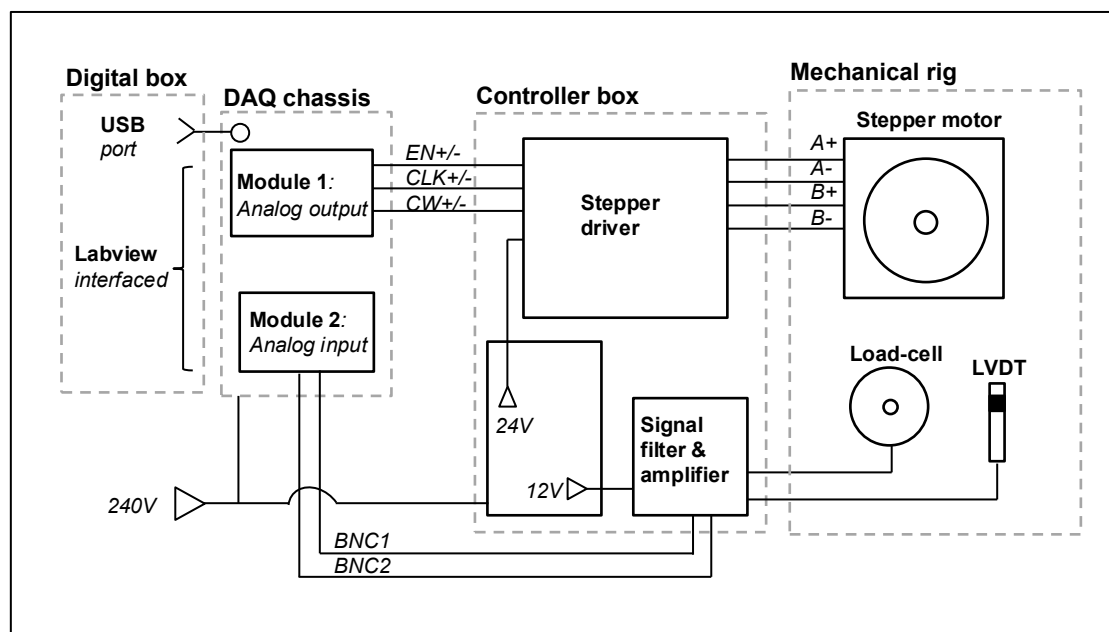


Fig. 5-7: General assembly technical sheet illustrating main components of a fully-integrated new in-situ micro-loading rig.

5.4.1. The mechanical components

Fig. 5-8 shows the design layout with all mechanical components of the new rig. The three main mechanical components are: (i) a frame tube, (ii) metallic dies and (iii) a loading mechanism (linear actuator). The metallic dies are attached to the ends of the loading tube and are able to accommodate multiple scanning tubes. The frame tube is made in clear Perspex to allow imaging and data capture. The Perspex loading tubes are glued at both ends with outer restraining parts to avoid cracking.

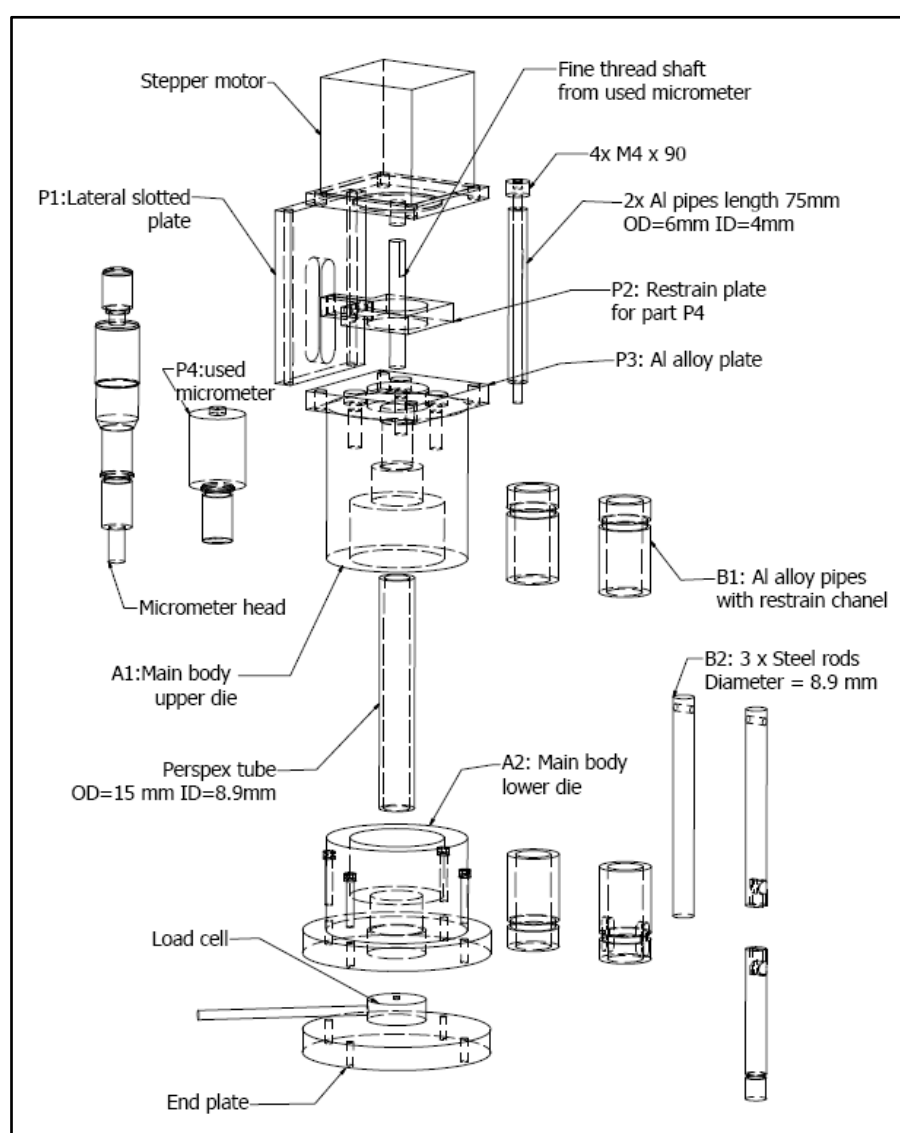


Fig. 5-8: Mechanical components of a new in-situ loading rig.

5.4.2. Data acquisition system and sensors

The data acquisition was integrated using National Instruments (NI) modules. Two load-cell sensors of 500 N and 2000 N are currently available. The voltage reading resolution is 10 μV . The reading resolutions are equivalent to 0.1 N/step and 0.4 N/step respectively. The load-cell socket is at the bottom of the rig as shown in Fig. 5-8. The force signal acquisition is intermediated by an in-house design and manufactured filter-amplifying circuit (see the controller box in Fig. 5-7). This circuit is powered separately and communicates directly with the DAQ reading module. For the displacement measurements, a linear vertical displacement transducer (LVDT) is used. The LVDT sits laterally on the actuator loading frame. The lateral LVDT sensor has a maximum travelling distance of 11.8 mm and the voltage resolution equals to 10 μV . This leads to the reading resolution of 23 μm /step. The lateral LVDT was only used as a proof of concept in this version since the LVDT model available was not fully integrated with the current rig controller box.

The filter-amplifying circuit was designed and manufactured at University of Manchester. This circuit has a bi-channel interface that accommodates two load-cell sensors at the same time. In future designs, this circuit may accommodate a third compatible micro-voltage LVDT or other linear encoders.

5.4.3. Force and displacement data readings

The force readings are recorded from the same button load-cells for both tension and compression rig loading modes. This is possible owing to the innovative design of the outer tube. This tube works as a loading frame transferring the sample load from the grip of the frame. In other words, the tensile forces are transferred through the outer tube in compression and the compression forces are transferred through the outer tube in tension. The button load-cell is

suitable in both cases. The tensile rod has a restraint channel at the bottom side. The restriction of the tensile rod is facilitated by four slotted holes in the restrain pipe. The sensor trigger in tension mode is made via the outer tube compression that presses against the load-cell. The sensor trigger in compression mode is simply made via the steel rod that is placed in the tube and presses against the load-cell.

5.4.4. Automation and loading control

The new rig can be operated in two modes: tension or compression. A built-in loading mechanism that works as a linear actuator (shown in Fig. 5-8), allows adjustment of loading from outside the X-rays radiation hutch. This also improves the operability during the in-situ X-ray CT experiments owing to the flexibility of allowing various loading programmes digitally controlled by Labview. The linear actuator shaft has fine threads of 0.5 turns per mm and is operated by a stepper motor as seen in Fig. 5-8. The resolution of the stepper motor is 1.8 °/step. The holding torque at the 2-phase energisation of this particular motor is 1.0 Nm. For higher coupling torques, a planetary gearbox can be added to the actuator assembly. However, such a gearbox was not used in the current design.

The motor is connected to a stepper driver. The driver is interfaced with three out of four output channels of an analog output module. These channels were wired to the enabling and direction terminals of the stepper motor. The trigger is made by sending digital output signals. Typically, the control of the motor speed is achieved with a differential frequency of a digital signal (square shape) sent to the driver. This ultimately defines the traveling speed of the linear actuator. Conversely, the actuator positioning and loading can be controlled using a displacement sensor and a feedback module. In this case, the feedback is recorded using an input module and the motor can stop almost instantly.

5.4.5. Digital controller system

It is possible to synchronize the displacements and force readings with the motor controller using Labview. This is particularly useful when using specific in-situ X-ray CT loading programmes. In this project, the static in-situ loading with manual control has been used during the synchrotron in-situ X-ray CT loading experiments.

The in-situ loading programme can be input manually into the Labview code or can be automated accordingly to the optimum loading steps of various loading programmes. If the auto loading mode is used, the corresponding scan time periods need to be pre-planned. In this case, some waiting times have to be added to account for possible load-relaxation effects during the X-ray CT scanning time.

5.4.6. Loading modes

Typically, the displacement-controlled loading is recommended during the in-situ X-ray CT tests. The force-controlled reading can be used but the force readings can be misleading due to local damage spike effects. Typically, in fibre composites, multiple damage instances can occur at the same applied force level due to the localisation of damage. In this case, unequal displacement steps can be applied but non-X-ray CT loading trials need to be carefully analysed.

5.4.7. Loading setups and preparation of samples

In the loading system, different loading configurations can be accommodated including: (i) uniaxial tensile, (ii) three-point bending and (iii) localised compression via a punch rod, as shown in Fig. 5-9.

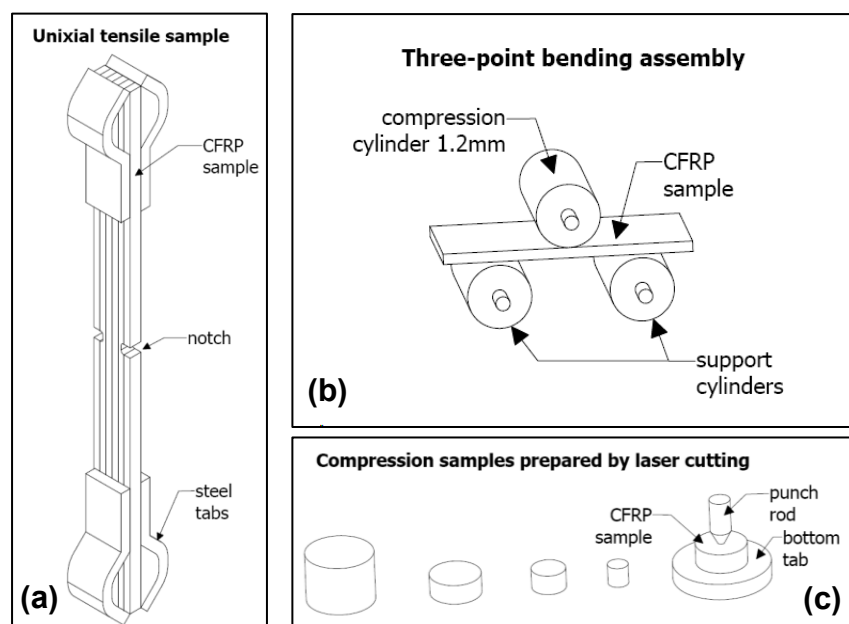


Fig. 5-9: Illustration of loading setups and sample support configurations.

The preparation of samples depends mainly on the loading setups illustrated in Fig. 5-9. In this study, the CFRP samples prepared for tensile and three-point bending tests were mechanically cut using a diamond water blade. For the tensile samples, thin metal tabs were attached to the tensile samples at both ends. These were necessary to secure the tensile supports. The tensile samples were notched on two sides as shown in Fig. 5-9-a. The cutting of notches was done using an ultra-thin carbide blade of 0.3 mm. The tabs were glued to the CFRP surfaces as shown in Fig. 5-9. The adhesive is a bi-component epoxy glue of relatively good strength.

In three-point bending tests, the samples were considerably smaller than those tested using the Deben loading rig in Section 5.3. The supports of the three-point bending setup in Section 5.4.7 were achieved using three cylinder pins of 1.2 mm diameter. The samples were temporarily stacked for positioning with the supports using double sided sticky tape. The span between the two cylinder supports was approximately 3 mm. The assembly was then positioned into the mechanical loading tube. The sketch of such a three-point bending assembly is shown in Fig. 5-9-b.

5.5. Data acquisition at Diamond-Manchester Branchline I13-2

It is known that the CFRP material has relatively low phase-contrast in X-ray CT due to similar material densities between the carbon fibres and the epoxy resin (Wright et al., 2009; Moffat et al., 2010). To enhance the quality of reconstructed X-ray CT images, various phase-contrast technologies are used and they can be classified into five categories: (1) crystal interferometry, (2) propagation-based imaging, (3) analyser-based imaging, (4) edge-illumination and (5) grating-based imaging. Depending on the category, the intensity scatter may be measured directly which is most common in cone emitter sources, or may be interfered by various X-ray modifiers such as: beam splitter chambers (sitting mostly before the actual sample but in some systems, the chambers can be prolonged to contain the sample in between the mirrors), ionisation chambers (Bliznakova et al., 2015), detector masks (Thuring et al., 2014; Endrizzi et al., 2013), absorption grating and foils (Fu et al., 2014; Wenz et al., 2015) and many others. The Diamond-Manchester Branchline I13-2 at Diamond Light Source enhances the phase-contrast of CFRPs using a special crystal monochromator that converts the X-ray beam into pink visible light radiation. This can also increase the contrast between fibres and matrix but can also make distinguishing the fibre - matrix interfaces and crack areas more difficult.

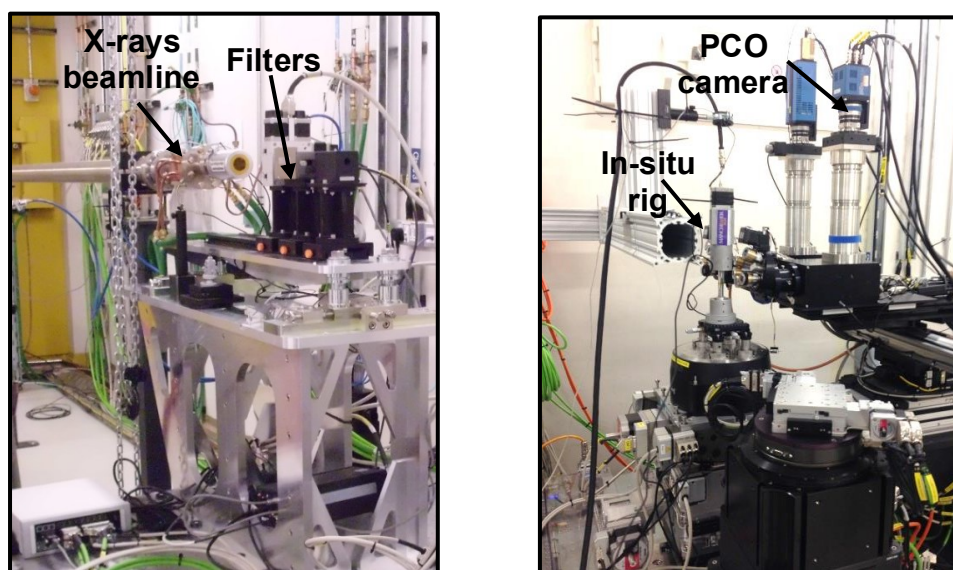


Fig. 5-10: Branchline I13-2 setup configuration at Diamond Light Source in Oxfordshire.

For data acquisition, these experiments utilised a PCO edge 5.5 CMOS detector based microscope system with 14 bit dynamic range. The system images the light generated by the X-rays via a GGG:Eu scintillator using a $10\times$ objective. A $2\times$ tube lens is also present in the microscope providing a total magnification of $20\times$ of the scintillated image. This provides an effective pixel size at the CMOS detector of around 300 nm; enough for the diffraction limited resolution of 600 nm provided by this numerical aperture at the scintillator wavelength. The fast readout of this detection system (up to 100 Hz) combined with the high flux from the beamline allowed tomographs to be collected in fly-scan mode at around 0.2 s per exposure. More detailed information about the instrumentation used can be found in (Diamond, 2016).

5.6. Experimental strategy at I13-2 branchline

Although attractive, X-ray CT volume stitching technique where multiple volumes can be acquired and tessellated in the post-processing was not used in this study. This was due to a series of experimental challenges such as: difficulties with automating the tessellated image acquisition, manual scatter reconstruction, the need to acquire a large number of datasets in limited available beamtime, data storage, computer manipulation of high-resolution images, long holding times during the in-situ loading and sample load-relaxation effects.

For this experiment, intense radiation over an extended energy bandwidth was used to increase the speed of acquisition with enhancing phase contrast (Rau et al., 2011). The gap of the undulator (a 2 m long U22) was set to 5.5 mm for increased flux. To tune the energy bandwidth, and hence increase the contrast of the image, 3 mm of Al filters were inserted into the beam path to attenuate soft X-rays below 18 keV. This complemented the cut-off of the platinum mirror stripe at 25 keV allowing good penetration of the sample whilst maintaining sample visibility. This mirror can also be slightly focussed to collimate in the horizontal direction to

counteract the large horizontal divergence of the source, giving around 7×10^{13} photons per second into the roughly 800 μm field of view used.

Because of the similarity in density between the carbon fibres and the epoxy resin, it was necessary to increase the contrast by allowing the beam to propagate slightly (~ 30 mm) before detection, making use of the edge enhancement from the inline phase-contrast to pick up individual carbon fibres in the matrix.

5.7. Reconstruction of image projections

The reconstruction of the X-ray CT scatter data to form detailed geometrical images at micro-scale was carried out using a manual in-built software package, operated on Linux. This reconstruction software converts the ‘in-rotation’ image projections into their physical spaces by using a manual reconstruction centre that can be only tested by trial and error. However, the reconstruction is based on a filtered back scattered algorithm and more details can be found in (Basham et al., 2015). The format of the final reconstructed slice is type float 32 bit comprising of 2560×2560 pixels. The effective/ physical image resolution of one slice at 20X magnification is approximately 845×845 μm . A typical reconstructed X-ray CT volume consists of a stack of 2160 slices.

5.8. In-situ X-ray CT tests

Two series of in-situ X-ray CT tests were carried out (i) uniaxial tensile tests using double edge notched samples and (ii) three-point bending test. The results are presented and discussed in this section.

5.8.1. In-situ X-ray CT uniaxial tensile test

Fig. 5-11 shows the experimental loading setup and Fig. 5-12 gives the dimensions of the sample.

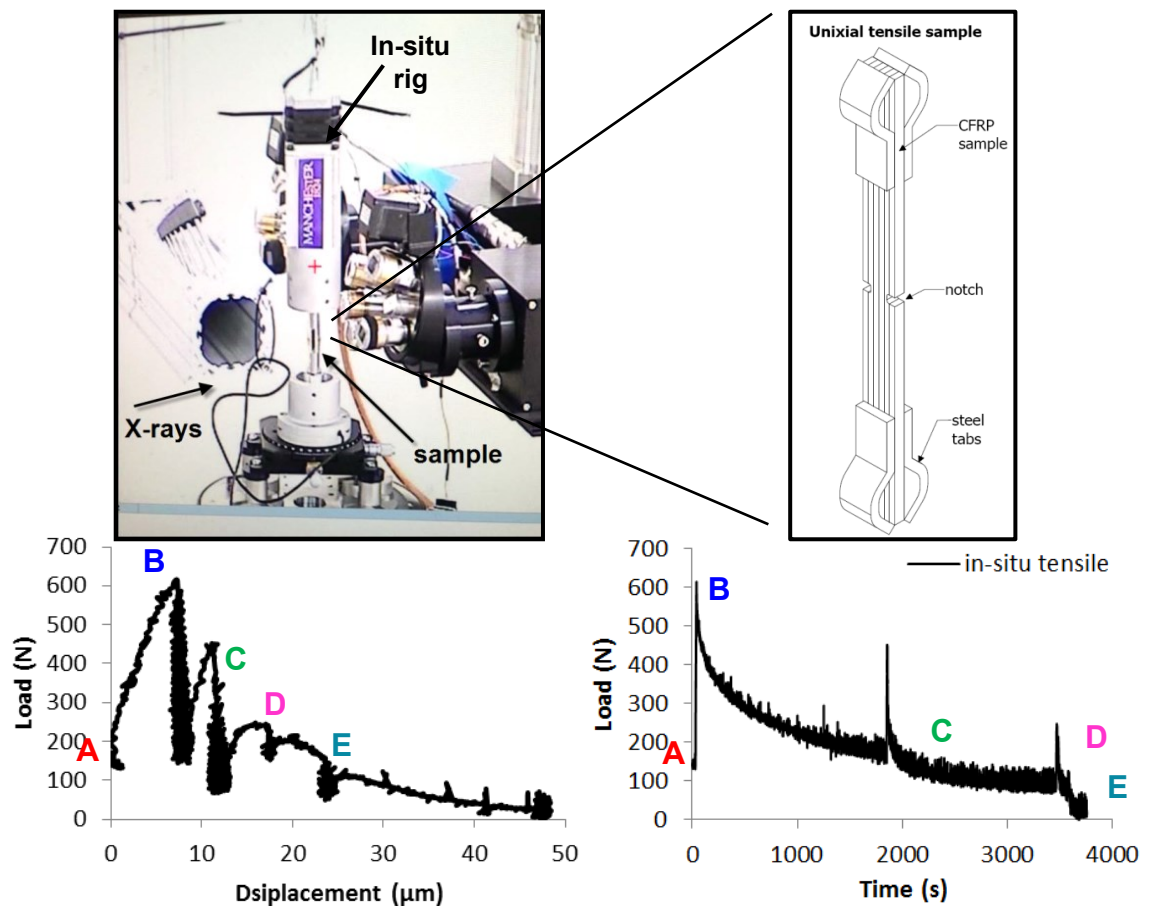


Fig. 5-11: In-situ X-ray CT tensile test setup and loading steps.

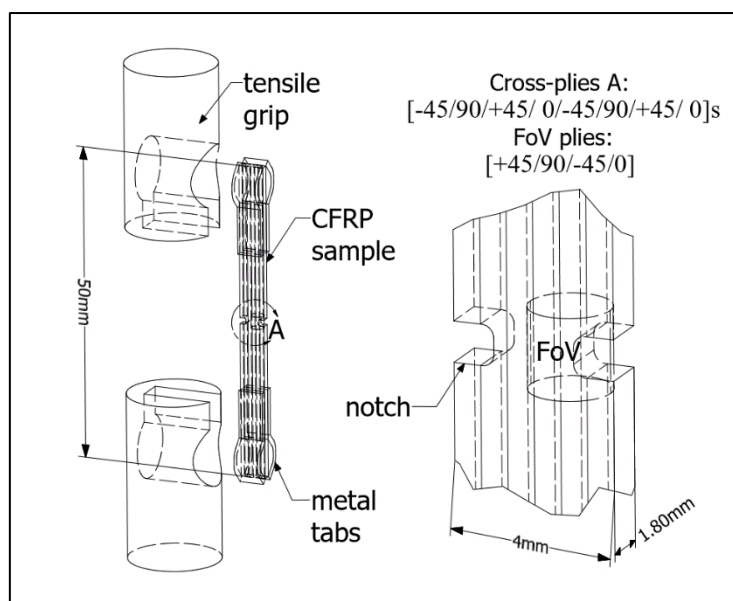


Fig. 5-12: Sample dimensions and in-situ tensile loading setup.

Because a large dataset (in the order of 120 Gb) is generated for each X-ray CT scan, only a few scans were conducted at selected loading steps. Five steps were chosen based on the load-displacement and shown in Fig. 5-11 and Fig. 5-14. The steps were based on the results of a preliminary static loading test shown in Fig. 5-13.

A – this step corresponds to the initial scan before the actual in-situ loading program. A small force is typically necessary for fixing the sample. However, the initial force in this case was approximately 130 N. This force introduced some visible initial cracks in the cross-ply layers of this sample. These crack can be seen in Fig. 5-14 at step-A.

B – this loading step illustrated in Fig. 5-11 at step-B corresponds to 90% the preliminary peak load of the sample in Fig. 5-13. However, the scan at step-B captured the initial pre-peak deformation, while an extension of damage occurred at this step (observed in the load-time data in Fig. 5-11-b part B to C). This can be seen as a load-relaxation effect. However, this has not affected imaging results due to the small deformations observed in the load-displacement curve shown in Fig. 5-11-a.

C – due to the extension of damage at step-B that was associated with some load-relaxation, a reloading was necessary at step-C. The applied force exceeded the remaining capacity of the sample (see steep loading drop at the start of step-C on the load-time curve in Fig. 5-11) and the X-ray CT scan was acquired over the almost constant force plateau.

D – at this step a reloading was performed again. The reloading was done in small increments in order to generate some new visible crack surfaces in the X-ray CT image. The scan started similarly to step-C after the loading drop effect.

E – similar to step-D and step-E a reloading was performed. At this step, the failure of the specimen occurred. This was associated with the visible cross-ply matrix failures and further delamination. The delamination of two resin-rich interfaces grew over the full height of the specimen. Finally, this extensive delamination problem led to failure of the bottom support, which moved the FoV out of the X-ray CT focus.

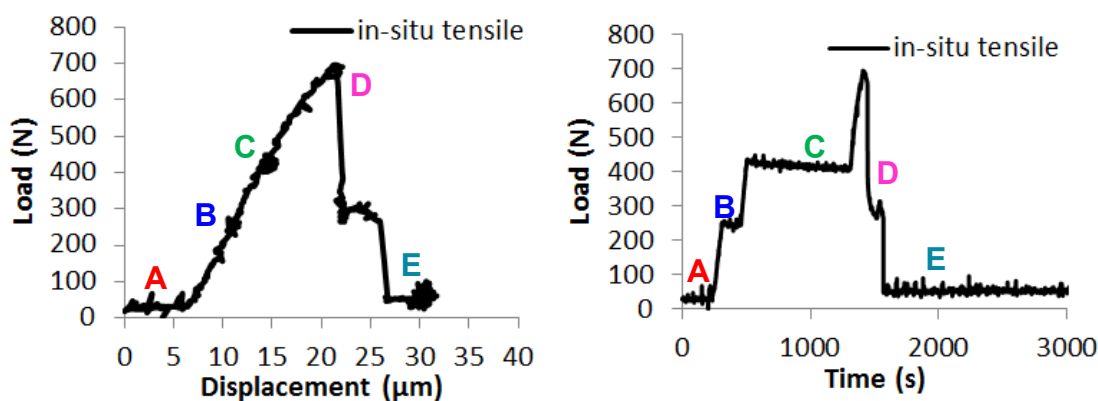


Fig. 5-13: Load-displacement relationship of the preliminary in-situ tensile loading test.

Fig. 5-14 shows images obtained for these different loading steps, confirming the success of their selection as they represent different stages of damage during the loading process. The step-A, step-B and step-C images in Fig. 5-14 show the initiation and progression of damage throughout all the plies and the initiation of ply-to-ply delaminations. This was followed by a substantial delamination at step-D. This progression was visible in the FoV of the experiment.

However, after the redistribution of load, further damage moved outside the original FoV and scan at step-E was taken above the X-ray CT volume shown at step-A and due to specimen rotation also captured the cutting edge of the sample.

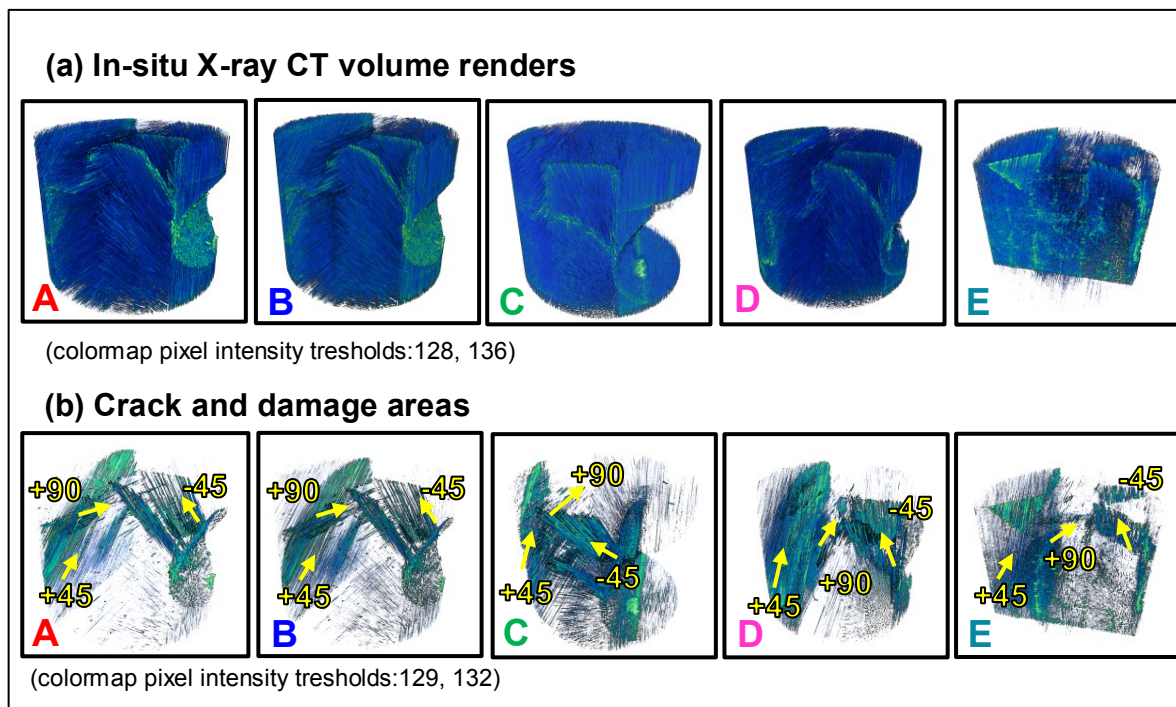


Fig. 5-14: In-situ X-ray CT volume renders of a cross-ply fibre composite under tensile loading. The images correlate to loading curves in Fig. 5-11.

5.8.2. In-situ X-ray CT three-point bending test

Fig. 5-15 shows the dimensions of the three-point bending test sample and the setup in the I13-2 branchline facility. The sample in this case was made of a cross-ply carbon fibre/ epoxy resin composite. The composite panel contained a total of 8 plies made of a 0° - 90° braided woven fabric as opposed to unidirectional plies used in the tensile test.

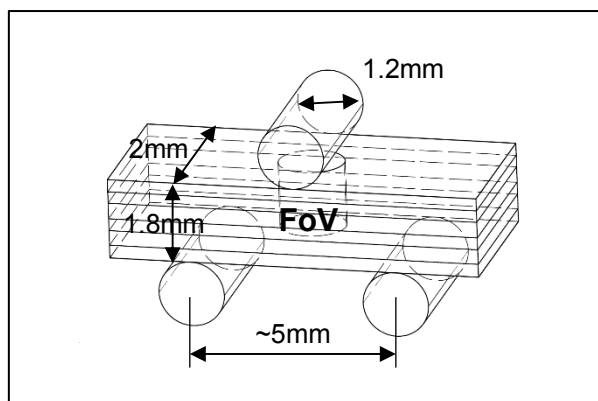


Fig. 5-15: Illustration of general dimensions and in-situ three point bending setup of an unnotched CFRP sample.

The X-ray CT scans in this case were taken at four loading steps. These were based on the expected behaviour of three-point bending and loading data obtained in Fig. 5-4. These steps are:

A – initial scan corresponding to a small fixing load.

B – a first loading increment of approximately 200 N is applied at this step as shown in Fig. 5-16. The specimen was expected to produce visible matrix cracking but no fibre breaks. A combination of compression damage and sliding of the braided fibre tows was observed in this scan (see Fig. 5-17 step-B). The fibre continuity was confirmed by the further load-carrying capacity in the following loading step-C.

C – this step corresponds to the pre-peak bending strength of the specimen. Therefore, this scan was captured before the complete failure. Severe damage was observed at this loading step, including a combination of matrix cracking, dislocations of several fibre tows, fibre breaks and tow ruptures.

D – this scan was taken after the complete failure, characterised with complicated dislocations and fibre tow failures as shown in Fig. 5-17.

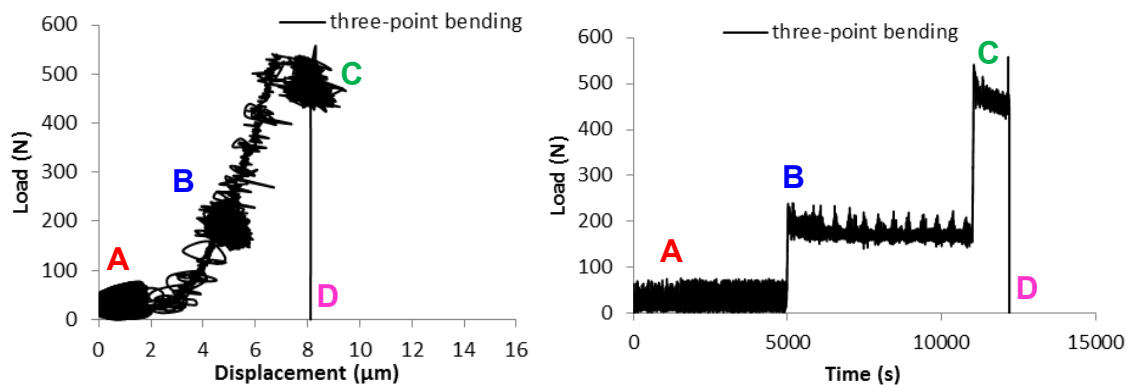


Fig. 5-16: Loading data from three-point bending in-situ test.

Fig. 5-17 shows the images corresponding to the four scanned loading steps. These scans successfully captured the initiation of damage (step-B), the failure mode of the sample (step-C) at the maximum load and the final post-failure condition of the sample (step-D).

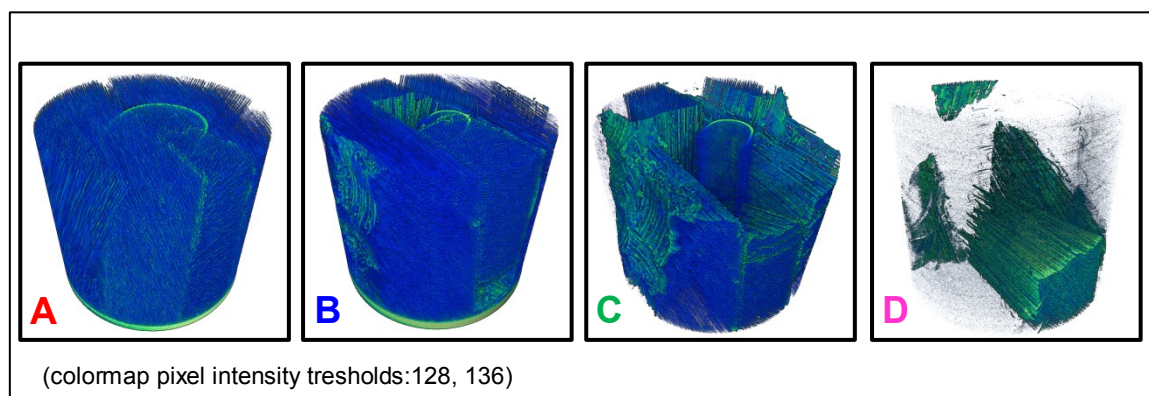


Fig. 5-17: In-situ X-ray CT volume renders of a braided carbon fibre composite under three-point bending test. The images correlate to the loading curves in Fig. 5-16.

Several in-situ X-ray CT volume renders are also shown in Fig. 5-18 to visualize the complicated fracture processes that often featured severe composite cracks and fibre breaks. These could be captured here thanks to the three-point bending setup and the use of a braided fabric sample. As previously suggested, the braided fabric restricted transverse crack propagation and tow sliding effects, which further allowed the rupture of several fibre tows. The fractured fibre tows are clearly seen in Fig. 5-18.

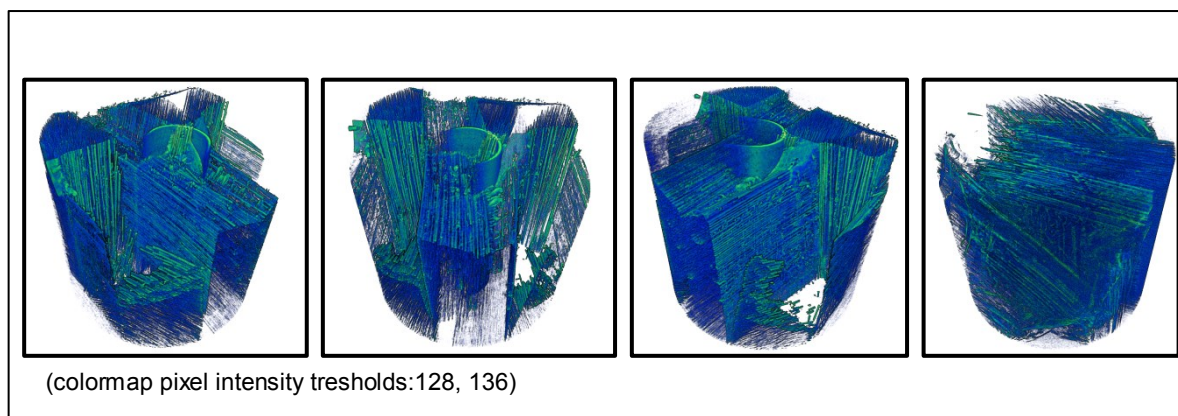


Fig. 5-18: Rotated views of X-ray CT volume renders showing severe damage, fibre breaks and fracture from three-point bending in-situ loading test in braided carbon fibre composites.

Fig. 5-16-b also shows some load-relaxation effects. Fortunately, these effects do not affect the image quality because deformations are small. However, in all the X-ray CT scans there were a number of sources for image distortions including: ring artifacts, pixel noise effects, low phase-contrast, optical blurring and lens induced oversaturation. The lens induced oversaturation can be observed in first three volume renders of Fig. 5-18.

5.9. Summary and conclusions

This chapter has presented the rationale and the strategy of the in-situ synchrotron X-ray CT imaging tests, the development of an innovative micro- loading rig and the test setups for uniaxial tensile and three-point bending tests. The main conclusions are:

- (i) The in-situ experiment was necessary to provide multiscale crack propagation data to check accuracy of the image-based numerical modelling methods, to be developed in CHAPTER 6 and CHAPTER 7 of this thesis.
- (ii) The experiments were carried out at the Diamond-Manchester Imaging Branchline I13-2 at Diamond Light Source. The existing experimental facility required additional developments to enable it to achieve the goal of this research. A key component of the

device is the in-situ micro- loading rig. A new rig was designed by the author and manufactured in the School of Mechanical Aerospace and Civil Engineering, University of Manchester.

- (iii) Using the experimental facilities, two sets of tests on CFRP specimens were carried out, one under tensile loading and another under three-point bending. The recorded imaging datasets show that the experimental facility successfully captured the main features of multiscale crack propagation.
- (iv) Due to time limitation of this PhD project, only the tensile loading case was further used to develop the image-based fibre mesh generation to inform the multiscale modelling method. These two main contributions (i.e. integration of image-based FE models and FE multiscale modelling) are presented in CHAPTER 6 and CHAPTER 7 respectively.

CHAPTER 6. X-RAY CT IMAGE-BASED MODEL GENERATION OF CARBON FIBRE REINFORCED POLYMER COMPOSITES

6.1. Introduction

This chapter develops a numerical algorithm for the generation of image-based models in carbon fibre composites at fibre scale. The algorithm is needed to convert X-ray CT datasets captured with large field of view (FoV) that contain a large number of fibres. Due to the large number of fibres it is not possible to accurately resolve the fine details for the many thousands of individual fibres in the reconstructed volume with conventional segmentation routines. The reconstruction approach in this chapter is based on a combined approach that identifies the fibre centres first using a local maxima method and tracks these centres from slice to slice using a Bayesian inference model. The slices are arranged in stacks with reduced widths that are overlapped to ensure 3D fibre continuity. A major advantage of the Bayesian approach is that it facilitates the identification of fibres that would otherwise be segmented as discontinuous or dislocated fibres with low computational effort. It is shown that the proposed method is able to provide quality fibre centrelines (skeletons) from an X-ray CT scan of a CFRP multidirectional laminate sample. The fibre centrelines are then used to reconstruct the 3D geometry to generate partitioned meshes for multiscale damage evolution modelling. The approach is illustrated for a multidirectional fibre orientation region that contains different orientation plies [+45/90/-45/0].

6.2. Imaging and high-fidelity modelling challenges

One of the current limitations of X-ray CT is that the imaged volumes are often limited to very small regions. This means that the model can be insufficiently informed at the constituent length-scale and may not capture the external support boundaries. Stitching together of multiple images to increase the size of high resolution images has been examined (Kyrielleis et al., 2009)

and has recently been applied for 3D woven composites (Yu et al., 2015a). This method comes with additional experimental and numerical post-processing costs due to the multiple images that must be acquired and the larger image reconstructions.

An improved understanding of the multiscale mechanical behaviour of composite materials can be obtained through detailed numerical modelling of damage evolution. Traditionally such approaches have relied on simplistic unit cells or representative volume elements (RVE) approaches that often cannot accurately capture manufacturing artefacts (variations in fibre alignment, touching fibres etc.) or entrained defects (fibre-free matrix regions, pores, delamination etc.). This can only be done by using larger more faithful microstructural models. One way of obtaining such models is to use the X-ray CT to capture 3D microstructure images as the basis for faithful numerical modelling. Such image-based modelling has become very popular in recent years (Maire and Withers, 2013) but is still very rare for cross-ply composites or 3D woven composites.

6.3. Overview of existing segmentation models

The approaches for generation of FE models from X-ray CT images can be categorised into two classes: (i) direct voxel (or pixel) to mesh mapping and (ii) phasic segmentation based meshing. In the first class, each voxel or pixel in the image is directly transformed into a finite element, and the resultant sharp bi-material interfaces in the mesh can be further smoothed. The material constituents are distinguished based on their respective grayscale intensity values. Such approaches are widely reported, e.g., the direct voxel mapping methods (Requena et al., 2009; Ren et al., 2015), the discrete Fourier transform approach (Hamad et al., 2012; Landi et al., 2010), and the enhanced volumetric marching cubes (Young et al., 2008). A problem of these approaches is that automatic meshing algorithms are difficult to apply and the element sizes are usually too uniform. In the second class of approaches, the X-ray CT image is

segmented into different constituent phases based on the grayscale value thresholds for each phase. The bi-material interfaces or boundaries can be naturally identified and smoothed if necessary. Examples for fibre reinforced composites include the combined segmentation and voxel-based fibre tracking algorithm (Yang and Lindquist, 2000), the simplified marching cubes method (Coindreau et al., 2011; Vignoles et al., 2011; Coindreau et al., 2003), the fibre contacts and orientation method (Viguié et al., 2013; Latil et al., 2011) and the intersecting fibre cluster method (Soltani et al., 2014). The main advantage of direct segmentation for fibre composites is that various 3D skeletonisation algorithms can be applied to extract fibre centrelines (Viguié et al., 2013; Soltani et al., 2014) after segmentation, so that the fibres can be modelled as exact cylinders. Another advantage of these approaches is that the segmented image can be automatically meshed with flexible control so that dense meshes can be used in stress concentration areas such as bi-material interfaces.

However, most of the above-mentioned approaches are difficult to implement for fibre reinforced composites with highly congested fibres and/or touching fibres, before the numerical models can be built. The difficulties include finding exact segmentation boundaries, nonlinear fibre tracking due to the inherent X-ray CT noise and fibre discontinuities, and high computational cost due to very large X-ray CT datasets. The low image contrast between the polymer matrix and the thin fibres ($\sim 5.2 \mu\text{m}$) may also lead to FE models with inaccurate material interfaces. New reconstruction methods with advanced image filtering and stack conditioners have thus been developed for feature tracking and noise reduction. For example, Czabaj and co-workers developed a template matching (TM) algorithm to determine the fibre centre points for X-ray CT images of unidirectional carbon fibre reinforced polymers (CFRP) (Czabaj et al., 2014; Whitacre and Czabaj, 2015). The fibre centre points are then converted into higher-order splines followed by sweeping non-overlapping 3D volumes along each spline. However, the method has not been tested on multidirectional fibre ply volumes.

This chapter aims at building high-fidelity micro-scale image-based FE models for 3D, cross-ply, multidirectional woven fibre reinforced composites by developing a new set of reconstruction algorithms to resolve some of the above issues. The images of a CFRP cylinder with $[+45/90/-45/0]$ fibre orientation sequence are captured by fast synchrotron X-ray CT scanning with a voxel resolution of 330 nm. The images are then analysed in the commercial software Avizo and segmented in the open-source code ImageJ (ImageJ). FE models are finally built in ABAQUS.

6.4. X-ray CT dataset for reconstruction and modelling

The datasets consist of stacks of 2160 slices each comprising 2560×2560 pixels. The FoV volume size is therefore approximately $712 \mu\text{m}(\text{height}) \times 840 \mu\text{m}(\text{diameter})$. Fig. 6-1 shows the rendered FoV in the software Avizo (FEI/Avizo) using the volrenGreen tool. It contains 11954 fibres in total.

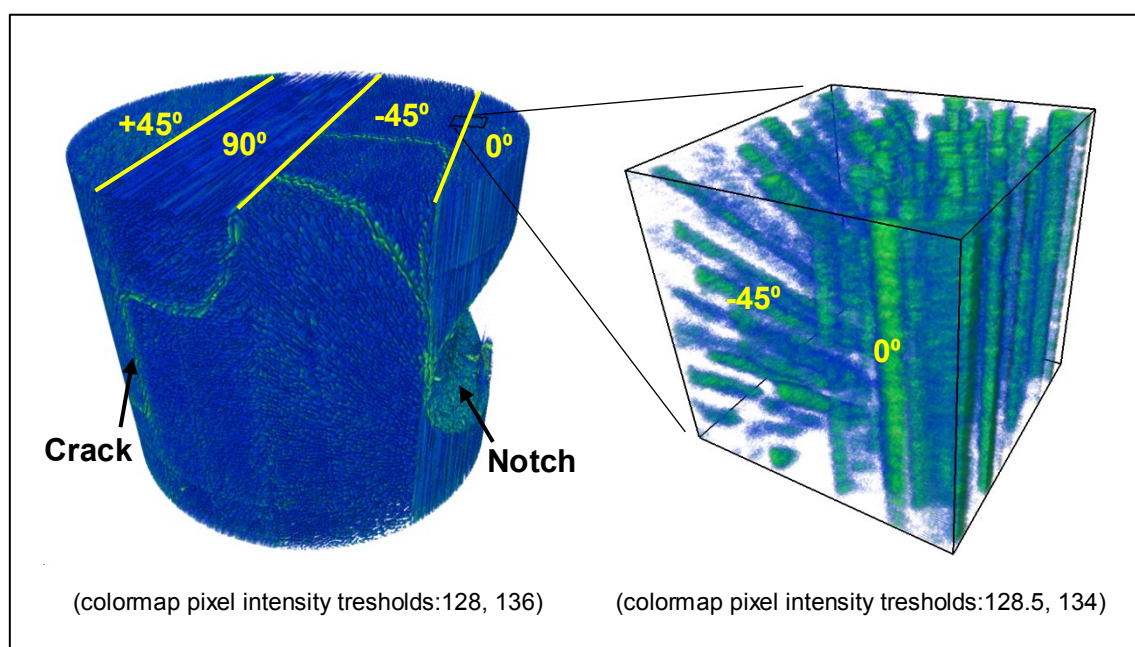


Fig. 6-1: An in-situ X-ray CT volume render of the multidirectional CFRP sample under tension.

6.5. Image-based model generation

Fig. 6-2 shows the main steps to extract the CFRP material geometry from X-ray CT image slices. The method converts grayscale images to geometrical models. Two numerical strategies to obtain continuous fibre centrelines will be discussed in Sections 6.5.5 and 6.5.6 respectively. Firstly, effective filters were identified and applied to the stack of X-ray CT images to remove noises and facilitate fibre identification. The 3D dataset was then delineated into plies according to fibre orientations. The fibre centres were then identified using the ultimate eroding point approach. Image binarisation was also tried using the traditional watershed splitting and skeletonisation techniques. The conventional approaches presented in Section 6.5.5 failed to obtain continuous fibre centrelines. Therefore, a new algorithm for fibre tracking with two steps using stack conditioning incorporating a Bayesian inference was developed. The obtained fibre centrelines were finally processed with consideration to manufacturing practice of CFRP, before they are used to generate FE models in ABAQUS assuming a constant fibre diameter.

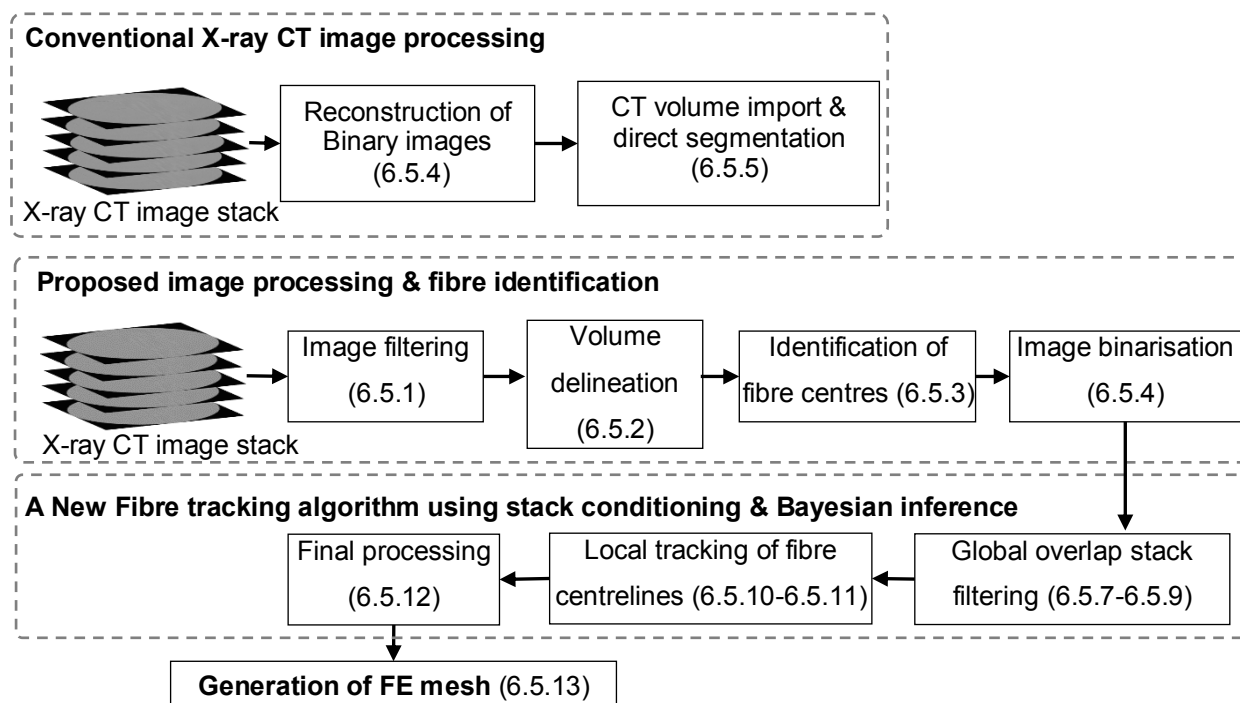


Fig. 6-2: Illustration of image-based model extraction framework from X-ray CT images to FE meshes.

6.5.1. Images filtering and pre-processing

Fig. 6-3 shows that due to the presence of cracks and damage some pixel oversaturation was observed near the crack surfaces. In addition, from a segmentation viewpoint, the X-ray CT image slices exhibit poor phase-contrast and too few pixels per individual fibre domain. The commonly used filtering operations use fixed stencil and gradient based kernels. They often fail to enhance the detectability and shape of congested fibres. Many combined filters including those in Table 6-1 were tried and evaluated. They were implemented using the JavaScript library in the open source package ImageJ. None of the filters in Table 6-1, namely the *Filter-A* to *Filter-D* alone were found sufficient for the purpose of direct segmentation of the X-ray CT datasets.

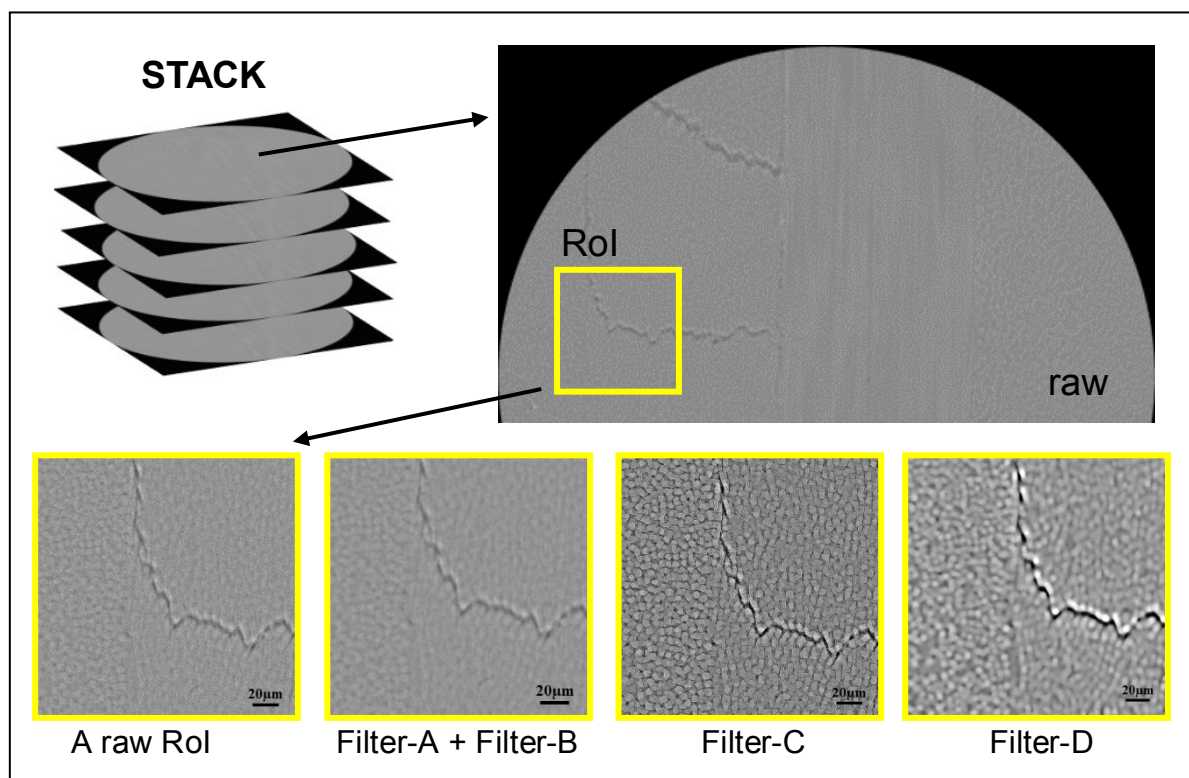


Fig. 6-3: De-noising of raw X-ray CT image stack using three different filter combinations explained in Table 6-1.

Table 6-1: Image filters for X-ray CT datasets.

Reference	Image Filter Combinations & Order	Intended use
<i>Filter-A</i>	Mean 2 pixels – Smooth	De-noising, intensity smoothening.
<i>Filter -B</i>	Mean 2 pixels– Mean 2 pixels – Smooth – Unsharp mask (radius: 7 pixels, mask weight: 0.2)	Phase contrast, Edge enhancing, Interface threshold.
<i>Filter-C</i>	Smooth – Mean 2 pixels – Min maxima & region growth 2.5 pixels – Max maxima & region growth 3 pixels	Pragmatic fibre centreline search.
<i>Filter-D</i>	Smooth – Median 7 pixels – Min maxima 3 pixels - Max maxima 2.5 pixels – Unsharp mask (radius: 7 pixels, mask weight: 0.2), Enhance contrast (saturated pixels: 0.01% & normalisation)	High fidelity fibre centres & fibre identification.
<i>Filter-E</i>	Smooth – Mean 2 pixels – Kernel convolution – Max maxima 2.5 pixels – local maxima search for fibre identification.	Fidelity fibre centroids & Fast processing.

The identified image filter strategy with best effect was a combination of a series of filters (*Filter-E* in Table 6-1). A fixed size kernel convolves all the pixels contained within the image slices. The convolution uses a continuous stencil pattern (pixel-wise) and the new images are obtained through multiplication and weight summation of the 2D matrices overlaid as demonstrated by Eq. 6-1:

$$conv(f, k) = f_{xy} \otimes k_{xy} = \sum_{e_w = -\frac{w}{2}}^{\frac{w}{2}} \sum_{e_h = -\frac{h}{2}}^{\frac{h}{2}} f[x + e_w][y + e_h] * k_{xy}[w/2 - e_w][h/2 - e_h] \quad \text{Eq. 6-1}$$

where f_{xy} are the pixel intensities from the image overlay and k_{xy} is the processing kernel of size $[(w+1) \times (h+1)]$ with the square size kernel property $w=h$. This approach has been widely used in the image processing, especially for edge detection and target tracking (Wu et al., 2013; Wang et al., 2015a). Typically, 2D convolution operations have been implemented using vector operations such as the one-dimensional convolution approach. In particular, Habibi et al. (Habibi et al., 2014) describe a decomposition strategy using two consecutive vertical and horizontal convolution steps for a 3×3 kernel size. Instead, in this study the size of kernel and convolution factors were semi-empirically estimated based on Eq. 6-2 that represents the general probability density kernel (Epanechnikov, 1969). This was fitted iteratively by trial and error adjusting the sample values x_i .

$$k_{xy} = k_e(x) = \frac{1}{nh} \sum_{i=1}^n k_s \left(\frac{x - x_i}{h} \right), \quad -\infty < x < \infty. \quad \text{Eq. 6-2}$$

where n is the kernel size, k_s is the kernel smoothing function and h is the bandwidth ($h=1$). A similar model can be found in (Comte and Genon-Catalot, 2012). Fig. 6-4 shows the parametric estimation of the convolution factors based on few most popular smoothing functions used in Eq. 6-2.

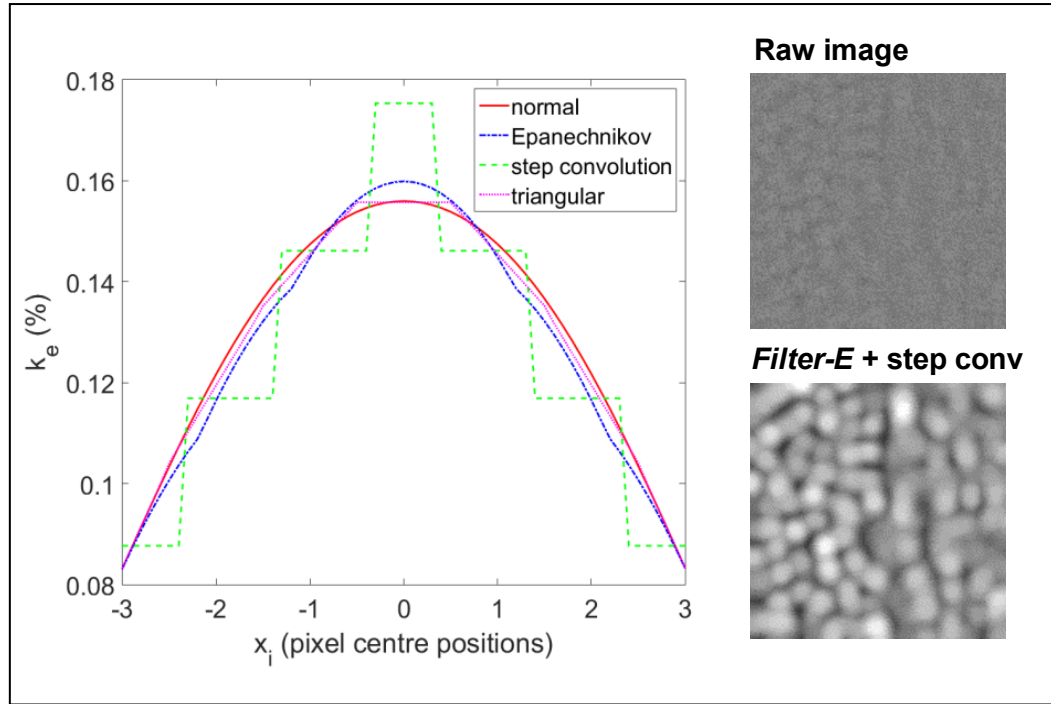


Fig. 6-4: Estimation of the convolution factors based on different smoothing functions; the insets typify the effect of the combined filter *Filter-E* and convolution using the step function estimates at the boundary between 0° to -45° plies.

The step function k_e illustrated in Fig. 6-4 is used to estimate the convolution factors k_{xy} in Eq. 6-1. Once the 2D convolution kernel k_{xy} is established, all the X-ray CT slices are processed according to the volume delineation strategy in Section 6.5.2. In this case, because the average fibre diameter is $5.2 \mu\text{m}$ and due to high fibre congestion in the X-ray CT datasets, the size of the convolution and local filtering kernels in Eq. 6-1 and Eq. 6-2 were set at 5×5 pixels. Therefore, the convolution factors are collected from step function range $(-2, 2)$ in Fig. 6-4.

6.5.2. Volume delineation of different plies

Prior to the fibre identification and further reconstruction steps it is necessary to split the X-ray CT volume into plies. This step removes the composite plies that are not transverse to the fibres prior the image processing and fibre identification steps. The delineation of the plies can be also situated after the image processing, but prior to the fibre identification. The delineation was organised as a RoI parameter tool to fit variable volume extractions from the 3D stack. These volumes are based on a changing polygon algorithm with linear pitch between the corresponding extraction corner points. The corner points in this case belong to the margin slices (first and last slices of the X-ray CT dataset).

Due to the transverse eroding basin approach that ultimately leads to a single point identification (Ferreira and Rasband, 2011), the current reconstruction method requires transverse scans with fibre orientations $< 50^\circ$. Consequently, the X-ray CT image was separated into two sub-domains, one with fibres oriented at $< 50^\circ$ (the 0° , $\pm 45^\circ$ plies in Fig. 6-5-a) and the other with fibres $> 50^\circ$ (the 90° ply illustration in Fig. 6-5-b). The former was analysed using the *Filter-E* in the X - Z plane and the other in the X - Y plane. The two reconstructed datasets were then combined to form a single volume geometry (illustrated in Fig. 6-5-f).

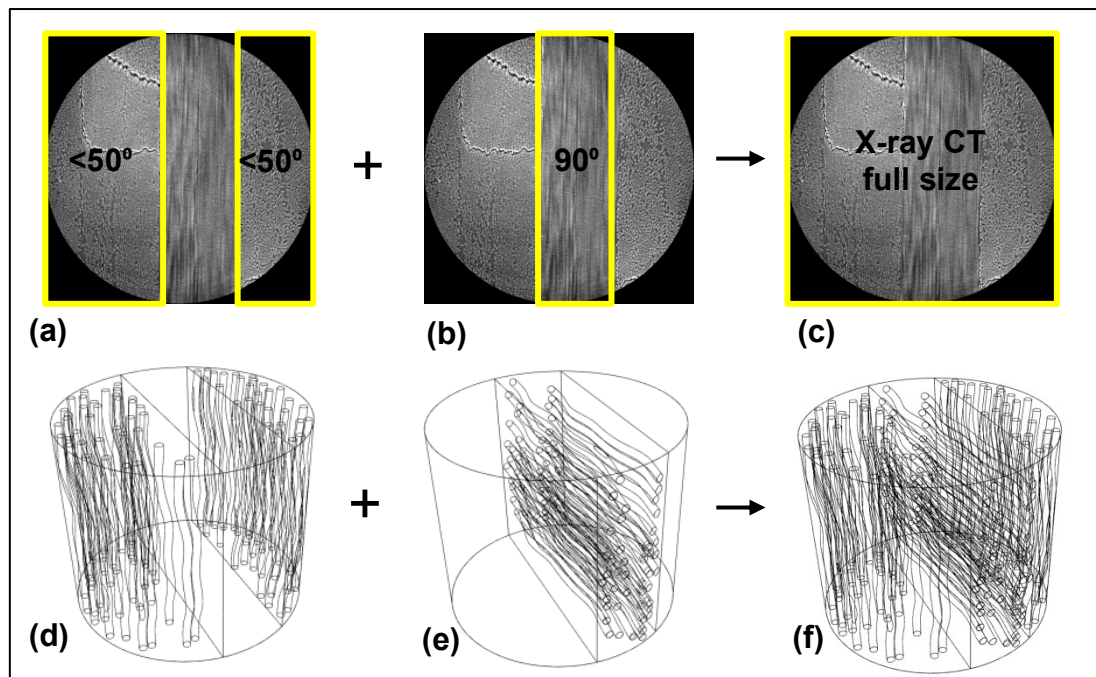


Fig. 6-5: Illustration of the volume delineation tool used to delineate X-ray CT datasets based on fibre orientations (a,b,c). The schematic volume re-composition (f) is shown after combining the two orthonormal volumes (d,e).

For convenience, the image filtering and fibre identification procedure in the following sections are applied to delineated image slices that are transverse to the fibre direction. Other more complicated material architectures containing ply orientations beyond the 50° angle orientation limit in Fig. 6-5 were not contained in the current dataset. However, to solve this, two further routes may be applied as follows: (1) reconstruction of transverse image masks based on inclined volume cuts and (2) combined 3D segmentation to evaluate the fibre inclination angle a priori.

6.5.3. Fibre identification algorithm

To identify the fibre centres, the well-established local maxima finding algorithm in ImageJ, based on an ultimate eroding point (*UEP*) approach (Ferreira and Rasband, 2011), was applied. The *UEPs* were obtained using a procedure combining watershed delimitation basins and eroding Euclidean maps. The algorithm is able to retrieve the fibre centre points from the 0.33

μm image resolution datasets in this study with relatively low error, as can be seen from the tortuosity of fibre volumes shown in Fig. 6-6-a and b.

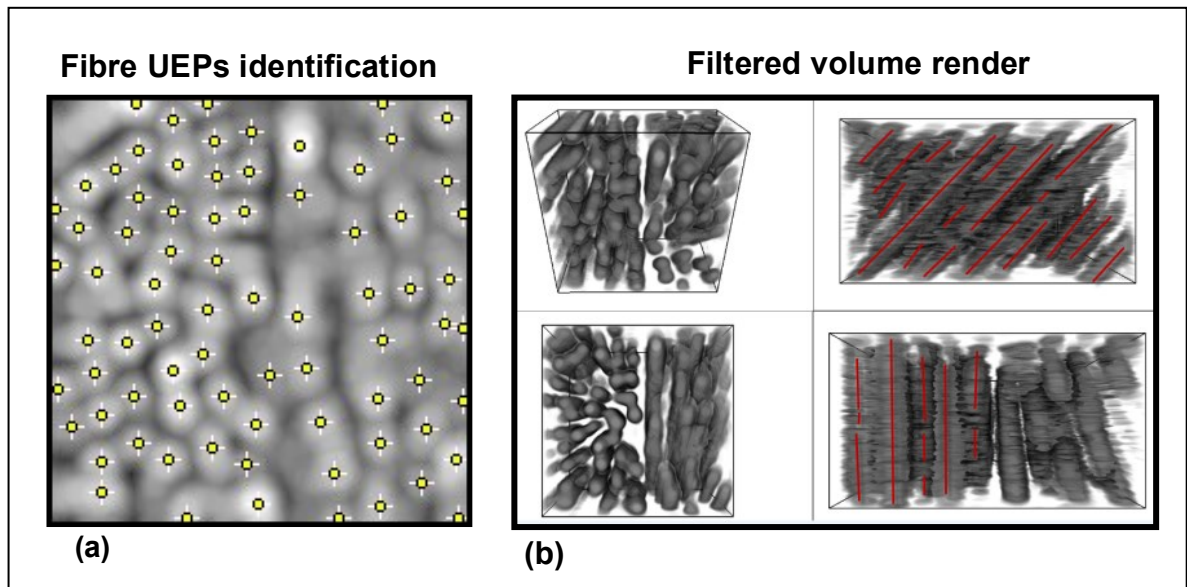


Fig. 6-6: Identification of the fibre centroids after applying *Filter-E* and image convolution. The RoI was taken at the $0^\circ/-45^\circ$ ply boundary illustrating: (a) the fibre *UEPs* identification and (b) corresponding filtered volume render. Discontinuities are most significant in the inclined ply as shown with solid red lines.

Fig. 6-6-b shows that multiple fibre discontinuities still arise due to the misidentification of local fibre *UEPs*. This can be attributed to the highly-congested areas which make the identification of separate Euclidean maps difficult. This artifact was most evident when inclined ply regions were processed. The discontinuity problem was tackled using a stack overlapping procedure as discussed in Section 6.5.6. As explained in this section, the overlapping procedure also minimises noise fibre identifications.

6.5.4. Image binarisation

Further to the image filtering and the identification of *UEPs* in previous sections (6.5.1 and 6.5.3), the 2D image slices were converted into binary images by growing uniform intensity fibre domains of equal diameters centred on the *UEPs*. The well-known water basins approach

was used to separate touching fibres when necessary. A volume render based on the binary image slices is shown in Fig. 6-6-b, from which either direct segmentation or skeletonisation to retrieve the fibre centrelines by volume shrinking can be carried out. However, it was found that this reconstruction method was not only computationally expensive due to the large number of fibres, it could also result in imprecise boundaries and discontinuous fibres in volume renders (see Fig. 6-8-b).

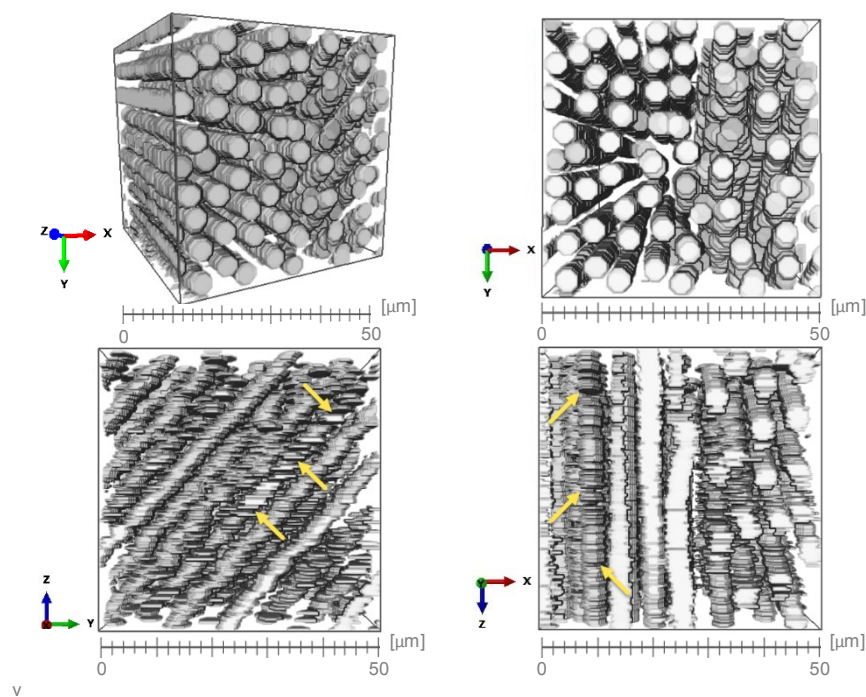


Fig. 6-7: Fibre tracking from binary images in a RoI at the $0^\circ/-45^\circ$ ply boundary (the fibre discontinuities are highlighted using yellow arrows).

6.5.5. Hybrid reconstruction using binary images

To explore the possibility of skeletonisation methods that also retrieve 3D fibre centrelines, a volume segmentation attempt was first carried out. This step is applied after a combined image processing to binary conversion algorithm. The image filter before binarisation in this case is the same *Filter-E* in Table 6-1. The conversion of filtered slices into binary images is done by growing uniform intensity fibre domains of equal diameters centred on the identification *UEPs*

discussed in the paper. If the reconstructed binary images contain touching fibres, they are separated based on the well-known water basins approach. An example of binary reconstructed images and corresponding volume from the *UEP* approach is shown in Fig. 6-8-b.

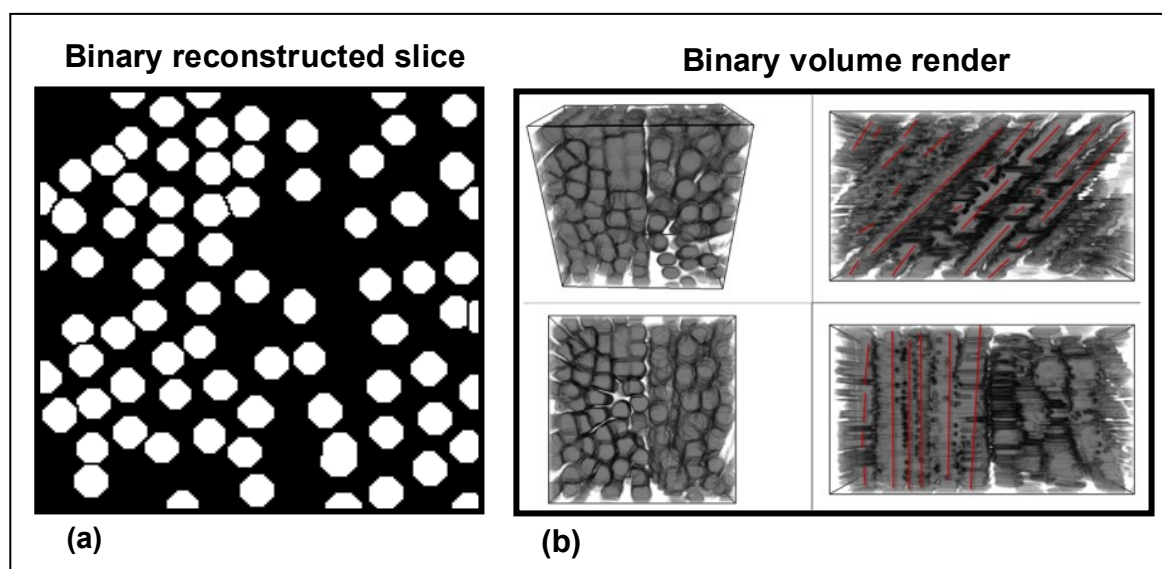


Fig. 6-8: Illustration of fibre centroid identification from binary slices. The RoI was taken at the $0^\circ / -45^\circ$ ply boundary same position as in Fig. 6-6 boundary illustrating: (a) a binary reconstructed slice and (b) the corresponding binary dataset volume render. Discontinuities are most significant in the inclined ply as shown with solid red lines.

Following this procedure, the binary images were used for volume segmentation and labelling. When the discontinuity problem will be resolved, this strategy could open two further routes, namely: (1) direct export of the volume model (e.g. into mesh generation packages) and (2) skeletonisation to retrieve the fibre centrelines by volume shrinking. However, it was found that the hybrid reconstruction method was also computationally expensive due to the very large number of fibres and discontinuities contained within the CFRP dataset. It also led to imprecise segmented boundaries in 3D (see Fig. 6-8-b). As a result, the fibre centrelines could not be distinguished and their continuity within the 3D stack could not be ensured. Therefore, a more sophisticated reconstruction method based on stack conditioning and local to global fibre

tracking was necessary. This method is based on a Bayesian inference model presented in Section 6.5.6.

6.5.6. New fibre tracking algorithm with stack conditioning

After the fibre *UEP* identification, the fibre centrelines are tracked using a stack reduction algorithm that reduces the computational overload. In (Czabaj et al., 2014), the fibre tracking algorithm was based on a Kalman filter with two main steps: a predictor and a corrector step. A linear extrapolation of the fibre centre points is used in the predictor step. This is followed by the correction step that minimises local mean square error based on the adjacent slices. However, this algorithm follows a bottom-up approach and may not capture the continuity of inclined fibres if certain number of fibre centroids is misidentified over the stack and further noise presence.

To acquire more continuous fibre centrelines with lower computational cost than the conventional image processing techniques tried and discussed above, a new fibre tracking algorithm has been developed. It consists of two steps: a global stack overlap filtering and a local fibre centreline tracking, both employing a Bayesian inference algorithm, as explained below.

In the global stack conditioning, an overlapping discretisation of the continuous slices is used to find the best matching slices. This step is necessary to test the continuity of fibres and transpose data in best possible filtered stack. The step is discussed in details in Sections 6.5.7 to 6.5.9. The local tracking step then searches only within the filtered slices for the individual fibre coordinate datasets using a local updating approach as discussed in Sections 6.5.10 and 6.5.11. This strategy is used to track fibres in 3D and ensure the continuity across fibre oriented domains. Therefore, to capture the fibre composite geometry, these two main steps are necessary because the material contains long, continuous, curvilinear and inclined fibres.

6.5.7. Global overlapping stack filtering

After the identification of fibre centre points equivalent to *UEPs* and the image binarisation, an overlapping discretisation of the continuous slices was conducted to find the best matching slices. This step is necessary to test continuity of the fibres and to transpose data in the best possible filtered stack. It can also lower the computational cost compared with tracking fibres in 3D within the full stack.

The idea of stack overlap filtering is illustrated in Fig. 6-9. The total stack domain D comprises 2160 CT image slices. The images within the kernel stack domain d are iteratively correlated in pairs covering all combinations with respect to the stack centre. A first global filter can be then applied according to the degree of matching between all image pairs.

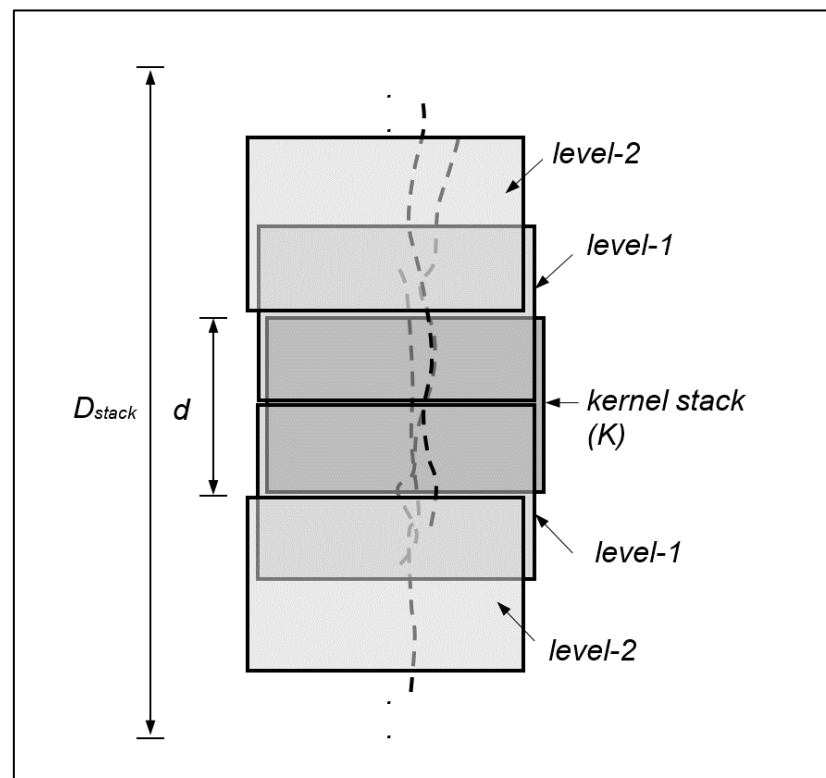


Fig. 6-9: Bayesian inference domains for fibre tracking applications with kernel stack domain d and stack overlap $d/2$.

6.5.8. Estimation of image matching and fibre shifts

Two main parameters can be used as initial estimates in further reconstruction algorithm steps. In general, the covariance of two images f and g or slice to slice using a typical pixel block searching strategy is:

$$\text{cov}(f, g) = E \left[(f(x, y) - \bar{f})(g(x+i, y+j) - \bar{g})^T \right] \quad \text{Eq. 6-3}$$

where \bar{f} and \bar{g} are the average pixel intensity values of the images and i and j are the integer image shift. The mathematical expectation of pixel intensity of an image with $m \times n$ pixels is

$$E(f - \bar{f}) = \sum_{m,n} [f(x, y) - \bar{f}] \quad \text{Eq. 6-4}$$

Note that the variance of a reference image f can be generally written as:

$$\text{cov}(f, f) = E(f - \bar{f})^2 = \sigma^2(f) \quad \text{Eq. 6-5}$$

The total variation index can be calculated by the Normalised Correlation Coefficient (NCC):

$$C_{NCC} = \text{corr}(f, g) = \frac{\text{cov}(f, g)}{\sqrt{(E(f, \bar{f})^2 E(g, \bar{g})^2)}} \quad \text{Eq. 6-6}$$

The NCC index measures the degree of similarity and ranges between 0 and 1. Furthermore, a global integer shift can be obtained by maximising the NCC index. Similarly, by maximising the NCC index a local integer fibre shift can be found by using smaller image masks. If needed, a sub-pixel shift can be then found by applying the local quadratic fitting around the peak value $(\Delta x, \Delta y)$ of the correlation results:

$$\delta x = \frac{\text{corr}(\Delta x - 1, \Delta y) - \text{corr}(\Delta x + 1, \Delta y)}{2[\text{corr}(\Delta x - 1, \Delta y) + \text{corr}(\Delta x + 1, \Delta y) - 2\text{corr}(\Delta x, \Delta y)]} \quad \text{Eq. 6-7}$$

$$\delta y = \frac{corr(\Delta x, \Delta y - 1) - corr(\Delta x, \Delta y + 1)}{2[corr(\Delta x, \Delta y - 1) + corr(\Delta x, \Delta y + 1) - 2corr(\Delta x, \Delta y)]}$$

where δx and δy range between -0.5 and +0.5 pixels. For completeness, the total image shift can be estimated by the summation of results in Eq. 6-7 to a simple integer estimate based on subset searching by the maximising criterion in Eq. 6-6. This becomes useful mainly to estimate the total metric threshold for fibre tracking when inclined angle plies are contained within the reconstruction dataset. Herein, the estimated threshold is further used with the local Bayesian inference model to track the individual fibres (see Sections 6.5.10 and 6.5.11).

6.5.9. Global Bayesian inference model for optimal kernel width

To reduce the large number of slices from an X-ray CT dataset, the slices within a kernel are correlated in pairs with respect to the overlapping stack centre. The filtered slices can be selected by maximising the *NCC* index over each kernel domains (meaning the selected slice contains most similar pixel patterns out of the total number of pairs). Instead of using pixels, the slices can be simplified to separate sets of independent fibre *UEPs*. Therefore, the filter iterates over a prescribed number of half overlapping kernel stacks as shown in Fig. 6-9. The overlapping stacks were thus divided in two equal subdomains ($K_d = \mathbf{K} + \mathbf{N}$). For all slices contained in half of a kernel stack (\mathbf{K}), the prior probability field $P(\mathbf{K})$ was defined as the total number of *UEPs* contained within the slice \mathbf{K} . The neighbouring slices in \mathbf{N} were also defined in a similar manner via prior probability $P(\mathbf{N}|\mathbf{K})$ that contain the corresponding *UEPs*. By iterating over the slices in \mathbf{K} , the slice *UEP* filtering from similar probabilities $P(\mathbf{K}|\mathbf{N})$ could be found by maximising the following Bayesian equation:

$$P(\mathbf{K}|\mathbf{N}) = \frac{P(\mathbf{N}|\mathbf{K})}{\sum P(\mathbf{N}|\bar{\mathbf{K}})P(\bar{\mathbf{K}})} \cdot P(\mathbf{K}) \quad \text{Eq. 6-8}$$

where $\mathbf{N} = \{n_1, n_2, n_3, \dots, n_k\}$ represent the *UEP* sets from the corresponding slices within half the kernel width (i.e. $k=d/2$). In Eq. 6-8 $\bar{\mathbf{K}}$ denotes the slice that contains the average number of *UEPs* over stack \mathbf{K} . $P(\mathbf{N}|\mathbf{K})$ represents the probability of all slices within kernel K_d .

This method can be applied when the kernel stack is relatively narrow and the overlapping region captures the inclined fibre plies as illustrated in Fig. 6-10. In contrast, the number of correlated fibres is relatively large for the aligned fibre plies as shown by the correlated images in Fig. 6-10-d and e (shown by the left-hand ply points). Because the method correlates all slices within a given stack width, the fibres that do not cross this full-width are not detected.

To solve this problem, the method was calibrated using a sensitivity study as explained below. Results in Fig. 6-10 indicate that a kernel width of 8 slices can be used that reduces the computational stack 4 times.

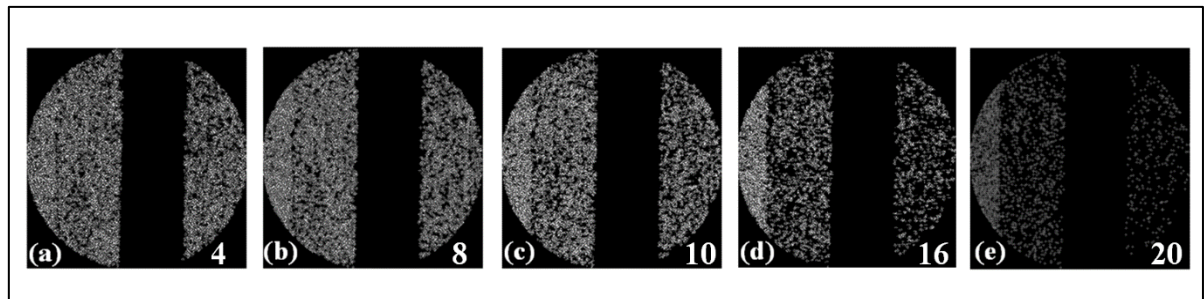


Fig. 6-10: Sensitivity of fibre tracking *UEPs* with different Bayesian overlapped stack widths, using the parameters in Table 2.

In order to capture fibre continuity, the kernel width d should be sufficiently large to avoid misidentified *UEP* centres, while same width should also be reasonably small to reduce the computational time. The optimal kernel width is determined by inspection of fibre discontinuity visually in the volume render in Avizo, for example Fig. 6-6. In this study, it was found that the method could be applied to kernel widths equal to approximately half the fibre diameter, namely, 8 voxels, as demonstrated in Fig. 6-10-b and the optimum overlapping distance was found to be 4 slices.

Table 6-2: Bayesian overlapped stack width sensitivity study.

X-ray CT experiment reference:	Kernel width d in number of slices	Overlapping distance in number of slices	Initial number of fibre $UEPs$	Matched number of fibres	Image reference in Fig. 6-10
CFRP-001-MT10456-2 Transverse ortho-1: binary 2pixels	4	2	6198	4847	(a)
	8	4		4497	(b)
	10	5		4267	(c)
	16	8		3017	(d)
	20	10		2029	(e)

6.5.10. Local Bayesian inference model for tracking individual fibres

This local tracking step searches only within the filtered slices for individual fibre coordinates to ensure fibre continuity.

The general Bayesian inference theory was tailored to map the identified fibres in a kernel slice to the globally filtered neighbouring slices as follows:

$$P(K|N) = \frac{P(N|K)}{\sum P(N|\bar{K})P(\bar{K})} \cdot P(K) \quad \text{Eq. 6-9}$$

where N are the *UEP* fibre centres coming from the neighbouring/overlapping domains with unknown probability $P(N|K)$ and K are the *UEPs* from the searching slice, the process being updated from slice to slice. The fibre *UEPs* from kernel slice K here, are seen as events representing the total number of identified fibres in the slice. The probability $P(K|N)$ is therefore stored in a vector defined over a slice that can be also unequal to the neighbouring slice after the global filter due to errors in the identification process (especially in inclined fibre plies).

The denominator $P(N|\bar{K})$ represents a local conditional probability of a perpendicularly projected point that is the degree of belief of each fibre in N to match its projection *UEP* point \bar{K} versus the probability of the same point, i.e. $P(\bar{K})$. However, the denominator in Eq. 3-1 plays a minor role and can be also dropped or used for normalisation and calibration purposes.

The numerator in Eq. 9 is the probability $P(N|K)$ calculated using the asymmetric power law metric in Eq. 6-8, or can be directly limited by a prescribed fibre shift distance. When the power law metric is used to map and threshold the matching fibre coordinates, the probability can be expressed as follows:

$$P(N|K) = xe^p + ye^q \quad \text{Eq. 6-10}$$

where (x, y) are the coordinates of a fibre *UEP* and (p, q) are two arbitrary power law indices with the asymmetric property $(p \neq q; p, q < 1)$. In this case, an initial threshold of 10 pixels is approximated as the equivalent to a maximum inclination angle of approximately 50° . The probability is then substituted back into Eq. 3-1, which is updated iteratively until processing of the filtered stack. Alternatively, a fibre shift distance can also be used. This shift can be estimated by maximising the *NCC* index in Eq. 6-6 or by calculating the distance between each two consecutive fibres. For more accurate geometric estimates, Eq. 6-7 can be used to quantify the fibre shift with sub-pixel precision. In this paper, the threshold distance is 8 pixels, namely, approximately half the fibre diameter.

6.5.11. Calibration of local inference model

The local Bayesian model discussed in Section 6.5.10 is calibrated using a series of restrictive fibre shift trials. These were implemented by an inverse exponential fitting to find the adaptive threshold coefficients using the power law in Eq. 6-10. Fig. 6-11 shows two such cases used to estimate the threshold values based on the two corresponding shifted probability distributions.

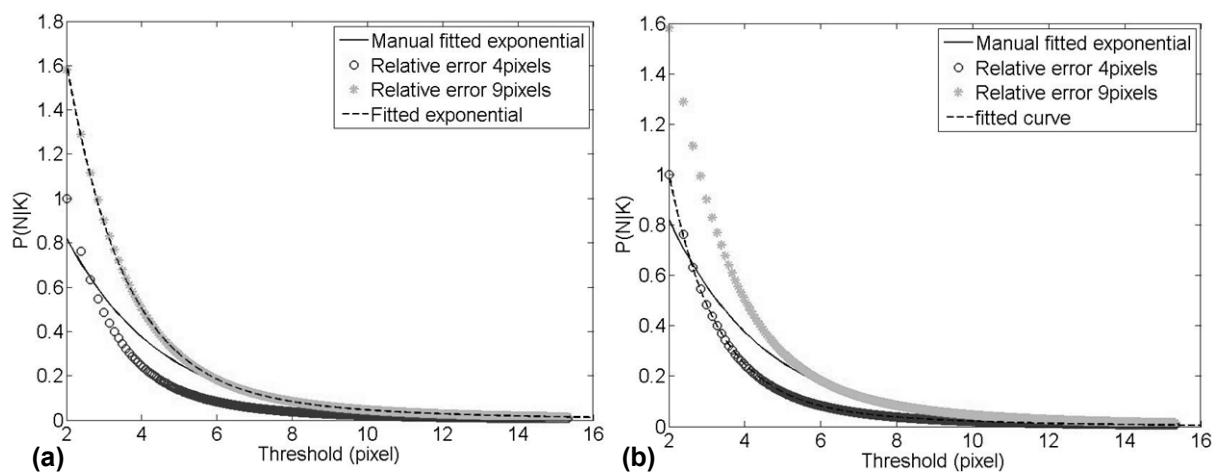


Fig. 6-11: Calibration of the local Bayesian tracking approach using Eq. 6-10 by inverse fitting for: (a) tolerant fibre shifts equivalent to less than 9 pixels and (b) restrictive fibre shifts to less than 4 pixels (the power law factors are: $p=0.2$, $q=0.3$).

In summary, the advantage of the fibre tracking algorithm using stack conditioning presented in this section is that the applied filters can identify the fibres within individual slices by cutting the local minimum and maxima intensities until a suitable eroding radius kernel localises the fibre centre. After the fibre centre identification in each slice and further corrections to ensure 3D continuity, the fibre centrelines can be reconstructed using a constant fibre cross-section. The volume can then be re-imported into rendering and analysis packages for further data analyses and inspections. The reconstructive geometry of fibres of the small region in Fig. 6-1-b is shown in Fig. 6-12. It can be seen that the fibres are now clearly defined.

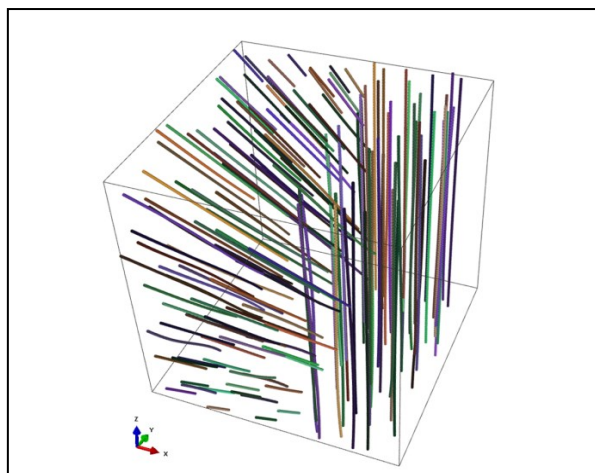


Fig. 6-12: Reconstructed fibre centrelines of Fig. 6-1-b.

6.5.12. Reconstructed data filtering before final mesh generation

In the final reconstruction step, a series of filters are added. These data filtering operations aim at rendering the realistic reconstruction data.

The first filter after fibre tracking is done, is the deletion of some of the fibres. These fibres may be deleted from the final geometry if their length is unfeasibly small, i.e. less than fibre diameter size.

The second filter is a duplicate removal and coordinate averaging filter. This filter identifies where multiple *UEPs* correspond to same fibre over the same slice, averages their coordinates and replaces the multiple *UEP* coordinates with a final centre point coordinates.

The third filter allows fibres to split into several segmented fibres. The fibre splitting option separates interrupted fibres that may be present in the dataset. This option is important due to two main reasons: presence of a notch or other physical discontinuity in the reconstructed dataset and realistic interrupted fibres that come from manufacturing. Such interrupted fibres arising from manufacturing process can still be aligned with each other ends along same 2D projected coordinate locus, but different volume heights. However, the splitting of fibres was set to a minimum distance of 50 μm . Therefore, whenever the minimum distance that lies

between two consecutive centre identifications is found, the existing fibre splits in two. This is possible by simply tracking the fibre centres after height coordinates in the stack direction and comparing the first order derivative using shifted dummy vector containing same coordinate values.

Finally, the inclined fibres are tracked in two modes, namely forward and reverse. The forward mode means that the procedure follows the filtered slice to slice approach, starting with first slice up to the last slice, while the reverse mode repeats same operations starting from last slice up to the first slice. This is necessary in order to capture the 45° inclination fibres contained in the present case study and should be tuned accordingly to other X-ray CT datasets containing new geometrical features. The final reconstructed fibre centrelines are combined from the two modes by removing any duplicate fibres. In this case the duplicate centrelines are easily removed based on their overlapping over the aligned fibre plies at 0° .

6.5.13. Geometry reconstruction and mesh generation

The reconstructed fibre centrelines in each ply are then integrated into a single domain of FoV as shown in Fig. 6-13, followed by image-based mesh generation. The fibre centrelines are modelled by third-order splines.

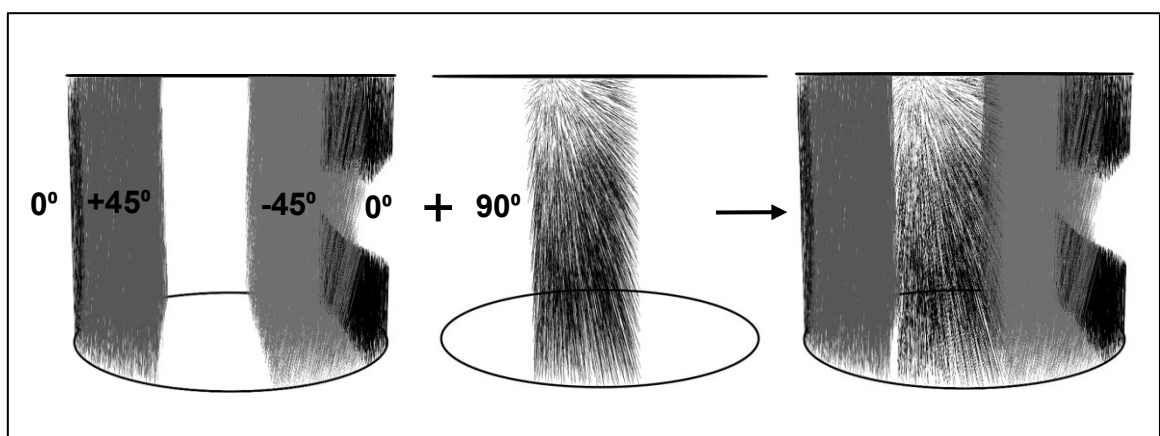


Fig. 6-13: Full size X-ray CT reconstructed fibre centrelines.

It is known that the FE mesh size for accurate modelling of composite materials should be at least one order of magnitude lower than the size of the inclusions or reinforcements (Sencu et al., 2015). The free meshing capability in ABAQUS offers full user flexibility in terms of element types, integration order and model size. However, an extracted cube model of smaller size equal to $100\text{ }\mu\text{m}$ was converted into a FE mesh shown in Fig. 6-14-a. The mesh model has an element size of $\sim 1.0\text{ }\mu\text{m}$ (note that the fibre diameter is $5.2\text{ }\mu\text{m}$) and was generated in approximately 2 minutes. The model contains 149 number of fibres shown in Fig. 14-b. In total, the FE mesh contains about 4 million of C3D4 elements.

Therefore, due to the large FoV domain ($712\text{ }\mu\text{m}$ height \times $840\text{ }\mu\text{m}$ diameter) containing 11954 fibres, converting the full geometry will lead to a gigantic number (over 10 billions) of finite elements that even supercomputers may struggle to model. This makes multiscale modelling a must.

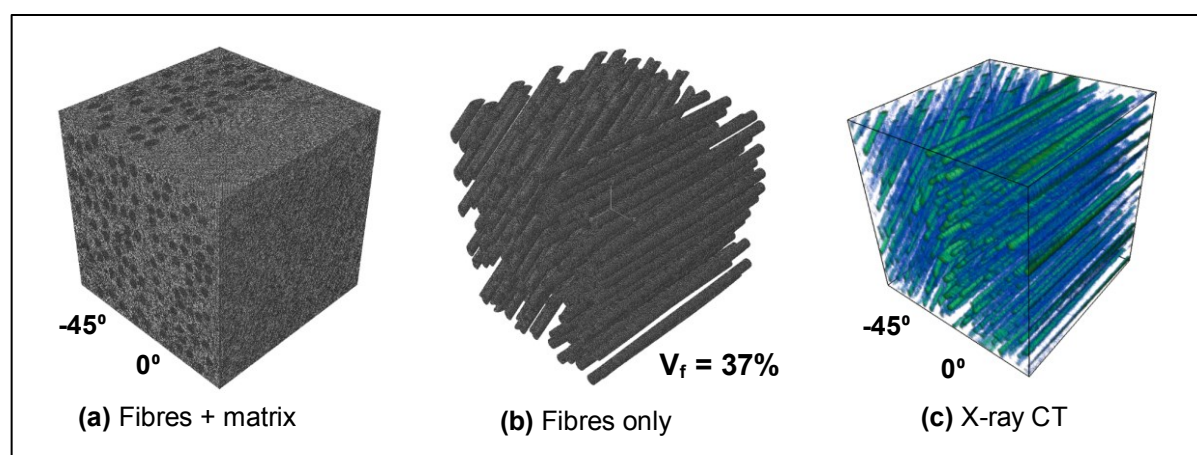


Fig. 6-14: X-ray CT image-based FE model with reconstructed fibre volume fraction $V_f = 37\%$.

Table 6-3 gives two other examples of partition grids that can be used to generate such meso-scale FE mesh models. The meso-scale models are smaller than thickness of composite plies. The output from this chapter will be used in CHAPTER 7 towards development and validation of new anisotropic macro-scale elements.

Table 6-3: An overlapped partition strategy to extract image-based fibre meshes for multiscale modelling.

X-ray CT experiment reference:	Non-overlapped extraction grid	Size of overlapping MeE model (increased to double the size of extraction grid)	Total number of MeE partitions
CFRP-001-MT10456-2 712 × 840 μm	14 × 14 × 14	100×100×100 μm	(14 ³) 2744
	28 × 28 × 28	50×50×50 μm	(28 ³) 21952

6.6. Summary

A special reconstruction algorithm to convert low phase-contrast X-ray CT images into finite element models was developed. Typically, using large scanning FoVs is leading to fewer pixels per fibre features. This makes the high-fidelity image-based models (e.g. by direct segmentation) not only unsuitable from a FE limitation point of view, but also leading to inexact boundary segmentations. An alternative solution is to reconstruct image-based models from a combined approach that includes: local maxima identification to obtain individual fibre centres and Bayesian inference filtering. The Bayesian model is applied to overlapped stacks to track the fibres in 3D. A major advantage of the Bayesian model in this chapter is that it facilitates the identification of potentially biased and discontinuous fibres with low computational effort that is necessary in nonlinear fibre datasets. It is shown that the proposed method is able to provide quality fibre centreline models from the initial in-situ X-ray CT scan of a CFRP multidirectional region. Because, the sample was subjected to uniaxial tension, the fibre centrelines are further used to reconstruct the 3D geometry via partitioned models. These models will be used in multiscale damage evolution and fracture modelling in CHAPTER 7.

To summarise, the new reconstruction model includes the following main features to overcome the various shortcomings of existing models:

- (i) The identification of fibre centre points is enhanced by using a combination of various image filters and the image convolution.
- (ii) A delineation of the X-ray CT dataset is proposed using a region of interest parameter tool to further allow identification of fibres in multidirectional CFRP laminates.
- (iii) The reconstruction process is made computationally efficient by the implementation of a global Bayesian filter that reduces the number of tracking slices. This feature is

necessary to lower the computational overload while re-iterating the fibre tracking algorithm locally to detect inclined ply margins.

- (iv) The fibre tracking algorithm update the fibre centre coordinates incrementally using the local Bayesian inference model. This is necessary to track inclined fibres.
- (v) The FE models can be built naturally once the fibre centrelines are identified.

Finally, the potential of reconstruction method presented here is to quantify several geometric features such as: constituent volume fractions (e.g. volumes and wetting surface), fibre lengths, global versus local fibre orientations and distributions, fibre/ ply waviness and fibre centreline tortuosity. These features are enabled for further explorations which can be either as a function of manufacturing conditions or during in-situ loading steps and valued with powerful image-based modelling.

CHAPTER 7. 3D X-RAY CT IMAGE-BASED MODELLING OF DAMAGE AND FRACTURE OF FIBRE REINFORCED COMPOSITES AND VALIDATION

7.1. Introduction

3D Modelling of discrete crack propagation in composite materials has hardly been carried out using realistic microstructures. This is mainly due to high computational costs and a lack of reliable numerical frameworks capable of modelling complicated damage and fracture processes in composites. So far, discrete crack propagation modelling based on X-ray CT images has been rarely carried out for concrete in 3D (Huang et al., 2015) and 2D (Ren et al., 2015). A few studies have simulated fibre reinforced composites with microstructural fibres using computer generated (CG) models but they based on continuum damage mechanics rather than discrete crack propagation (Wang et al., 2014; Mishnaevsky, 2012). Multiscale modelling of 3D fracture in fibre reinforced composites considering realistic random distribution of fibres and scale transfer has also hardly been reported.

In this chapter, sophisticated FE models for complicated 3D discrete crack propagation in fibre reinforced composites were developed and validated, using both CG models and micro-scale X-ray CT image-based multiscale stochastic models. A set of innovative in-house computer programs, written in Matlab, Javascript and Python, were developed to assist modelling and manipulation of big datasets. These programs perform insertion of cohesive interface elements in multi-phase materials in 3D, automatic boundary assignments, data imports and exports, post-processing and data analysis. The programs support the X-ray CT image damage and fracture modelling framework.

The CG models were used to test the capability of various computer programs developed for simulating realistic damage and fracture in fibre reinforced composites. The multiscale

stochastic fracture modelling framework in 2D, presented in CHAPTER 3 and CHAPTER 4 was extended to 3D, using the X-ray CT images obtained from the in-situ tests presented in CHAPTER 6. Several stochastic and overlapping image-based models are extracted from the reconstructed X-ray CT dataset and simulated first. The new stochastic and overlapping strategy allows a smoother scale transfer by preserving the fracture energy and crack propagation paths. In this sense, the MeEs and the macro-scale model were purposely designed by combining efficient parallel computation and enhanced capability of modelling complicated ply deformations, damage and fracture at macro-scale. The global multiscale stochastic model that incorporates the results of the image-based models is also simulated. The results are then compared with the in-situ X-ray CT tensile test in terms of load-deformation and fracture mechanisms.

7.2. Methodology of multiscale modelling and validation

Highly refined models of a large X-ray CT scanned region at the fibre scale are currently not possible due to high computational cost in generating and solving gigantic models. Therefore, a limited number of overlapping image-based MeEs (meso-scale elements) are modelled in this study. The image-based geometries are extracted in pairs from different fibre orientation plies. Although it may be possible to generate a fully detailed multiscale model to incorporate multiple MeEs by stitching smaller sized X-ray CT volumes at different locations, this is not undertaken here due to an enormous numerical cost. Instead, the anisotropic behaviour of the CFRP material is tested using a computationally feasible size MeE equal to 50 μm . The anisotropic behaviour is simulated using different boundary conditions explained described in Section 7.3. The knowledge is then transferred into a global multiscale model using a hierarchical multiscale approach. The procedure is in-line with the bottom-up hierarchical

approaches currently accepted by automotive and aerospace industries (Morishima, 2015; Orchard, 2015; Richardson, 2015).

Because of these limitations, the validation process follows the approach illustrated in Fig. 7-1. It includes two main sections as follows: (1) comparison of global failure mechanisms in terms of fracture surfaces and (2) comparison of mechanical loading data of in-situ versus FE modelling. The local crack surfaces obtained from X-ray CT scans could be also compared with MeE image-based modelling results, but it was not conducted due to the time limit.

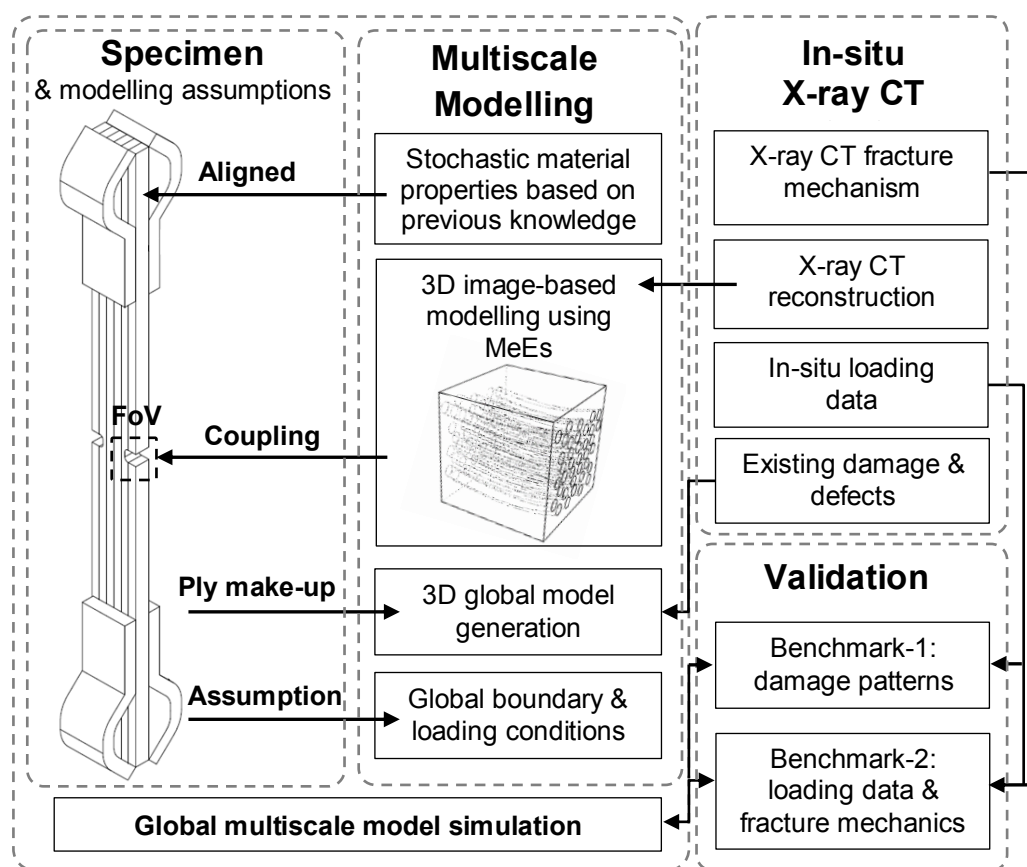


Fig. 7-1: Modelling framework and validation with in-situ X-ray CT experiments.

Five key steps are implemented to assist the proposed multiscale modelling framework as presented in Fig. 7-1. These steps include: (1) mesh generation and simulation of image-based MeEs, (2) random generation of material responses based on previous knowledge and MeE anisotropy diagrams, (3) global model generation taking into account the realistic ply sequence

and specimen boundaries (for example the notch shape cylinder shown in CHAPTER 6), (4) coupling of MeE simulation responses and assignment of further randomly generated material properties and (5) assignment of boundary conditions and simulation of global macro-scale model.

7.3. Modelling of damage and fracture in fibre reinforced composites

In this section, several CG models were simulated for crack propagation at fibre scale. The models consist of three phases: fibres, matrix and fibre-matrix interfaces. The meshes are generated using ABAQUS and have micro-scale cohesive interface elements inside the matrix and fibres, and on the fibre-matrix interfaces. The considered boundary conditions in 3D are illustrated in Fig. 7-2: (a) uniaxial tensile with restrained sides (*type-A*), (b) shearing using central bandwidth (*type-B*) and (c) uniaxial tensile with single restrained side (*type-C*). To avoid numerical difficulties, the shearing bandwidth for *type-B* conditions was assumed one-third the size of MeE edge. However, this shearing bandwidth may decrease when using highly refined meshes.

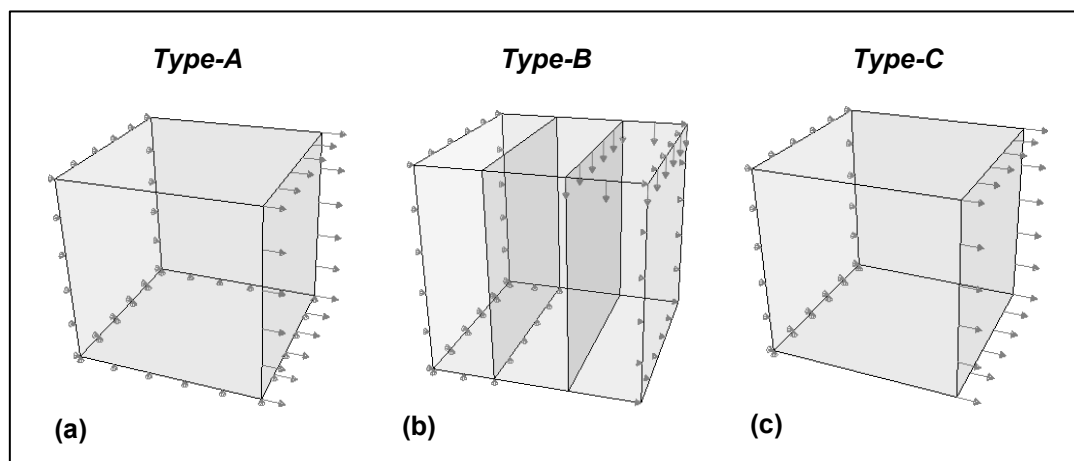


Fig. 7-2: Boundary conditions considered at meso-scale: (a) uniaxial tensile with restrained sides, (b) shearing using central bandwidth, and (c) uniaxial tensile with single restrained side.

7.3.1. Three-fibre models

In this section, a CG model containing three randomly oriented, tortuous fibres is solved under nine boundary conditions (three on each type of boundary type in Fig. 7-2), to see if different failure modes could be modelled. The fibres are not touching each other. The size of cubic model is 100 μm and the fibre diameter is 10 μm . Weak bonding between the fibres and matrix, with material properties in CHAPTER 3, was modelled.

Fig. 7-3 shows different failure modes obtained under tensile (*type-A* and *type-C*) and shear (*type-B*) boundary conditions. One or two dominant crack surfaces are identified for tensile boundary conditions along the fibre longitudinal direction as seen in Fig. 7-3-a and d respectively. Fig. 7-3-d shows that the failure modes with two cracks are associated with rotation of the core region between the two cracks. This was also observed in 2D modelling in CHAPTER 4. The failure mode with two cracks is most prevalent when the *type-C* boundary conditions are used.

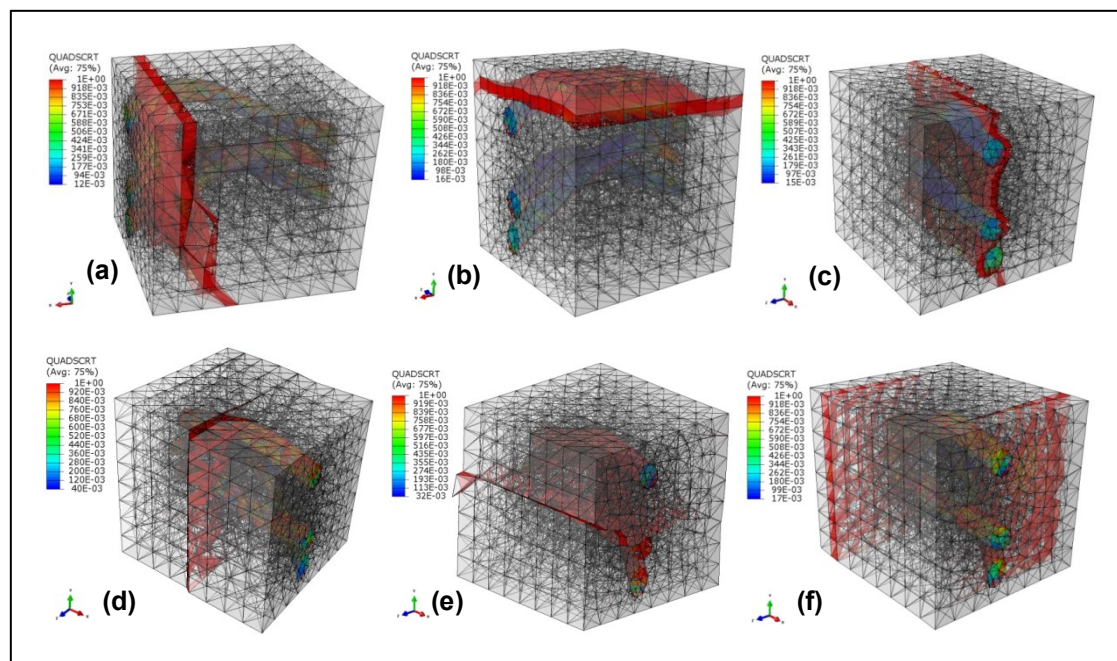


Fig. 7-3: Crack simulation results in three fibres model using different boundary conditions: *type-A*: a-b-c, *type-B*: d-e, *type-C*: f.

7.3.2. Modelling FRP with high volume fraction of fibres

Due to random distribution and waviness of fibres, most common cube models induce sharp edges at interfaces between matrix and fibres as shown in Fig. 7-4-a. In FE mesh generators, these edges automatically create localised mesh refinements due to knot geometrical approximation of the cutting curves. Such knots lead to distorted mesh refinements in Fig. 7-4-a. In general, due to the reduction in mesh size caused by mesh refinements, modelling crack propagation using cohesive elements is often problematic because solver instabilities can arise from integrating steep stress gradients, thus affecting the crack initiation criteria. In addition to numerical convergence problems, locally refined models may have a total number of degrees of freedom (DoF) up to millions which require high performance computing resources. These challenging situations are illustrated in Fig. 7-4 as follows: (a) mesh refinements with steep changes of aspect ratio and (b) inconformity problems with interfacial nodes when the fibres and matrix are meshed separately.

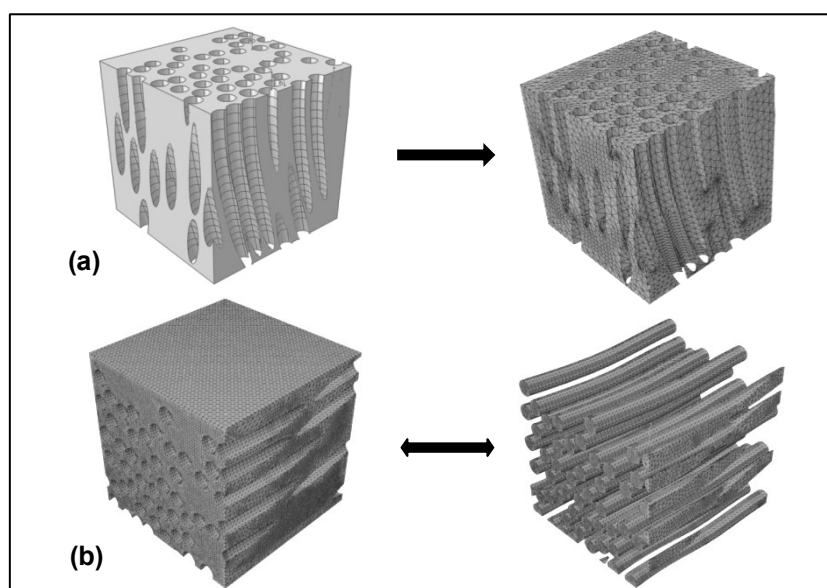


Fig. 7-4: Illustration of numerical challenges induced by curvilinear fibres and local cutting edges.

One way to avoid the computational bottleneck associated with these problems is to divide the region of interest into smaller and computationally feasible parts and restrict mesh refinement options. Small geometrical tolerances and precise intersection tools are necessary in such cases. Although FE meshes containing cohesive interface elements with various mesh densities can be obtained, models generated using small geometrical tolerances do not always ensure convergence of results. Another strategy will be proposed for image-based models in Section 7.4 where edges intersecting fibres are removed before mesh generation.

7.4. Assumptions of multiscale modelling informed by in-situ X-ray CT tensile test

Three modelling assumptions were made: (1) image-based models at fibre scale are overlapping and computed in parallel using a prescribed set of boundary conditions, (2) meso-scale responses are coupled hierarchically to a global model (sample size) via macro-scale cohesive interface elements and (3) random material properties with small variances are used at global scale where microstructure images and models are inexistent. The third assumption is based on previous 2D modelling knowledge in CHAPTER 4 and should be replaced with full image-based information where possible. The three distinct constitutive phases (matrix, fibres and interfaces) at meso-scale are modelled with different material properties.

7.4.1. X-ray CT image-based models at fibre scale

Eight individual image-based MeEs are extracted from a reconstructed X-ray CT geometry at fibre scale and presented in Table 7-2. The MeE are taken in pairs of two from each reconstructed ply as shown in Fig. 7-5. The size of cubic MeE is 50 μm . The overlapping volume of the MeE pairs is 50 \times 50 \times 25 μm . The fibre orientation angles contained in these MeEs are therefore directly based on the multidirectional ply sequence and X-ray CT volume

captured. Fig. 7-5 shows the reconstructed ply sequence from right to left that includes fibre orientations $[+45/90/-45/0]$ and the image-based model positions.

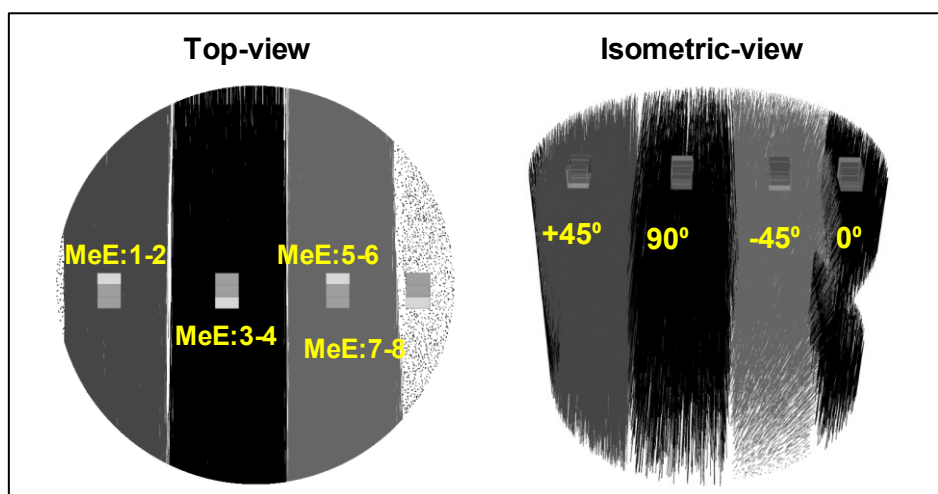


Fig. 7-5: X-ray CT image-based models extraction from a multidirectional CFRP reconstructed region.

Fig. 7-6 shows a typical mesh for MeE-8 in Table 7-2, generated using the reconstruction methodology in CHAPTER 6. The modelling of crack propagation and fracture processes usually requires a fine mesh. This is to avoid local mesh distortions and FE sensitivity problems. However, a relatively coarse element size $1\ \mu\text{m}$ was used here because the fibre diameter is assumed as a constant $5.2\ \mu\text{m}$. The solid element size is approximately five times smaller than the fibre diameter. These allow a computationally feasible cohesive-model of size $50\ \mu\text{m}$.

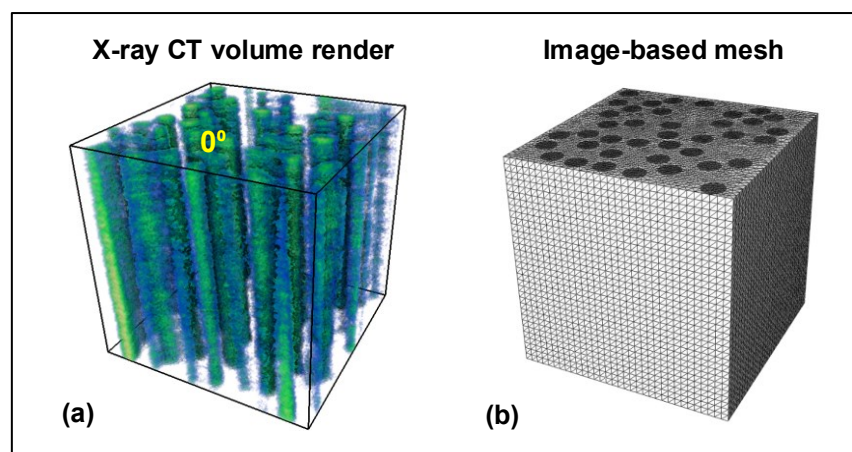


Fig. 7-6: An X-ray CT region render in 0° fibre oriented CFRP and the reconstructed image-based mesh associated with MeE-8 in Table 7-2.

7.4.2. Meso-scale element modelling

The cohesive interface elements are then inserted into the solid element meshes in Fig. 7-6 to model crack initiation and propagation in fibres, matrix and interfaces. The resultant mesh is shown in Fig. 7-7. The mesh consists of two finite element types, namely, 4-node tetrahedral solid elements C3D4 and 6-node cohesive elements COH3D6 with zero thickness, both of single integration type available in ABAQUS. There are 1527588 nodes, 383375 C3D4 elements and 760739 COH3D6 elements in Fig. 7-7.

Linear elasticity material models are used to define all material phases at meso-scale (Simulia/Abaqus). The fracture process is modelled in any of the three constituent phases (fibres, matrix and interfaces) using meso-scale CIEs (cohesive interface elements) that are pre-inserted accordingly. The crack growth is allowed to transit any of the three cohesive element sets.

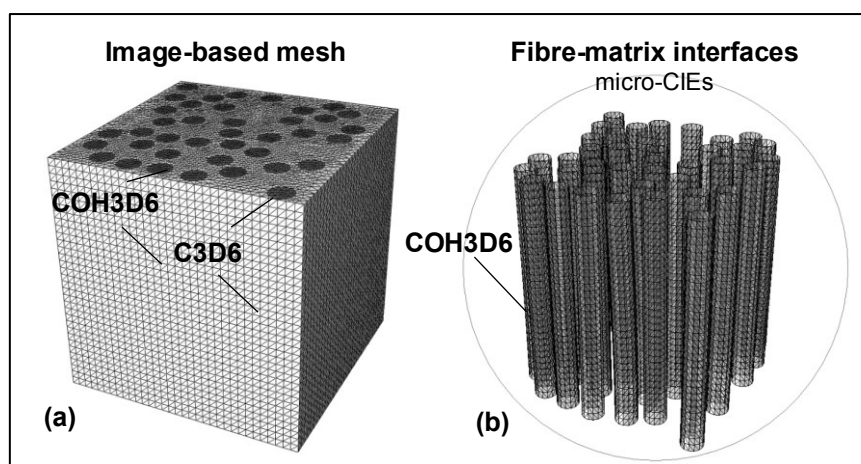


Fig. 7-7: Image-based mesh reconstructed from in-situ X-ray CT dataset of a CFRP region.

Crack propagation can be decided based on two criteria, namely the maximum stress criterion (MAXS), or the quadratic traction-interaction criterion (QUADS) in mixed-mode behaviour. The QUADS criterion was used in this study. The softening (after crack initiation) follows the energy-based evolution (ENERGY) and the softening element control in mixed-mode behaviour is based on the power-law (POWER) available in ABAQUS (Simulia/Abaqus).

As seen in Fig. 7-7, the solid and cohesive interface elements are distributed in a uniform manner without mesh refinements. In all simulations, the explicit dynamic solver is used with displacement control and adequate loading time for quasi-static loading condition. The meso-scale material modelling properties are given in Table 7-1. The meso-scale boundary conditions are identical to Section 7.3.1. For completeness, a set of nine boundary conditions are simulated on each MeE model. These boundary conditions are performed in separate numerical runs along the global directions X , Y and Z . The three responses are accurately transferred to macro-scale depending on the fibre orientations contained in the MeE domain and further ply sequence of the CFRP sample. The MeE modelling responses are presented in Section 7.4.3.

Table 7-1: Material specifications and properties for meso-scale fracture modelling.

Parameters	SI Units	Carbon fibre	Epoxy resin	Interface
Elastic modulus (chord 6k-10k)	GPa	276	3.35	3.35
Tensile strength $t_n=t_s=t_t$ (6k)	MPa	5515	50	25
Poisson's ratio ν	-	0.22	0.35	0.37
Fracture energy $G_{11}=G_{22}=G_{33}$	N/mm	0.287	50e-03	25e-03
Density	kg/mc	1500		
Volume fraction	%	50	50	-
Filament diameter	mm	5.2e-03	-	-
Ultimate elongation at failure	%	1.9	2	2
Twist	-	never twisted	-	-

7.4.3. Meso-scale modelling responses

To ensure numerical efficiency, Fig. 7-5 shows that the partitioned MeEs of relatively small sizes (edge equal to 50 μm) become computationally feasible. The modelling procedure starts with simulation of a single MeE using boundary condition type-A in Fig. 7-2-a. The complete set of simulations in Fig. 7-2 (*type-A* to *type-C*) is then performed for all global directions as explained previously. The simulations provide essential information for transferring crack propagation process at macro-scale more accurately. For example, Fig. 7-8 presents the sequence of damage and crack propagation in MeE-8 model subjected to tensile loading. The response corresponds to *type-A* boundary conditions along *Z* axis direction (parallel to fibre centrelines).

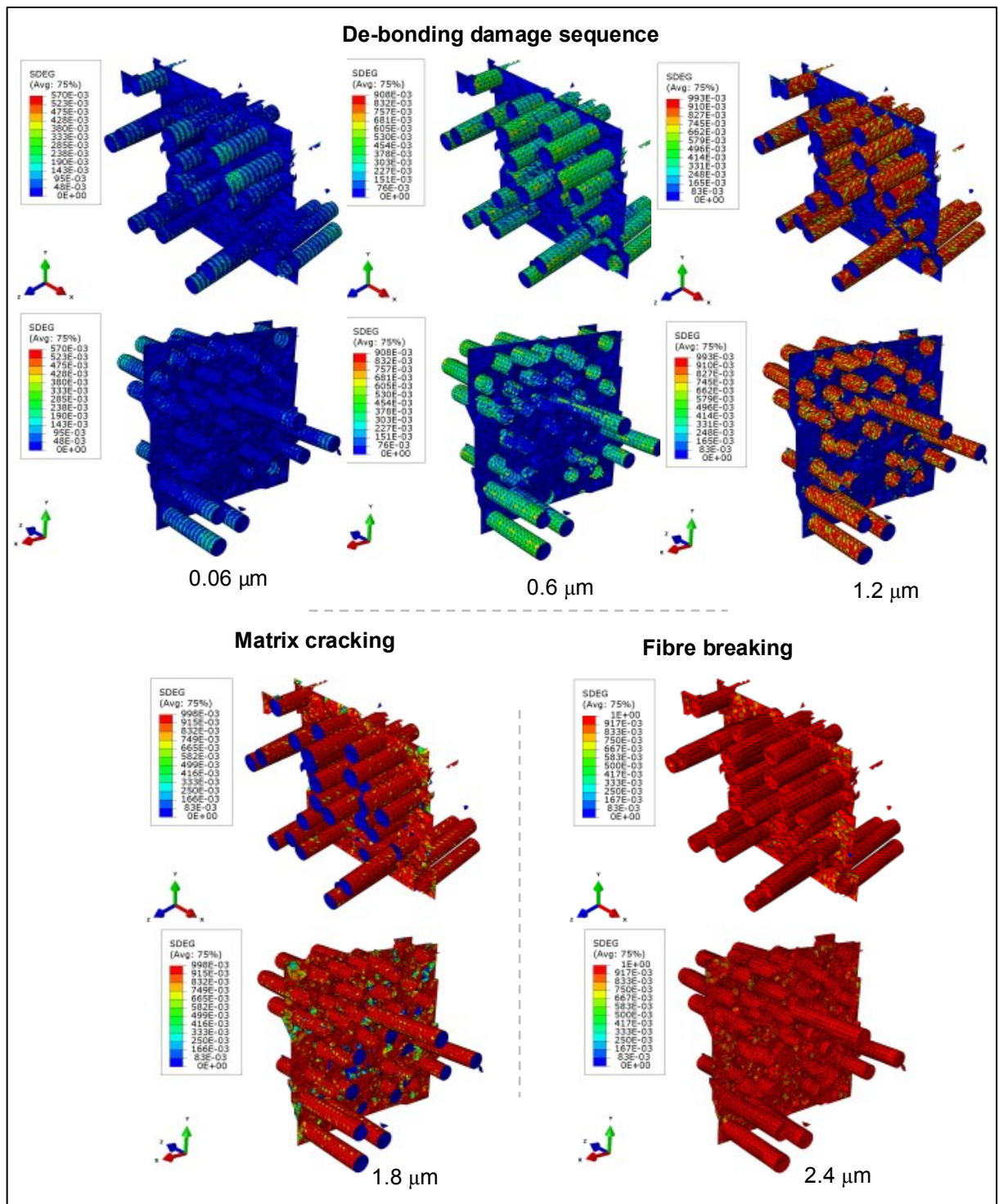


Fig. 7-8: Sequence of damage and crack propagation in image-based model MeE-8 subjected to tensile loading along Z axis (parallel to fibre centrelines).

Fig. 7-9 shows the most common examples of fracture surfaces obtained from MeEs that contain 0° and 90° fibre orientation plies. Fig. 7-10 illustrates some typical examples of fracture surfaces obtained from MeEs that contain -45° and $+45^\circ$ fibre orientation plies.

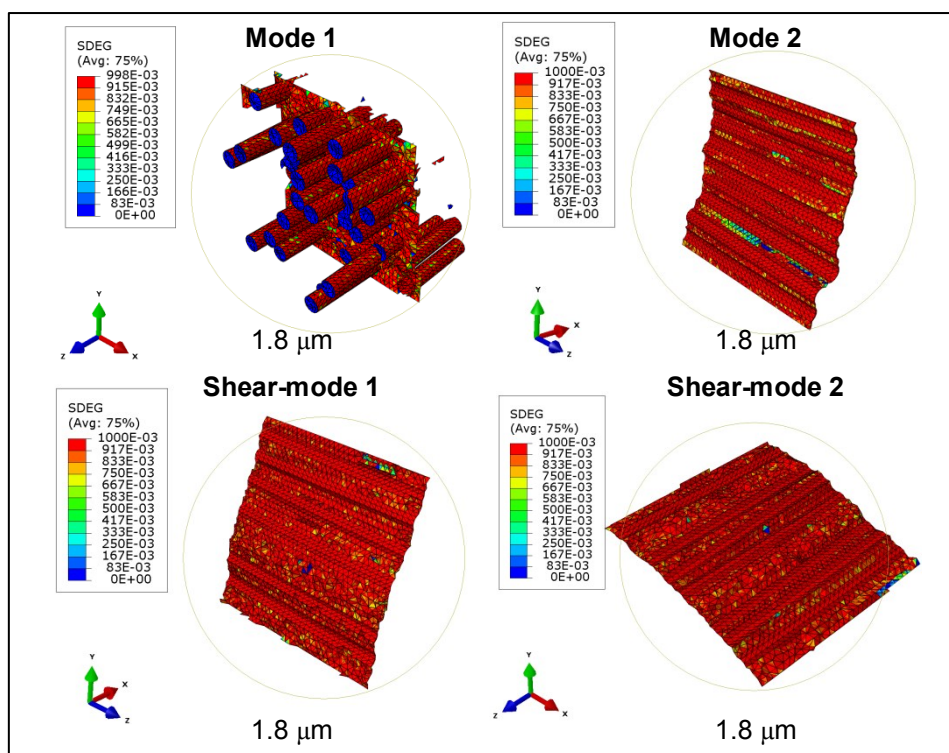


Fig. 7-9: Fracture surfaces of CFRPs obtained from MeEs containing 0° and 90° fibre orientation plies.

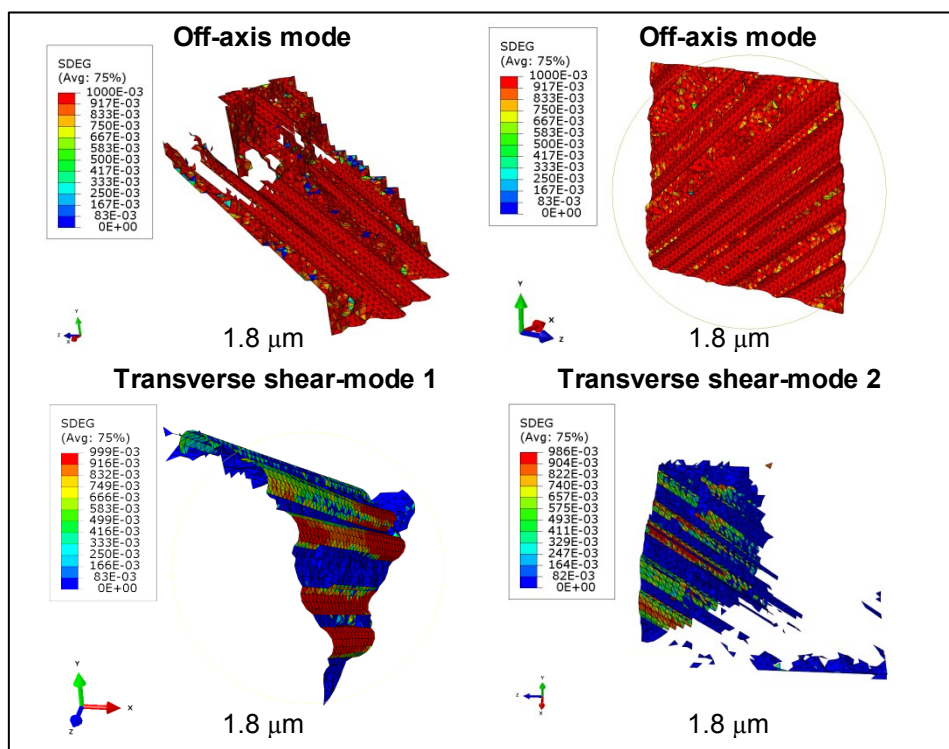


Fig. 7-10: Fracture surfaces of CFRPs obtained from MeEs containing -45° and $+45^\circ$ fibre orientation plies.

Fig. 7-11 and Fig. 7-12 give the stress-displacement curves from $-45^\circ/45^\circ$ and 90° simulations respectively. These curves are used in macro-scale modelling according to the scale coupling methodology in CHAPTER 3.

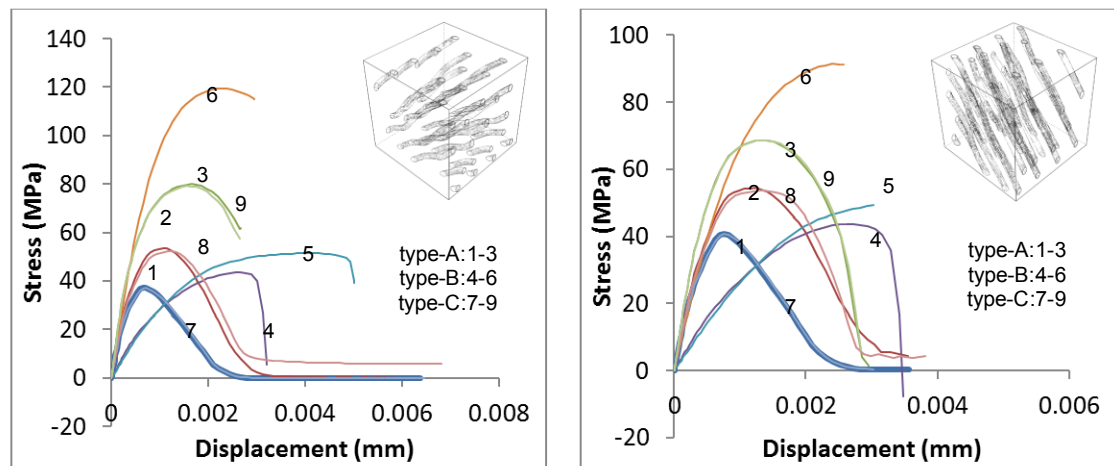


Fig. 7-11: Stress-displacement curves of CFRPs at fibre scale obtained from MeE simulations that contain (a) -45° and (b) $+45^\circ$ oriented fibres and different fracture modes.

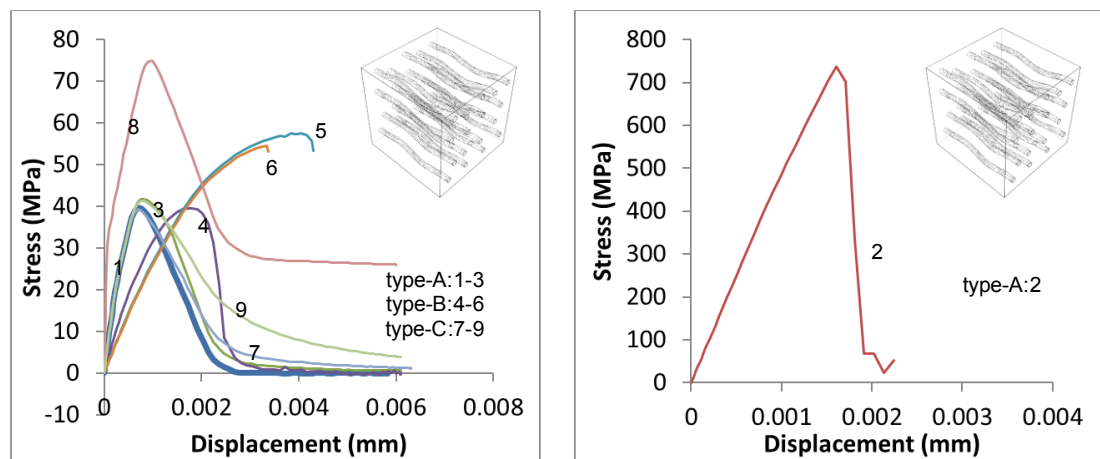


Fig. 7-12: Stress-displacement curves of CFRPs at fibre scale scale obtained from MeE simulations that contain 90° oriented fibres and different fracture modes.

Table 7-2: X-ray CT image-based models extracted in overlapping pairs from a multidirectional CFRP sample as shown in Fig. 7-5.

Image based model reference	Coordinates of non-overlapping extraction grid (μm)	Ply orientation angle	Reconstructed fibre volume fraction	Mesh model information							
				Fibre C3D4	Fibre COH3D6	Matrix C3D4	Matrix COH3D6	Interface COH3D6	Total number of elements	Total number of nodes	Insertion CPU time (s) Intel(R) i7@ 3.40Ghz
MeE-1	P1(100,385,50) P2(125,410,75)	+45°	25%	91314	166418	264008	508469	29839	1060048	1417668	647140
MeE-2	P1(100,410,50) P2(125,435,75)	+45°	20%	69727	126775	267230	518523	22834	1005089	1343688	548132
MeE-3	P1(350,385,50) P2(375,410,75)	90°	15%	50871	92782	270852	527530	16629	958664	1277544	357343
MeE-4	P1(350,410,50) P2(375,435,75)	90°	15%	50347	91730	272222	530362	16631	961292	1280764	566716
MeE-5	P1(585,385,50) P2(610,410,75)	-45°	38%	139395	254198	249367	470815	45042	1158817	1552048	792675
MeE-6	P1(585,410,50) P2(610,435,75)	-45°	37%	141152	257280	247583	467455	45759	1159229	1551988	803531
MeE-7	P1(755,385,50) P2(780,410,75)	0°	34%	122823	223587	271143	515826	40402	1173781	1575144	525211
MeE-8	P1(755,410,50) P2(780,435,75)	0°	31%	110360	201310	273015	523401	36028	1144114	1527588	563613

7.4.4. Strength anisotropy diagrams

The advantage of modelling multidirectional CFRP materials at meso-scale is that most common fibre orientations can be captured with a limited number of numerical jobs. To further benefit from this advantage, the anisotropic material behaviour is investigated in this section. This investigation is conducted by combining the results obtained in Section 7.4.3 for tensile and shearing boundary conditions in different directions. Because in this study, the prescribed set of boundary types are only simulated along global X , Y and Z directions, the complete anisotropy diagrams are interpolated between local fibre orientations and shown in Fig. 7-13 and Fig. 7-14. The two diagrams in Fig. 7-13 and Fig. 7-14 are obtained using tensile boundaries *type-A*, and shearing boundary conditions *type-B*, respectively. The diagrams show high contrast of ultimate strengths under tension with different fibre orientations, and a relatively low contrast for shearing boundary conditions. Similar effects can be observed combining other results in Fig. 7-11 and Fig. 7-12.

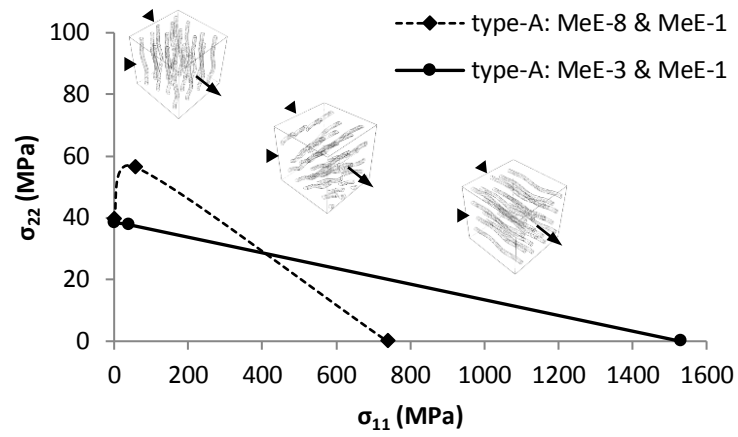


Fig. 7-13: Tensile strength anisotropy diagram of CFRPs at fibre scale using *type-A* boundary conditions.

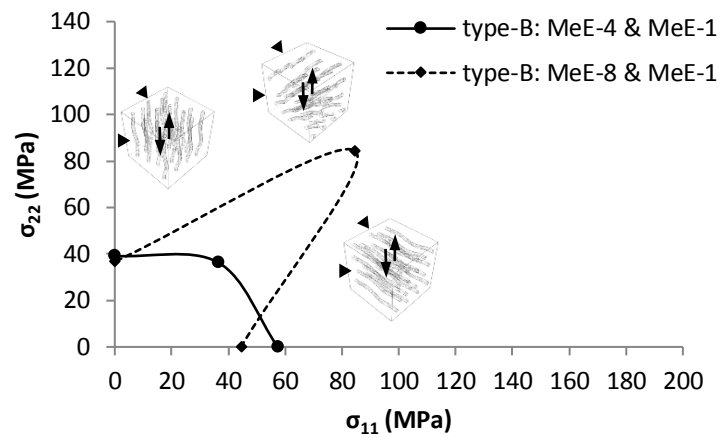


Fig. 7-14: Shearing strength anisotropy diagram of CFRPs at fibre scale using *type-B* boundary conditions.

7.4.5. Scale transfer

The elastic part of stress-displacement curves is first converted into stress-strain. The elastic stress-strain relationship is decomposed into an orthotropic 3D elasticity tensor that combines the results from different MeE boundary simulations. The 3D elasticity tensor is then linked to the solid elements contained in the global model. The plasticity (non-linear) part between the upper linear-elastic point and the maximum stress point, is used in the scale transfer as a pseudo-orthotropic plasticity input. This pseudo-orthotropic plasticity model is actually only taken from the major boundary response in this study. For example, the tensile boundary conditions along the MeE fibre direction. To ensure numerical convergence, the plasticity curve continues after maximum stress point. The continuation is done in a ramp-manner taking the local slope of the curve and infinite strain. Typically, when an elastoplastic model with a monotonically increasing plasticity is used, there should be no dissipative competition between the bulk elements' plasticity versus the cohesive elements opening. This is due to the fixed initiation criterion, such as the QUAD or MAXS criteria available in ABAQUS.

The pseudo-plasticity material model is attached to solid elements contained in the global model to ensure that the cohesive crack initiation stress at interfaces is kept at approximately the same initiation value. Therefore, the cohesive interface elements will then take over once their crack initiation criterion is reached. As before, after the first crack initiation, the fracture softening is dictated by an evolution criterion.

The softening criterion can be estimated based-on the actual fracture energy released by the corresponding MeEs. This input can be delivered in ABAQUS using a tabular definition or an equivalent fracture energy release dictated by a power-law as previously explained in CHAPTER 3. However, when the power-law is used, the meso-scale sequence of damage/ fibre breaks cannot be transferred very accurately. For simplicity, the total energy released in MeEs

are first calculated and used with second order power-law in the scale transfer of this study. This step is essential to ensure the conservation of fracture energy in scale transfer. The details about further discretisation linkage to preserve more accurate crack paths at global scale and the afferent FE modelling parameters are given below in Section 7.4.6.

7.4.6. Macro-scale mesh generation and preparation for scale transfer

In this section, the macro-scale mesh is generated using an in-house Python script that uses the ABAQUS/CAE library (Simulia/Abaqus). The model is prepared for scale transfer by a special structured mesh. The mesh contains interfaces that are aligned with most expected crack surfaces based on the ply sequence of the multidirectional CFRP material. The expected crack surfaces at macro-scale refer to matrix transverse cracking, fibre bundle and matrix breaks and resin-rich failure as shown in Table 7-3. As mentioned above, the mesh interfaces at macro-scale also contain macro-CIEs shown in Fig. 7-15. The macro-CIEs incorporate the responses obtained from meso-scale modelling. The coupling of MeEs to macro-CIEs that belong to different CFRP plies is discussed in details in Section 7.4.7.

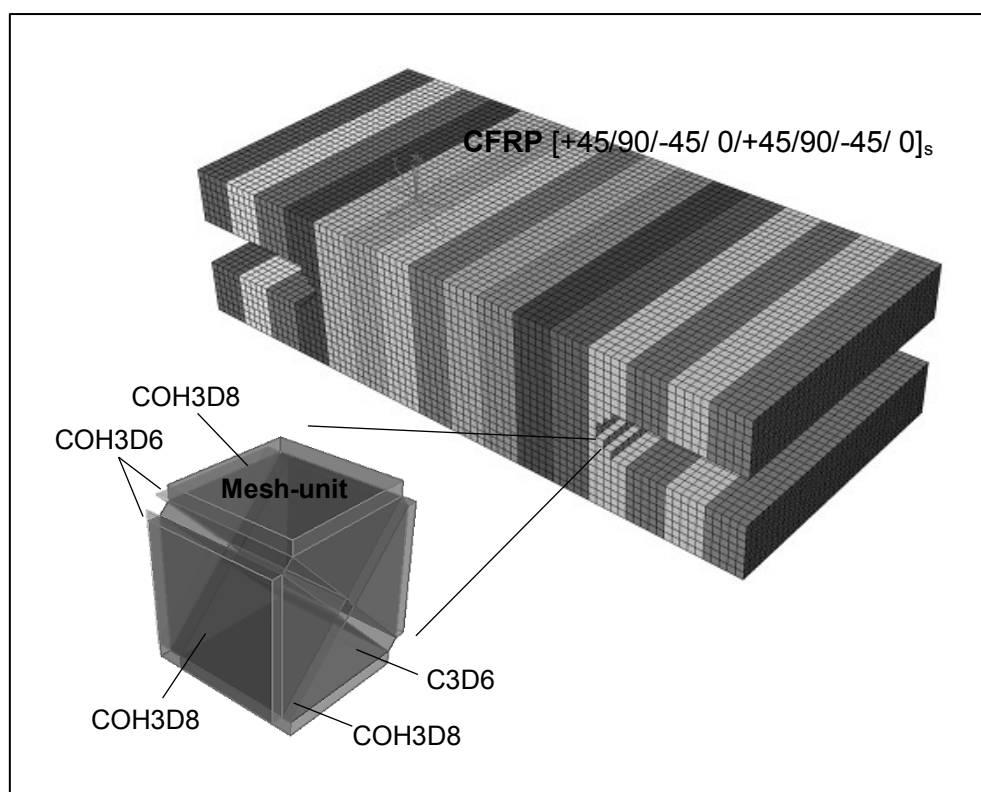


Fig. 7-15: Multiscale model at global scale showing geometrical idealisation and mesh-unit for scale transfer.

Fig. 7-15 shows that the global mesh consists of a mixture of solid elements type C3D6 and two types of cohesive interface elements, namely COH3D6 and COH3D8. COH3D8 refers to zero thickness cohesive elements with 8 nodes and single edge integration. These elements are available in ABAQUS and can be mixed in a single model. The aligned/ structured mesh has two advantages such as: (1) easy FE post-processing due to visualisation of the entire detailed crack surfaces after thresholding, and (2) better control with material sub-routines including the orientation sub-routine encountered in this study. The solid elements are assigned orthotropic material properties obtained from meso-scale modelling and were able to simulate the complicated multidirectional response of CFRPs. The orientations are established using the ORIENT subroutine available in ABAQUS. The constitutive formulation of these elements is linked with elasto-plastic responses of the MeE simulations above. Further material properties are generated randomly by assuming a maximum parameter variation of 10%. Although, the

extent of random material properties holds no exact continuity due to unavailable meso-scale information, this practice is currently a competing alternative to solving the complete computational domain. In addition, this modelling tool may also be necessary due to limited field-of-views that can be currently captured with the X-ray CT technologies and further characterisation challenges. A few of the experimental challenges were previously discussed in CHAPTER 5 when running the current in-situ X-ray CT tests.

Table 7-3: Meso-scale information and global multiscale modelling using ABAQUS.

Boundary type/ Failure mode at meso-scale	Macro- element types	Anisotropy considerations at macro-scale	FE sub-routines for initiation/ propagation / mixed modes control/ orientation
Type-A transverse to fibres/ Matrix cracking with 3D decohesion (M)	Cohesive: COH3D6, COH3D8	3D orthotropic	QUADS, ENERGY, BK or power law for mixed modes
Type-A along fibres/ Matrix cracking with fibre bundle breaks (F)	Cohesive: COH3D8	3D orthotropic	QUADS, ENERGY, BK or power law for mixed modes
Type-A transverse to fibres/ Transverse matrix cracking (T) (inclined fibre orientations at +45°/ -45°)	Cohesive: COH3D8	3D orthotropic	QUADS, ENERGY, BK or power law for mixed modes
Type-A along fibres/ Off-axis matrix cracking (O) (inclined fibre orientations at +45°/ -45°)	Cohesive: COH3D8	3D orthotropic	QUADS, ENERGY, BK or power law for mixed modes
Type-A transverse to fibres/ Resin-rich opening failure mode (RO) (bulk delamination)	Cohesive: COH3D6	3D orthotropic	QUADS, ENERGY, BK or power law for mixed modes
Type-B along fibres/ Resin-rich transverse failure mode (RT) (bulk delamination)	Cohesive: COH3D6	3D orthotropic	QUADS, ENERGY, BK or power law for mixed modes
Elastic-plastic deformations (EP)	Solid: C3D6	Poisson elasticity or 3D orthotropic	ORIENT, UMAT

7.4.7. Macro-scale element sets

To assist the scale transfer, the orthotropic elasto-plastic responses of MeEs are linked to the macro- solid elements using the orientation sub-routine ORIENT available in ABAQUS as follows. Each ply contains a unique macro- element set of solid elements (C3D6). Because the exact failure surfaces of MeEs are integrated using reduced order elements, they are also mapped to the closest macro-CIEs. However, different failure modes are mapped to different cohesive macro- element sets. For example, the matrix cracking that comes from MeE transverse simulations are linked using separate macro- cohesive element sets that are ply dependent. Another example is the fibre ply breaks of MeE that contain longitudinal fibres. Those are also linked using separate macro cohesive element sets that are ply orientation dependent. The delamination of ply-to-ply are modelled using a single set of macro cohesive elements, although different responses can be linked to resin-rich layers bridging different bi-layer orientations such as 0° to 90° plies and $\pm 45^\circ$ to 90° or $\pm 45^\circ$ to 0° plies.

Table 7-4: Coupling information of macro element sets contained in different fibre orientation plies.

Modelling instance	Links of macro-CIE orientation sets to MeE responses in Table 3	Element types	Number of similar instances
0° plies	Coh 0° ::M, Coh 90° ::F, Coh $\pm 45^\circ$::O, Coh $\pm 45^\circ$::O, S::EP	COH3D6, COH3D8, C3D6	4
90° plies	Coh 0° ::F, Coh 90° ::M, Coh $\pm 45^\circ$::O, Coh $\pm 45^\circ$::O, S::EP	COH3D6, COH3D8, C3D6	4
$\pm 45^\circ$ plies	Coh 0° ::T, Coh 90° ::O, Coh $\pm 45^\circ$::F, Coh $\pm 45^\circ$::M, S::EP	COH3D6, COH3D8, C3D6	4
$\pm 45^\circ$ plies	Coh 0° ::O, Coh 90° ::T, Coh $\pm 45^\circ$::M, Coh $\pm 45^\circ$::F, S::EP	COH3D6, COH3D8, C3D6	4
Resin-rich interfaces	Coh 0° ::RO Coh 0° ::RT (3D orthotropic)	COH3D6	15

The fracture energy release for macro-CIEs is kept less than the elasto-plastic energy as recommended in (Lopes et al., 2015). In fact, this is true in cohesive crack modelling in fibre reinforced composites due to the relatively small mesh-size requirement of the global scale model. This is somewhat fixed because the global mesh quality and element sizes are primarily required to capture the deformation of plies. In this particular case study, the ply thickness is approximately $\sim 250 \mu\text{m}$.

7.4.8. Multiscale model simulation and validation

This section presents the final multiscale model used for validation. The simulation is based on the following simplifications: (1) the metal end tabs and rig tensile grips present in the in-situ tensile test are not modelled due to complicated contact interactions, (2) the global modelling is isolated to a local region of the specimen while the remaining domain is rigid and (3) the resin-rich material properties are assumed 10% weaker than epoxy matrix due to potential fibre bridging effects of plies. First and second assumptions are made to reduce numerical cost when generating the complicated mesh containing mixed elements. The third assumption is necessary because of realistic fibre bridging effects. The fibre bridging effects are predominantly in plies and can also occur in resin-rich layers if special manufacturing specifications are given. In this case, although such fibre bridging effects could be visualised in the off-axis tensile type boundary simulations conducted in Section 7.4.3, they were usually hard to be captured with modelling of relatively small volumes. The maximum principal stresses at different loading steps during the global simulation are shown in Fig. 7-16. Because the maximum principal stresses occur in different ‘principal’ directions, they are important to understand the load distribution across each ply. It is predicted that the inclined fibre plies fail before the transverse fibre plies oriented at 90° . The delamination of the resin-rich layers also begins before stress at

failure in inclined fibre plies (i.e. below 14 μm loading extension in Fig. 7-16-a). The extensive delamination can be visualised in the overstressed single element rows in Fig. 7-16-c and d.

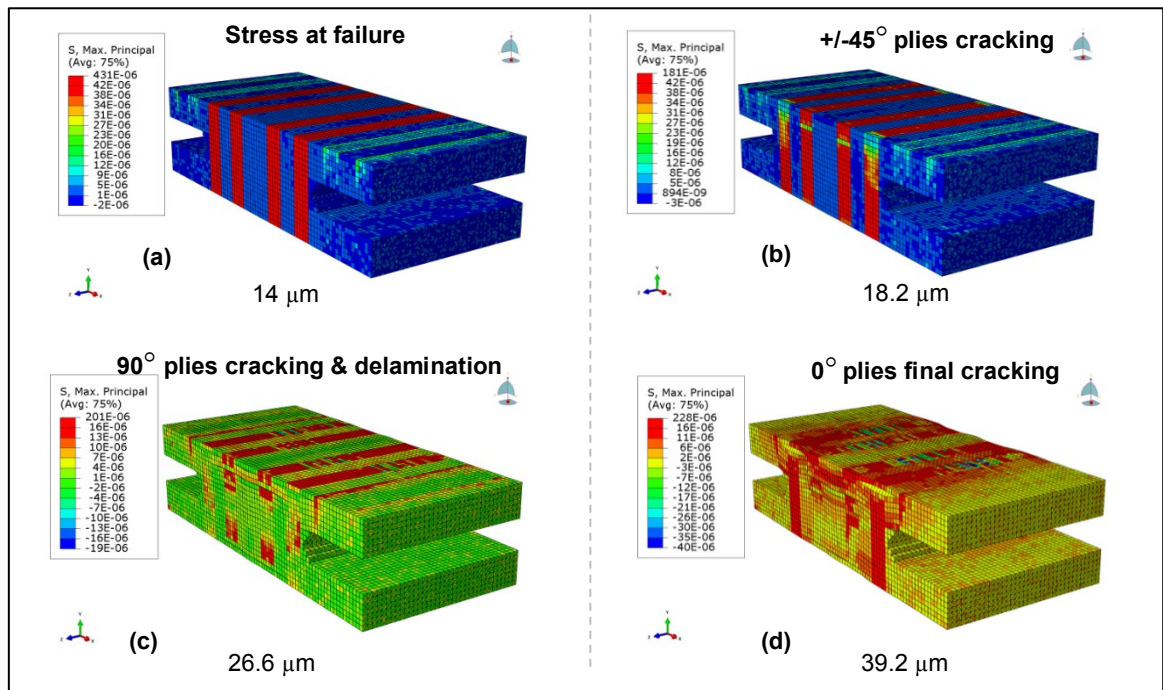


Fig. 7-16: Maximum stress contours in multiscale model at different damaging steps.

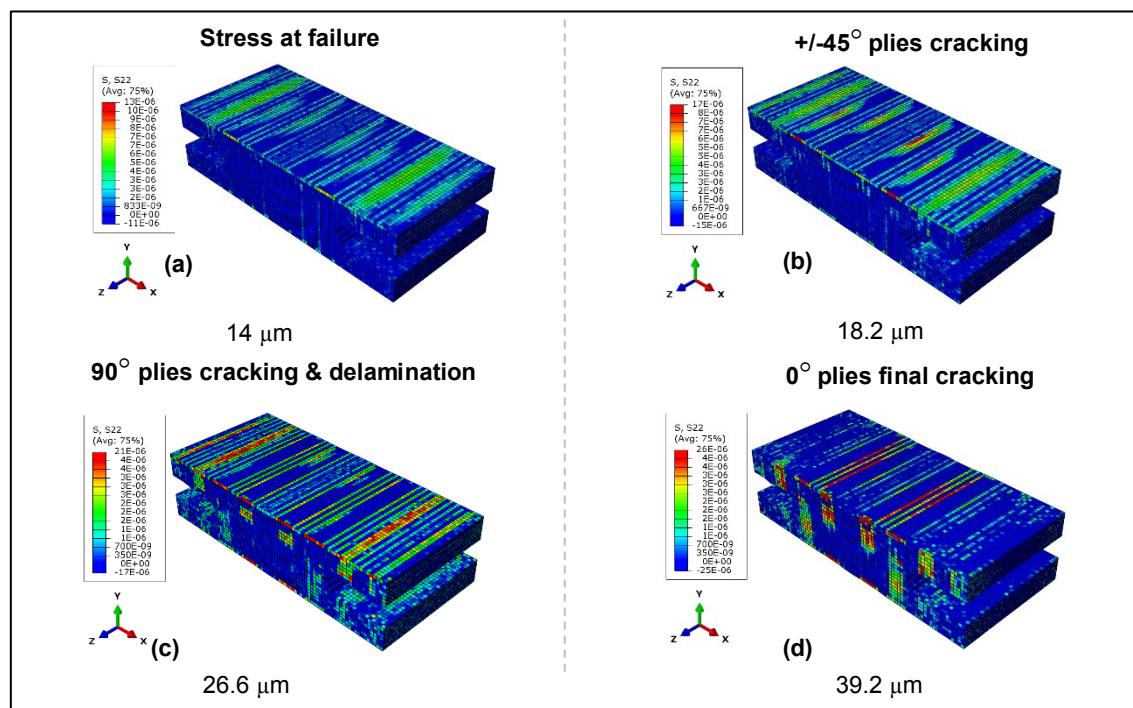


Fig. 7-17: Contour stresses along vertical loading direction Y in multiscale model at different damaging steps corresponding to Fig. 7-16.

Fig. 7-18 gives a comparison between the multiscale model and the X-ray CT failure mechanisms in terms of fracture surfaces. The modelled fracture surface is extracted based on the damage index variable $SDEG > 0.9$. It appears that the complicated global failure mechanism can be simulated using the multiscale model in this study.

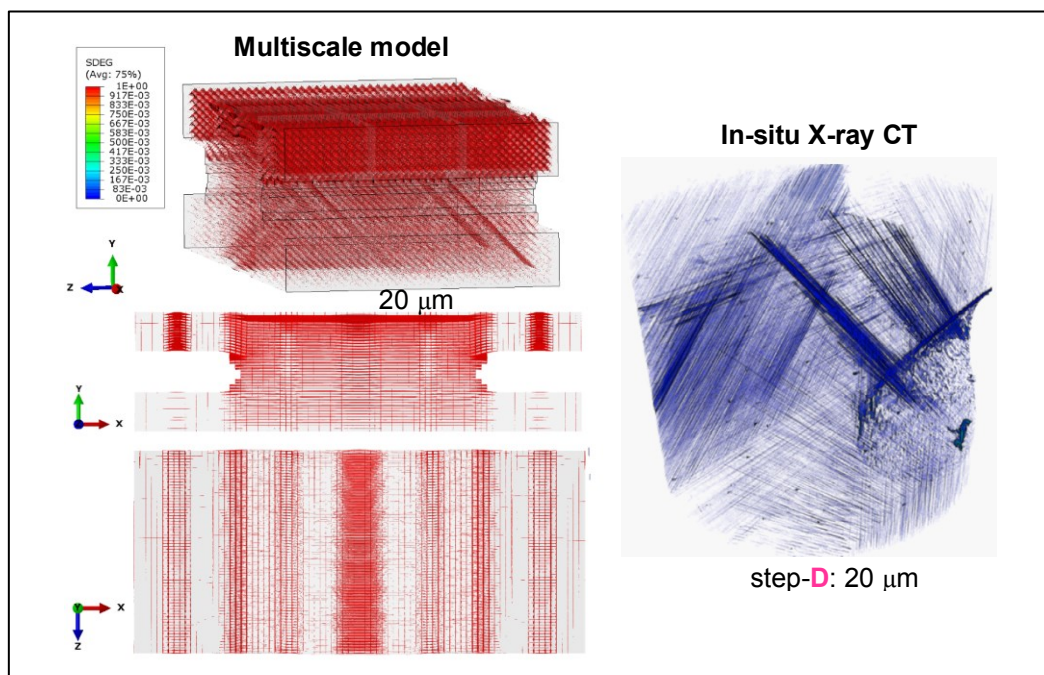


Fig. 7-18: Comparison of damage and crack patterns in multidirectional CFRP sample from FE multiscale modelling and in-situ tensile test.

Fig. 7-19 shows the comparison in terms of the load-displacement curves.

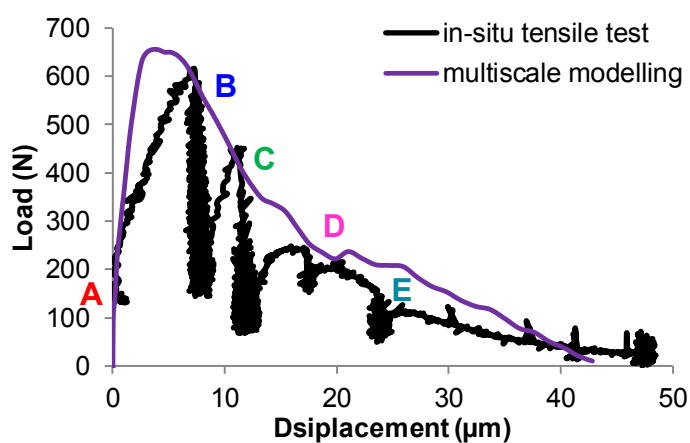


Fig. 7-19: Comparison of load-displacement curves in CFRP sample from FE multiscale modelling and in-situ tensile test.

It was observed that the failure mechanisms in multidirectional fibre reinforced composites involve a sequence of matrix cracking, fibre ply breaks and delamination of resin-rich layers. Although, some local fibre breaks have potentially initiated during the mechanical loading, a complete fibre ply breaking could not be captured during the in-situ tensile test due to a premature failure of support. However, one of the main advantages of carrying detailed fracture modelling at meso-scale is that the fibre breaking and resin fracture mechanisms can be inspected in greater details and incorporated in macro-scale modelling. The macro-scale simulation also suffices a predicted fracture energy release that depends on meso-scale responses. This fracture energy can be calculated as a total in the modelling or as a cumulative function of damage created during several in-situ loading steps.

Finally, the multiscale modelling implementation in this chapter is directly contributing to an enhanced understanding of CFRP material's reliability and caters additional parametric studies to optimise various microstructures.

7.4.9. FE simulation runtimes and use of high performance computing facility

The total number of simulations at meso-scale in 3D is 72 jobs. Each MeE simulation set contains 9 jobs as a result of the three boundary types along X , Y and Z orthotropic directions. The jobs were run using batch scripts programmed on 12, 24 or 32 cores using the high performance computing (HPC) facility at University of Manchester. The maximum duration of a single MeE simulation on the HPC's parallel environment using ABAQUS-6.12-2 is approximately 60 hours to complete.

The final global simulation has ~ 3.5 million degrees of freedom (DoF) and consumes approximately 4 hours on a desktop computer using an Intel(R) processor i7-2600 @ 3.40 Ghz with 8 threads and 16.0 Gb installed memory (RAM). The global simulation runtime is expected

to increase slightly with increasing number of DoFs. However, this sensitivity study is not further investigated.

7.5. Summary and conclusions

In the first part of this chapter, the cohesive crack interface model was tested on a number of computer generated (CG) models. Several computational tools have been developed to make modelling flow easier. The resulting crack surfaces from different boundary conditions were also identified and shown for better visualisation and understanding of fracture in fibre reinforced composites. As a result, CG models can also be used instrumentally to prove the suitability of crack numerical frameworks at dealing with complicated fibre reinforced composite.

In the second part of this chapter, the developed multiscale stochastic fracture mechanics modelling method has been tested and validated in 3D. Typically, in discrete fracture mechanics (where crack propagation is included), the assumption of using bulk discretisation models without a clear understanding of meso-scale mechanics cannot be used in conjunction with incommunicative or statistical material properties to accurately simulate crack propagation and fracture processes in composite structures. To overcome this situation, the multiscale stochastic fracture mechanics modelling method has been applied to image-based models from X-ray CT reconstructed volume of a CFRP sample. The method is therefore capable of modelling quasi-brittle materials with multi-phasic microstructures such as the fibre reinforced composite, various degrees of bonding and feature distributions.

Following conclusions may be drawn from this chapter:

- (i) The image-based simulations show that CFRP's responses including elasticity, fracture energy and crack surfaces, have dissimilar results for different sampling positions which invalidates the classical RVE approach.

- (ii) Various boundary conditions can be used to study the CFRP behaviour in a more comprehensive meso-scale study. In this study, MeEs that contain different fibre orientations were used to understand strength anisotropy by illustrating their contrast in two main diagrams namely the tensile and shearing boundary conditions.
- (iii) Image-based models of CFRP material can now be used to realistically capture crack propagation and fracture processes at fibre scale.

CHAPTER 8. CONCLUSIONS AND RECOMMENDATIONS FOR FUTURE RESEARCH

8.1. Conclusions

Through a comprehensive research programme, a new multiscale stochastic fracture mechanics modelling framework informed by in-situ X-ray Computed Tomography (X-ray CT) tests has been developed for fibre reinforced composite materials.

The following tasks have been undertaken:

- (i) development of cohesive interface crack models for modelling multi-phase composites in 2D and 3D;
- (ii) development and validation of a new multiscale stochastic coupling procedure capable of conducting the meso to macro scales transfer;
- (iii) development of an innovative in-house micro- loading rig incorporated into the X-ray CT facility at Diamond Light Source;
- (iv) design and undertaking of in-situ X-ray CT scanning tests of CFRP;
- (v) reconstruction of low phase-contrast X-ray CT datasets of CFRP;
- (vi) development X-ray CT image-based FE models for cohesive fracture simulations in CFRP; and
- (vii) validation of a partially informed multiscale stochastic modelling method by direct comparisons with in-situ X-ray CT tensile test results.

The main achievements and novelties of this research are:

- (i) the existing cohesive interface crack model has been extended to multi-phasic materials in 2D and 3D, and image-based modelling in an object oriented way;
- (ii) the multiscale coupling holds the microstructural stochastic continuity using the innovative overlapping meso-scale elements procedure;

- (iii) in-situ X-ray CT imaging of crack propagation has been successfully captured at fibre scale using the new in-house loading rig which is fully integrated and can be controlled manually or automatically by computers;
- (iv) a repository of X-ray CT datasets of CFRP from in-situ experiments is available for further research. However, due to the limited time a single X-ray CT volume dataset was used to generate meshes for the multiscale finite element modelling in this work;
- (v) micro-scale X-ray CT image-based models were built and tested partially validated for the first time for CFRP;
- (vi) validation of modelling crack propagation at macro-scale is achieved using a partially informed multiscale stochastic model, which incorporates meso-scale image-based modelling responses and randomly generated material properties when the material's microstructure is not available.

8.2. Recommendations for future research

The modelling framework developed in this thesis can be further improved in a few ways. Firstly, the various codes and scripts developed can be improved to achieve higher efficiency by optimisation. For example, the object-oriented CIE insertion program can be further parallelised and tested in multiphasic datasets.

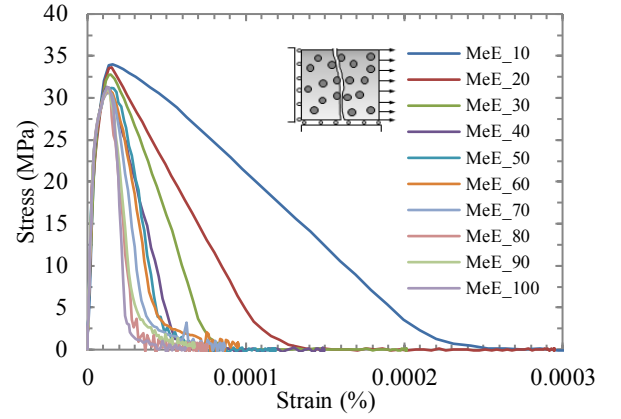
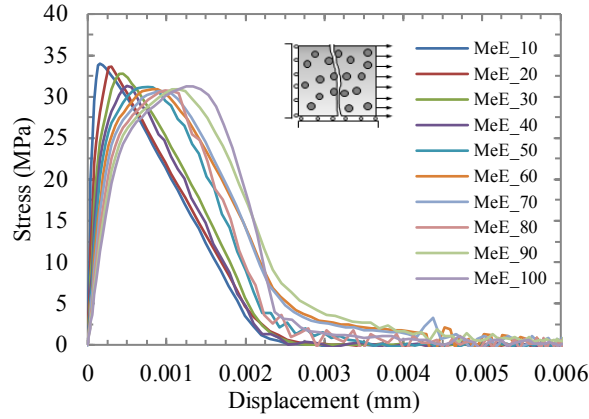
Secondly, the reliability of the proposed X-ray CT testing, imaging and reconstruction to image-based modelling framework can be verified part by part and used with other CFRP datasets available from the testing repository. Several research directions may develop from the reconstruction methodology herein, for example, analyses and in-situ quantification of kink-band failure mechanisms, quantification of localised damage and failure mechanism to global component mechanics, quantification of different fabric and manufacturing parameters, image-based modelling of various fibre reinforced material systems.

The image-based modelling also opens various opportunities towards realistic multi-physics, shape and deformation analyses (with realistic volume fractions, fibre distributions, labelled phases and interfaces), deformation tracking, local to global multiscale interactions and visualisation of realistic 3D fibre reinforced composites. Given the simplicity of the proposed modelling framework, it can be linked in the future with multiscale models that incorporate more than two scales and mesh insensitive heterogeneities (e.g. ultra-fine voids, uniformly distributed porosity etc.).

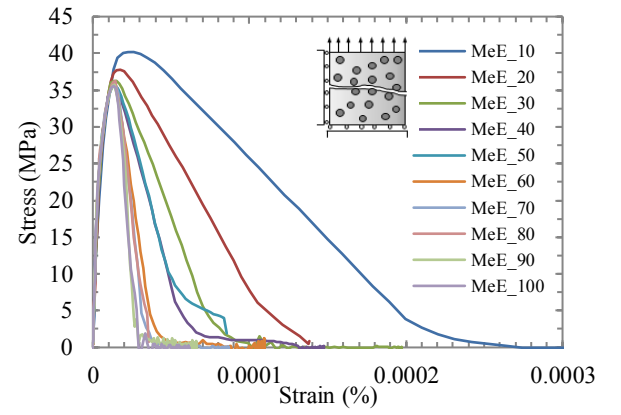
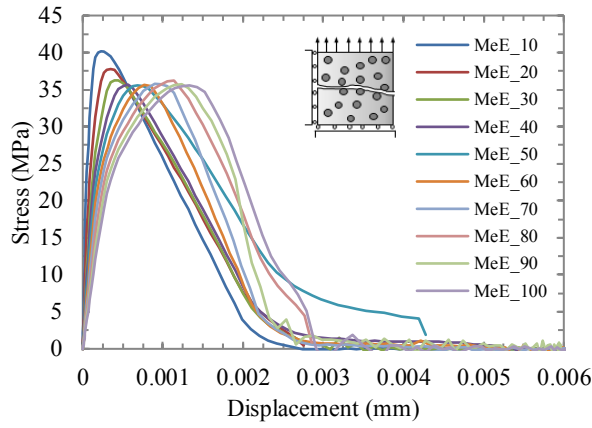
Finally, as demonstrated by the various sensitivity analyses carried out in 2D and 3D, the cohesive interface crack model is capable modelling of complicated failure mechanisms in FRP under quasi-brittle loading conditions. It may also be extended to model dynamic scenarios, such as FRP plates under impact and blast with further development of constitutive relations.

APPENDIX-A: 2D MESO-SCALE STRESS-DISPLACEMENT AND STRESS STRAIN RESPONSES

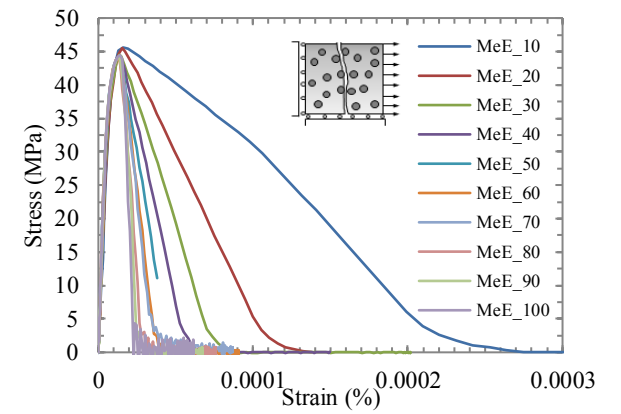
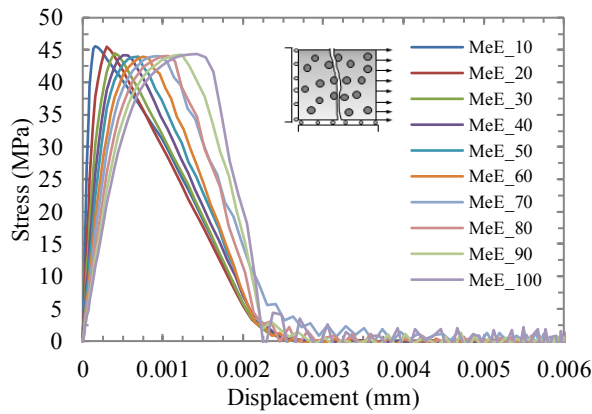
B1-X/ W



B1-Y/ W



B1-X/ S



B1-Y/ S

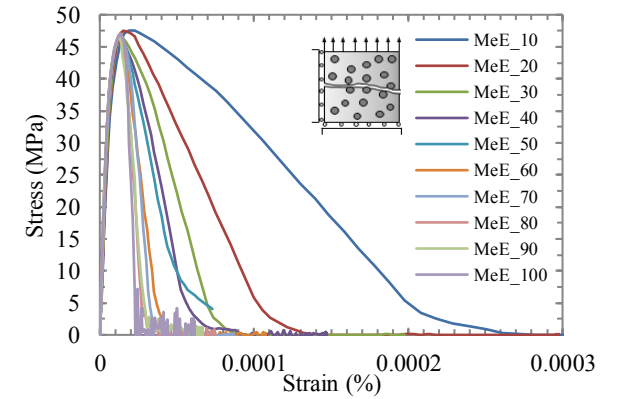
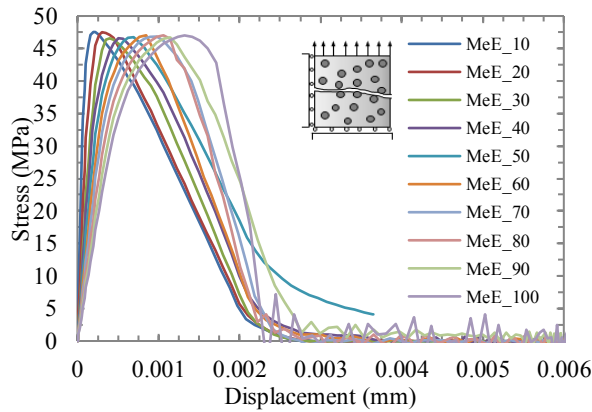
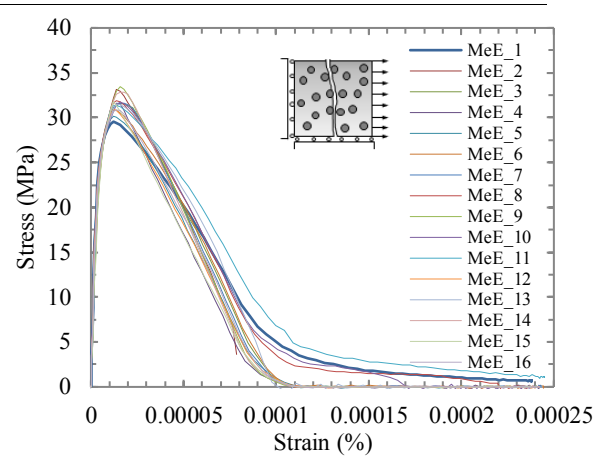
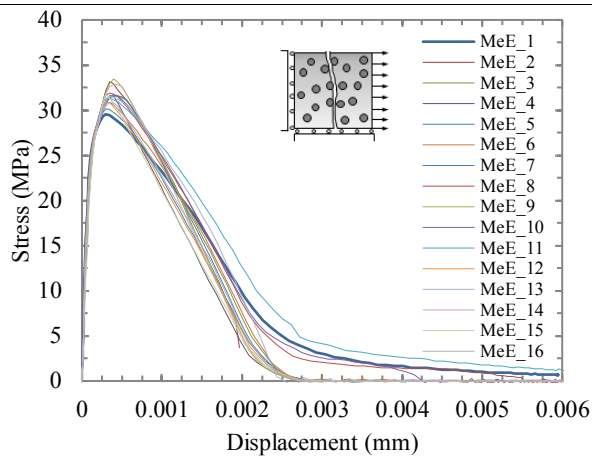
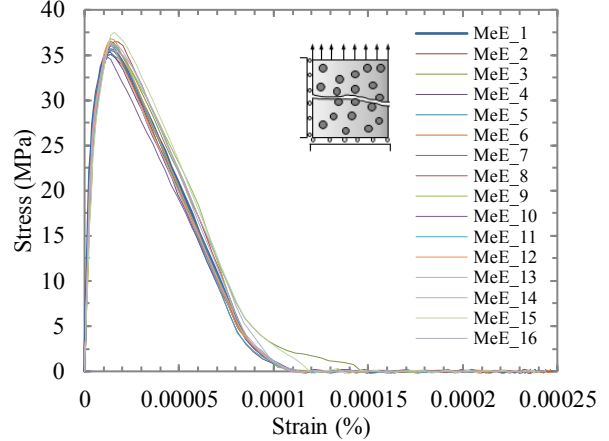
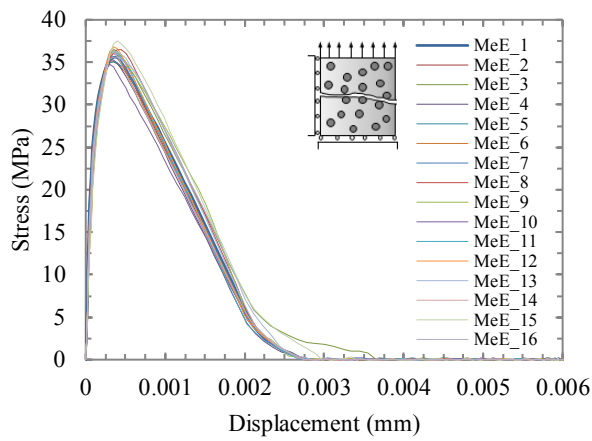


Fig. A-1: Stress-displacement and stress-strain curves for B1 boundary conditions for MeE step 10 to 100 μm using weak interface (a, b) and strong interface properties (c,d).

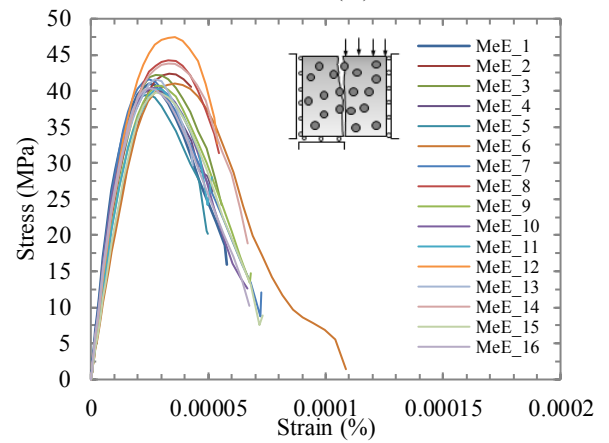
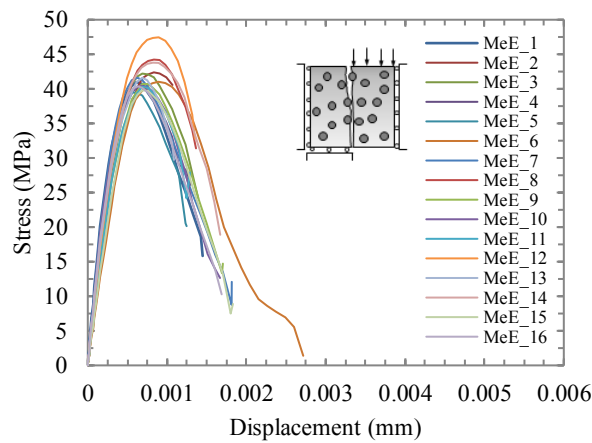
B1-X/ W



B1-Y/ W



B2-X/ W



B2-Y/ W

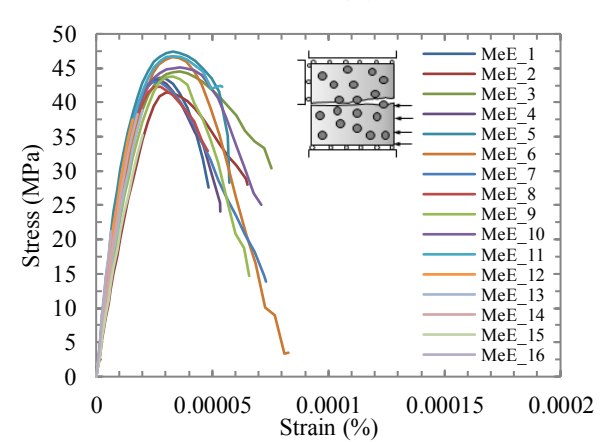
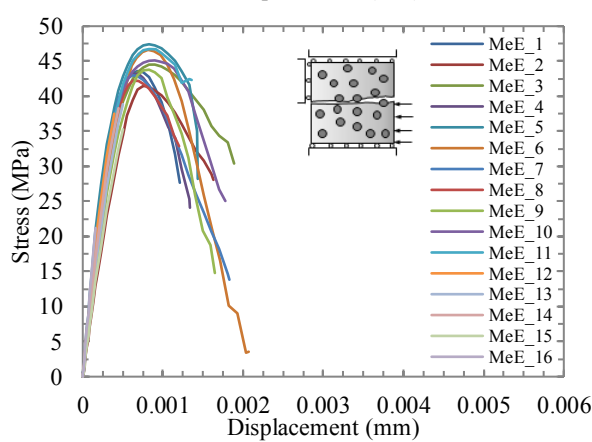


Fig. A-2: Stress-displacement and stress-strain curves for the non-overlapping series

MeE-16 \times 25/W: $t_{n,s}$ =25 MPa, $G_{11,22}$ =25 N/mm.

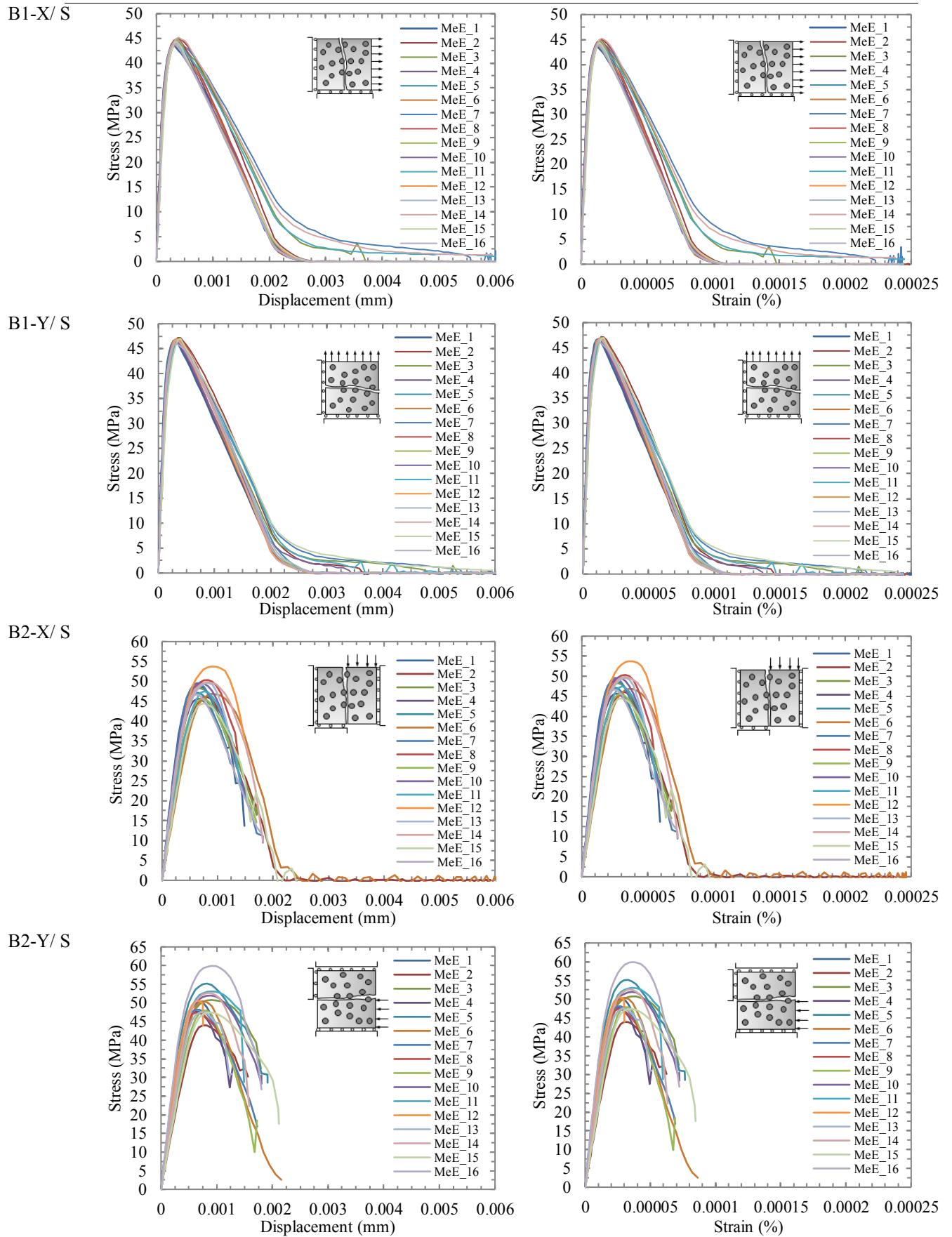
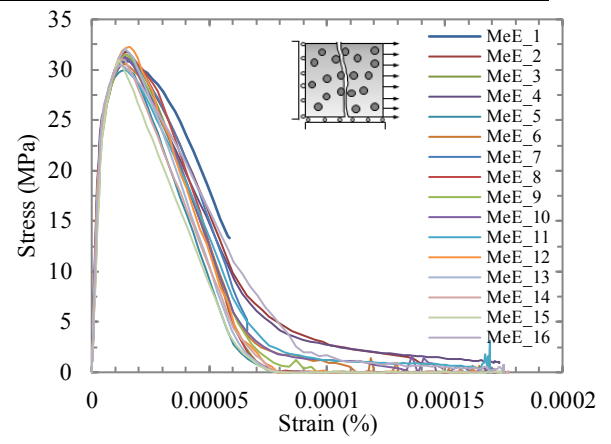
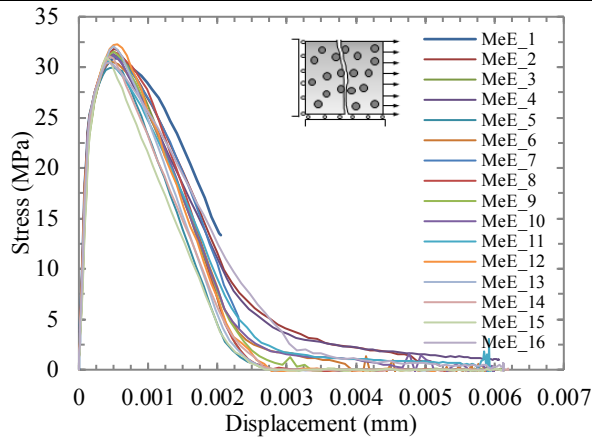


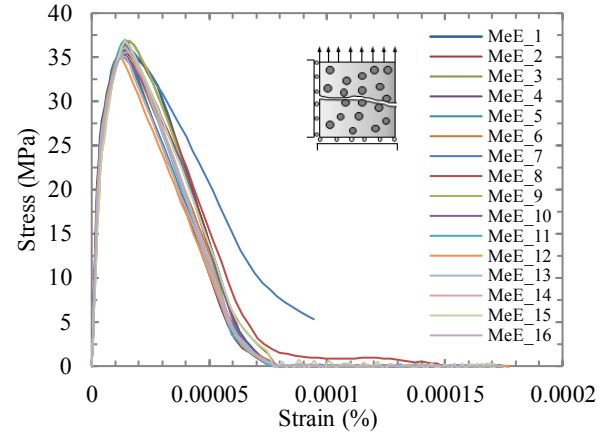
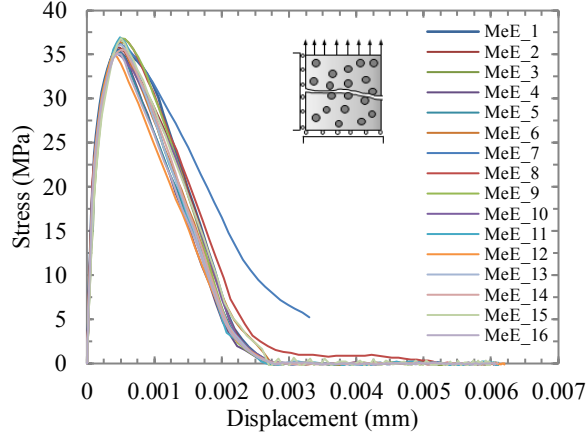
Fig. A-3: Stress-displacement and stress-strain curves for the non-overlapping series

MeE-16×25/S: $t_{n,s}=40$ MPa, $G_{11,22}=40$ N/mm.

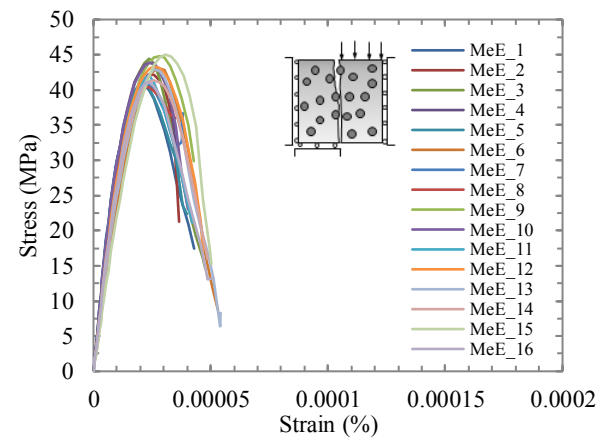
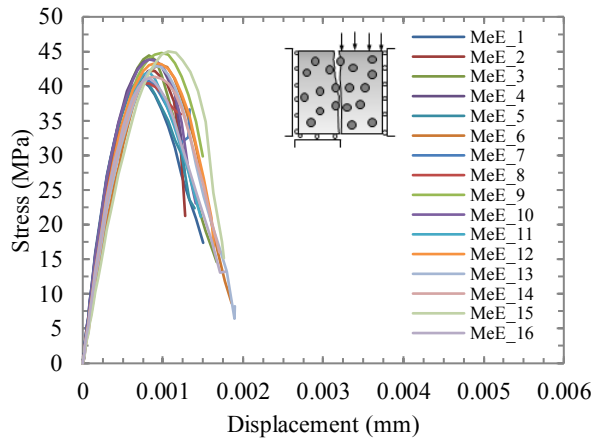
B1-X/ W



B1-Y/ W



B2-X/ W



B2-Y/ W

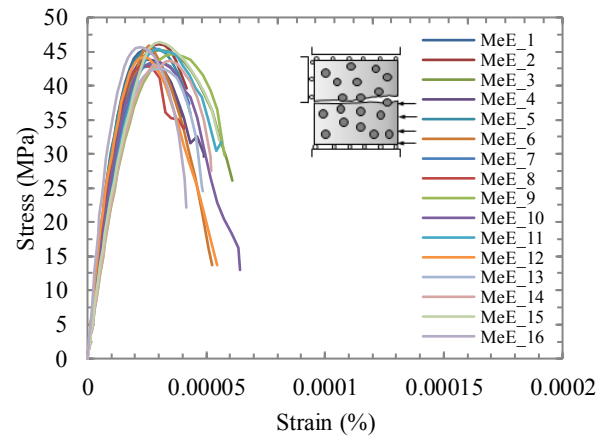
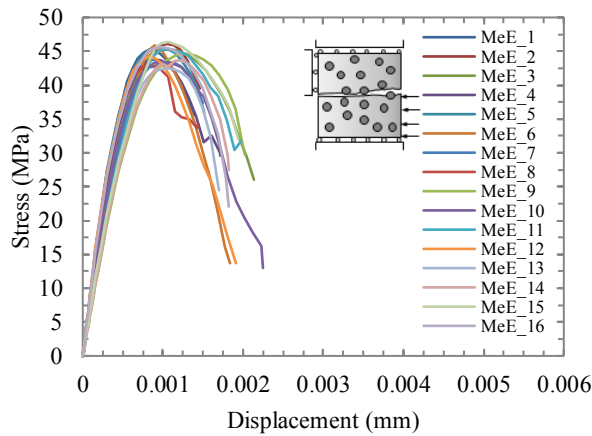
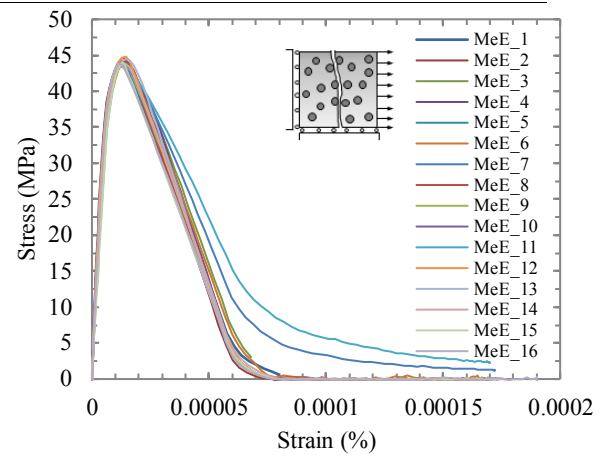
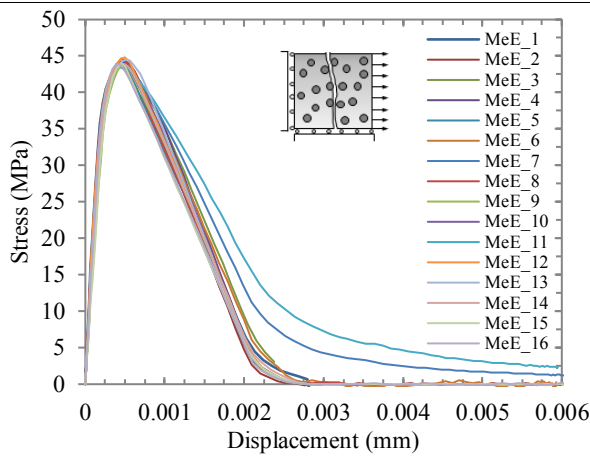


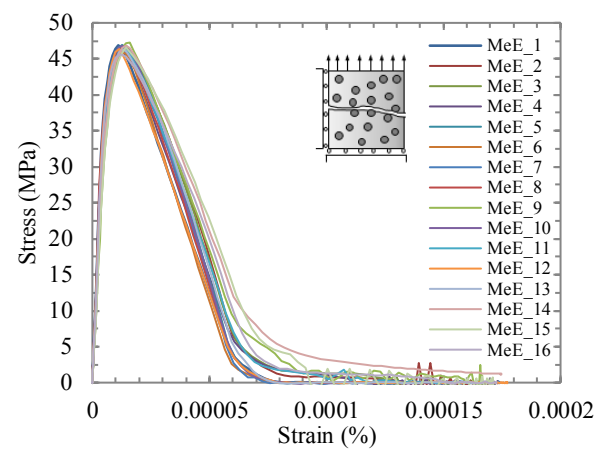
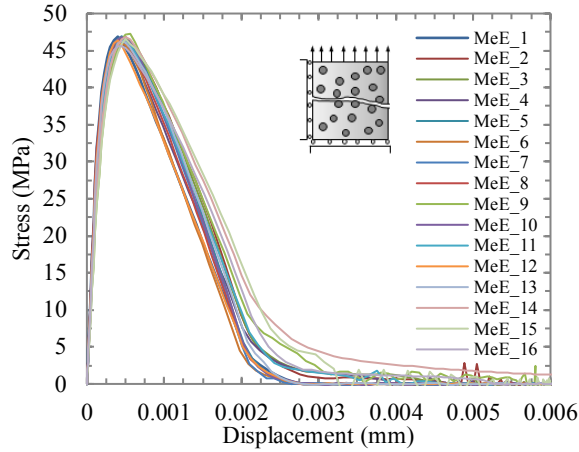
Fig. A-4: Stress-displacement and stress-strain curves for the overlapping series

MeE-16×35/W: $t_{n,s}=25$ MPa, $G_{11,22}=25$ N/mm.

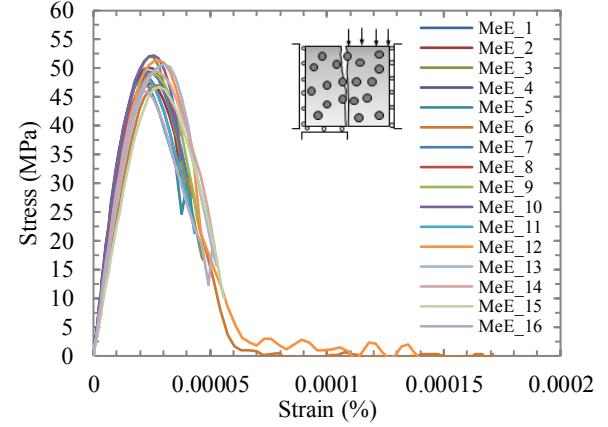
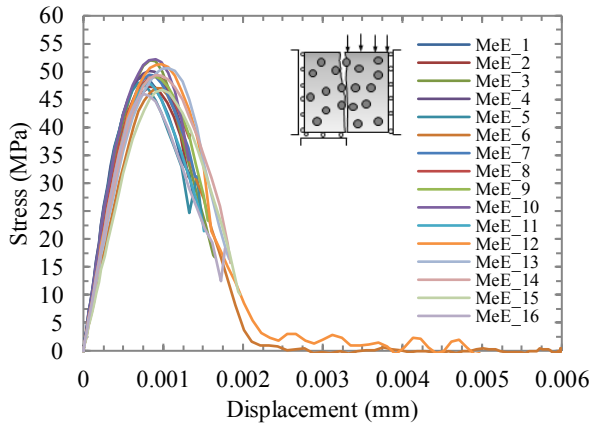
B1-X/ S



B1-Y/ S



B2-X/ S



B2-Y/ S

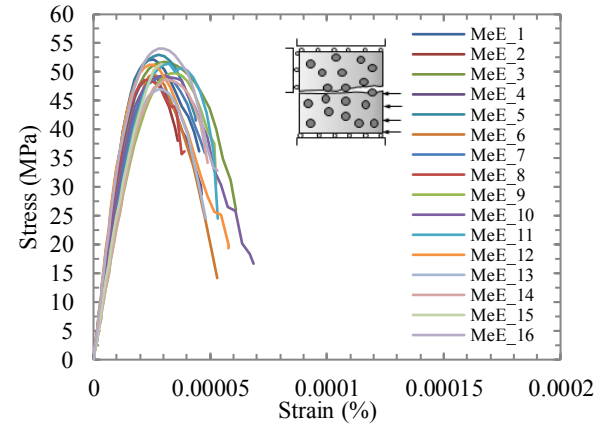
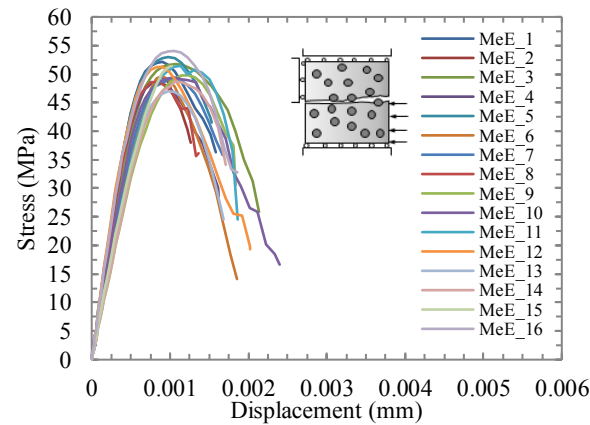
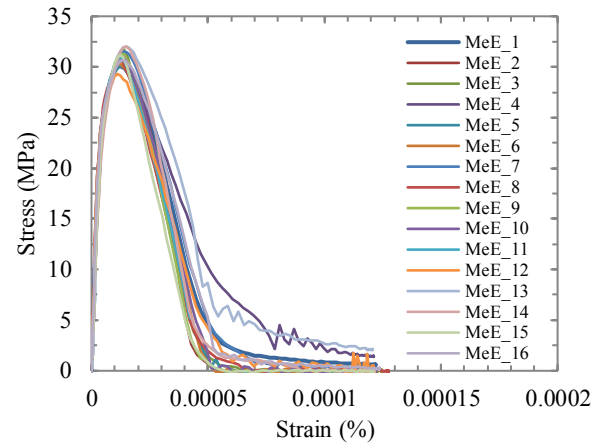
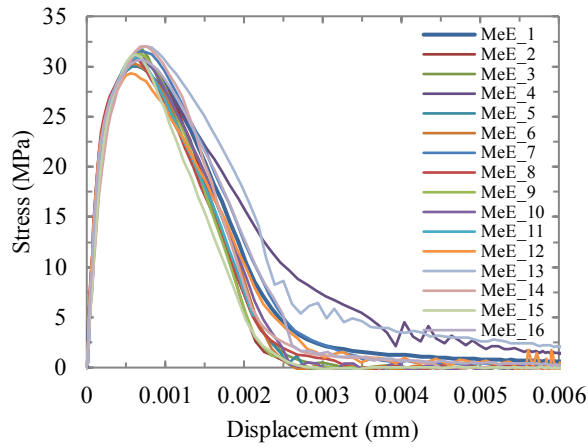


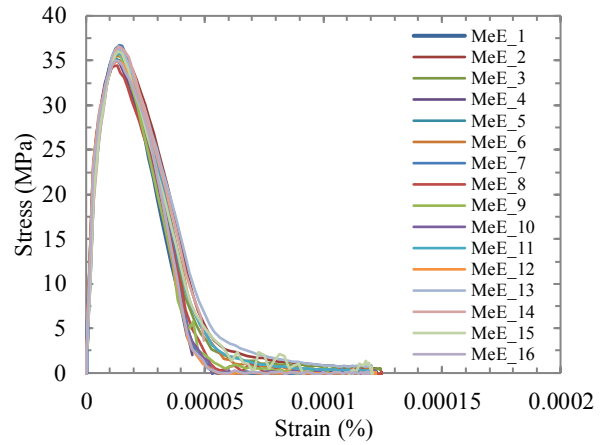
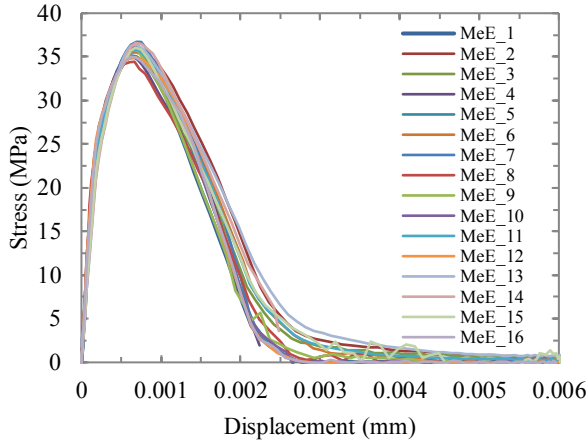
Fig. A-5: Stress-displacement and stress-strain curves for the overlapping series

MeE-16×35/S: $t_{n,s}=40$ MPa, $G_{11,22}=40$ N/mm.

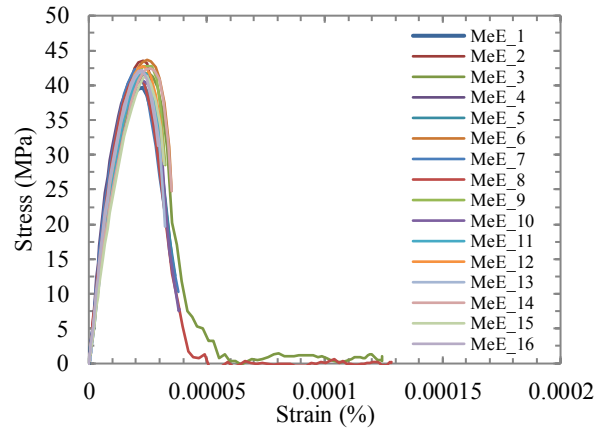
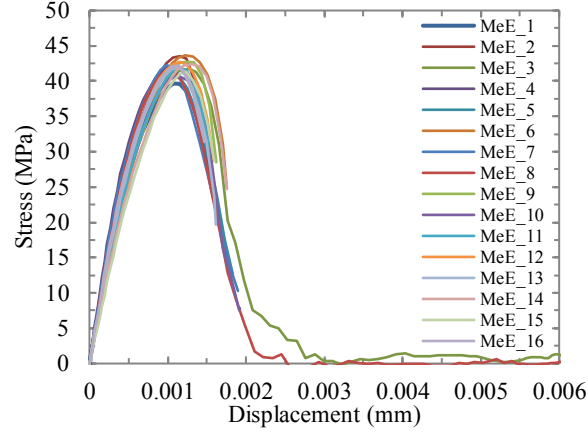
B1-X/ W



B1-Y/ W



B2-X/ W



B2-Y/ W

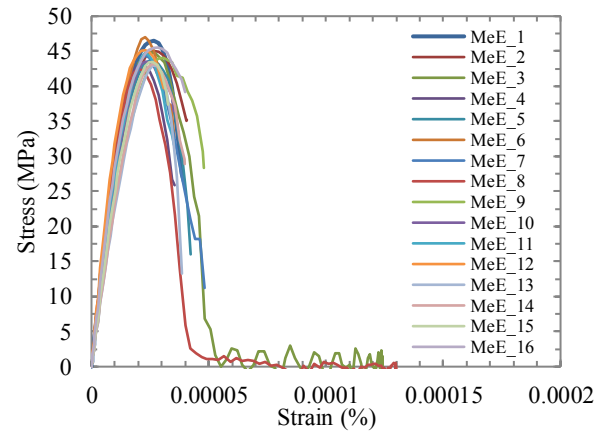
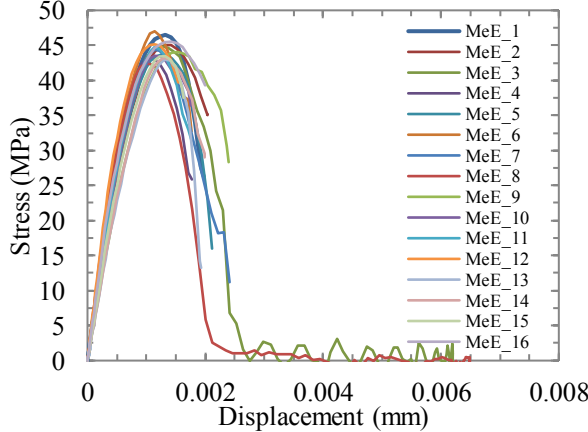
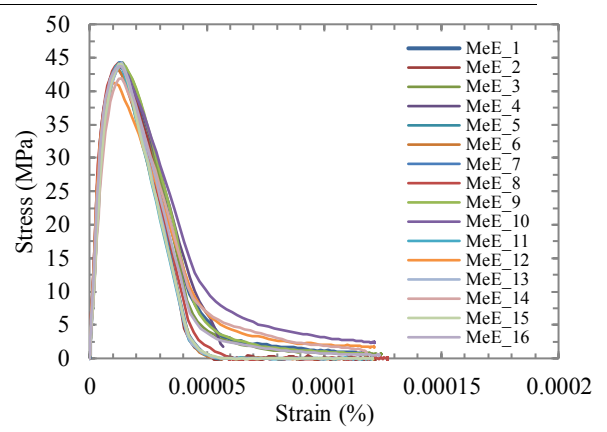
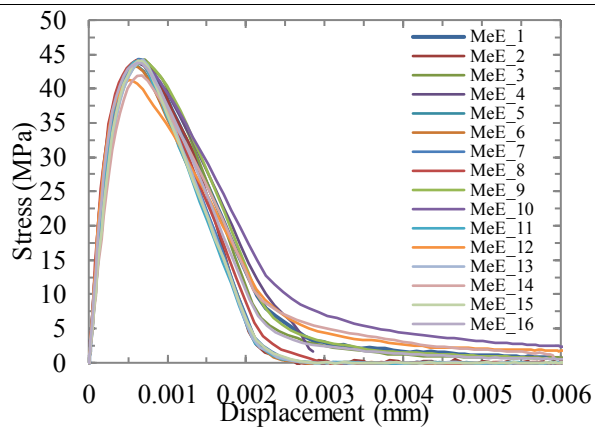


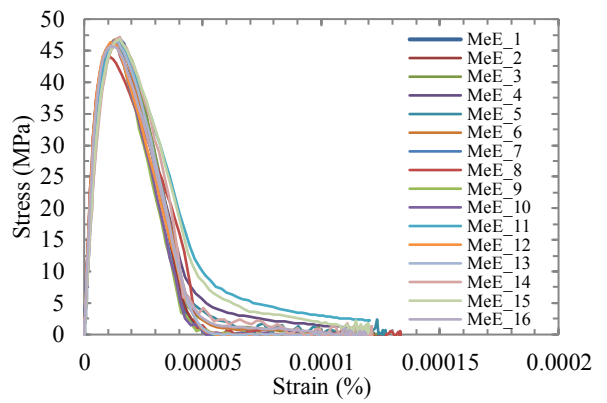
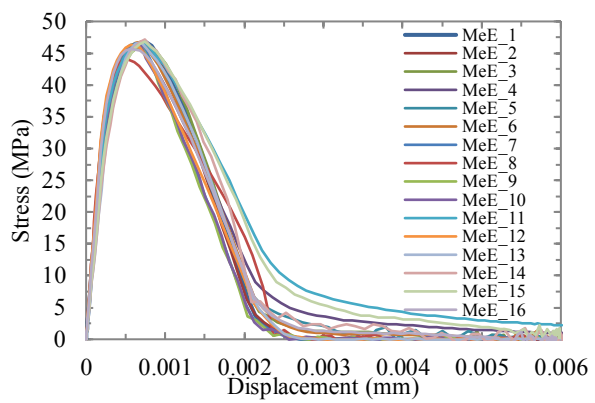
Fig. A-6: Stress-displacement and stress-strain curves for the overlapping series

MeE-16 \times 50/W: $t_{n,s}=25$ MPa, $G_{11,22}=25$ N/mm.

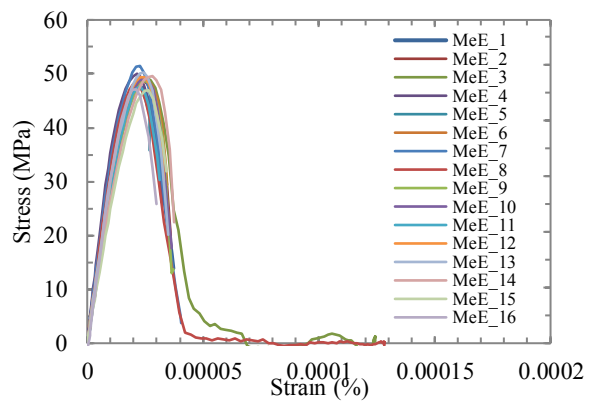
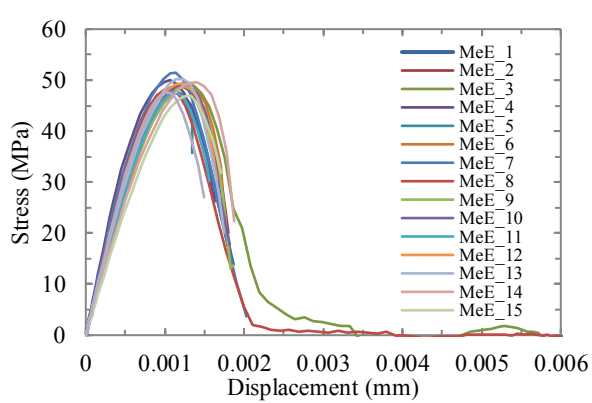
B1-X/ S



B1-Y/ S



B2-X/ S



B2-Y/ S

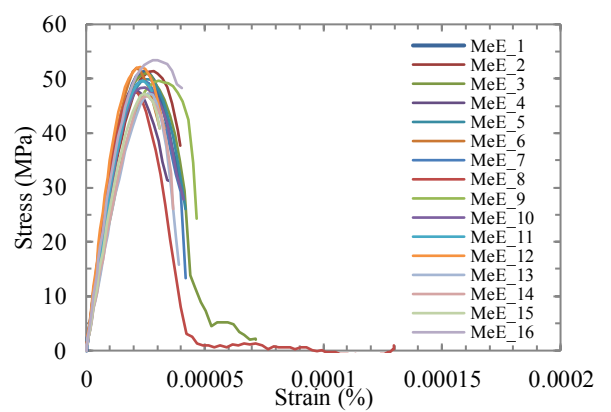
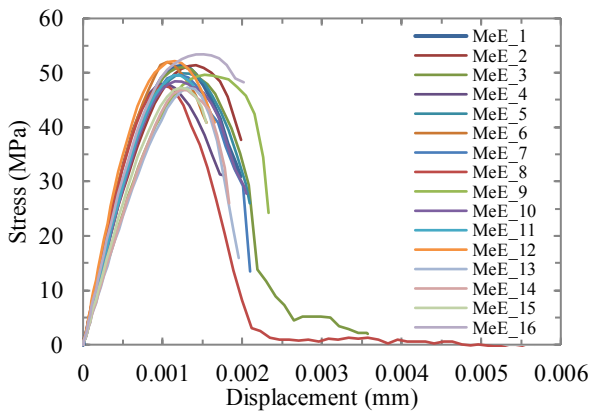


Fig. A-7: Stress-displacement and stress-strain curves for the overlapping series

MeE-16 \times 50/S: $t_{n,s}$ =40 MPa, $G_{11,22}$ =40 N/mm.

REFERENCES

- Aarnes, J. E., Krogstad, S. & Lie, K.-A. (2006) A Hierarchical Multiscale Method for Two-Phase Flow Based upon Mixed Finite Elements and Nonuniform Coarse Grids. *Multiscale Modeling & Simulation*, 5(2), 337-363.
- Amini, S. & Kumar, R. S. (2014) A high-fidelity strain-mapping framework using digital image correlation. *Materials Science and Engineering: A*, 594(0), 394-403.
- Bale, H. A., Haboub, A., MacDowell, A. A., Nasiatka, J. R., Parkinson, D. Y., Cox, B. N., Marshall, D. B. & Ritchie, R. O. (2012) Real-time quantitative imaging of failure events in materials under load at temperatures above 1,600 °C.
- Barenblatt, G. I. (1959) The formation of equilibrium cracks during brittle fracture: general ideas and hypothesis, axially symmetric cracks. *Applied Mathematics and Mechanics* 23, 622–636.
- Basham, M., Filik, J., Wharmby, M. T., Chang, P. C. Y., El Kassaby, B., Gerring, M., Aishima, J., Levik, K., Pulford, B. C. A., Sikharulidze, I., Sneddon, D., Webber, M., Dhesi, S. S., Maccherozzi, F., Svensson, O., Brockhauser, S., Naray, G. & Ashton, A. W. (2015) Data Analysis WorkbeNch (DAWN). *Journal of Synchrotron Radiation*, 22(3), 853-858.
- Bažant, Z. & Oh, B. (1983) Crack band theory for fracture of concrete. *Materials and Structures*, 16(3), 155-177.
- Belytschko, T. (2007) Research directions in computational and composite mechanics. *A Report of the United States National Committee on Theoretical and Applied Mechanics*.
- Belytschko, T., Loehnert, S. & Song, J.-H. (2008) Multiscale aggregating discontinuities: A method for circumventing loss of material stability. *International Journal for Numerical Methods in Engineering*, 73(6), 869-894.
- Bliznakova, K., Russo, P., Mettivier, G., Requardt, H., Popov, P., Bravin, A. & Buliev, I. (2015) A software platform for phase contrast x-ray breast imaging research. *Comput Biol Med*, 61, 62-74.
- Bosco, E., Kouznetsova, V. G. & Geers, M. G. D. (2015) Multi-scale computational homogenization-localization for propagating discontinuities using X-FEM. *International Journal for Numerical Methods in Engineering*, 102(3-4), 496-527.
- Calo, V. M., Efendiev, Y., Galvis, J. & Ghommem, M. (2014) Multiscale empirical interpolation for solving nonlinear PDEs. *Journal of Computational Physics*, 278, 204-220.
- Canal, L. P., González, C., Segurado, J. & Llorca, J. (2012) Intraply fracture of fiber-reinforced composites: Microscopic mechanisms and modeling. *Composites Science and Technology*, 72(11), 1223-1232.
- Carpinteri, A. (1989) Softening and snap-back instability in cohesive solids. *International Journal for Numerical Methods in Engineering*, 28(7), 1521-1537.
- Carpinteri, A. & Chiaia, B. (1997) Multifractal Scaling Laws in the Breaking Disordered Materials.
- Carpinteri, A., Chiaia, B. & Cornetti, P. (2002) A scale-invariant cohesive crack model for quasi-brittle materials. *Engineering Fracture Mechanics*, 69(2), 207-217.

- Chen, Y., Durlofsky, L. J., Gerritsen, M. & Wen, X. H. (2003) A coupled local–global upscaling approach for simulating flow in highly heterogeneous formations. *Advances in Water Resources*, 26(10), 1041-1060.
- Chung, E. T., Efendiev, Y. & Fu, S. (2014) Generalized Multiscale Finite Element Method for Elasticity Equations. *ArXiv e-prints*, (1408.5929).
- Cid Alfaro, M. V., Suiker, A. S. J. & de Borst, R. (2010a) Transverse Failure Behavior of Fibre-epoxy Systems. *Journal of Composite Materials*.
- Cid Alfaro, M. V., Suiker, A. S. J., Verhoosel, C. V. & de Borst, R. (2010b) Numerical homogenization of cracking processes in thin fibre-epoxy layers. *European Journal of Mechanics - A/Solids*, 29(2), 119-131.
- Clément, A., Soize, C. & Yvonnet, J. (2013) Uncertainty quantification in computational stochastic multiscale analysis of nonlinear elastic materials. *Computer Methods in Applied Mechanics and Engineering*, 254(0), 61-82.
- Coenen, E. W. C., Kouznetsova, V. G., Bosco, E. & Geers, M. G. D. (2012a) A multi-scale approach to bridge microscale damage and macroscale failure: a nested computational homogenization-localization framework. *International Journal of Fracture*, 178(1-2), 157-178.
- Coenen, E. W. C., Kouznetsova, V. G. & Geers, M. G. D. (2012b) Multi-scale continuous–discontinuous framework for computational-homogenization–localization. *Journal of the Mechanics and Physics of Solids*, 60(8), 1486-1507.
- Coenen, E. W. C., Kouznetsova, V. G. & Geers, M. G. D. (2012c) Novel boundary conditions for strain localization analyses in microstructural volume elements. *International Journal for Numerical Methods in Engineering*, 90(1), 1-21.
- Coindreau, O., Mulat, C., Germain, C., Lachaud, J. & Vignoles, G. L. (2011) Benefits of X-Ray CMT for the Modeling of C/C Composites. *Advanced Engineering Materials*, 13(3), 178-185.
- Coindreau, O., Vignoles, G. & Cloetens, P. (2003) Direct 3D microscale imaging of carbon–carbon composites with computed holotomography. *Nuclear Instruments and Methods in Physics Research Section B: Beam Interactions with Materials and Atoms*, 200(0), 308-314.
- Comte, F. & Genon-Catalot, V. (2012) Convolution power kernels for density estimation. *Journal of Statistical Planning and Inference*, 142(7), 1698-1715.
- Cusatis, G. & Cedolin, L. (2007) Two-scale study of concrete fracturing behavior. *Engineering Fracture Mechanics*, 74(1-2), 3-17.
- Czabaj, M. W., Riccio, M. L. & Whitacre, W. W. (2014) Numerical reconstruction of graphite/epoxy composite microstructure based on sub-micron resolution X-ray computed tomography. *Composites Science and Technology*, 105(0), 174-182.
- de Borst, R. (2003) Numerical aspects of cohesive-zone models. *Engineering Fracture Mechanics*, 70(14), 1743-1757.
- de Borst, R. (2008) Challenges in computational materials science: Multiple scales, multi-physics and evolving discontinuities. *Computational Materials Science*, 43(1), 1-15.
- de Frías, G. J., Aquino, W., Pierson, K. H., Heinsteins, M. W. & Spencer, B. W. (2014) A multiscale mass scaling approach for explicit time integration using proper orthogonal

- decomposition. *International Journal for Numerical Methods in Engineering*, 97(11), 799-818.
- DEBEN. Micro- loading rig CT500.
- Desmorat, R. & Lemaitre, J. (2001) A Two-Scale Model for Quasi-Brittle and Fatigue Damage. In: Jean, L. (ed.) *Handbook of Materials Behavior Models*. Burlington: Academic Press.
- Diamond. (2016) Website [Online]. Available: http://www.diamond.ac.uk/Beamlines/Materials/I13/Diamond-Manchester_Imaging_Branchline/Facilities_and_equipment_Imaging.html [Accessed].
- Doškář, M. & Novák, J. (2013) Compression of Heterogeneous Material Systems Based on Wang Tilings. *Key Engineering Materials*, 592-593, 149-152.
- Dugdale, D. S. (1960) Yielding of steel sheets containing slits. *Journal of the Mechanics and Physics of Solids*, 8(2), 100-104.
- Efendiev, Y., Galvis, J., Li, G. & Presho, M. (2014) Generalized multiscale finite element methods: Oversampling strategies. 12(6), 465-484.
- Efendiev, Y., Hou, T. Y. & Ginting, V. (2004) Multiscale Finite Element Methods for Nonlinear Problems and Their Applications. 553-589.
- Endrizzi, M., Diemoz, P. C., Munro, P. R. T., Hagen, C. K., Szafraniec, M. B., Millard, T. P., Zapata, C. E., Speller, R. D. & Olivo, A. (2013) Applications of a non-interferometric x-ray phase contrast imaging method with both synchrotron and conventional sources. *Journal of Instrumentation*, 8(05), C05008-C05008.
- Enfedaque, A., Molina-Aldareguía, J. M., Gálvez, F., González, C. & LLorca, J. (2010) Effect of Glass Fiber Hybridization on the Behavior Under Impact of Woven Carbon Fiber/Epoxy Laminates. *Journal of Composite Materials*.
- Epanechnikov, V. (1969) Non-Parametric Estimation of a Multivariate Probability Density. *Theory of Probability & Its Applications*, 14(1), 153-158.
- FEI/Avizo. Software Version Avizo 8 Fire - Educational License at University of Manchester.
- Ferreira, T. & Rasband, W. (2011) The ImageJ User Guide, The Process . Find Maxima. . . command is based on a plugin contributed by Michael
- Schmid. 1.44.
- Fish, J. (2011) Multiscale Modeling and Simulation of Composite Materials and Structures Multiscale Methods in Computational Mechanics. In: de Borst, R. & Ramm, E. (eds.). Springer Berlin / Heidelberg.
- Fish, J. & Shek, K. (1999) Finite deformation plasticity for composite structures: Computational models and adaptive strategies. *Computer Methods in Applied Mechanics and Engineering*, 172(1-4), 145-174.
- Fu, J., Biernath, T., Willner, M., Amberger, M., Meiser, J., Kunka, D., Mohr, J., Herzen, J., Bech, M. & Pfeiffer, F. (2014) Cone-beam differential phase-contrast laminography with x-ray tube source. *EPL (Europhysics Letters)*, 106(6), 68002.
- Gálvez, J. C., Červenka, J., Cendón, D. A. & Saouma, V. (2002) A discrete crack approach to normal/shear cracking of concrete. *Cement and Concrete Research*, 32(10), 1567-1585.

- Gao, K., Fu, S., Gibson Jr, R. L., Chung, E. T. & Efendiev, Y. (2014) Generalized Multiscale Finite-Element Method (GMsFEM) for elastic wave propagation in heterogeneous, anisotropic media.
- Gasser, T. C. & Holzapfel, G. A. (2005) Modeling 3D crack propagation in unreinforced concrete using PUFEM. *Computer Methods in Applied Mechanics and Engineering*, 194(25–26), 2859-2896.
- Geers, M. G. D., Kouznetsova, V. G. & Brekelmans, W. A. M. (2010) Multi-scale computational homogenization: Trends and challenges. *Journal of Computational and Applied Mathematics*, 234(7), 2175-2182.
- Ghosh, S. (2008) Adaptive Concurrent Multi-Level Model for Multiscale Analysis of Composite Materials Including Damage. Springer US.
- Ghosh, S., Bai, J. & Raghavan, P. (2007) Concurrent multi-level model for damage evolution in microstructurally debonding composites. *Mechanics of Materials*, 39(3), 241-266.
- Ghosh, S. & Paquet, D. (2013) Adaptive concurrent multi-level model for multi-scale analysis of ductile fracture in heterogeneous aluminum alloys. *Mechanics of Materials*, 65(0), 12-34.
- Gitman, I. M., Askes, H. & Sluys, L. J. (2007) Representative volume: Existence and size determination. *Engineering Fracture Mechanics*, 74(16), 2518-2534.
- Gitman, I. M., Askes, H. & Sluys, L. J. (2008) Coupled-volume multi-scale modelling of quasi-brittle material. *European Journal of Mechanics - A/Solids*, 27(3), 302-327.
- González, C. & Llorca, J. (2006) Multiscale modeling of fracture in fiber-reinforced composites. *Acta Materialia*, 54(16), 4171-4181.
- González, C. & Llorca, J. (2007a) Mechanical behavior of unidirectional fiber-reinforced polymers under transverse compression: Microscopic mechanisms and modeling. *Composites Science and Technology*, 67(13), 2795-2806.
- González, C. & Llorca, J. (2007b) Virtual fracture testing of composites: A computational micromechanics approach. *Engineering Fracture Mechanics*, 74(7), 1126-1138.
- Graham, S. & Yang, N. (2002) Representative volumes of materials based on microstructural statistics.
- Greco, F., Leonetti, L. & Lonetti, P. (2013) A two-scale failure analysis of composite materials in presence of fiber/matrix crack initiation and propagation. *Composite Structures*, 95(0), 582-597.
- Guilleminot, J., Soize, C. & Kondo, D. (2009) Mesoscale probabilistic models for the elasticity tensor of fiber reinforced composites: Experimental identification and numerical aspects. *Mechanics of Materials*, 41(12), 1309-1322.
- Habibi, M., Bafandeh, A. & Montazerolghaem, M. A. (2014) A digital array based bit serial processor for arbitrary window size kernel convolution in vision sensors. *Integration, the VLSI Journal*, 47(4), 417-430.
- Hamad, F. A.-H., Giacomo, L. & Surya, R. K. (2012) Multi-scale modeling of the elastic response of a structural component made from a composite material using the materials knowledge system. *Modelling and Simulation in Materials Science and Engineering*, 20(5), 055001.

- Hashin, Z. (1965) On elastic behaviour of fibre reinforced materials of arbitrary transverse phase geometry. *Journal of the Mechanics and Physics of Solids*, 13(3), 119-134.
- Hautefeuille, M., Colliat, J. B., Ibrahimbegovic, A., Matthies, H. G. & Villon, P. (2012) A multi-scale approach to model localized failure with softening. *Computers & Structures*, 94-95, 83-95.
- Hill, R. (1963) Elastic properties of reinforced solids: Some theoretical principles. *Journal of the Mechanics and Physics of Solids*, 11(5), 357-372.
- Hillerborg, A., Mod  r, M. & Petersson, P. E. (1976) Analysis of crack formation and crack growth in concrete by means of fracture mechanics and finite elements. *Cement and Concrete Research*, 6(6), 773-781.
- Hou, T. Y. & Wu, X.-H. (1997) A Multiscale Finite Element Method for Elliptic Problems in Composite Materials and Porous Media. *Journal of Computational Physics*, 134(1), 169-189.
- Huang, Y., Yang, Z., Ren, W., Liu, G. & Zhang, C. (2015) 3D meso-scale fracture modelling and validation of concrete based on in-situ X-ray Computed Tomography images using damage plasticity model. *International Journal of Solids and Structures*, 67-68, 340-352.
- ImageJ. Opensource Software Version 1.60 - Public License at URL: <https://imagej.nih.gov/ij/>.
- Kabele, P. (2007) Multiscale framework for modeling of fracture in high performance fiber reinforced cementitious composites. *Engineering Fracture Mechanics*, 74(1-2), 194-209.
- Kaczmarczyk, L., Pearce, C. J. & Bi  ani  , N. (2008) Scale transition and enforcement of RVE boundary conditions in second-order computational homogenization. *International Journal for Numerical Methods in Engineering*, 74(3), 506-522.
- Kaczmarczyk, L., Pearce, C. J., Bi  ani  , N. & de Souza Neto, E. (2010) Numerical multiscale solution strategy for fracturing heterogeneous materials. *Computer Methods in Applied Mechanics and Engineering*, 199(17-20), 1100-1113.
- Kanout  , P., Boso, D., Chaboche, J. & Schrefler, B. (2009) Multiscale Methods for Composites: A Review. *Archives of Computational Methods in Engineering*, 16(1), 31-75.
- Karpov, E. G., Yu, H., Park, H. S., Liu, W. K., Wang, Q. J. & Qian, D. (2006) Multiscale boundary conditions in crystalline solids: Theory and application to nanoindentation. *International Journal of Solids and Structures*, 43(21), 6359-6379.
- Kassner, M. E., Nemat-Nasser, S., Suo, Z., Bao, G., Barbour, J. C., Brinson, L. C., Espinosa, H., Gao, H., Granick, S., Gumbsch, P., Kim, K.-S., Knauss, W., Kubin, L., Langer, J., Larson, B. C., Mahadevan, L., Majumdar, A., Torquato, S. & van Swol, F. (2005) New directions in mechanics. *Mechanics of Materials*, 37(2-3), 231-259.
- Kinney, J. H. & Nichols, M. C. (1992) X-ray tomographic microscopy (XTM) using synchrotron radiation.
- Kouznetsova, V. G., Geers, M. G. D. & Brekelmans, W. A. M. (2004) Multi-scale second-order computational homogenization of multi-phase materials: a nested finite element solution strategy. *Computer Methods in Applied Mechanics and Engineering*, 193(48-51), 5525-5550.

- Kwak, H. G. & Filippou, F. C. (1990) Finite element analysis of reinforced concrete structures under monotonic loads. *A Report on Research Conducted under Grant RTA-59M848 from the California Department of Transportation*.
- Kyrleis, A., Ibison, M., Titarenko, V. & Withers, P. J. (2009) Image stitching strategies for tomographic imaging of large objects at high resolution at synchrotron sources. *Nuclear Instruments and Methods in Physics Research Section A: Accelerators, Spectrometers, Detectors and Associated Equipment*, 607(3), 677-684.
- Landi, G., Niezgoda, S. R. & Kalidindi, S. R. (2010) Multi-scale modeling of elastic response of three-dimensional voxel-based microstructure datasets using novel DFT-based knowledge systems. *Acta Materialia*, 58(7), 2716-2725.
- Larsson, F. & Runesson, K. (2011) On two-scale adaptive FE analysis of micro-heterogeneous media with seamless scale-bridging. *Computer Methods in Applied Mechanics and Engineering*, 200(37-40), 2662-2674.
- Latil, P., Orgéas, L., Geindreau, C., Dumont, P. J. J. & Rolland du Roscoat, S. (2011) Towards the 3D in situ characterisation of deformation micro-mechanisms within a compressed bundle of fibres. *Composites Science and Technology*, 71(4), 480-488.
- Li, J. (2011) Establishment of strain gradient constitutive relations by homogenization. *Comptes Rendus Mécanique*, 339(4), 235-244.
- Li, Y., McDowell, D. L. & Zhou, M. (2013) Computational prediction of fracture toughness of polycrystalline metals. *13th International Conference on Fracture, Beijing, China*, (June 16–21, 2013).
- Li, Y. & Zhou, M. (2013a) Prediction of fracture toughness of ceramic composites as function of microstructure: I. Numerical simulations. *Journal of the Mechanics and Physics of Solids*, 61(2), 472-488.
- Li, Y. & Zhou, M. (2013b) Prediction of fracture toughness of ceramic composites as function of microstructure: II. analytical model. *Journal of the Mechanics and Physics of Solids*, 61(2), 489-503.
- Liu, B., Raabe, D., Roters, F., Eisenlohr, P. & Lebensohn, R. A. (2010) Comparison of finite element and fast Fourier transform crystal plasticity solvers for texture prediction. *Modelling and Simulation in Materials Science and Engineering*, 18(8), 085005.
- Liu, G. R., Ma, W. B. & Han, X. (2002) An inverse procedure for identification of loads on composite laminates. *Composites Part B: Engineering*, 33(6), 425-432.
- Llorca, J., González, C., Molina-Aldareguía, J. M. & López, C. S. (2013) Multiscale Modeling of Composites: Toward Virtual Testing ... and Beyond. *JOM*, 65(2), 215-225.
- Loehnert, S. & Belytschko, T. (2007) A multiscale projection method for macro/microcrack simulations. *International Journal for Numerical Methods in Engineering*, 71(12), 1466-1482.
- Lopes, C. S., Sádaba, S., González, C., Llorca, J. & Camanho, P. P. (2015) Physically-sound simulation of low-velocity impact on fiber reinforced laminates. *International Journal of Impact Engineering*.
- Luscher, D. J., McDowell, D. L. & Bronkhorst, C. A. (2010) A second gradient theoretical framework for hierarchical multiscale modeling of materials. *International Journal of Plasticity*, 26(8), 1248-1275.

- Maire, E. & Withers, P. J. (2013) Quantitative X-ray tomography. *International Materials Reviews*, 59(1), 1-43.
- Markovic, D. & Ibrahimbegovic, A. (2004) On micro–macro interface conditions for micro scale based FEM for inelastic behavior of heterogeneous materials. *Computer Methods in Applied Mechanics and Engineering*, 193(48–51), 5503-5523.
- Markus, P. (2007) Modellierung von Rissausbreitung unter Verwendung der p-Version der XFEM mit einer adaptiven Integrauibsmethode. *PhD Thesis, Ruhr University, Germany*.
- Matsuda, T., Ohno, N., Tanaka, H. & Shimizu, T. (2003) Effects of fiber distribution on elastic–viscoplastic behavior of long fiber-reinforced laminates. *International Journal of Mechanical Sciences*, 45(10), 1583-1598.
- McCombe, G. P., Rouse, J., Trask, R. S., Withers, P. J. & Bond, I. P. (2012) X-ray damage characterisation in self-healing fibre reinforced polymers. *Composites Part A: Applied Science and Manufacturing*, 43(4), 613-620.
- Meschke, G. & Dumstorff, P. (2007) Energy-based modeling of cohesive and cohesionless cracks via X-FEM. *Computer Methods in Applied Mechanics and Engineering*, 196(21–24), 2338-2357.
- Miehe, C. & Bayreuther, C. G. (2007) On multiscale FE analyses of heterogeneous structures: from homogenization to multigrid solvers. *International Journal for Numerical Methods in Engineering*, 71(10), 1135-1180.
- Mishnaevsky Jr, L. & Brøndsted, P. (2009) Micromechanisms of damage in unidirectional fiber reinforced composites: 3D computational analysis. *Composites Science and Technology*, 69(7–8), 1036-1044.
- Mishnaevsky, L., Jr. (2012) Composite materials for wind energy applications: micromechanical modeling and future directions. *Computational Mechanics*, 50(2), 195-207.
- Moffat, A. J., Wright, P., Helfen, L., Baumbach, T., Johnson, G., Spearing, S. M. & Sinclair, I. (2010) In situ synchrotron computed laminography of damage in carbon fibre–epoxy [90/0]s laminates. *Scripta Materialia*, 62(2), 97-100.
- Molent, L., Callinan, R. J. & Jones, R. (1989) Design of an all boron/epoxy doubler reinforcement for the F-111C wing pivot fitting: Structural aspects. *Composite Structures*, 11(1), 57-83.
- Morishima, R. (2015) Prototyping a streamlined model build process. *The 9th UK Altair Technology Conference*.
- Müller, B. R., Léonard, F., Lange, A., Kupsch, A. & Bruno, G. (2015) X-Ray Refraction Techniques for Fast, High-Resolution Microstructure Characterization and Non-Destructive Testing of Lightweight Composites. *Materials Science Forum*, 825-826, 814-821.
- Nguyen, V. P., Lloberas-Valls, O., Stroeve, M. & Sluys, L. J. (2012a) Computational homogenization for multiscale crack modeling. Implementational and computational aspects. *International Journal for Numerical Methods in Engineering*, 89(2), 192-226.
- Nguyen, V. P., Stroeve, M. & Sluys, L. J. (2011) Multiscale continuous and discontinuous modeling of heterogeneous materials: a review on recent developments. *Journal of Multiscale Modelling*, 03(04), 229-270.

- Nguyen, V. P., Stroeve, M. & Sluys, L. J. (2012b) An enhanced continuous–discontinuous multiscale method for modeling mode-I cohesive failure in random heterogeneous quasi-brittle materials. *Engineering Fracture Mechanics*, 79(0), 78-102.
- Nguyen, V. P., Stroeve, M. & Sluys, L. J. (2012c) Multiscale failure modeling of concrete: Micromechanical modeling, discontinuous homogenization and parallel computations. *Computer Methods in Applied Mechanics and Engineering*, 201–204(0), 139-156.
- Novák, J., Kučerová, A. & Zeman, J. (2012) Compressing random microstructures via stochastic Wang tilings. *Physical Review E*, 86(4), 040104.
- Oden, J. T., Belytschko, T., Babuska, I. & Hughes, T. J. R. (2003) Research directions in computational mechanics. *Computer Methods in Applied Mechanics and Engineering*, 192(7–8), 913-922.
- Ooi, E. T. & Yang, Z. J. (2009) Modelling multiple cohesive crack propagation using a finite element–scaled boundary finite element coupled method. *Engineering Analysis with Boundary Elements*, 33(7), 915-929.
- Ooi, E. T. & Yang, Z. J. (2011) Modelling crack propagation in reinforced concrete using a hybrid finite element–scaled boundary finite element method. *Engineering Fracture Mechanics*, 78(2), 252-273.
- Orchard, M. (2015) Commercial aerospace evolution - technology and market place. *The 9th UK Altair Technology Conference*.
- Ostoja-Starzewski, M. (1998) Random field models of heterogeneous materials. *International Journal of Solids and Structures*, 35(19), 2429-2455.
- Ostoja-Starzewski, M. (2005) Scale effects in plasticity of random media: status and challenges. *International Journal of Plasticity*, 21(6), 1119-1160.
- Özdemir, I., Brekelmans, W. A. M. & Geers, M. G. D. (2008) computational homogenization for the thermo-mechanical analysis of heterogeneous solids. *Computer Methods in Applied Mechanics and Engineering*, 198(3-4), 602-613.
- Panchal, J. H., Kalidindi, S. R. & McDowell, D. L. (2012) Key computational modeling issues in Integrated Computational Materials Engineering. *Computer-Aided Design*, (0).
- Park, K. & Paulino, G. H. (2012) Computational implementation of the PPR potential-based cohesive model in ABAQUS: Educational perspective. *Engineering Fracture Mechanics*, 93, 239-262.
- Pham, H. B., Al-Mahaidi, R. & Saouma, V. (2006) Modelling of CFRP–concrete bond using smeared and discrete cracks. *Composite Structures*, 75(1–4), 145-150.
- Pham, K., Kouznetsova, V. G. & Geers, M. G. D. (2013) Transient computational homogenization for heterogeneous materials under dynamic excitation. *Journal of the Mechanics and Physics of Solids*, 61(11), 2125-2146.
- Phu Nguyen, V., Lloberas-Valls, O., Stroeve, M. & Johannes Sluys, L. (2010) On the existence of representative volumes for softening quasi-brittle materials – A failure zone averaging scheme. *Computer Methods in Applied Mechanics and Engineering*, 199(45–48), 3028-3038.
- Pyrz, R. (1994) Quantitative description of the microstructure of composites. Part I: Morphology of unidirectional composite systems. *Composites Science and Technology*, 50(2), 197-208.

- Rahman, S. & Chakraborty, A. (2011) Stochastic multiscale fracture analysis of three-dimensional functionally graded composites. *Engineering Fracture Mechanics*, 78(1), 27-46.
- Rau, C., Wagner, U., Pešić, Z. & De Fanis, A. (2011) Coherent imaging at the Diamond beamline I13. *physica status solidi (a)*, 208(11), 2522-2525.
- Reis, F. J. P. & Andrade Pires, F. M. (2013) An adaptive sub-incremental strategy for the solution of homogenization-based multi-scale problems. *Computer Methods in Applied Mechanics and Engineering*, 257(0), 164-182.
- Ren, W., Yang, Z., Sharma, R., Zhang, C. & Withers, P. J. (2015) Two-dimensional X-ray CT image based meso-scale fracture modelling of concrete. *Engineering Fracture Mechanics*, 133, 24-39.
- Requena, G., Fiedler, G., Seiser, B., Degischer, P., Di Michiel, M. & Buslaps, T. (2009) 3D-Quantification of the distribution of continuous fibres in unidirectionally reinforced composites. *Composites Part A: Applied Science and Manufacturing*, 40(2), 152-163.
- Réthoré, J., Gravouil, A. & Combescure, A. (2004) A stable numerical scheme for the finite element simulation of dynamic crack propagation with remeshing. *Computer Methods in Applied Mechanics and Engineering*, 193(42-44), 4493-4510.
- Richardson, A. (2015) Delivering robust engineering through simulation whilst launching 50 new products in 5 years. *The 9th UK Altair Technology Conference*.
- Roubin, E., Vallade, A., Benkemoun, N. & Colliat, J.-B. (2015) Multi-scale failure of heterogeneous materials: A double kinematics enhancement for Embedded Finite Element Method. *International Journal of Solids and Structures*, 52(0), 180-196.
- Rouse, J. E. (2012) Characterisation of impact damage in carbon fibre reinforced plastics by 3D X-ray tomography. *A Doctor of Engineering (EngD) Thesis, University of Manchester*.
- Ruggles, T. J., Rampton, T. M., Rose, S. A. & Fullwood, D. T. (2013) Reducing the microstructure design space of 2nd order homogenization techniques using discrete Fourier Transforms. *Mechanics of Materials*, 59(0), 14-23.
- Scott, A. E., Mavrogordato, M., Wright, P., Sinclair, I. & Spearing, S. M. (2011) In situ fibre fracture measurement in carbon-epoxy laminates using high resolution computed tomography. *Composites Science and Technology*, 71(12), 1471-1477.
- Seagraves, A. & Radovitzky, R. (2010) *Advances in Cohesive Zone Modeling of Dynamic Fracture*. Springer US.
- Sencu, R. M., Yang, Z. & Wang, Y. C. (2014) A multiscale stochastic fracture modelling calibration using Monte Carlo simulations. *Proceedings of the 22nd UK Conference of the Association for Computational Mechanics in Engineering*, (2014), 105-108.
- Sencu, R. M., Yang, Z. & Wang, Y. C. (2015) From micro to macro: simulating crack propagation in carbon fibre composites. *Structural Integrity and Durability of Advanced Composites*. Elsevier.
- Sencu, R. M., Yang, Z. & Wang, Y. C. (2016) An adaptive stochastic multi-scale method for cohesive fracture modelling of quasi-brittle heterogeneous materials under uniaxial tension. *Engineering Fracture Mechanics*.

- Shen, B. & Paulino, G. H. (2011) Identification of cohesive zone model and elastic parameters of fiber-reinforced cementitious composites using digital image correlation and a hybrid inverse technique. *Cement and Concrete Composites*, 33(5), 572-585.
- Shen, J., Mao, J., Reyes, G., Chow, C. L., Boileau, J., Su, X. & Wells, J. M. (2009) A Multiresolution Transformation Rule of Material Defects. *International Journal of Damage Mechanics*, 18(8), 739-758.
- Shen, L. & Xu, X. (2010) Multiscale stochastic finite element modeling of random elastic heterogeneous materials. *Computational Mechanics*, 45(6), 607-621.
- Simulia/Abaqus. - Abaqus analysis user's manual. Online version 6.12.
- Simulia/Abaqus. - Abaqus theory manual. Online version 6.12.
- Simulia/Abaqus. - Abaqus user subroutines reference manual. Online version 6.12.
- Singh, C. V. & Talreja, R. (2013) A synergistic damage mechanics approach to mechanical response of composite laminates with ply cracks. *Journal of Composite Materials*, 47(20-21), 2475-2501.
- Sket, F., Seltzer, R., Molina-Aldareguía, J. M., Gonzalez, C. & Llorca, J. (2012) Determination of damage micromechanisms and fracture resistance of glass fiber/epoxy cross-ply laminate by means of X-ray computed microtomography. *Composites Science and Technology*, 72(2), 350-359.
- Soltani, P., Johari, M. S. & Zarrebini, M. (2014) Effect of 3D fiber orientation on permeability of realistic fibrous porous networks. *Powder Technology*, 254(0), 44-56.
- Su, X., Yang, Z. & Liu, G. (2009) Monte Carlo Simulation of Complex 2D Cohesive Fracture in Random Heterogeneous Quasi-Brittle Materials. In: Yuan, Y., Cui, J. & Mang, H. (eds.) *Computational Structural Engineering*. Springer Netherlands.
- Su, X., Yang, Z. & Liu, G. (2010a) Finite Element Modelling of Complex 3D Static and Dynamic Crack Propagation by Embedding Cohesive Elements in Abaqus. *Acta Mechanica Sinica*, 23(3), 271-282.
- Su, X. T., Yang, Z. J. & Liu, G. H. (2010b) Monte Carlo simulation of complex cohesive fracture in random heterogeneous quasi-brittle materials: A 3D study. *International Journal of Solids and Structures*, 47(17), 2336-2345.
- Thuring, T., Abis, M., Wang, Z., David, C. & Stampanoni, M. (2014) X-ray phase-contrast imaging at 100 keV on a conventional source. *Sci Rep*, 4, 5198.
- Tjahjanto, D. D., Eisenlohr, P. & Roters, F. (2010) A novel grain cluster-based homogenization scheme. *Modelling and Simulation in Materials Science and Engineering*, 18(1), 015006.
- Trias, D., Costa, J., Fiedler, B., Hobbiebrunken, T. & Hurtado, J. E. (2006a) A two-scale method for matrix cracking probability in fibre-reinforced composites based on a statistical representative volume element. *Composites Science and Technology*, 66(11-12), 1766-1777.
- Trias, D., Costa, J., Mayugo, J. A. & Hurtado, J. E. (2006b) Random models versus periodic models for fibre reinforced composites. *Computational Materials Science*, 38(2), 316-324.

- Trias, D., Costa, J., Turon, A. & Hurtado, J. E. (2006c) Determination of the critical size of a statistical representative volume element (SRVE) for carbon reinforced polymers. *Acta Materialia*, 54(13), 3471-3484.
- Tvergaard, V. & Hutchinson, J. W. (1992) The relation between crack growth resistance and fracture process parameters in elastic-plastic solids. *Journal of the Mechanics and Physics of Solids*, 40(6), 1377-1397.
- Unger, J. F. (2013) An FE2-X1 approach for multiscale localization phenomena. *Journal of the Mechanics and Physics of Solids*, 61(4), 928-948.
- Vaughan, T. J. & McCarthy, C. T. (2011) Micromechanical modelling of the transverse damage behaviour in fibre reinforced composites. *Composites Science and Technology*, 71(3), 388-396.
- Verhoosel, C. V., Remmers, J. J. C., Gutiérrez, M. A. & de Borst, R. (2010) Computational homogenization for adhesive and cohesive failure in quasi-brittle solids. *International Journal for Numerical Methods in Engineering*, 83(8-9), 1155-1179.
- Vignoles, G. L., Donias, M., Mulat, C., Germain, C. & Delesse, J.-F. (2011) Simplified marching cubes: An efficient discretization scheme for simulations of deposition/ablation in complex media. *Computational Materials Science*, 50(3), 893-902.
- Viguié, J., Latil, P., Orgéas, L., Dumont, P. J. J., Rolland du Roscoat, S., Bloch, J. F., Marulier, C. & Guiraud, O. (2013) Finding fibres and their contacts within 3D images of disordered fibrous media. *Composites Science and Technology*, 89(0), 202-210.
- Volant, S., Martin Magniette, M.-L. & Robin, S. (2012) Variational Bayes approach for model aggregation in unsupervised classification with Markovian dependency. *Computational Statistics & Data Analysis*, 56(8), 2375-2387.
- Wang, H. W., Zhou, H. W., Ji, H. W. & Zhang, X. C. (2014) Application of extended finite element method in damage progress simulation of fiber reinforced composites. *Materials & Design*, 55(0), 191-196.
- Wang, J., Kobayashi, E. & Sakuma, I. (2015a) Coarse-to-fine dot array marker detection with accurate edge localization for stereo visual tracking. *Biomedical Signal Processing and Control*, 15, 49-59.
- Wang, X. F., Yang, Z. J., Yates, J. R., Jivkov, A. P. & Zhang, C. (2015b) Monte Carlo simulations of mesoscale fracture modelling of concrete with random aggregates and pores. *Construction and Building Materials*, 75, 35-45.
- Wenz, J., Schleede, S., Khrennikov, K., Bech, M., Thibault, P., Heigoldt, M., Pfeiffer, F. & Karsch, S. (2015) Quantitative X-ray phase-contrast microtomography from a compact laser-driven betatron source. *Nat Commun*, 6, 7568.
- Whitacre, W. W. & Czabaj, M. W. (2015) Automated 3D Digital Reconstruction of Fiber Reinforced Polymer Composites. *AIAA Guidance, Navigation, and Control Conference*. American Institute of Aeronautics and Astronautics.
- Williams, T. O. & Baxter, S. C. (2006) A framework for stochastic mechanics. *Probabilistic Engineering Mechanics*, 21(3), 247-255.
- Withers, P. J., Lopez-Crespo, P., Kyrieleis, A. & Hung, Y. C. (2012) Evolution of crack-bridging and crack-tip driving force during the growth of a fatigue crack in a Ti/SiC

- composite. *Proceedings of the Royal Society A: Mathematical, Physical and Engineering Sciences*, 468(2145), 2722-2743.
- Wright, P., Moffat, A. J., Renault, A., Sinclair, I. & Spearing, S. M. (2009) High resolution computed tomography for modelling laminate damage. *ICCM17proceedings*.
- Wu, X., Zhang, J.-q., Huang, X. & Liu, D.-l. (2013) Separable convolution template (SCT) background prediction accelerated by CUDA for infrared small target detection. *Infrared Physics & Technology*, 60, 300-305.
- Xie, D. & Waas, A. M. (2006) Discrete cohesive zone model for mixed-mode fracture using finite element analysis. *Engineering Fracture Mechanics*, 73(13), 1783-1796.
- Xu, Q., Chen, J., Li, J. & Wang, M. (2013) Multi-scale numerical model for simulating concrete material based on fractal theory. *Acta Mechanica Sinica*, 26(4), 344-352.
- Xu, X. F. & Chen, X. (2009) Stochastic homogenization of random elastic multi-phase composites and size quantification of representative volume element. *Mechanics of Materials*, 41(2), 174-186.
- Xu, X. F., Chen, X. & Shen, L. (2009) A Green-function-based multiscale method for uncertainty quantification of finite body random heterogeneous materials. *Computers & Structures*, 87(21-22), 1416-1426.
- Xu, X. F. & Graham-Brady, L. (2005) A stochastic computational method for evaluation of global and local behavior of random elastic media. *Computer Methods in Applied Mechanics and Engineering*, 194(42-44), 4362-4385.
- Yang, H. & Lindquist, W. B. (Year) Three-dimensional image analysis of fibrous materials. *In*, 2000. 275-282.
- Yang, Z. & Chen, J. (2004) Fully automatic modelling of cohesive discrete crack propagation in concrete beams using local arc-length methods. *International Journal of Solids and Structures*, 41(3-4), 801-826.
- Yang, Z. & Xu, F. X. (2008) A heterogeneous cohesive model for quasi-brittle materials considering spatially varying random fracture properties. *Computer Methods in Applied Mechanics and Engineering*, 197(45-48), 4027-4039.
- Yang, Z. J., Su, X. T., Chen, J. F. & Liu, G. H. (2009) Monte Carlo simulation of complex cohesive fracture in random heterogeneous quasi-brittle materials. *International Journal of Solids and Structures*, 46(17), 3222-3234.
- Yin, A., Yang, X. & Yang, Z. (2013) 2D and 3D Fracture Modeling of Asphalt Mixture with Randomly Distributed Aggregates and Embedded Cohesive Cracks. *Procedia IUTAM*, 6, 114-122.
- Young, P. G., Beresford-West, T. B. H., Coward, S. R. L., Notarberardino, B., Walker, B. & Abdul-Aziz, A. (2008) *An efficient approach to converting three-dimensional image data into highly accurate computational models* (Vol. 366).
- Yu, B., Blanc, R., Soutis, C. & Withers, P. J. (2015a) Evolution of damage during the fatigue of 3D woven glass-fibre reinforced composites subjected to tension-tension loading observed by time-lapse X-ray tomography. *Composites Part A: Applied Science and Manufacturing*.

- Yu, B., Bradley, R. S., Soutis, C., Hogg, P. J. & Withers, P. J. (2015b) 2D and 3D imaging of fatigue failure mechanisms of 3D woven composites. *Composites Part A: Applied Science and Manufacturing*, 77, 37-49.
- Zhuang, X., Wang, Q. & Zhu, H. (2015) A 3D computational homogenization model for porous material and parameters identification. *Computational Materials Science*, 96, 536-548.